



Universidade do Minho  
Escola de Engenharia

Lyudmil Valentinov Todorov

Multiscale morphology evolution of PET  
and its nanocomposites under deformation

Lyudmil Valentinov Todorov  
Multiscale morphology evolution of PET  
and its nanocomposites under deformation





Universidade do Minho  
Escola de Engenharia

Lyudmil Valentinov Todorov

Multiscale morphology evolution of PET  
and its nanocomposites under deformation

Tese de Doutoramento  
Ciência e Engenharia de Polímeros e Compósitos

Trabalho efectuado sob a orientação de  
Professor Doutor Júlio César Machado Viana  
Professora Doutora Carla Isabel Domingues Correia  
Martins

Dezembro de 2010

*На родителите ми*

*To my parents*





## Acknowledgements

I would like to extend my gratitude to the following individuals and institutions for their valuable contribution in the completion of this thesis:

Prof. Júlio C. Viana, scientific supervisor, for the continuous support, the scientific guidance which contributed to the coherence and value-added scientific research.

Prof. Carla I. Martins, co-supervisor, for provided support and guidance throughout the course of this research work.

Dr. Iva Pashkuleva, for her friendship and backing up in most difficult moments of my long stay in Portugal. I hope she will continue to be meritorious of her unconditional trust.

I am thankful to all the researchers, administrative officials for their direct and indirect contribution for this work as well as for their friendly acceptance and help.

I am appreciative to the hosting institution the Institute of Polymer and Composites/I3N at University of Minho for the facilities and equipment provided for this research.

I am indebted to the Portuguese Foundation for Science and Technology (Fundação para a Ciência e a Tecnologia), FCT, for the financial support through PhD student grant - SFRH/BD/44917/2008.



# Resumo

O presente trabalho pretende investigar os mecanismos de desenvolvimento estrutural do PET e nanocompósitos de PET, durante a aplicação de deformações uniaxiais. São objectivos de trabalho estudar:

- a influência estatística das variáveis de estiramento no desenvolvimento estrutural do PET em deformações efectuados a temperaturas acima de  $T_g$  (patamar de borracha),
- o efeito da morfologia inicial do PET no seu desenvolvimento após deformação a frio,
- o efeito da utilização de nanocargas (montemorilonite, MMT, dióxido de titânio,  $TiO_2$ , e dióxido de sílica,  $SiO_2$ ) na morfologia e propriedades do PET reforçado (propriedades térmicas e mecânicas),
- a influência de diferentes tipos de nanocargas (MMT,  $TiO_2$ , e  $SiO_2$ ) no comportamento à deformação do PET e na sua evolução estrutural durante deformações a frio.

Esta investigação procura propor modelos estruturais multi-escala adequados à compreensão da evolução estrutural do PET e dos seus nanocompósitos durante a aplicação de esforços uniaxiais.

A influência estatística das variáveis de estiramento: (temperatura,  $T_{st}$ , taxa de deformação,  $\dot{\epsilon}_{st}$ , e razão de estiramento,  $\lambda_{st}$ ) no desenvolvimento estrutural do PET em deformações efectuadas no patamar de borracha do material (acima de  $T_g$ ) foi investigada através das técnicas de WAXD, birrefringência e DSC. Concluiu-se que: i) a transformação da fase amorfa em mesofase é controlada maioritariamente por  $\lambda_{st}$  e a interacção entre  $\lambda_{st}$  e  $\dot{\epsilon}_{st}$ ; ii) o fenómeno de cristalização induzida por deformação é governado pela  $T_{st}$ ,  $\lambda_{st}$  e a interacção entre ambos, o mesmo acontecendo para os nível de orientação molecular; iii) a temperatura de transição vítrea é governada pela  $\lambda_{st}$  e a sua interacção com  $T_{st}$ , no entanto, a contribuição individual de  $T_{st}$  é estatisticamente baixa; iv) a influência sobre a temperatura de cristalização a frio,  $T_{cc}$ , está associada a  $T_{st}$  seguida de  $\lambda_{st}$  e a interacção entre ambas.

O estudo sobre a influência do estado morfológico inicial na subsequente evolução estrutural do PET durante o estiramento uniaxial, a frio, foi efectuado usando dois tipos de amostras: (i) quasi-amorfa, QA, e (ii) semicristalina, SC, neste caso, com ordem cristalina 2D e 3D, respectivamente. A evolução estrutural foi acedida através da deformação uniaxial das amostras em simultâneo com a sua caracterização *in situ* por WAXS. As amostras QA e SC com ordem 2D evoluem seguindo 3 etapas: i) Etapa I, a um nível de orientação quase constante, uma pequena quantidade da fase amorfa desenvolve-se para mesofase; ii) Etapa II, há um rápido aumento da orientação do polímero, acompanhado pelo aumento significativo da mesofase. Na amostra QA há também a formação de uma mesofase periódica. Finalmente, iii) na Etapa III, a

orientação média do polímero atinge um patamar máximo, verificando-se a existência de relaxação parcial da mesofase periódica e da mesofase, no caso da amostra QA, enquanto que a amostra semicristalina evolui para uma estrutura 3D. A evolução da amostra semicristalina de ordem 3D consiste na contínua, mas lenta, orientação da fase cristalina e no aumento da fracção mássica de mesofase.

Os nanocompositos de PET com MMT, TiO<sub>2</sub>, e SiO<sub>2</sub> foram preparados através de diferentes processos de mistura por fusão, respectivamente: i) moldação por injeção, IM, ii) moldação por extrusão seguida de injeção, MEI e iii) utilizado um mini-misturador assimétrico de polímeros, MAP. Pela análise de SAXS, os nanocompósitos de PET com 3wt% de MMT, apresentam a existência de uma morfologia intercalada do MMT quando as técnicas de IM e MEI são utilizadas e uma melhor dispersão/desaglomeração do TiO<sub>2</sub> e do SiO<sub>2</sub> para MEI, comparativamente com MI. Os resultados de TEM sobre PET com 0.3wt% de nanopartículas, processados por MAP, mostram que a estrutura dos MMTs no compósito é dependente do tamanho dos aglomerados em pó, isto é, para aglomerados de pequena dimensão é obtida uma estrutura tactoide enquanto que para aglomerados de maiores dimensões é obtida uma estrutura intercalada. No caso de compósitos com TiO<sub>2</sub> ou SiO<sub>2</sub> é obtida uma boa dispersão. Comparativamente ao PET virgem, a incorporação de nanopartículas teve como efeito: i) o aumento da degradação do PET; ii) a redução de T<sub>g</sub> do polímero; iii) actuam como agente nucleante, independentemente do seu tipo; iv) reduzem a deformabilidade do PET para nanocompósitos com 3wt% e aumentam para os de 0.3wt%. Neste último caso, o aumento é mais significativo quanto menor for a dimensão das nanocargas incorporadas e também se estas forem esféricas.

O estudo da evolução estrutural multi-escala de nanocompósitos de PET foi efectuado a partir de experiências *in situ* de WAXS/SAXS. Concluiu-se que, independentemente do tipo de nanopartículas usadas, existem três etapas de desenvolvimento: Etapa I, antes da formação de pescoço, em que uma pequena percentagem de fase amorfa é transformada em mesofase, a um nível quase constante de orientação; Etapa II, coincidente com a propagação do pescoço, onde existe um rápido aumento da orientação molecular e da mesofase e o aparecimento de mesofase periódica. Simultaneamente é observado o aparecimento de fissuras na matriz e vazios entre os aglomerados de partículas. Na Etapa III, pescoço, corresponde ao aumento de fissuras e vazios e à estabilização da orientação molecular num patamar máximo. Há um ligeiro aumento da mesofase e é atingido o máximo de mesofase periódica. Em comparação com o PET, todos os tipos de nanocompositos mostraram: o aumento da quantidade de mesofase e o máximo da mesofase periódica formada a mais baixa deformação; o atraso no crescimento de fissuras no polímero; igual orientação máxima no final da deformação. Baseado nestes resultados foram sugeridos modelos estruturais multi-escala.

# Abstract

The present work deals with the investigation of the structural evolution mechanisms of PET and its nanocomposites under uniaxial deformation. The study is focused on:

- the statistical influence of the stretching variables on the structure development of PET upon deformation in the rubbery state,
- the effect of initial morphological state on the structural evolution under deformation in the solid state,
- the effect of nanofillers (montmorillonite, MMT, titanium dioxide, TiO<sub>2</sub>, and silica dioxide, SiO<sub>2</sub>) on the morphology and final properties of reinforced PET (thermal and mechanical properties), and
- the influence of different types nanofillers on the deformation behaviour of PET and its structure evolution during solid state stretching.

This investigation aims at proposing multiscale structural models adequate to understand the morphological evolution of PET and its nanocomposites under uniaxial stretching.

The statistical influence of the stretching variables: (temperature,  $T_{st}$ , rate,  $\dot{\epsilon}_{st}$ , and ratio,  $\lambda_{st}$ ) on the structural development of PET during the rubbery state uniaxial stretching is investigated by means of WAXS, optical birefringence, BIR, and DSC. It is concluded that: i) the transformation of amorphous phase into mesophase is mainly controlled by  $\lambda_{st}$  and its interaction with  $\dot{\epsilon}_{st}$ ; ii) the strain-induced crystallization is governed by  $T_{st}$ ,  $\lambda_{st}$  and the interaction among them. The same is happening with the level of molecular orientation; iii) the glass transition temperature is governed by the  $\lambda_{st}$  and its interaction with  $T_{st}$ , however the individual contribution of  $T_{st}$  is statistically low; iv) the influence over the cold crystallization temperature,  $T_{cc}$ , is associated to  $T_{st}$ , followed by  $\lambda_{st}$  and the interaction among them.

The study of the influence of the initial morphological state on further structure evolution under solid state step uniaxial stretching was carried out using two types of samples: (i) a quasi-amorphous, QA, and (ii) a semi-crystalline with 2D and 3D crystalline order, SC, respectively. The structural evolution was assessed by *in situ* WAXS performed simultaneously to the uniaxial stretching of the samples. The initial QA and 2D crystalline order SC samples evolve following three stages, described as: *Stage I*, before neck, at almost constant orientation level, the amorphous phase evolves into mesophase; *Stage II*, neck formation, there is a fast increase of polymer molecular orientation accompanied by large formation of mesophase. In the case of QA sample it is also observed the formation of periodical mesophase. Finally, *Stage III*, necking propagation, is characterized by the leveling off of the average polymer molecular orientation. In

the case of the QA sample, a partial relaxation of periodical mesophase and mesophase is observed during this stage, while the SC sample evolves into a 3D crystalline order. The evolution of SC sample with 3D crystalline order mainly feature the continuous, but slow, increase of crystalline phase orientation and mesophase mass fraction.

PET nanocomposites with MMT, TiO<sub>2</sub>, and SiO<sub>2</sub> were prepared via different melt blending techniques, namely: i) direct injection moulding, DIM, ii) extrusion blending and injection moulding, EIM, and iii) asymmetric batch minimixer, ABM. SAXS analyses of PET 3 wt% nanocomposites revealed an intercalated MMT morphology for DIM and EIM, and also a better dispersion/deagglomeration of TiO<sub>2</sub> and SiO<sub>2</sub> for EIM than for DIM. The TEM results of PET 0.3 wt% nanocomposites processed via ABM shows that the structure of MMTs on the composite are dependent on the size of the powder agglomerate size, i.e., for agglomerates of small dimension, a tactoid morphologies is obtained while for larger dimensions of agglomerates an intercalated structure is observed. A good dispersion is obtained in the case of TiO<sub>2</sub> and SiO<sub>2</sub>. The comparison of the nanocomposites with neat PET, revealed that the incorporation of the nanofillers: i) increases the polymer matrix degradation, ii) reduces the glass transition temperature of the polymer; iii) act as nucleating agents, regardless of their type; iv) reduces the deformability of the nanocomposite when 3wt% of filler is used but enhances it with 0.3wt% of filler. In this last case a greater improvement on deformation is observed when nanofillers of smaller size and spherical shape are incorporated in the PET matrix.

Multiscale structure evolution of PET and its 0.3wt% nanocomposites during solid state uniaxial stretching were studied via *in situ* WAXS and SAXS. Despite the type of nanoreinforcements, three common stages were indentified: *Stage I*, before necking, is characterized by a small amount of amorphous phase evolving into mesophase at almost constant molecular orientation level; *Stage II*, at neck propagation, where a rapid increase of polymer molecular orientation is accompanied by a sharp increase of the mesophase and by the formation of a periodical mesophase; it is also observed the appearance of crazes in the polymer matrix, and voids within the nanoparticles agglomerates. *Stage III*, during necking, corresponds to the transformation of crazes and voids into micro-voids, at a plateau of average molecular orientation. The highest periodical mesophase content is achieved together with a slight increment of mesophase. In comparison to the neat PET structure evolution, all kind of nanocomposites showed: i) improved amount of mesophase and maximum periodical mesophase formed at earlier deformations; ii) retarded crazes widening/growing within the polymer bulk, and iii) similar maximum orientation level are achieved. Multiscale structures modelling are suggested based on the results obtained.

# Contents

<b>Acknowledgements</b> .....	v
<b>Resumo</b> .....	vii
<b>Abstract</b> .....	ix
<b>Contents</b> .....	xi
<b>List of symbols</b> .....	xix
<b>List of abbreviations</b> .....	xxi
<b>List of figures</b> .....	xxiii
<b>List of tables</b> .....	xxix
<b>Chapter I. Introduction</b> .....	1
1.1.1. History, market and applications .....	1
1.1.2. Characterization of PET .....	2
1.1.2.1. Synthesis .....	2
1.1.2.2. Molecular weight .....	3
1.1.2.3. Thermal properties .....	4
1.1.2.4. Crystallization behaviour .....	4
1.1.3. Morphology .....	4
1.2. Polymer nanocomposites, PNC .....	7
1.2.1. Definition .....	7
1.2.2. History, market and applications .....	7
1.2.3. Preparation methods .....	8
1.2.4. Why PNCs? .....	9
1.3. References .....	11
<b>Chapter II. Literature Review</b> .....	13
2.1. Structure development during the uniaxial stretching of amorphous PET .....	13
2.1.1. Stretching in the rubbery state .....	13
2.1.1.1. Conformational development .....	15
2.1.1.2. Chain orientation and relaxation .....	16
2.1.1.3. Mesophase as a precursor to strain induced crystallization .....	17
2.1.1.4. Strain induced crystallization .....	18
2.1.1.5. Mechanisms of structure development .....	24
2.1.1.6. Effect of the stretching parameters on the mechanical and thermal	



properties .....	28
2.1.2. Stretching in the solid state.....	29
2.1.2.1. Conformational development .....	29
2.1.2.2. Deformation mechanism.....	31
2.2. PET nanocomposites.....	33
2.2.1. Montmorillonite.....	33
2.2.2. PET/MMT nanocomposites.....	36
2.2.2.1. <i>In situ</i> polymerization .....	36
2.2.2.2. Solvent-assisted .....	38
2.2.2.3. Melt blending.....	38
2.2.3. Nanotitanium dioxide .....	43
2.2.4. PET/TiO <sub>2</sub> nanocomposites .....	45
2.2.5. Nanosilica .....	45
2.2.6. PET/SiO <sub>2</sub> nanocomposites.....	47
2.2.6.1. <i>In situ</i> polymerization .....	47
2.2.6.2. Solvent-assisted .....	50
2.2.6.3. Melt blending.....	51
2.2.6.4. Cryomilling blending.....	51
2.3 Deformation mechanism of PNC during uniaxial stretching.....	52
2.3.1. Polymer/1D nanocomposites deformation mechanism .....	52
2.3.2. Polymer/3D nanocomposites deformation mechanism .....	54
2.4. References.....	58
<b>Chapter III. Motivation, objectives and research approach .....</b>	<b>67</b>
3.1. Motivation and objectives.....	67
3.2. Research approach .....	68
3.2.1. Chapter V .....	69
3.2.2. Chapter VI .....	70
3.2.3. Chapter VII.....	71
3.2.4. Chapter VIII .....	72
3.2.5. Chapter IX .....	73
3.2.6. Chapter X .....	74
<b>Chapter IV. Materials and methods .....</b>	<b>77</b>
4.1. Materials .....	77

4.1.1. Poly (ethylene terephthalate), PET .....	77
4.1.2. Nanoparticles.....	77
4.1.2.1. 1D nanoparticles.....	78
4.1.2.2. 3D nanoparticles.....	78
4.2. PNC preparation techniques .....	79
4.2.1. Direct injection moulding, DIM.....	79
4.2.2. Extrusion blending followed by injection moulding, EIM .....	80
4.2.3. Asymmetric Batch Minimixer, ABM .....	80
4.3. Processing techniques.....	81
4.3.1. Compression moulding, CM .....	81
4.3.2. Stretching in rubbery state, SRS .....	81
4.3.3. Injection moulding, IM .....	83
4.4. Statistical tools.....	83
4.5. Characterization techniques.....	84
4.5.1. X-ray scattering techniques.....	84
4.5.1.1. Wide Angle X-ray Scattering, WAXS .....	84
4.5.1.2. WAXS data analysis.....	86
4.5.1.3. Small angle X-ray scattering, SAXS.....	91
4.5.2. In-plane optical birefringence, BIR.....	91
4.5.3. Intrinsic viscosity measurement.....	92
4.5.4. Differential scanning calorimetry, DSC.....	92
4.5.5. Dynamic mechanical analysis, DMA.....	92
4.5.6. Tensile testing .....	93
4.5.7. Transmission electron microscopy, TEM .....	93
4.5.8. Optical properties .....	94
4.5.8.1. Gloss.....	94
4.5.8.2. Haze.....	94
4.6. References .....	95

<b>Chapter V. Structure development of PET during uniaxial stretching above the glass transition temperature: study of the statistical influence of the stretching variables .....</b>	<b>97</b>
5.1. Introduction .....	98
5.2. Experimental.....	100
5.2.1. Material .....	100
5.2.2. Samples preparation .....	100

5.2.3. Wide angle X-ray scattering, WAXS .....	101
5.2.4. Optical birefringence, BIR .....	103
5.2.5. Differential scanning calorimetry, DSC .....	103
5.2.6. Statistical data treatment.....	104
5.3. Results and Discussion .....	104
5.3.1. As-moulded PET .....	104
5.3.2. Stretched PET samples .....	105
5.3.3. Statistical influence of the stretching variables on the structure developed.....	110
5.3.3.1. Phase mass fraction .....	111
5.3.3.2. Molecular orientation .....	112
5.3.3.3. Transition temperatures and degree of crystallinity .....	114
5.4. Conclusions.....	116
<b>Chapter VI. Solid state structural evolution of PET during step uniaxial stretching from different initial morphologies: an in situ WAXD study .....</b>	<b>121</b>
6.1. Introduction.....	122
6.2. Experimental.....	123
6.2.1. Material .....	123
6.2.2. Samples .....	123
6.2.3. Solid state stretching and in situ WAXS characterization.....	124
6.2.4. WAXS data analysis.....	125
6.2.4.1. Phase mass fraction .....	125
6.2.4.2. Polymer molecular orientation .....	126
6.2.4.3. Crystallite dimensions .....	127
6.3. Results and discussion .....	128
6.3.1. Structural evolution from quasi-amorphous morphologies.....	128
6.3.2. Structural evolution from semicrystalline morphologies .....	132
6.3.3. Structural models.....	138
6.4. Conclusions.....	141
6.5. References.....	143
<b>Chapter VII. Characterization of PET nanocomposites produced by different melt-based production methods .....</b>	<b>147</b>
7.1. Introduction.....	148
7.2. Experimental.....	149

7.2.1. Materials.....	149
7.2.2. Preparation of PET nanocomposites .....	149
7.2.2.1. Extrusion blending .....	150
7.2.2.2. Injection moulding .....	150
7.2.3. Determination of PET intrinsic viscosity .....	150
7.2.4. Characterization techniques .....	151
7.2.4.1. Small angle X-ray scattering, SAXS.....	151
7.2.4.2. Differential scanning calorimetry, DSC.....	152
7.2.4.3. Mechanical characterization.....	152
7.2.4.4. Optical properties .....	152
7.3. Results and discussion .....	153
7.3.1. Intrinsic viscosity .....	153
7.3.2. X-ray diffraction studies .....	154
7.3.3. Differential scanning calorimetry, DSC.....	156
7.3.4. Mechanical Characterization.....	159
7.3.4.1. Structure-mechanical property relationships.....	161
7.3.5. Optical properties .....	162
7.3.5.1. Gloss characterization .....	162
7.3.5.2. Haze.....	163
7.4. Conclusions .....	164
7.5 References .....	165

***Chapter VIII. Characterization of PET nanocomposites produced by asymmetric batch mixer***

.....	167
8.1. Introduction .....	168
8.2. Materials and preparation of PNCs .....	168
8.2.1. Materials.....	168
8.2.2. Preparation of PET nanocomposites .....	169
8.2.3. Characterization .....	169
8.2.3.2. Transmission electron microscope, TEM.....	169
8.2.3.3. Dynamic mechanical analysis, DMA.....	169
8.2.3.4. Differential Scanning Calorimetry, DSC .....	170
8.2.3.5. Mechanical characterization.....	170
8.3. Results and discussion .....	170
8.3.1. Intrinsic viscosity .....	170

8.3.2. Transmission electron microscopy, TEM.....	170
8.3.3. Dynamic mechanical analysis, DMA.....	171
8.3.4. Thermal characterization.....	172
8.3.5. Mechanical behaviour.....	173
8.4. Conclusions.....	174
8.5. References.....	176
<b>Chapter IX. In situ WAXS/SAXS structural evolution study during uniaxial stretching of PET nanocomposites in solid state: PET/MMT nanocomposites.....</b>	<b>177</b>
9.1. Introduction.....	178
9.2. Experimental.....	179
9.2.1. Materials.....	179
9.2.2. Nanocomposites characterization.....	180
9.2.2.1. Low-angle region Wide Angle X-ray Scattering, WAXS.....	180
9.2.2.2. Transmission Electron Microscope, TEM.....	180
9.2.3. <i>In situ</i> synchrotron characterization.....	181
9.3. Results and discussion.....	182
9.3.1. Neat PET structure evolution by WAXS.....	182
9.3.2. PET/MMT nanocomposites.....	186
9.3.2.1. Nanocomposites morphology.....	186
9.3.2.2. Structure evolution by WAXS.....	186
9.3.3. Structure evolution by SAXS.....	190
9.4. Multi scale structure evolution model.....	191
9.4.1. Multiscale structure evolution of neat PET.....	191
9.4.2. Multiscale structure evolution of PET/MMT nanocomposites.....	193
9.5. Conclusions.....	195
9.6. References.....	196
<b>Chapter X. In situ WAXS/SAXS structural evolution study during uniaxial stretching of PET nanocomposites in solid state: PET/SiO<sub>2</sub> and PET/TiO<sub>2</sub> nanocomposites.....</b>	<b>201</b>
10.1. Introduction.....	202
10.2. Experimental.....	203
10.2.1. Materials.....	203
10.2.2. Transmission Electron Microscope, TEM.....	203
10.2.3. <i>In situ</i> synchrotron characterization.....	204

10.3. Results and discussion .....	206
10.3.1. Nanocomposites morphology.....	206
10.3.2. Structure evolution by WAXS .....	206
10.3.3. Structure evolution by SAXS.....	211
10.4. Multi scale structure evolution model .....	212
10.5. Conclusions .....	213
10.6. References .....	214
<b>Chapter XI. Conclusions.....</b>	<b>217</b>
<b>Appendix.....</b>	<b>223</b>
A.1. Datasheet of Poly (ethylene terephthalate), PET S41T .....	224
A.2. Datasheet of Poly (ethylene terephthalate), PET T74 F9 .....	225
A.3. DSC thermographs of PET T74 F9 .....	226
A.4. Datasheet of Nanofil 5, MMT5 .....	227
A.5. Datasheet of Nanofil 32, MMT32 .....	228
A.6. Datasheet of Nanofil 2, MMT2 .....	229
A.7. Datasheet of AEROXIDE® TiO <sub>2</sub> P 25, TiO <sub>2</sub> .....	230
A.8. Datasheet of AEROSIL® 200, SiO <sub>2</sub> .....	231
A.9. List of publications .....	232

## List of symbols

$T_{st}$ [C°]	<i>Stretching temperature</i>
$V$ [mm.min <sup>-1</sup> ]	<i>Stretching velocity</i>
$\dot{\epsilon}_{st}$ [s <sup>-1</sup> ]	<i>Stretching rate</i>
$\lambda_{st}$ [a.u.]	<i>Stretching ratio</i>
$l_0$ [mm]	<i>Initial length of tensile bar</i>
$d$ [mm]	<i>Displacement</i>
$f_{av}$ [a.u.]	<i>Average polymer orientation</i>
$f_{am}$ [a.u.]	<i>Amorphous phase orientation</i>
$f_c$ [a.u.]	<i>Crystallite orientation calculated</i>
$T_g$ [°C]	<i>Glass transition temperature</i>
$T_{cc}$ [°C]	<i>Cold crystallization peak temperature</i>
$T_m$ [°C]	<i>Melting peak temperature</i>
$\Delta H_{cc}$ [J.g <sup>-1</sup> ]	<i>Enthalpy of cold crystallization</i>
$\Delta H_m$ [J.g <sup>-1</sup> ]	<i>Enthalpy of melting</i>
$\Delta H_f$ [J.g <sup>-1</sup> ]	<i>Enthalpy of 100 % crystalline PET</i>
$\chi_c$ [%]	<i>Degree of crystallinity</i>
$\phi$ [°]	<i>Azimuthal angle</i>
$\Theta$ [°]	<i>Diffraction angle</i>
$I$ [a.u.]	<i>Diffacted intensity</i>
$\langle \cos\phi \rangle$	<i>Average angle that the normal makes with principal stretching direction</i>
$\rho$ [g.cm <sup>-3</sup> ]	<i>Solid density</i>
$M_w$ [g.mol <sup>-1</sup> ]	<i>Average molecular weight</i>
$\tan\delta$ [a.u.]	<i>Loss factor</i>
$E^{\perp}$ [GPa]	<i>Storage modulus</i>
$E$ [GPa]	<i>Elastic modulus</i>
$\sigma_y$ [MPa]	<i>Yield stress</i>
$\epsilon_b$ [%]	<i>Strain at break</i>
$\eta$ [dl.g <sup>-1</sup> ]	<i>Intrinsic viscosity</i>
$\eta_{red}$ [%]	<i>Percentage of reduction of intrinsic viscosity</i>
$\eta_x$ [dl.g <sup>-1</sup> ]	<i>Intrinsic viscosity of each of the processed specimens</i>
$\eta_{pristine}$ [dl.g <sup>-1</sup> ]	<i>Intrinsic viscosity of pristine PET granules</i>
$t$ [mm]	<i>Actual sample thickness</i>
$t_0$ [mm]	<i>Initial sample thickness</i>

*List of symbols*

---

$\sigma_N$ [MPa]	<i>Homogeneous stress</i>
F [KN]	<i>Force</i>
$A_0$ [mm <sup>2</sup> ]	<i>Initial tensile specimen cross-section area</i>
$D_{av}$ [nm]	<i>Average agglomerate diameter</i>
$t_{pl.}$ [nm]	<i>Approximate platelet thickness</i>
$d_i$ [nm]	<i>Main diameters of each particle</i>
n	<i>Number of considered agglomerates</i>
$d_{(hkl)}$ [nm]	<i>Spacing between diffraction lattice planes</i>
$A_{anis}^{eq}$ [a.u.]	<i>Area of the deconvoluted anisotropic peak in equatorial profile</i>
$A_{iso}^{mer}$ [a.u.]	<i>Area of the deconvoluted isotropic peak in meridional profile</i>
$A_{(10-3)}^{mer}$ [a.u.]	<i>Area of the deconvoluted (10-3) peak in meridional profile</i>
$A_{(010)}^{eq}$ [a.u.]	<i>Area of the deconvoluted (010) peak in equatorial profile</i>
$A_{(100)}^{eq}$ [a.u.]	<i>Area of the deconvoluted (100) peak in equatorial profile</i>
$A_{(-110)}^{eq}$ [a.u.]	<i>Area of the deconvoluted (-110) peak in equatorial profile</i>
$A_{total}$ [a.u.]	<i>Area of assumed as a total</i>



## List of abbreviations

ABM	<i>Asymmetric batch minimixer</i>
Aggl.	<i>Agglomerates</i>
Amor. [%]	<i>Amorphous phase mass fraction</i>
ANOVA	<i>Analysis of variance</i>
BIR [a.u.]	<i>In-plane optical birefringence</i>
CM	<i>Compression moulding</i>
Cryst. [%]	<i>Crystalline mass fraction</i>
CSRS	<i>Continuous uniaxial stretching in rubbery state</i>
DIM	<i>Injection moulding blending</i>
DMA	<i>Dynamic mechanical analysis</i>
DMT	<i>Dimethyl terephthalate</i>
DSC	<i>Differential scanning calorimetry</i>
EG	<i>Ethylene glycol</i>
EIM	<i>Extrusion and subsequent injection moulding</i>
FTIR	<i>Fourier transform infrared spectroscopy</i>
Meso. [%]	<i>Mesophase mass fraction</i>
MFI [g/10min]	<i>Melt flow index</i>
MMT	<i>Montmorillonite</i>
MMT2	<i>Nanofil 2</i>
MMT32	<i>Nanofil 32</i>
MMT5	<i>Nanofil 5</i>
oMMT	<i>Organically modified montmorillonite</i>
PET	<i>Poly(ethylene terephthalate)</i>
QA	<i>Quasi-amorphous</i>
rPET	<i>Recycled poly(ethylene terephthalate)</i>
SAXS	<i>Small angle X-ray scattering</i>
SC	<i>Semi-crystalline</i>
SEM	<i>Scanning electron microscopy</i>
TA	<i>Terephthalic acid</i>
TEM	<i>Transmission electron microscopy</i>
TGA	<i>Thermo-gravimetric analysis</i>
UTBD [g <sup>-1</sup> ]	<i>Untamped bulk density</i>
WAXS	<i>Wide angle X-ray scattering</i>

*List of abbreviations*

---

XRD      *X-ray diffraction*

## List of figures

<b>Figure 1.1.</b> Global consumption of PET (2007).....	2
<b>Figure 1.2.</b> World market for PET packaging (2006).....	2
<b>Figure 1.3.</b> Synthesis of PET: a) ethylene glycol, EG, with terephthalic acid, TA, and b) ethylene glycol, EG, and dimethyl terephthalate, DMT .....	3
<b>Figure 1.4.</b> Repeating unit of PET.....	3
<b>Figure 1.5.</b> Model of a lamellar stack; the crystalline regions are shaded. $z$ is the stretching direction of the film and the direction in which the load was applied. $\varnothing$ and $\Theta$ are the angles of the lamellar normal, the chain-axis in the crystalline layers, and the fibril-axis with respect to $z$ -axis. $d_2$ is the long period, $d_2a$ the thickness of the amorphous layer. $w$ is the width of the stack, $d_1 = d_2 \cos\varnothing$ is the periodicity in the stretching direction.....	5
<b>Figure 1.6.</b> Schematic presentation of semi-crystalline structure .....	5
<b>Figure 1.7.</b> Triclinic crystal structure of PET.....	6
<b>Figure 1.8.</b> a) Schematic representation of WAXS reflexes of oriented and semi-crystalline PET. b) unit cell plan which correspond to the equatorial scattering reflexes (010), (-110) and (100)..	6
<b>Figure 1.9.</b> Worldwide market for polymer PNC (2004).....	8
<b>Figure 2.1.</b> Basic features of the stress–strain behaviour of amorphous PET in the rubber state	14
<b>Figure 2.2.</b> Influence of stretching variables on the stress-strain curves: a) effect of stretching temperature at constant stretching rate ( $\dot{\epsilon} = 0.005 \text{ s}^{-1}$ ) and b) effect of stretching rate at constant stretching temperature ( $T = 95^\circ\text{C}$ ).....	15
<b>Figure 2.3.</b> Trans and gauche conformer's fraction as function of stretching ratio for amorphous films drawn at $80^\circ\text{C}$ and $2 \text{ cm}\cdot\text{min}^{-1}$ .....	16
<b>Figure 2.4.</b> True stress versus stretching ratio at three strain rates. The onset of crystallization, $E_1$ , and the onset of regime 2 crystallization, $E_2$ , are indicated .....	20
<b>Figure 2.5.</b> Variation of density and crystallinity with stretching ratio $2x$ at three strain rates ...	20
<b>Figure 2.6.</b> Plot of the variation in stretching ratio and crystallinity calculated from the sequence of X-ray diffraction patterns of the PET sample recorded during the stretching at $90^\circ\text{C}$ to a final stretching ratio 4:1. The arrow indicates first frame with detectable crystallinity and end of stretching).....	21
<b>Figure 2.7.</b> Schematic map of estimated chain relaxation rates as a function of temperature, illustrating changes in oriented crystallization behaviour.....	22
<b>Figure 2.8.</b> In-plane mechano-optical behaviour of LPET stretched with different types of deformation profiles, in uniaxial constrained width mode at $85^\circ\text{C}$ .....	24
<b>Figure 2.9.</b> Strain-induced “phase” diagram of PET during deformation at $70^\circ\text{C}$ and schematic	

diagrams of phase transition and structure development pathways as well as corresponding SAXS/WAXD patterns during PET deformation at 70°C in (A) zone I, (B) zone II, and (C) zone III (drawing not to scale). The cylinder in the nematic and smectic phases represents the mesogenic unit in PET with an aspect ratio of 2..... 25

**Figure 2.10.** Schematic kinetics of microstructure development in PET..... 26

**Figure 2.11.** Schematic diagrams to illustrate the evolution of superstructure during deformation of amorphous PET sample above T<sub>g</sub> (stretching at 90°C). The background color of the microfibril is varied from white to dark gray gradually. The darkness represents the density of the region (darker color indicates higher density). The microfibril is composed of oriented mesophase and tilted crystalline lamellae ..... 27

**Figure 2.12.** a) The load-strain curve and selected WAXD oriented images (after subtraction of the isotropic fraction). The arrows indicate the average position where each image was taken, b) The proposed molecular structural models for zone I, II, III-1, and III-2 ..... 28

**Figure 2.13.** Stress–strain behaviour of a necking tensile specimen..... 30

**Figure 2.14.** Schematic representation of the morphological changes: (a) nematic phase, (b) smectic phase and (c) triclinic structure..... 31

**Figure 2.15.** Schematic diagram of two possible packing models for the mesophase in PET. Z and c\* represent the stretching direction and the c\*- axis, respectively ..... 32

**Figure 2.16.** Typical stress-strain curve of an amorphous thermoplastic polymer ..... 33

**Figure 2.17.** Structure of layered silicates..... 34

**Figure 2.18.** Three types of nanocomposite structures: a) tactoid, b) intercalation, and c) exfoliation structure ..... 35

**Figure 2.19.** Two approaches of graft polymerization ..... 44

**Figure 2.20.** Schematic illustrations of three types of surface silanol ..... 46

**Figure 2.21.** Schematic of aggregate formation between adjacent fumed silica particles through hydrogen bonding among the silanol groups ..... 46

**Figure 2.22.** Schematic drawings of agglomerated nanoparticles dispersed in a polymer matrix..... 46

**Figure 2.23.** Schematic models of micromechanical deformation processes of the stacked MMT layers, tactoids, depending on the orientation (arrow indicates the load direction): a) splitting mode, b) opening mode and c) sliding mode ..... 53

**Figure 2.24.** Schematic deformation processes in the intercalated nanomorphology system (arrow indicates the load direction): (a) splitting mode, (b) opening mode and (c) sliding mode ..... 53

**Figure 2.25.** Single debonding process: PP/Al(OH)<sub>3</sub> polymer composite ..... 55

**Figure 2.26.** Multiple debonding process: PE/SiO<sub>2</sub> polymer composite ..... 57

**Figure 2.27.** Schematic illustration of energy dissipation and stress state during uniaxial

stretching.....	56
<b>Figure 2.28.</b> Schematic representations of the debonding process around 50 nm (left) and 12 nm (right) particle.....	56
<b>Figure 3.1.</b> Scheme of thesis research strategy .....	69
<b>Figure 3.2.</b> Scheme of research approach used in Chapter V.....	70
<b>Figure 3.3.</b> Scheme of research approach used in Chapter VI .....	71
<b>Figure 3.4.</b> Scheme of research approach used in Chapter VII.....	72
<b>Figure 3.5.</b> Scheme of research approach used in Chapter VIII.....	73
<b>Figure 3.6.</b> Scheme of research approach used in Chapter IX .....	74
<b>Figure 3.7.</b> Scheme of research approach used in Chapter X.....	74
<b>Figure 4.1.</b> Chemical fictionalization of MMTs: a) MMT5 and b)MMT32 and MMT2.....	78
<b>Figure 4.2.</b> ABM design .....	81
<b>Figure 4.3.</b> Asymmetrical rotor of ABM.....	81
<b>Figure 4.4.</b> Geometry of the rectangular tensile bar specimen.....	82
<b>Figure 4.5.</b> Geometry of the laterally gated rectangular plaques specimen .....	83
<b>Figure 4.6.</b> Geometry of the rectangular tensile bar specimen.....	83
<b>Figure 4.7.</b> Geometry of the rectangular tensile bar specimen.....	85
<b>Figure 4.8.</b> Geometry of curved axisymmetric shape tensile bar specimen.....	85
<b>Figure 4.9.</b> Intensity profiles extracted from the 2D WAXD patterns used for mass fraction calculation of QA samples at low strains: a) equatorial and b) meridional .....	87
<b>Figure 4.10.</b> Peak fitting with Gaussian peaks of intensity profiles extracted from the 2D WAXD patterns used for mass fraction calculation of QA samples at high strains: a) equatorial and b) meridional.....	88
<b>Figure 4.11.</b> Peak fitting with Gaussian peaks of intensity profiles extracted from the 2D WAXD patterns used for mass fraction calculation of SC samples at high strains: a) equatorial and b) meridional.....	89
<b>Figure 5.1.</b> WAXS patterns of PET samples stretched in the rubbery state.....	105
<b>Figure 5.2.</b> a) equatorial and b) meridional linear intensity profiles extracted from 2D WAXS pattern.....	106
<b>Figure 5.3.</b> (a) Percentage of mass fractions and (b) amorphous phase, $f_{am}$ , and average polymer, $f_{av}$ , orientations calculated from 2D WAXS patterns and polymer chains orientation determined by birefringence measurements, BIR.....	107
<b>Figure 5.4.</b> DSC thermograms obtained at 20 oC.min <sup>-1</sup> heating rate .....	109
<b>Figure 5.5.</b> Effect of stretching variables on the amorphous; mesophase and crystalline phase mass fractions: a) percent of contribution and b) effects graph .....	112

<b>Figure 5.6.</b> Effect of stretching variables on the level of amorphous phase orientation, $f_{am}$ , level of average polymer orientation, $f_{av}$ , and birefringence, BIR,; a) percent of contribution and b) effects graph.....	113
<b>Figure 5.7.</b> Effect of stretching variables on the glass transition temperature, $T_g$ ; the cold crystallization temperature, $T_{cc}$ ; and the degree of crystallinity, $\chi_c$ (calculated from DSC): a) percent of contribution and b) effects graph.....	115
<b>Figure 6.1.</b> Average polymer orientation, $f_{av}$ , evolution with strain and selected 2D WAXS patterns of samples QA1 and QA2. (fitted by Boltzmann function, $R^2 = 0.99$ ).....	129
<b>Figure 6.2.</b> Linear intensity profiles extracted from 2D WAXS patterns: a) equatorial and b) meridional of QA1; c) equatorial and d) meridional of QA2.....	130
<b>Figure 6.3.</b> Phase's mass fractions and amorphous phase orientation, $f_{am}$ , evolution of samples: a) QA1 and b) QA2. (fitted by Boltzmann function amorphous phase orientation curves, $R^2 = 0.99$ ).....	132
<b>Figure 6.4.</b> Average polymer orientation, $f_{av}$ , and selected 2D WAXS patterns collected during the stretching of SC1 (fitted by Boltzmann function, $R^2 = 0.99$ ) and SC2.....	133
<b>Figure 6.5.</b> Linear intensity profiles extracted from 2D WAXS patterns: sample SC1 a) equatorial and b) meridional, samples SC2 c) equatorial and d) meridional.....	135
<b>Figure 6.6.</b> Phase's mass fractions and amorphous phase, $f_{am}$ , and crystalline orientation, $f_c$ , evolution of samples: a) SC1( $f_{am}$ results fitted by Boltzmann function, $R^2=0.99$ ) and b) SC2.....	136
<b>Figure 6.7.</b> Changes of estimated crystal size from three nearly orthogonal planes (010), (100) and (-103) calculate by Scherer equation during uniaxial deformation from 2D WAXS patterns: a) SC1 and b) SC2.....	137
<b>Figure 6.8.</b> Schematic diagrams to illustrate the structural evolution during in solid state stop uniaxial stretching of PET with QA morphology.....	139
<b>Figure 6.9.</b> Schematic diagrams to illustrate the structural evolution during in solid state stop uniaxial stretching of PET with SC morphology with 2D crystalline order.....	140
<b>Figure 6.10.</b> Schematic diagrams to illustrate the structural evolution during in solid state stop uniaxial stretching of PET with SC morphology with 3D crystalline order.....	141
<b>Figure 7.1.</b> SAXS patterns for PET and PET composites processed by: a) direct injection moulding (inj) and b) by extrusion-injection moulding (ex inj).....	155
<b>Figure 7.2.</b> DSC thermograms at $20\text{ }^\circ\text{C}\cdot\text{min}^{-1}$ for PET and PET composites processed by: a) extrusion (ex); b) injection moulding (inj) and c) by extrusion-injection moulding (ex inj).....	156
<b>Figure 7.3.</b> Experimental stress-strain curves for pure PET and its nanocomposites processed by: a) direct injection moulding; and b) extrusion followed by injection moulding.....	160
<b>Figure 7.4.</b> Variation of yield stress, $\sigma_y$ , glass transition temperature, $T_g$ , and cold crystallization	

temperature, $T_{cc}$ .....	162
<b>Figure 7.5.</b> Gloss measurements of pure PET and its nanocomposites processed by: a) injection moulding (inj); and b) extrusion injection moulding (ex inj).....	163
<b>Figure 7.6.</b> Dependence of gloss and degradation ratio .....	163
<b>Figure 8.1.</b> TEM micrographs of nanocomposites: a) PET/MMT32, b) PET/MMT2, c) PET/TiO <sub>2</sub> and d) PET/SiO <sub>2</sub> .....	171
<b>Figure 8.2.</b> Effect of the nanofillers on the $E'$ and $\tan\delta$ peak from DMA.....	172
<b>Figure 8.3.</b> DSC thermograms at 20 °C.min <sup>-1</sup> heating rate for all stretched conditions.....	173
<b>Figure 8.4.</b> Experimental stress-strain curves .....	174
<b>Figure 9.1.</b> Neat PET normalized stress-strain curve and selected 2D WAXS patterns.....	183
<b>Figure 9.2.</b> <i>In situ</i> video images of neat PET sample: a) prior deformation, b)neck initiation, c)neck formation, d) neck propagation and e)tensile bar rupture .....	184
<b>Figure 9.3.</b> Linear intensity profiles extracted from 2D WAXS patterns of neat PET: a) equatorial and b) meridional .....	184
<b>Figure 9.4.</b> Neat PET phase fraction and average polymer orientation evolution .....	185
<b>Figure 9.5.</b> PET/MMT32 and PET/MMT2 nanocomposites normalized stress-strain curve and selected 2D WAXS patterns.....	187
<b>Figure 9.6.</b> Linear intensity profiles of: PET/MMT32 nanocomposite a) equatorial and b) meridional and PET/MMT2 nanocomposite: c)equatorial and d) meridional, extracted from 2D WAXS patterns .....	188
<b>Figure 9.7.</b> Phase fraction and average polymer orientation, $f_{av}$ , of: a) PET/MMT32 nanocomposites and b) PET/MMT2 nanocomposites .....	189
<b>Figure 9.8.</b> Selected 2D SAXS patterns and corresponding normalized strain, $\ln\lambda$ , obtained during the <i>in situ</i> SAXS characterization.....	191
<b>Figure 9.9.</b> Schematic diagram illustrates the multiscale structure evolution during in solid state uniaxial stretching of neat PET .....	192
<b>Figure 9.10.</b> Schematic diagram illustrates the multiscale structure evolution during in solid state uniaxial stretching of intercalated PET/MMT nanocomposites.....	193
<b>Figure 9.11.</b> Schematic diagram illustrates the multiscale structure evolution during in solid state uniaxial stretching of tactoid PET/MMT nanocomposites .....	194
<b>Figure 10.1.</b> PET/TiO <sub>2</sub> and PET/SiO <sub>2</sub> nanocomposites normalized stress-strain curves and selected 2D WAXS patterns.....	206
<b>Figure 10.2.</b> <i>In situ</i> video images of PET/TiO <sub>2</sub> and PET/SiO <sub>2</sub> nanocomposites: a) prior deformation, b)neck initiation, c)neck formation, d) neck propagation and e)tensile bar rupture .....	206

**Figure 10.3.** Linear intensity profiles extracted from 2D WAXS patterns of: PET/TiO<sub>2</sub> a) equatorial and b) meridional and PET/SiO<sub>2</sub> c) equatorial and d) meridional ..... 207

**Figure 10.4.** Phase fraction evolutions (amorphous, mesophase and periodical mesophase) and corresponding normalized strain-stress: a)PET/TiO<sub>2</sub> and b) PET/SiO<sub>2</sub> nanocomposites..... 208

**Figure 10.5.** Selected 2D SAXS patterns and corresponding normalized strain,  $\ln\lambda$ , obtained during the in situ SAXS characterization..... 211

**Figure 10.6.** Schematic diagram illustrates the multiscale structure evolution during in solid state uniaxial stretching of PET/3D (spherical) nanocomposites..... 212



## List of tables

<b>Table 1.1.</b> PET general properties.....	2
<b>Table 1.2.</b> PET unit cell parameters.....	5
<b>Table 4.1.</b> Technical specification of PET S41T.....	77
<b>Table 4.2.</b> Technical specification of PET T74 F9.....	77
<b>Table 4.3.</b> MMTs technical specification.....	78
<b>Table 4.4.</b> 3D nanoparticles technical specification.....	79
<b>Table 4.5.</b> Processing parameters of DIM used injection moulding.....	79
<b>Table 4.6.</b> Stretching program according to a L8 Taguchi orthogonal array.....	82
<b>Table 5.1.</b> Stretching program according to a L8 Taguchi orthogonal array.....	101
<b>Table 5.2.</b> Structural parameters of as-moulded PET.....	104
<b>Table 5.3.</b> DSC results.....	110
<b>Table 5.4.</b> Effect of stretching variables upon all assessed parameters (in bold are the main contributing factors; double arrows in factors means strong effect; for interactions the arrow size is related to the importance of the variation; horizontal arrows means no influence).....	115
<b>Table 6.1.</b> Structure parameters calculated from the 2D WAXS patterns.....	124
<b>Table 7.1.</b> Injection moulding processing parameters.....	150
<b>Table 7.2.</b> Percentage reduction of the intrinsic viscosity of the processed PET composite samples with respect to the virgin PET pellets.....	153
<b>Table 7.3.</b> DSC calculated parameters.....	157
<b>Table 7.4.</b> Mechanical test values.....	161
<b>Table 8.1.</b> Nanoparticles specifications.....	169
<b>Table 8.2.</b> Percent of reduction of intrinsic viscosity.....	170
<b>Table 8.3.</b> Thermo-mechanical parameters.....	172
<b>Table 8.4.</b> Thermo parameters.....	173
<b>Table 8.5.</b> Mechanical test values.....	174
<b>Table 9.1.</b> Nanoparticles specifications.....	180
<b>Table 9.2.</b> As-moulded PET/MMT nanocomposites.....	186
<b>Table 10.1.</b> Nanoparticles specifications.....	202
<b>Table 10.2.</b> PET nanocomposites.....	205





# CHAPTER I

## Introduction

### 1.1. Poly(ethylene terephthalate), PET

#### 1.1.1. History, market and applications

Poly(ethylene terephthalate), PET, belongs to the generic family of polyesters and finds its major commercial applications as fibres, bottles and films. PET was first developed to be used as synthetic fibres by British Calico Printers in 1941. The patent rights were then sold to DuPont and ICI who, in turn, sold regional rights to many other companies. Although originally produced for fibres, PET began to be used for packaging films in the mid 1960s and, in the early 1970s, for bottles [1].

PET global demand over the last 15 years marked a substantial growth, as it is shown in *Figure 1.1*. The outlook for 2020 is a growth of about 5.5 times, following the demand trend for films, bottles and fibres [2]. Particularly PET enjoys considerable growth as a packaging material as a replacement for glass, metal and other plastic materials. In many applications, PET is a commodity polymer competing directly with polyethylene, polypropylene and polystyrene in the markets of food and beverage packaging. PET is used to make containers for soft drinks, juices, alcoholic drinks, water, edible oils, household cleaners and other food and non-food applications. PET bottles for the carbonated soft drink and water industries play the most important role in the global consumption of PET, being responsible for 38% and 32%, respectively, of the world market of PET packaging (*Figure 1.2*) [3].

PET is widely implanted in industry due to its unique properties, which are listed in *Table 1.1*. Other noteworthy features of PET are:

- i) excellent gloss and clarity,
- ii) good processability,
- iii) good dimensional stability

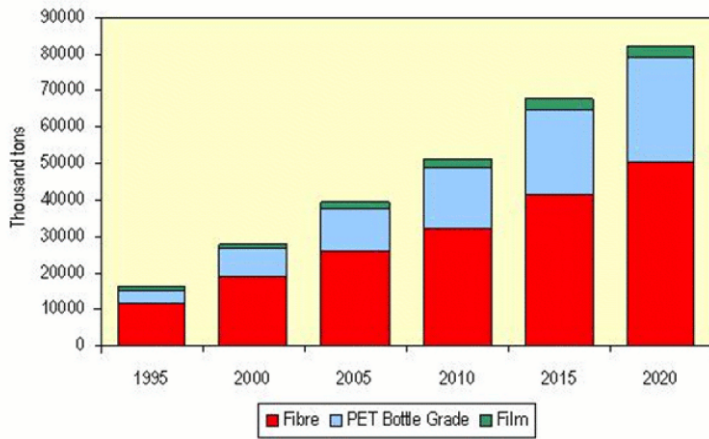


Figure 1.1. Global consumption of PET (2007) [2].

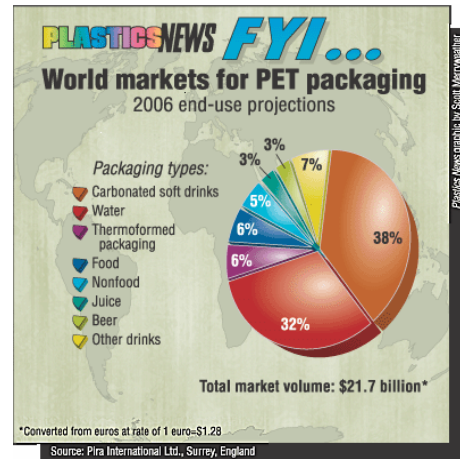


Figure 1.2. World market for PET packaging (2006)[3].

Table 1.1. PET general properties [1].

Property	Value
Density [g.cm <sup>-3</sup> ]	1.410
Continuous use temperature [°C]	120
3-Point flexural modulus [MPa]	19620
Tensile modulus [MPa]	16677
Tensile strength [MPa]	490.5
Elongation [%]	180
Permeability to oxygen at 20°C [cm <sup>3</sup> mm m <sup>-2</sup> d <sup>-1</sup> bar <sup>-1</sup> ]	1.16-1.55
Permeability to carbon dioxide at 20°C [cm <sup>3</sup> mm m <sup>-2</sup> d <sup>-1</sup> bar <sup>-1</sup> ]	5.81-9.68
Water vapor transmission at 20°C [g.mm m <sup>-2</sup> d <sup>-1</sup> bar <sup>-1</sup> ]	1.00

### 1.1.2. Characterization of PET

#### 1.1.2.1. Synthesis

PET is produced by two main reactions with industrial importance [1]: i) the reaction of the ethylene glycol, EG, with the purified terephthalic acid, TA, (**Figure 1.3.a**) and ii) the reaction of the ethylene glycol, EG, and the dimethyl terephthalate, DMT, (**Figure 1.3.b**). Both reactions involve two stages:

i) *prepolycondensation*, leads to products which mainly contain bis(2-hydroxyethyl) terephthalate, and low oligomers. The reaction of TA and EG is carried out at 230-260°C, under vacuum at 0.3-0.5 MPa. In the case of EG and DMT reaction (**Figure 1.3.b**) is performed under vacuum at temperatures from 160 to 180°C. The addition of a catalyst, most often metallic salts, such as Pb, Zn, Mn, Ca, or Cd acetate, is required.

ii) *polycondensation*, leads to PET; in most cases it is catalyzed by Sb<sub>2</sub>O<sub>3</sub> or GeO<sub>2</sub>. The process conditions are: temperature at 280-300°C and vacuum about 10-50 Pa, where the EG is removed.



### 1.1.2.3. Thermal properties

Amorphous PET exhibits a glass transition temperature,  $T_g$ , about 69°C (342 K) with a change in the heat capacity at  $T_g$ ,  $\Delta C_p$ , of 77.8 J.K<sup>-1</sup>.mol<sup>-1</sup> [4]. The cold crystallization temperature,  $T_{cc}$ , is around 150°C and the melting temperature,  $T_m$ , is 250°C [4]. PET 100% crystalline is characterized with a  $T_m$  of 280°C (533K) [4] and a heat of fusion,  $\Delta H_f$ , of 120 Jg<sup>-1</sup> [5].

### 1.1.2.4. Crystallization behaviour

PET is a slow crystallizing material, being a prime example of a polymer whose crystallinity can be totally controlled via processing. The crystallization behaviour of PET has been broadly studied [1, 6] and can be generally achieved by one of the following pathways:

i) *quiescent crystallization*: The amorphous PET is exposed to temperatures above the  $T_g$ . The thermal energy imparts mobility into the polymer chains, allowing for reorganization into a crystalline structure. When crystallization takes place PET becomes white and opaque, due to the growth of spherulitic structures large enough to interfere with visible light [7].

ii) *strain-induced crystallization, SIC*: If amorphous PET is stretched (oriented) under the proper conditions (i.e. stretching temperature (in range between its  $T_g$  and  $T_{cc}$ ), stretching rate and stretching ratio), the material will form a strain-induced crystallization morphology which has three dimensional packing order - triclinic unit cell [8-16]. The domain sizes of the crystals remain small enough for optical transparency to be maintained. This method is commercially important for processing of films, bottles, and other.

iii) *combination of strain induced and thermal crystallization*: PET sample with strain-induced crystallization morphology can be exposed to additional thermal energy, by annealing above its  $T_{cc}$ , in order to further crystallization [17]. The crystallization time in this case is between a few minutes to a few hundred milliseconds to a few milliseconds [6, 18, 19], depending on the annealing temperature and on the morphology stat of the sample. The annealing process promotes the growth of the crystals and residual stress relaxation that improves the uniformity and the thermal resistance of the products.

### 1.1.3. Morphology

Morphology of PET determined by X-ray diffraction is described as microfibrillar structure in stretched films [20-23]. This model assumes existence of stacks of crystalline layers separated by amorphous phase (**Figure 1.5**).

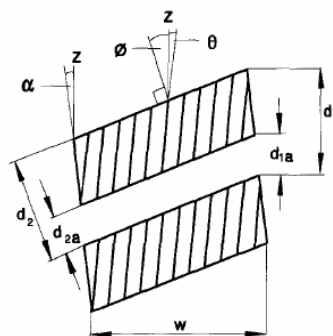


**Figure 1.5.** Model of a lamellar stack; the crystalline regions are shaded [24].

$z$  is the stretching direction of the film and the direction in which the load was applied.  $\phi$  and  $\Theta$  are the angles of the lamellar normal, the chain-axis in the crystalline layers, and the fibril-axis with respect to  $z$ -axis.  $d_2$  is the long period,  $d_{2a}$  the thickness of the amorphous layer.  $w$  is the width of the stack,  $d_1 = d_2 \cos\phi$  is the periodicity in the stretching direction.

The exact nature of the layers making up the fibrils remains unknown. Given the topology supported by the channels, it is unclear whether lamellar crystals can be formed from the folding of pre-oriented chains, at least in the absence of additional heat treatments that would be favourable for molecular mobility. It seems more likely to consider a crystal growth in the form of micelles with fringes [23] as shown in **Figure 1.6**.

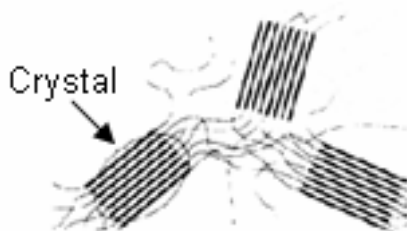


**Figure 1.6.** Schematic representation of a semi-crystalline structure [25].

A single triclinic crystal structure of PET is reported in the literature. The cohesive chains *trans* conformers are ensured by intermolecular forces resulting from the polarity of the ester groups and the regular stacking phenyls groups (**Figure 1.7**).

The unit cell parameters are described in **Table 1.2**, although slightly different crystalline unit cell parameters, depending on the thermo-mechanical history of the material, can be found in the literature [1]. The commonly used lattice parameters are those determined by Daubeny et al. [26] of PET fibre stretched at 75°C and annealed at 280°C (as listed in the Table).



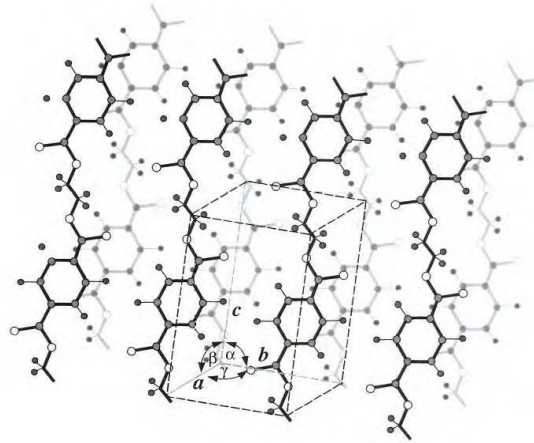


Figure 1.7. Triclinic crystal structure of PET [26].

Table 1.2. PET unit cell parameters [26].

<b>a</b> [Å]	<b>b</b> [Å]	<b>c</b> [Å]	<b><math>\alpha</math></b> [°]	<b><math>\beta</math></b> [°]	<b><math>\gamma</math></b> [°]
4.56	5.94	10.75	98.5	118	112

The theoretical 2D WAXS pattern of PET fibre as proposed by Gupte et al. [19] and following the Debye-Scherrer method is presented in **Figure 1.8a**) Peak reflections are represented as diffraction spots irregularly distributed in respect to the stretching direction. The main equatorial crystalline planes of PET unit cell are (010) at  $2\theta = 17.3^\circ$ , (-110) at  $2\theta = 22.5^\circ$ , and (100) at  $2\theta = 25.7^\circ$  [27], as represented in **Figure 1.8b**). Those reflections are related to the planes whose normal is almost collinear to the stretching direction and are placed at the equatorial. On the other hand the (-103) at  $2\theta = 26.6^\circ$  [28] and (-105) at  $2\theta \approx 43^\circ$  [27], which are assumed to be respectively third and fifth order from the same set of lattice planes [20], are related to the planes whose normal is almost perpendicular to the stretching direction and are placed at the meridian.

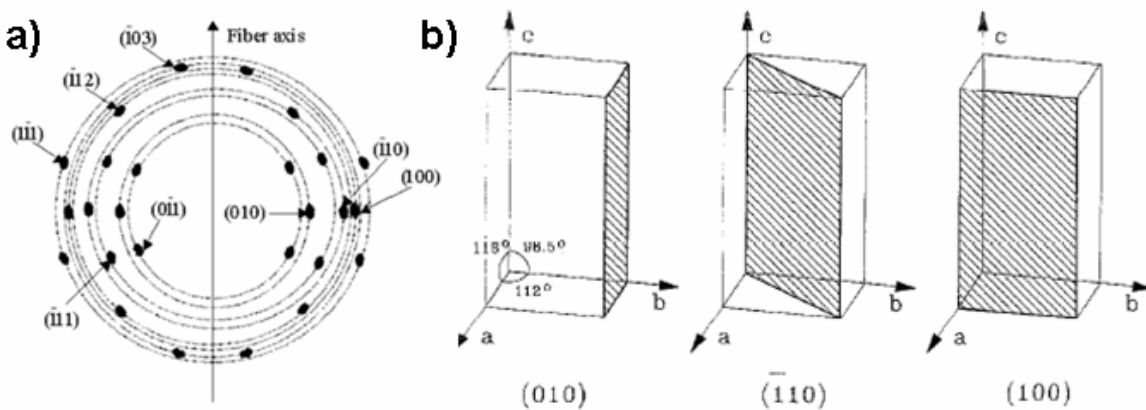


Figure 1.8. a) Schematic representation of WAXS reflexes of oriented and semi-crystalline PET [19]. b) unit cell planes which correspond to the equatorial scattering reflexes (010), (-110) and (100) [27].

## 1.2. Polymer nanocomposites, PNC

### 1.2.1. Definition

PNC consists of a polymeric material, e.g. thermoplastics, thermosets or elastomers, and a reinforcing nanoscale material, that is the nanoparticle. Nanoparticles are usually inorganic materials that have at least one dimension in the nanometer scale, from 1 nm up to 100 to 200 nm. Nanoparticles are divided into three main types depending on the number of dimensions in the nanometer scale [29]:

- i) *one dimension, 1D*, such as the platelet-like shape nanofillers with thickness of one to a few nanometers and hundreds to thousands nanometers length. Examples are nanoclays mainly MontMorillonite, MMT, and mica;
- ii) *two dimensions, 2D*, elongated structures, for instance the carbon nanotubes, which can be multiwall nanotubes, and single-wall nanotubes;
- iii) *three dimensions, 3D*, isodimensional nanoparticles, most commonly different oxides with spherical shape, for instance nanosilica, SiO<sub>2</sub>, nanotitanium dioxide, TiO<sub>2</sub>, nanoaluminum oxide, Al<sub>2</sub>O<sub>3</sub>, nanozirconium oxide, ZnO, and others.

In order to enhance the compatibility between the polymer, hydrophobic, and inorganic nanofillers, hydrophilic, [30], nanoparticles surface can be organically modified. The most common way for that is to attach suitable organic groups to the surface atoms which can result in favourable effects as:

- i) stabilization of nanoparticles against agglomeration,
- ii) compatibility improvement between nanoparticles and polymer matrix,
- iii) dispersion/deagglomeration/delamination enhancement.

### 1.2.2. History, market and applications

Layered silicate nanoclays were referenced for the first time in 1950's. In 1986 Toyota's Central Research and Development Laboratories began working with polyamide/nanoclay PNCs and this technology began to be studied widely [31]. Nowadays the most used nanoclay is MMT.

In 1941 Degussa patented a high temperature hydrolysis process of metallic oxides to produce extremely fine oxide particle, belonging to the class of 3D nanofillers as nanotitanium dioxide, TiO<sub>2</sub>, and nanosilica, SiO<sub>2</sub>, frequently termed fumed silica. This technology was converted into large scale production in the 1950s [29].

PNCs have been recognized as the next great frontier of materials for packaging. These materials were developed to improve barrier performance to gases such as oxygen and carbon dioxide. It also enhances the barrier performance to ultraviolet rays, as well as adding strength, stiffness, dimensional stability, and heat resistance. New packaging's created with this

technology demonstrate an increased shelf life and are less likely to shatter. PNC will offer these improved characteristics at competitive prices. It will also make them attractive for use in food, beverage and pharmaceutical packaging applications. In 2001, nearly 453 tonnes of nanocomposite materials were used in the packaging industry and by 2011, the market in the United States is expected to be around 453515 tonnes for rigid and flexible packaging [32]. **Figure 1.9.** shows the worldwide market of PNC, representing the very fast increase in demand of PNC, in particular with thermoplastic polymer matrix from 2003 to 2008.

Nowadays several industrial solutions are available for improving the gas barrier performance of bottles based on the PNC technology. PA/MMT PNCs are used as barrier layers for multilayer PET containers, showing to be two to three times better than the traditional ethylene vinyl alcohol, EVOH. When used in a 0.47 l beer bottle, Imperm<sup>®</sup> nanocomposite guarantees almost seven months of shelf life. Honeywell produces three versions of their nylon6/MMT nanocomposite Aegis<sup>®</sup>: i) OXCE, ii) HFX and iii) CDSE [33]. Aegis<sup>™</sup> OX contains an oxygen scavenging component intended for use in beer bottles that provides a shelf life of 6-12 months which is comparable to the glass bottles. In 2003, Aegis<sup>®</sup> was used in a three layer 1.6 litter structure for a South Korean brewery [34]. Beer was expected to be the biggest consumer of PNC by 2006 with 148.5 tonnes. Carbonated soft drinks bottles are projected to surpass that by 2011, with the use of 2474.7 tonnes of PNC [35].

The PET/PNC multilayer bottle is a relatively expensive solution and requires complex processing. As alternative, PET based PNCs can be used for production of monolayer containers with similar or superior, barrier and mechanical properties comparing to the multilayered one.

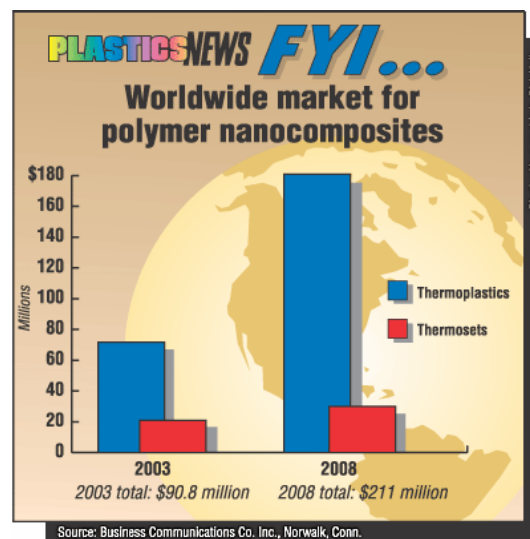


**Figure 1.9.** Worldwide market for polymer PNC (2004) [36].

### 1.2.3. Preparation methods

PNC preparation method [29] is the most critical part of the process defining the PNC

performance. Those methods can be divided into three categories:

i) *in situ polymerization* generally involves three continuous steps. First, the nanoscale additives are pretreated with appropriate surface modifiers and then the modified additives are dispersed into monomer(s). This is followed by bulk or solution polymerization. Then the nanocomposites are formed *in situ* during the polymerization reaction. The most important factors affecting the properties of the composites are the dispersion and the adhesion at the polymer/filler interfaces. Inorganic particles may disperse homogeneously in the polymer matrices when they are premodified by a coupling agent. There are several advantages of using the *in situ* polymerization method in respect to the other two methods, that are: ease of handling, speed of the process and better performance of the final products.

ii) *Solvent-assisted*, is a liquid-state powder processing method that results in a good molecular level of mixing and is widely used in materials preparation and processing. Some of the limitations of the other production methods can be overcome if both, the polymer and the nanoparticles, are dissolved or dispersed in solution but at a cost depending on the solvent and its recovery.

iii) *Melt blending* is a molten state method during which nanoparticles are mixed with the polymer matrix. Under these conditions and if the nanofillers surfaces are sufficiently compatible with the selected polymer, the particles can be homogeneously dispersed/delaminated. The first two methods are not appropriate for commercial production due to the difficulties associated with identifying a suitable monomer for the polymerization and a solvent compatible with both the polymer and the inorganic nanoparticle. This method has several advantages over the other methods [29], namely: i) is solvent free, so that makes it environmental friendly, ii) the residence time at high temperature is shorter than in the case of *in situ* polymerization, iii) commercial scale production can be applied with current industrial and processing methods, and iv) fast dispersion of nanofillers in the melt. However, the main limitations of this method are the dispersion/deagglomeration of the nanometric reinforcements within the polymer matrix as well as the thermal decomposition of the organic surfactants which may occur. Successful melt dispersion/deagglomeration requires presence of strong interactions between inorganic nanofillers and macromolecules and an adequate residence time of the stress field applied.

#### **1.2.4. Why PNCs?**

The development of PNC will enable to get beyond the classic material performance trade-off by accessing new properties and exploiting unique synergies between materials. This can be only possible when the length scale of morphological and the physics properties associated with a property coincide, i.e., on the nanoscale level. Multifunctional features attributed to PNC consist on improved thermal resistance and/or flame resistance, moisture

resistance, decreased permeability, charge dissipation, and chemical resistance. Through control/change of the additives at the nanoscale level, it is possible to maximize the properties of a selected polymer system allow to meet or exceed the requirements of current applications.

Many examples can be found in the literature demonstrating substantial improvements in physical and mechanical properties. However, the value of PNC is not based solely on mechanical enhancements of the neat polymer. Rather, its value comes from providing value-added properties not present in the pure polymer, without sacrificing the inherent physical and mechanical properties of the neat polymer. Traditionally, the preparation of a blend or composite with multifunctionality requires a close relationship between desired performance, mechanical properties and cost. Development of materials with multifunctionality, whether microscale or nanoscale, must simultaneously balance three interdependent areas: i) materials selection, ii) processing and iii) performance.

### 1.3. References

1. Fakirov, S., *Handbook of Thermoplastic Polymers: Homopolymers, Copolymers, Blends, and Composites*. 2002: WILEY-VCH Verlag GmbH, Weinheim.
2. <http://www.chemsystems.com>, *PET suffering from oversupply*. 2007 Nexant, Inc. .
3. <http://www.plasticsnews.com>, *World market for PET packaging* 2006.
4. <http://athas.prz.rzeszow.pl/Default.aspx?op=db>.
5. Viana, J.C., N.M. Alves, and J.F. Mano, *Morphology and Mechanical Properties of Injection Molded Poly(Ethylene Terephthalate)*. *Polymer engineering and science*, 2004. **44**(12): p. 2174-2184.
6. Jabarin, S.A., *Strain-induced crystallization of poly(ethylene terephthalate)*. *Polymer Engineering & Science*, 1992. **32**(18): p. 1341-1349.
7. Varma, P., E.A. Lofgren, and S.A. Jabarin, *Properties and kinetics of thermally crystallized oriented poly(ethylene terephthalate) (PET). II: Physical and optical properties*. *Polymer Engineering and Science*, 1998. **38**(2): p. 245-253.
8. le Bourvellec, G., L. Monnerie, and J.P. Jarry, *Kinetics of induced crystallization during stretching and annealing of poly(ethylene terephthalate) films*. *Polymer*, 1987. **28**(10): p. 1712-1716.
9. Marco, Y., L. Chevalier, and M. Chaouche, *WAXD study of induced crystallization and orientation in poly(ethylene terephthalate) during biaxial elongation*. *Polymer*, 2002. **43**(24): p. 6569-6574.
10. Marco, Y., et al., *Induced crystallization and orientation of PET during uniaxial and biaxial elongation*. *Macromolecular Symposia*, 2002. **185**: p. 15-34.
11. Zaroulis, J.S. and M.C. Boyce, *Temperature, strain rate, and strain state dependence of the evolution in mechanical behaviour and structure of poly(ethylene terephthalate) with finite strain deformation*. *Polymer*, 1997. **38**(6): p. 1303-1315.
12. Llana, P.G. and M.C. Boyce, *Finite strain behavior of poly(ethylene terephthalate) above the glass transition temperature*. *Polymer*, 1999. **40**: p. 6729-6751.
13. Blundell, D.J., et al., *Characterization of strain-induced crystallization of poly(ethylene terephthalate) at fast draw rates using synchrotron radiation*. *Polymer*, 1996. **37**(15): p. 3303-3311.
14. Mahendrasingam, A., et al., *Effect of draw ratio and temperature on the strain-induced crystallization of poly (ethylene terephthalate) at fast draw rates*. *Polymer*, 1999. **40**(20): p. 5553-5565.
15. Mahendrasingam, A., et al., *Observation of a transient structure prior to strain-induced crystallization in poly(ethylene terephthalate)*. *Polymer*, 2000(41): p. 1217-1221.
16. Matthews, R.G., et al., *The effects of stress relaxation on the structure and orientation of tensile drawn poly(ethylene terephthalate)*. *Polymer*, 2000. **41**(19): p. 7139-7145.
17. Smith, F.S. and R.D. Steward, *The crystallization of oriented poly(ethylene terephthalate)*. *Polymer*, 1974. **15**(5): p. 283-286.
18. Mahendrasingam, A., et al., *Influence of temperature and chain orientation on the crystallization of poly(ethylene terephthalate) during fast drawing*. *Polymer*, 2000. **41**: p. 7803-7814.
19. Gupte, K.M., H. Motz, and J.M. Schultz, *Microstructure rearrangement during the heattreatment of melt-drawn poly(ethylene terephthalate) fibers*. *Journal of Polymer Science: Polymer physics edition* 1983. **21**: p. 1927-1953.
20. Hofmann, D., et al., *Investigations on supermolecular structure of poly(ethylene terephthalate) samples of higher modulus*. *Polymer*, 1989. **30**(2): p. 242-247.
21. Goschel, U., *Two-dimensional small-angle X-ray scattering studies on oriented poly(ethylene terephthalate) films*. *Polymer*, 1995. **36**(6): p. 1157-1165.
22. Casey, M., *Studies of the morphology of one-way drawn poly(ethylene terephthalate) films by X-ray diffraction*. *Polymer*, 1977. **18**(12): p. 1219-1226.

23. Goschel, U. and G. Urban, *Supramolecular structure of oriented and semicrystalline poly(ethylene terephthalate) as revealed by the electron density correlation function from small-angle X-ray scattering studies*. *Polymer*, 1995. **36** (19): p. 3633-3639.
24. Stockfleth, J., L. Salamon, and G. Hinrichsen, *On the deformation mechanisms of oriented PET and PP films under load*. *Colloid and Polymer Science* 1993. **271**: p. 423-435.
25. Gorlier, E., *Caractérisation multiaxiale du comportement et de la microstructure d'un semi-cristallin : Application au cas du PET*, . 2001: Ecole Nationale Supérieure des Mines de Paris.
26. Daubley, R., C.W. Bunn, and B. C.J., *The crystal structure of polyethylene terephthalate*. *Proceeding of the royal Society of London, Series A, Mechanical and Physical Science*, 1954. **226**: p. 531-542.
27. Goschel, U., K. Deutschert, and V. Abetzt, *Wide-angle X-ray scattering studies using an area detector: crystalline orientation in semicrystalline PET structures*. *Polymer*, 1996. **37**(1): p. 1-6.
28. Parravicini, L., et al., *Crystallization of poly(ethylene terephthalate) (PET) from the oriented mesomorphic form*. *Journal of Applied Polymer Science*, 1994. **52**(7): p. 875-885.
29. Koo, J.H., *Polymer Nanocomposites Processing, Characterization, and Applications*. 2006, New York: McGraw-Hill.
30. Paul, D.R. and L.M. Robeson, *Polymer nanotechnology: Nanocomposites*. *Polymer*, 2008. **49**(15): p. 3187-3204.
31. Kawasumi, M., *The Discovery of Polymer-Clay Hybrids*. *Journal of Polymer Science: Part A: Polymer Chemistry*, 2004. **42**: p. 819-824
32. <http://www.packstrat.com/>, *Nanocomposites for packaging: New frontiers and future opportunities*. 2005.
33. Honeywell, <http://www51.honeywell.com/sm/aegis/>.
34. Downing-Perrault, A., *Polymer nanocomposites are the future* 03.2005: University of Wisconsin-Stout.
35. [http://www.packworld.com/cds\\_print.html?rec\\_id=17883](http://www.packworld.com/cds_print.html?rec_id=17883)., *Nanotechnology in packaging*. 07.2004.
36. <http://plasticsnews.com>, *Worldwide market for polymer nanocomposites*. 2004.

# CHAPTER II

## Literature review

### 2.1. Structure development during the uniaxial stretching of amorphous PET

The stress-strain behaviour of amorphous PET during deformation is intimately linked to the macro and microstructure evolution of the polymer, which in turn is determined by the imposed thermo-mechanical environment during stretching [1-3]. Various industrial processes, such as film blowing, double bubble film processing, tenter frame film processing and injection blow moulding involve the concept of the strain induce crystallization of amorphous PET to give rise to products of uniform thickness, better mechanical, physical and thermal properties. Due to that PET as been extensively investigated for a better understanding of the multi scale structure evolution during processing, using very sensitive characterization techniques. Two approaches have been established, namely:

i) *ex situ* that consists of a post-deformation characterization, by: i) densiometric measurements [4-6], ii) fluorescence spectroscopy [6-10], iii) raman spectroscopy [11, 12], iv) infra-red spectroscopy, [7, 13-18], v) X-ray diffraction, [1, 2, 4, 7, 13, 14, 18-28]; vi) optical birefringence [2, 6, 12, 13, 20, 28-32] and vii) differential scanning calorimetry [2, 16, 24, 28, 33, 34].

ii) *in situ* that consists in a real time characterization followed by: i) X-ray diffraction [16, 35-42], ii) optical birefringence [33] and Fourier transform infra-red [43].

In this section an up-to-date summary of the literature regarding the structure development of amorphous PET during uniaxial stretching in the *rubbery state* (above its  $T_g$ ) and in the *solid state* (at room temperature) is presented.

#### 2.1.1. Stretching in the rubbery state

During stretching of amorphous PET in the rubbery state, molecular orientation is promoted, inducing the crystallization of the material at high orientation levels. This process is called strain-induced crystallization, SIC [4, 5]. For the SIC process, orientation plays an



important role by bringing in the molecular chain segments into favourable positions and increasing the rate of crystallization. This mechanism is strongly governed by stretching parameters, mainly the stretching temperature,  $T_{st}$ , the stretching rate,  $\dot{\epsilon}_{st}$ , the stretching ratio,  $\lambda_{st}$ , and the mode of stretching [27, 33, 44].

Amorphous PET stretched in the rubbery state displays a highly non-linear stress-strain curve as observed in **Figure 2.1**. Four regions can be distinguished, that are described as follow [45]:

i) *elastic region* with a stiff initial response of slope  $E$  (Young modulus) extending up to the yielding point, as a result of a simple elastic extension. It represents the amount of force required to move molecular segments from their equilibrium position. The deformation in the elastic region is completely recovered after removal of the stress. However, further stretching will cause the movement into the viscous flow plateau.

ii) *flow region* consists on a rollover to flow with large viscoelastic movement taking place simultaneously to molecular chain segments rotation, translation, and unfolding which may lead to molecular alignment in the direction of stretching. Here the stress level remains almost unchanged with extension. Deformation in this region is not recovered after the load has been removed.

iii) *stress increase* is characterized by a steady increase in the stress with strain, with an initial strain hardening/stiffening modulus defined as  $h_i$ ,

iv) *strain hardening* is identified by a rapid increase in the stress level in a narrow strain range due to the reduction of the configurational entropy associated with the straightening of the chains as a result of deformation. As the stress level increases, due to the alignment and crystallization that are hindering the chains movement, also called “network formation”.

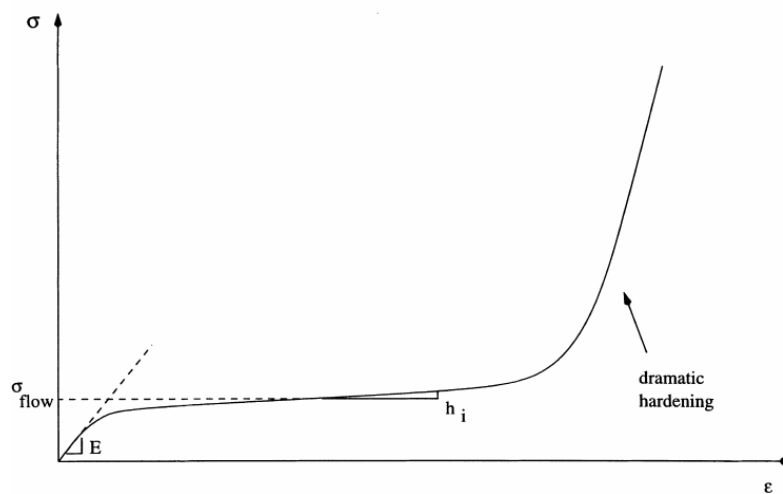


**Figure 2.1.** Basic features of the stress–strain behaviour of amorphous PET in the rubbery state[45].

The stress-strain behaviour of amorphous PET (as any other polymeric material) is strongly dependent mainly on the stretching variables as: i) stretching temperature and ii) stretching rate [46-48]. Decreasing the stretching temperature or increasing the stretching rate results in the increase of modulus, yield stress and flow stress. Also, the onset of strain hardening occurs at lower strains. The effect of the stretching variables is depicted in the **Figure 2.2**. Some authors identify the strain hardening with the onset of SIC [5, 9], however others dispute this statement showing that the crystallization process occurs only after the deformation is stopped [35, 37, 38]. Detailed discussion of the SIC process is presented in a further *section* (see 2.1.1.4.).

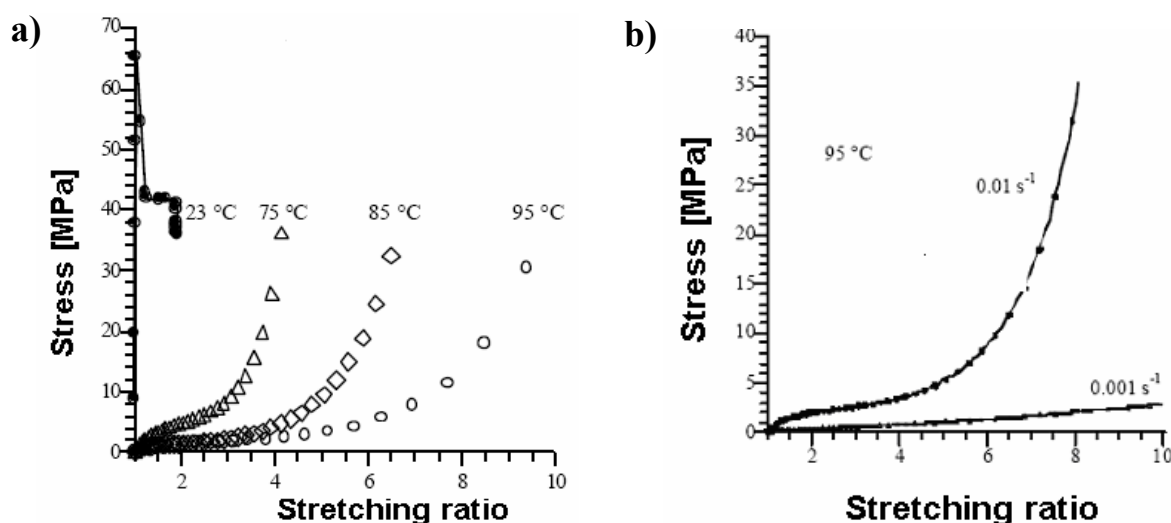


**Figure 2.2.** Influence of stretching variables on the stress-strain curves: a) effect of stretching temperature at constant stretching rate ( $\dot{\epsilon} = 0.005 \text{ s}^{-1}$ ) and b) effect of stretching rate at constant stretching temperature ( $T = 95^\circ\text{C}$ ) [44].

#### 2.1.1.1. Conformational development

Stretching of amorphous PET induces conformational changes followed by chain segment alignment/orientation and finally crystallization [13, 14]. In PET, the ethylene glycol linkages can exist in two rotational conformations: i) a *trans* or extended form and ii) a *gauche* or relaxed form. During stretching, some *gauche* isomers are converted into *trans* isomers, and some of the converted *trans* isomers can further crystallise. Un-crystallised *trans* isomers can relax back into *gauche* form or they can remain as an amorphous oriented chain [49]. In other words, the conformation in the crystalline phase of PET must be *trans*, whereas the amorphous phase consists of both *trans* and *gauche* isomers.

Ajji et al. [13, 14] carried out uniaxial stretching experiments at  $80^\circ\text{C}$  up to a strain rate of about  $1 \text{ s}^{-1}$ . They measured the evolution of the intensity of the bands at  $1340 \text{ cm}^{-1}$  and  $1370 \text{ cm}^{-1}$ , assigned to *trans* and *gauche* conformations, by using Fourier Transform Infrared spectrometer, FTIR. They found that stretching of amorphous PET results in the alignment of the

*trans* conformers in the stretching direction. Further deformation converts *gauche* into *trans* conformers and brings about their alignment. At a certain degree of local order, the aligned chains start to crystallize. They proposed a structural model which consists of three phases:

- i) *amorphous phase* composed solely of *gauche* conformers;
- ii) *mesophase* which consists of *gauche* and highly oriented *trans* conformers;
- iii) *crystalline phase* which consists only of *trans* conformers.

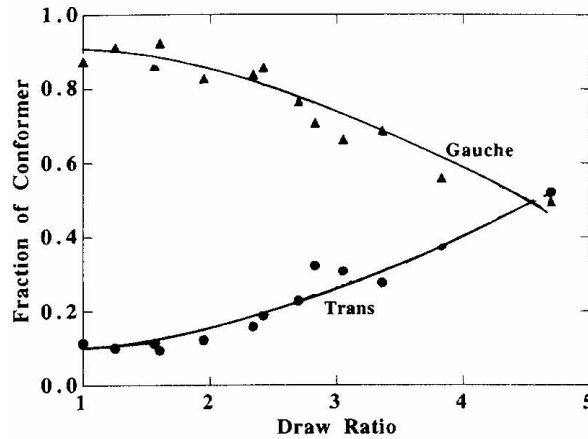


**Figure 2.3.** *Trans and gauche conformer's fraction as function of stretching ratio for amorphous films stretched at 80°C and 2 cm.min<sup>-1</sup> [13].*

#### 2.1.1.2. Chain orientation and relaxation

During the uniaxial stretching, the chains are able to align into the stretching direction due to constrain caused by the underlying macromolecular network. The integrity of the network is maintained by entanglements that unlike chemical crosslinks, the coupling they produce is non-permanent. Between the entangled regions the frictional resistance to conformational change is low, but rapid motions at the point of entangled regions is restricted [50]. These non-permanent crosslink regions place constraints on the motion of the molecules, thus hindering bulk flow during deformation and allowing orientation to be maintained. The level of orientation obtained during deformation is in certain conditions reduced by a relaxation process that occurs when the applied stress is removed. This phenomenon is attributed to the motion of polymeric chains in the amorphous regions, which reduce the extension of the chains and its orientation. During stretching, relaxation occurs mainly within non-permanent crosslink entangled regions which undergo a process of slippage. Thus, it is correct to state that four processes evolve during uniaxial stretching of PET in the rubbery state, that are: i) conformation changes, ii) orientation, iii) relaxation and iv) crystallization.

Several authors have studied the influence of the stretching variables on the orientation, finding out that the increase of the stretching rate and decreasing temperature would increase the

orientation [10, 27, 51]. The molecular chains are less mobile at lower stretching temperature, thus relaxation of the oriented chains can only occur at a low degree. With decreasing stretching rate, relaxation is found to increase, due to longer times of deformation, consequently orientation level decreases for stretching at slower stretching rates.

Duchesne et al. [52] investigate the molecular relaxation process via *in situ* polarisation modulation infrared spectroscopy. They found that, for deformations carried out at temperatures below 93°C, the orientation function decreased exponentially with time as a result of chain relaxation. However when the deformation is carried out above 93°C an initial decrease was followed by an increase in the orientation level. They suggested that this reorientation phenomenon is due to crystallization, as confirmed by *ex situ* DSC and WAXD analysis.

Apart from the effect of stretching rate and temperature on the molecular orientation process, stretching ratio is another significant variable. Mathews et al. [16] studied the relaxation behaviour of PET under a tensile deformation experiment by using a newly developed *in situ* birefringence method [30]. They found that relaxation is strongly dependent on the final reached stretching ratio. At stretch ratios less than 2.0x, orientation decreased linearly with time after deformation is stopped, which indicated the dominance of the relaxation process. For samples stretched to higher stretching ratio of 3.6x, birefringence decreased over a short period of time, of the order of 10 s, and remained constant thereafter. They concluded that some of the oriented amorphous chains can crystallise during the initial relaxation period, which will then inhibit the further relaxation because the crystallites tend to lock the oriented chains in the stretching direction.

The influence of the main stretching parameters: temperature, rate and ratio on the molecular orientation and relaxation processes, can be summarised as follows:

- i) higher oriented sample can be obtained by stretching at lower temperatures, higher stretching rate and at higher stretching ratio,
- ii) at sufficiently high orientation level there is a competition between the relaxation of the molecular oriented and entangled networks,
- iii) crystallization process effectively crosslinks the network to prevent further relaxation of oriented chains.

### **2.1.1.3. Mesophase as a precursor to strain induced crystallization**

Studies [36, 37, 53] about the strain induced crystallization of PET have revealed the existence of an intermediate structure (between the amorphous phase and the crystalline phase) acting as a precursor to the crystallization. This intermediate structure is called mesophase and it is characterized by having a degree of packing order between amorphous and crystalline phase and by appearing for very short time, that is about 0.2 s [53]. Ran et al. [54], by *in situ* WAXD

studies, observed a sharp meridional peak (00-1) at  $2\theta = 8.56^\circ$  with  $d=10.3 \text{ \AA}$ , smaller than the monomer length in the typical unit cell ( $c = 10.75 \text{ \AA}$ ), and attributed that to the mesophase formation. The intensity of this peak was found to increase upon stretching; however it would decrease once the triclinic PET crystalline structure began to form. In other words, [36, 37, 53] the simultaneous disappearance of the mesomorphic peak (00-1) at  $2\theta = 8.56^\circ$  in the meridian and the appearance of the triclinic crystalline peaks at equator, which supporting the hypothesis that the mesophase is an intermediate phase, acting as a precursor for SIC.

Kawakami et al. [55] correlated the mesophase development with the mechanical behaviour of PET. They observed the existence of a mesophase for deformations below to the strain hardening region and that increases with strain. For deformations above the strain hardening region, the corresponding mesophase fraction was found to decrease, as a result of its transformation into crystalline phase. When the material is stretched further, the mesophase and the crystalline fraction increase with strain increase, as result of the amorphous phase consumption. In summary crystallization could only be initiated within the mesophase and the resulting crystalline fraction continuously lags behind the mesophase fraction during the uniaxial stretching process.

#### 2.1.1.4. Strain induced crystallization

The strain induced crystallization behaviour of PET has been extensively studied for the past 50 years [10, 16, 35, 38, 46-48, 53, 56], being the correlation between the constitutive behaviour and the structural development leading to strain induced crystallization of particular interest [5, 27, 39, 55, 57]. A pioneering work in this area goes back to 1959 when Marshall and Thompson [58] studied the stress-extension behaviour of PET by using roller drawing. They reported that the drawing behaviour of PET is very sensitive to temperature and stretching rate. The strain needed for the onset of strain hardening was called by them as the *natural draw ratio*. It occurs after plastic flow of strain-stress curve (see **Figure 2.1**) and corresponds to the region where the neck is initiated. Where after in the region where the neck was initiated, the plastic deformation stops in this region while neck propagates over the whole length of the sample at nearly constant engineering stress [59]. The natural draw ratio is found to increase with decreasing temperature and increasing stretching rate.

Zaroulis and Boyce [47] performed a series of uniaxial compression test of initially amorphous PET samples in the solid state (25-60°C), near the quasi-rubbery state (60-76°C) and in the rubbery state (80°C) up to a strain rate of  $2 \text{ s}^{-1}$ . They found that the strain induced crystallization was only observed for deformations above the  $T_g$ , i.e. in rubbery state observing simultaneously a large strain hardening behaviour corresponding to the crystallization process. Below and around the  $T_g$ , only a network orientation was observed with no further

crystallization.

Other works [5, 13, 16, 50, 60] have tried to link the strain induced crystallization to the strain hardening region. A strong evidence of crystalline phase development was found from X-ray diffraction, differential scanning calorimetry, DSC, and density studies [5, 10, 27, 48]. Therefore strain hardening has been frequently assumed to be an indicator of strain induced crystallization. LeBourvellec et al. [10] and Salem [1, 5] concluded that the onset of strain induced crystallization always coincides with the inflection point in the stress-strain curve. Moreover, it was once more confirmed that the natural draw ratio is strongly dependent on the stretching temperature and the stretching rate: it shifts to higher stretching ratios with decreasing stretching rate and increasing temperature. Moreover, it only occurs at stretching ratios above  $2x$ , since no evidence of crystal formation is shown below this value [5, 13, 16, 50, 60].

LeBourvellec et al. [10] also concluded about the existence of a critical amorphous orientation associated to the strain induced crystallization, which is only dependent on the stretching temperature. For the same level of strain, the amorphous orientation of a material deformed at higher stretching temperature is expected to be less than the material deformed at lower stretching temperature, due to a higher relaxation process taking place simultaneously. Thus the material deformed at higher stretching temperature needs to be elongated further in order to achieve the same crystallinity level in both materials. Lower strain rates allow more time for the relaxation of oriented chains which result in a lower orientation level in the material. Thus it needs to be elongated further in order to achieve sufficient orientation level for SIC. They concluded that the crystallinity of PET is completely determined by the temperature and the level of amorphous orientation in the material.

In order to associate the mechanical behaviour of PET with the strain induced crystallization, Salem have proposed the regimes depicted in **Figure 2.4**. that are defined as follow:

- i) *low stress regime, regime I*, in which stress increases slowly with stretching ratio but crystallinity increases relatively fast,
- ii) *high stress regime, regime II*, in which stress increases rapidly but crystallinity increases slowly. The onset of regime II was found to occur at a characteristic level of 15% of crystallinity and it is independent of stretching rate (**Figure 2.5**).

The determination of the lateral crystallite dimension normal to the (010) at  $2\theta = 17.3^\circ$  and (100) at  $2\theta = 25.7^\circ$  planes, based on Wide Angle X-ray Scattering, WAXS, experiments, revealed that crystallization in *regime II* evolve through a modest growth of the crystallite, with the preferential growth occurring normal to (010). They also suggested that *regime I* involves the formation of a crystallite network, which at the characteristic level of crystallinity, is sufficiently

crosslinked, giving rise to large stress generation on further polymer deformation.

The two regime concept proposed by Salem is widely accepted by other authors [13, 50, 60]. Their investigations lead to the following conclusions:

- i) natural draw ratio is identified as an indicator of the onset of SIC,
- ii) natural draw ratio is found to occur at higher strain with increasing stretching temperature and decreasing stretching rate,
- iii) SIC is found not to occur for deformation below stretching ratios of  $2x$ ,
- iv) higher rate of SIC was found in the stretching ratio in range of  $2x - 3x$ , thereafter SIC occurs at a slower rate up to a saturation level of crystallinity.

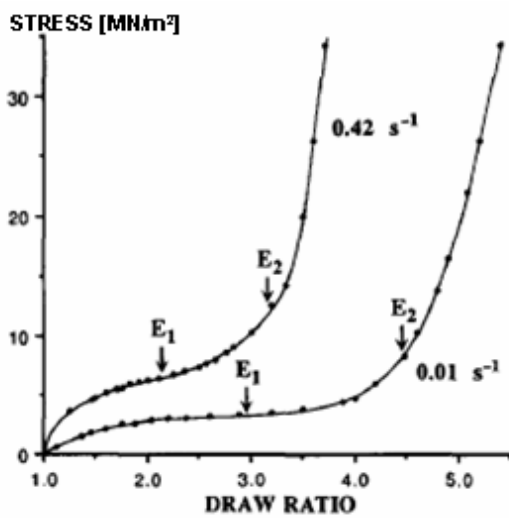


**Figure 2.4.** True stress versus stretching ratio at three strain rates. The onset of crystallization,  $E_1$ , and the onset of regime 2 crystallization,  $E_2$ , are indicated[5].

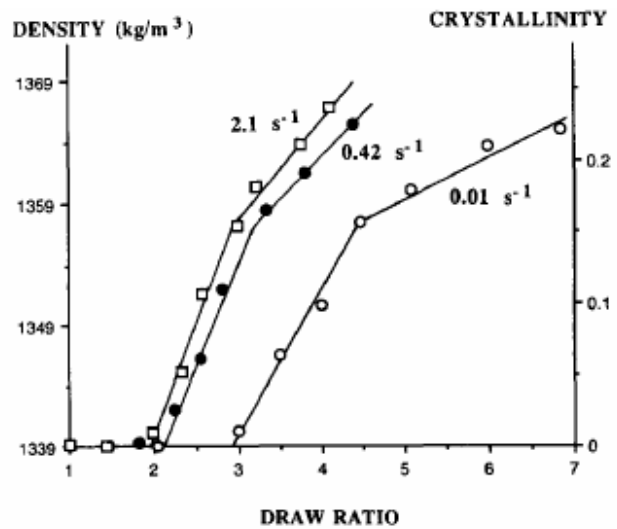


**Figure 2.5.** Variation of density and crystallinity with stretching ratio  $2x$  at three strain rates [5].

Other studies of Salem [61] revealed that the stretching rate is the most important factor in governing the final crystallinity level for strain rates below  $2 \text{ s}^{-1}$ . This is due to the fact that microstructure development is strongly influence by the time for molecular relaxation. They claimed that for stretching rates below  $2 \text{ s}^{-1}$ , crystallization is faster than the time scale of deformation, thus there is always time to reach the pseudo-equilibrium crystallinity level corresponding to a particular combination of non-crystalline orientation and temperature. However for high stretching rates, up to  $17 \text{ s}^{-1}$ , the stretching rate doesn't seem to affect the final crystallinity level. In this case, the temperature plays the most important role in determining the final crystallinity level.

Mahendrasingam et al. [35, 38] carried out *in situ* WAXS to investigate the effect of stretching ratio and temperature ( $80\text{-}125^\circ\text{C}$ ) at fast stretching rates, for instance,  $10 \text{ s}^{-1}$ . The

results are presented in **Figure 2.6**. Surprisingly, their studies led to conclusions that contradict the previous investigations in this field. They showed that the crystallization start to appear just after the deformation has been stopped and occurs for very short periods of time (less than 0.5s). The ability of local segments to provide the mobility for chains to organise into crystals is likely to be restricted while the extension and chain slippage are still in progress. However, when extension has been completed, onset of chain relaxation would restore the freedom of local organisation, allowing crystal nucleation to occur.

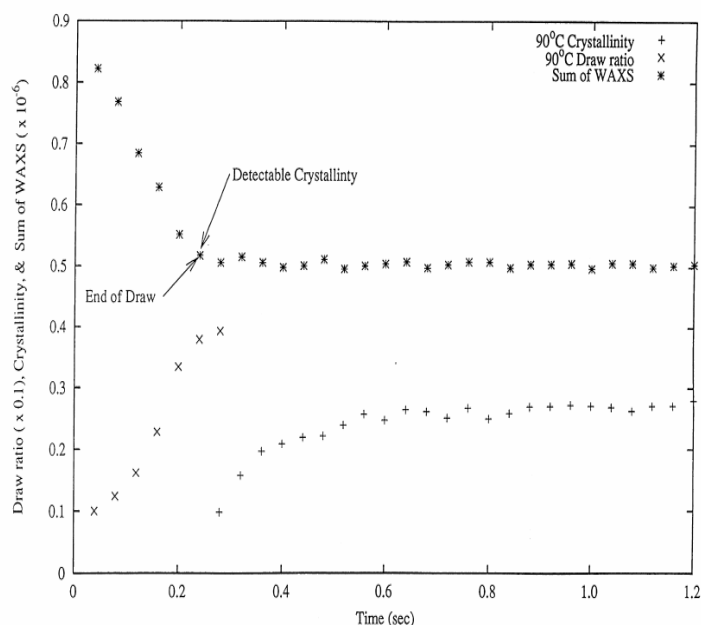


**Figure 2.6.** Plot of the variation in stretching ratio and crystallinity calculated from the sequence of X-ray diffraction patterns of the PET sample recorded during the stretching at 90°C to a final stretching ratio 4:1. The arrow indicates first frame with detectable crystallinity and end of stretching [35].

Apart from the contradicting results mentioned above, Mahendrasingam's [10] work closely matches with previous studies on the fact that orientation and crystallinity decreased with increasing temperature due to the domination of the relaxation process. They also found that for stretching ratios below 2x the strain induce crystallization doesn't take place upon deformation stops because the relaxation of the oriented segment is faster than the kinetics of crystallization. For stretching ratios above 2x, crystallization takes place and the final crystallinity and the crystallization rate increase with stretching ratio. Once more it is reinforced the notion that a sufficient level of molecular orientation is necessary to start the crystallization process, and that the increase of chain mobility with temperature allows chain relaxation to compete with the orientation applied by the external force.

Recently Mahendrasingam [37, 62] showed that the orientation texture of the developing crystals depends on the relationship between the stretching conditions and the chain relaxation



processes. They proposed a three regime schematic map, shown in **Figure 2.7.**, which estimates the chain relaxation rate as a function of deformation temperature (90 - 120°C) and stretching rate (0.05 - 12 s<sup>-1</sup>) based on the relaxation theoretical framework of Doi and Edward [63] of an enclosed tube concept:

i) *regime I*: corresponds to the deformation at high stretching rates and lower temperatures. With these conditions the stretching rate is found to be faster than the chain retraction rate. In this regime, the onset of crystallization occurs after the deformation is completed and the crystal chain axes is well oriented in the stretching direction;

ii) *regime II*: corresponds to the deformation at slower stretching rates and higher temperatures. The stretching rate is found to be slower than the chain retraction rate but higher than the reptation rate. In this case, the onset of crystallization is found to occur during stretching, with an increase of tilting of the crystal chain axis away from the stretching direction;

iii) *regime III*: engages deformation at even lower stretching rate and higher temperature conditions, where the stretching rate becomes comparable with chain reptation rate. No orientated crystallization was observed for deformation in this regime.

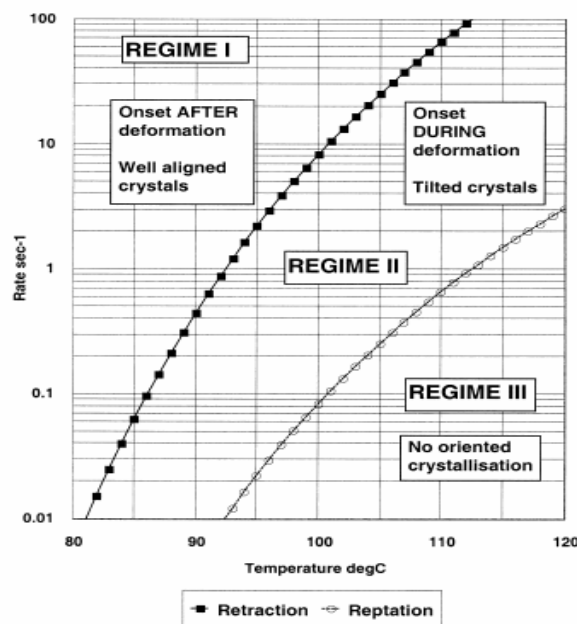


**Figure 2.7.** Schematic map of estimated chain relaxation rates as a function of temperature, illustrating changes in oriented crystallization behaviour [37].

Gorlier et al. [27] performed *ex situ* WAXS on stretched sample after quenching. Two types of quenching protocol were applied to the stretched sample: a poor quenching with an intermediate time of 30s before it was cooled down to 0°C, and a good quenching with an intermediate time of 3s. They found that the evolution of microstructure as a function of strain is much faster in the case of poor quenching than in good quenching, for which crystallization

seems to be less perfect. They concluded that there is no direct relationship between crystallinity and strain hardening. The final level of crystallinity measured after deformation is strongly dependent on the stretching ratio achieved during deformation and the cooling rate applied to the material after deformation.

Recently, Chaari et al. [39] carried out a series of *in situ* WAXD studies on the effect of stretching rates (up to  $0.75 \text{ s}^{-1}$ ) on PET at  $95^\circ\text{C}$  and stretching ratio of 5x. In their investigation, crystalline ratio and crystallite orientation were simultaneously recorded and correlated with the mechanical behaviour during the stretching process. They found that the crystallinity development corresponded to three different regimes:

i) *small enough stretching rate*: there was no measurable crystallinity during the stretching process although a strain hardening in the stress-strain curve was observed. The crystallization developed after cessation of deformation.

ii) *intermediate stretching rates*, the whole crystallization process took place during the deformation.

iii) *highest stretching rates*, crystallization started during the stretching process and continued after cessation of deformation.

Their results closely match the three regime mapped by Mahendrasingam et al. [37, 62]. However, due to the limitation of their *in situ* equipment, only relatively low stretching rates were considered (less than  $1 \text{ s}^{-1}$ ). With further increase of stretching rate they expected to observe similar results to those observed by Mahendrasingam et al. [35, 38] where crystallization was found not to occur until deformation stops. Furthermore, it was proclaimed by several authors that the amount of crystallinity induced by SIC is limited; the level of saturation is of 30 - 40% [5, 9, 35, 38].

Martins and Cakmak [33] investigated the effect of different uniaxial stretching modes, i.e. linear, sigmoidal, logarithmic and exponential, on the PET's strain-induced crystallization at  $85^\circ\text{C}$ , via *in situ* birefringence, WAXS and DSC measurements. They proposed three regimes of structure evolution, based on the mechano-optical behaviour of PET, common for all studied stretching modes (**Figure 2.8**):

i) *regime I*, at early stages of deformation, characterizes by a linear increase of birefringence with stress following the stress-optical rule, while the material remained amorphous,

ii) *regime II*, a fast increase of birefringence, at almost constant stress, accompanies formation of crystalline structure with establishment of long-range connected network,

iii) *regime III*, birefringence levels off as the chains approach their finite extensibilities, while the stress increased, corresponding the strain hardening of the material.

## 2.1.1.5. Mechanisms of structure development

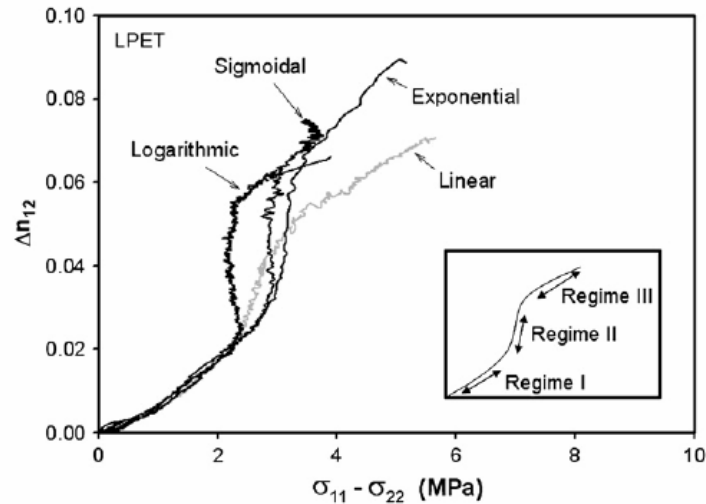


**Figure 2.8** In-plane mechano-optical behaviour of PET stretched with different types of deformation profiles, in uniaxial constrained width mode at 85°C [33].

Various authors have attempted to picture the structure development mechanisms of PET in the rubbery state, based on different *in situ* characterization techniques. Kawakami et al. [64] using *in situ* WAXS, Small Angle X-ray Scattering, SAXS, and Raman spectroscopy proposed the structural model depicted in **Figure 2.9.**, or an amorphous PET subjected to a continuous stretching in a quasi-rubbery state, i.e. at 70°C just below the  $T_g$ . Four stages were assumed:

- i) *stage I*: initial sample consisting of isotropic shushes of amorphous and nematic (mesophase) components are transformed into oriented slush with fibrillar-like structure;
- ii) *stage II*: starts with the appearance of a distinct (00-1) peak at  $2\Theta = 8.75^\circ$  ( $d=10.32 \text{ \AA}$ ) on the meridian WAXS pattern attributed to the formation of oriented slush (a mixture of oriented amorphous and nematic phases). Within the fibrillar superstructure a transition from oriented slush to smectic C is observed. With the increase of strain, the tilt angle of the smectic C layer decreases, forming a structure similar to the quasi-smectic A phase;
- iii) *stage III*: It is marked by the appearance of (010) equatorial reflection at  $2\Theta = 17.3^\circ$ , which indicates the occurrence of a triclinic crystalline phase. Thus, the main feature of the third stage is the transition of the oriented smectic slush into oriented crystalline phase. The formation of triclinic crystalline phase in the fibrillar superstructure leads to a crystalline lamellar structure with a long period of about 100 nm,
- iv) *stage IV*: corresponds to the final stage where the development of oriented crystalline phase becomes dominant but at relatively slow rate.

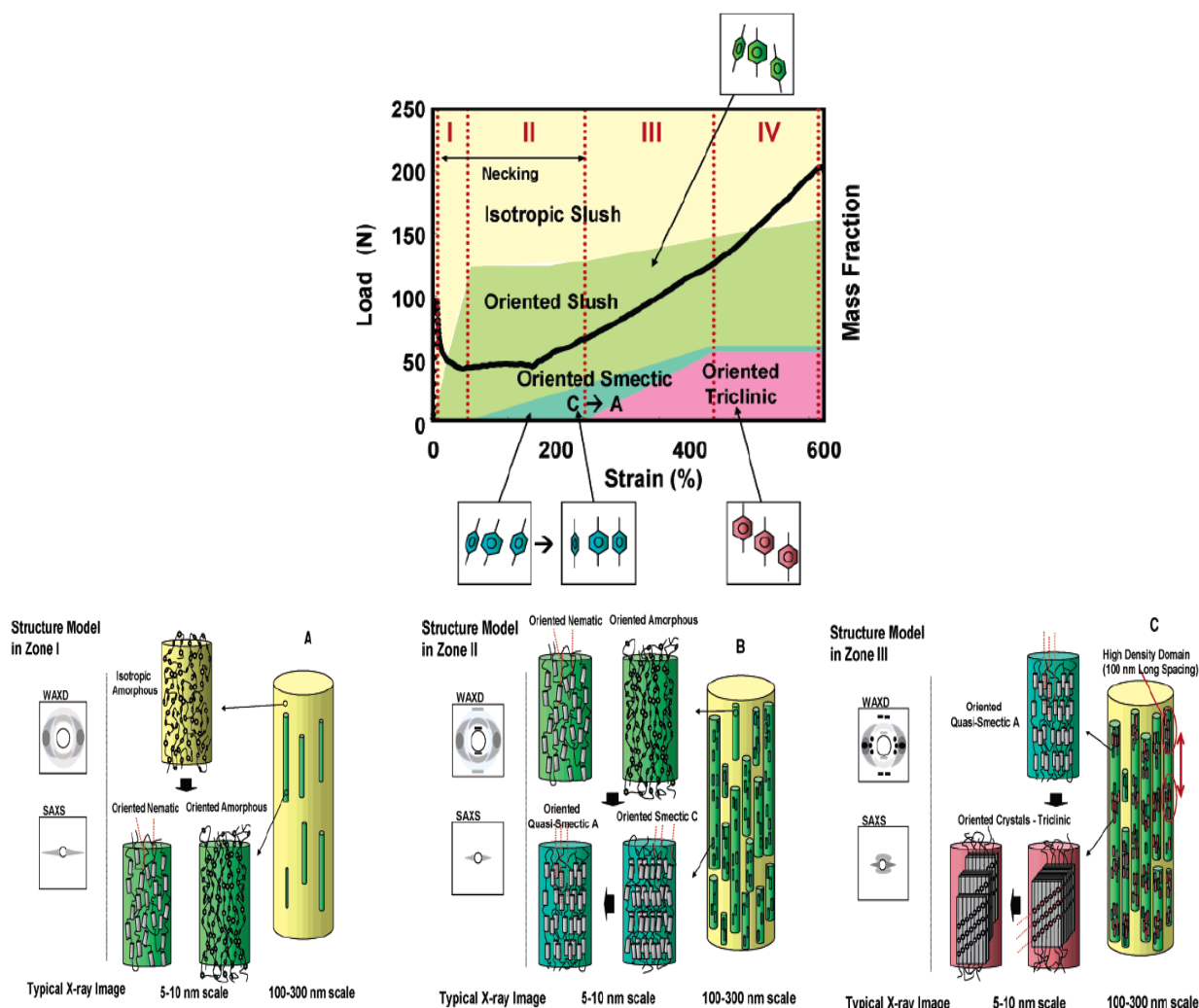


**Figure 2.9.** Strain-induced “phase” diagram of PET during deformation at 70°C and schematic diagrams of phase transition and structure development pathways as well as corresponding SAXS/WAXD patterns during PET deformation at 70°C in (A) zone I, (B) zone II, and (C) zone III (drawing not to scale). The cylinder in the nematic and smectic phases represents the mesogenic unit in PET with an aspect ratio of 2 [64].

Gorlier et al. [27] have suggested the structure development of uniaxially stretched amorphous PET in the rubbery state, at 85°C and  $0.01\text{s}^{-1}$ , based on *ex situ* WAXS characterization. The following stages were defined (**Figure 2.10.**):

- i) *orientation stage*, molecular orientation occurs due to strong molecular interactions,
- ii) *nucleation stage*, nuclei appear as a result of molecular orientation. At a given level of strain, the number of nuclei is fixed, forming a network structure that is responsible for strain hardening,
- iii) *growth stage*, crystallization develops through the growth process.

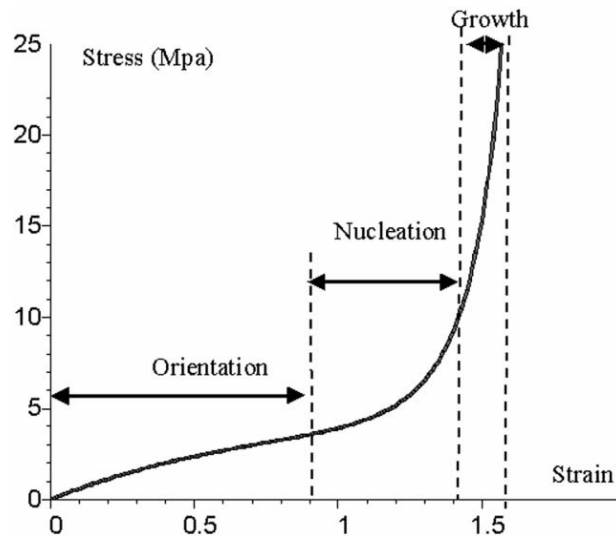


**Figure 2.10.** Schematic kinetics of microstructure development in PET [27].

Kawakami et al. [57] proposed a more complex mechanism of structure development evolving the superstructure evolution of amorphous PET during uniaxial deformation at 90°C and a stretching rate of  $0.003 \text{ s}^{-1}$  up to a stretching ratio of 6x by using *in situ* SAXS and WAXD analysis. They found from their real time investigation that the relationship between structure and mechanical behaviour can be divided into three zones (**Figure 2.11.**):

i) *zone I*: also called the plastic deformation zone, takes place until strain hardening region is initiated (plastic deformation region) and involves the formation of a mesophase with highly oriented chain segments. In this stage, the oriented mesophase was found to increase continuously with the applied strain without the actual formation of crystals. Stretching is accompanied by the appearance of an equatorial streak in SAXS patterns at the later phase of the stage, which indicates the formation of a microfibrillar structure;

ii) *zone II*: involves the initiation of crystallization from the mesophase through nucleation and growth processes. This stage occurs during the strain-hardening region. Imperfect crystals (2D crystals) were observed for strains up to the initiation of strain-hardening. Increasing strain was followed by further chain orientation and crystal perfection. SAXS analysis showed the existence of two sub-stages within the nucleation stage, consisting of: (i) formation of titled lamellar structure within the microfibrils in conjunction with lamellar insertion; (ii) lamellar insertion which occurred at a slower rate;

iii) *zone III*: corresponds to the stable crystal (3D crystals) growth phase, where the lamellar superstructure is responsible for the linear load increase with strain, which enables a good lattice PET triclinic unit cell to be registered in the WAXS patterns. However, at very high strains, some lamellar domains become fragmented, resulting in microfibrillar spinning and the prelude for catastrophic disruption of the crystalline phase.

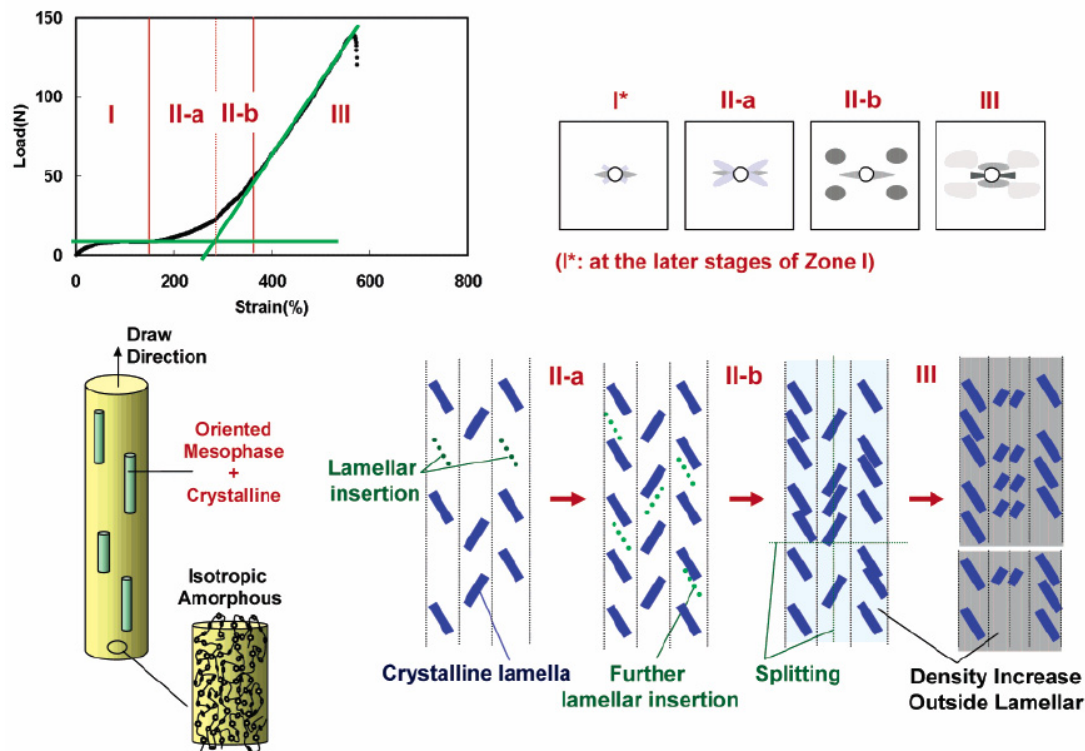


**Figure 2.11.** Schematic diagrams to illustrate the evolution of superstructure during deformation of amorphous PET sample above  $T_g$  (stretching at  $90^\circ\text{C}$ ). The background color of the microfibril is varied from white to dark gray gradually. The darkness represents the density of the region (darker color indicates higher density). The microfibril is composed of oriented mesophase and tilted crystalline lamellae [57].

Experiments carried at  $110^\circ\text{C}$  by Kawakami et al. [65] gave some new insights into the lamellar structure development of PET during uniaxial stretching, as related to mechanism of structure development zones of previous studies [55, 57, 64, 66] due to the higher stretching temperature (**Figure 2.12**). The main structural changes in the three zones are:

i) *zone I*: A small amount of isotropic crystalline domains begin to appear sporadically into the isotropic amorphous regions, where the stress may play a role to facilitate the nucleation process. No superstructure of dimension bigger than 10 nm length scale such as lamellae or fibrils is identified. The size and the amount of the crystallites are still so small that they cannot function as physical cross-linkers. The mechanical load is thus mainly supported by the molecular motion. Since the stress does not concentrate on the small crystallites, their orientation does not develop, and the applied load does not affect the structure formation.

ii) *zone II*: Spherical domains containing isotropic crystallites are formed initially. Then the anisotropic fibril domains start to appear, being oriented along the extensional direction. These fibrillar domains are embedded in the matrix of the isotropic amorphous phase. Within the fibrillar domain, isotropic crystallites formed a layered structure through the flocking motion during tensile elongation. The sample is significantly toughened by both fibrillar morphology and increased crystallinity, marking the region of strain hardening.

iii) *zone III*: All crystallites began to orient. The oriented (010) reflection appears first at the beginning of this zone (zone III-1) and continues to increase through zone III-2. The oriented (100) reflection, on the other hand, appears only in zone III-2. More crystallites are developed within the fibrillar domain, resulting in the decrease in long period. Finally, in zone III-3, the strain-induced crystalline structure and morphology appear to stabilize and the sample breaks apart eventually. In zone III, the applied load increases almost linearly with the applied strain. The mechanical hardening can be explained by both the crystallinity increase and the fibrillar formation induced by strain. However, a considerable amount of polymer chains remain to be the isotropic amorphous phase until they break.

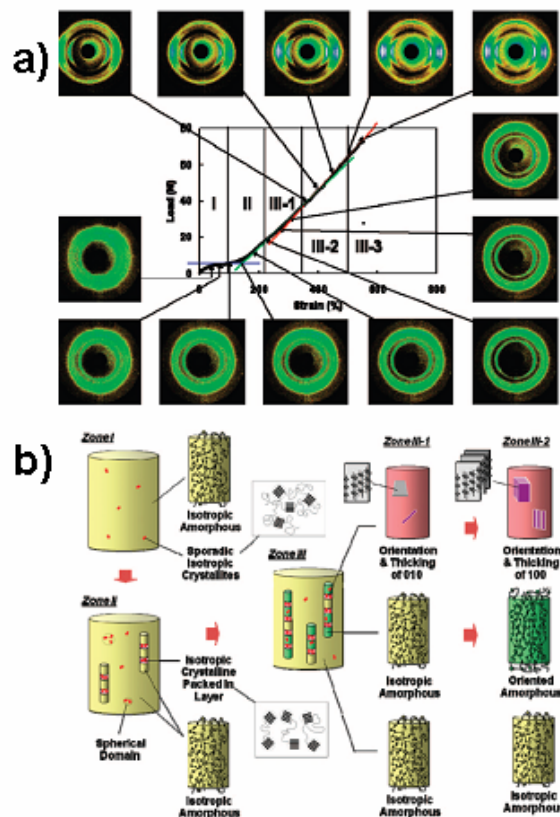


**Figure 2.12.** *a)* The load-strain curve and selected WAXD oriented images (after subtraction of the isotropic fraction). The arrows indicate the average position where each image was taken, *b)* The proposed molecular structural models for zone I, II, III-1, and III-2 [65].

#### 2.1.1.6. Effect of the stretching parameters on the mechanical and thermal properties

Mechanical properties of polymer are important in many of their applications. They reflect the material's susceptibility to deformation and failure under constant or transient loads.

It is generally agreed that the Young's modulus of stretched PET is mainly governed by the crystallinity level and the amount of orientation in the amorphous phase [67, 68]. Referring to *Section 2.1.1.2* and *2.1.2.4*, it is reasonable to say that a higher Young's modulus sample can be obtained by stretching of PET at: i) lower stretching temperatures, ii) higher stretching rates and iii) higher stretching ratios.

However most of the work carried out in previous studies is focused on the effect of stretching ratio on tensile properties. Few studies are concerned with the effect of stretching temperature and rate on tensile properties. Generally, for uniaxial stretched PET, the Young's modulus and yield stress are found to increase with stretching ratio [13, 14, 67] with only a slight increase in modulus for low stretching ratio up to 2x - 2.5x, followed by a more pronounced increase for higher stretching ratios.

The effect of the strain induced structure on the thermal properties of amorphous PET during the uniaxial stretching in the rubbery state was a subject of vast number of investigations. Those investigations were carried out mainly via *ex situ* DSC experiments [2, 16, 24, 28, 33, 34, 69] and were considered effect on the main thermal parameters/transitions, i.e.:

i) Glass transition temperature increase, as consider the review in section 2.1.1.2., could be promoted by stretching at: lower stretching temperature, higher stretching rate and higher stretching ratio.

ii) Cold crystallization temperature/transition is a sensitive measure of the state of the polymer chains. If amorphous chains are oriented but not crystallized during the stretching process, the  $T_{cc}$  decreases toward  $T_g$  as the amorphous phase orientation increases [24, 70]. In the literature it is well established that: the increase of stretching ratio leads to a shift of  $T_{cc}$  toward the  $T_g$  with a concomitant decrease of the crystallization enthalpy [14, 28, 33]. In summary the rise of  $T_{cc}$  values is promoted by: higher stretching temperature, lower stretching rate and lower stretching ratio.

iii) Melting temperature in general is not affected by the stretching process.

### **2.1.2. Stretching in the solid state**

Uniaxial stretching in the solid state means to deform the material below its  $T_g$ . The solid state stress-strain curve of amorphous polymer is shown in **Figure 2.13** [71]. Four distinct regions can be observed:

i) *region 1*: initially the stress rises in an approximately linear manner as the applied strain increases.

ii) *region 2*: where nominal stress reaches a maximum, i.e. yield point. During the subsequent fall in stress, the neck shape develops. From this point on, the strain in **Figure 2.13**. should be understood to be that at the centre of the neck.

iii) *region 3*: correspond to minimum of the nominal stress. The strain at this point corresponds to the natural drawn ratio. In tensile stretching, the strain stays at this approximately constant level for some considerable time as the neck propagates through the specimen and the specimen continues to be elongated – a phenomenon termed ‘stable necking’.

iv) *region 4*: along this region the specimen is of finite dimensions, so that at some



stage the propagating neck occupies the whole of its length – it reaches the grips at both ends of the tensile specimen. Now, further elongation causes an increase in strain and a corresponding increase in nominal stress as molecular chains are stretched – phenomenologically, this process may be termed “strain-hardening”.

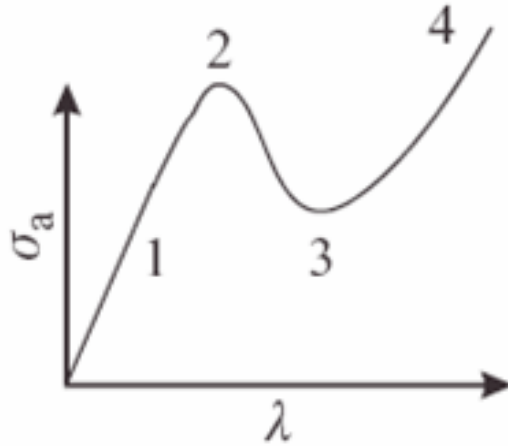


**Figure 2.13.** Stress–strain behaviour of a necking tensile specimen [71].

#### 2.1.2.1. Conformational development

During uniaxial stretching in the solid state of initially amorphous PET is formed extraordinarily large chain orientation and strain-induced a highly disordered metastable mesophormic structure without actual crystallization to occur. This mesophase transforms into the normal crystalline (triclinic) form by subsequent annealing above  $T_g$  mesophase [72, 73]. The mesomorphic structure was early identified by Bonart [72], studying the strain-induced structure of amorphous PET by X-ray diffraction techniques in the solid state. The diffuse nature of X-ray diffraction patterns was explained by Bonart [72] in terms of a nematic hexagonal (columnar) structure followed by formation of a smectic structure at higher temperatures and, then, crystallization into the triclinic form at temperature higher than  $T_g$ . The term “paracrystalline” form was also used by Bonart [72, 73] to address the disordered mesomorphic form, also commonly called mesophase, of PET.

Mesophase in PET was studied by different authors in the stretched initially amorphous samples. Auriemma et al. [74] characterized the mesophase by the presence of (00-1) reflection plane,  $d = 10.3 \text{ \AA}$ , slightly smaller than monomer length in the typical unit cell ( $c = 10.7 \text{ \AA}$ ), and (00-5) reflections in the X-ray patterns. They suggested that in the solid state oriented samples mesophase phase is an anisotropic amorphous, containing *trans* conformation chains. The mesophase transforms into triclinic crystalline one upon annealing at a temperature about  $100^\circ\text{C}$ .

Asano et al. [75] by annealing of amorphous PET uniaxially stretched in the solid state suggested the formation of an oriented nematic, with alternate position of the phenylene rings on

neighboring molecules. After annealing to 60°C nematic transform into smectic phase indicated by appearance of meridional peak (00-1) at  $2\theta = 8.56^\circ$  ( $d = 10.7 \text{ \AA}$ ), with neighboring rings aligned on plane perpendicular to the stretching direction and slight tilt of the molecules. Annealed at 80°C of nematic phase is results in the triclinic crystalline phase, with rings still planes normal to the stretching direction but with larger molecular tilt. Schematic presentation of the morphological changes is shown in **Figure 2.14**.

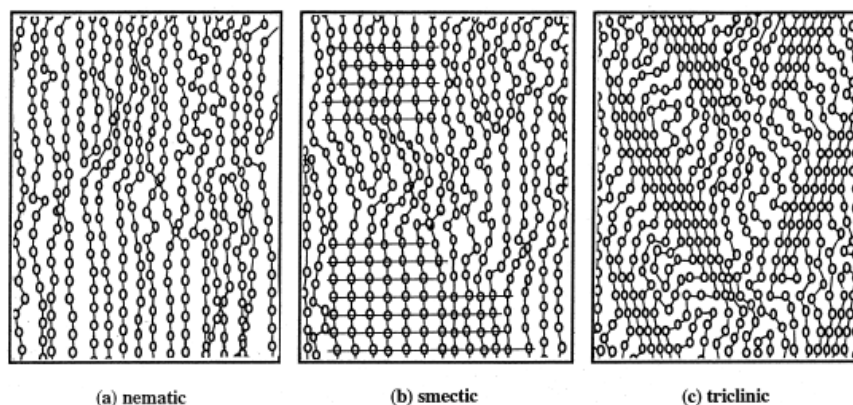


**Figure 2.14.** Schematic representation of the morphological changes: (a) nematic phase, (b) smectic phase and (c) triclinic structure [76].

Appearance of meridional peak (10-3) at  $2\Theta = 25.8^\circ$  ( $d = 3.45 \text{ \AA}$ ) in the not crystalline oriented PET during solid state stretching was associated to formation of mesomorphic conformational regularity [2, 21, 77]. This peak was present for PET annealed at 60°C and at annealing at 80°C and 180°C was replaced by typical for crystalline unit cell reflection (-103) at  $2\Theta = 26.6^\circ$  [77]. In more recent work, Ran et al. [54] proposed that development (10-3) peak indicates that chains in the mesophase already have a similar packing symmetry as in the crystalline phase.

Ran et al. [54] via *in situ* WAXS during stretching below  $T_g$  (at 50°C) and subsequent annealing, indicated that mesophase developed immediately upon the neck formation. Indicated by intensity increase upon stretching of meridian smectic mesophase peak (00-1) ( $d = 10.3 \text{ \AA}$ ), till crystalline structure began to form, thereafter drastically decrease. The  $d$ -spacing of this peak was smaller than the monomer length in the unit cell, which indicated that the chains in the mesophase formed an inclined smectic C structure. Schematic diagram of two possible packing models for the mesophase in PET was proposed and presented in **Figure 2.15**. Thus confirming that mesophase is a precursor of the crystalline structure.

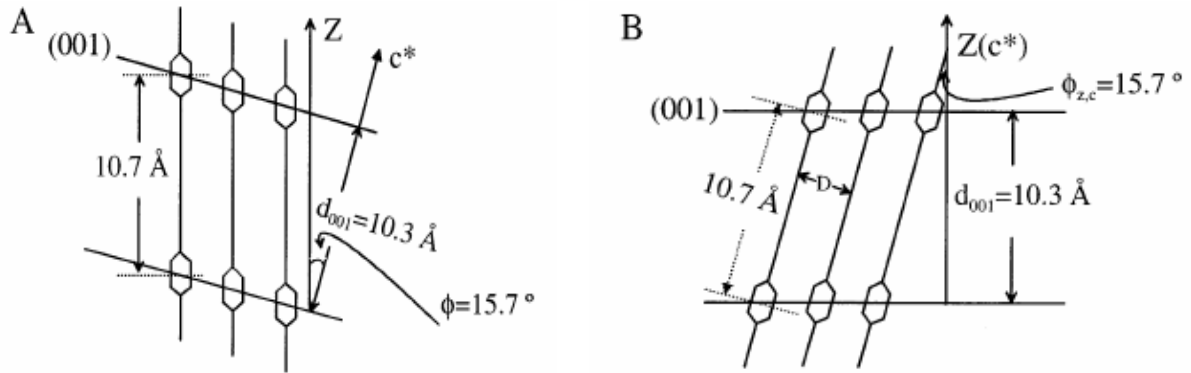


**Figure 2.15.** Schematic diagram of two possible packing models for the mesophase in PET.  $Z$  and  $c^*$  represent the stretching direction and the  $c^*$ -axis, respectively [54].

### 2.1.2.2. Deformation mechanism

It is well known from literature [78-80], that in amorphous polymers during stretching in the solid state occurs voids which nucleation and their propagation is accompanied by a substantial structural damage, as grounded on the *in situ* SAXS investigations. Macroscopically this is revealed by the whitening of the specimen upon deformation. Amorphous PET as all non-oriented amorphous polymers which are macroscopically homogeneous, subjected to uniaxial stretching in the solid state typically shows the stress-strain curve reproduced in **Figure 2.16**. [81]. This stress-strain curve consists of following regions:

i) *elastic region*: between 0 and 1 corresponding to uniform elastic with traces of anelastic deformation. Sample is deformed in a mechanically reversible manner by elastic extension (predominantly by an increase of the intersegmental distances) accompanied by uncorrelated intersegmental shear displacements and conformational changes.

ii) *anelastic region*: embraces the part of the curve between 1 and 2. Due to conformational changes in elastic region give rise to anelastic deformation (time- and strain-dependence of the elastic module), to stress relaxation and creep.

iii) *void and/or craze initiation region*: is among the point 2–3. The local microstructure begins to be modified by void and/or craze initiation and correlated segmental shear displacements.

iv) *yielding region*: corresponding to maximum stress 3. At this point specimen thins to smaller section at some point.

v) *necking region*: (3–4) where neck establish.

vi) *cold stretching region*: in at (4–5). During this region nucleated craze involves the genesis of voids in the neighborhood of a stress-concentrator and/or a plastically deformed local region of an amorphous polymer, whereas a heterogeneous mode of deformation is present. Three components competing along the region of elongation, i.e. one-dimensional *elastic* strain component, *plastic* shear strain and the *cavitation* strain component.

vii) *rupture region*: from 5 to 6 along which is observed extension of stretched material to final collapse.

The ultimate strain and the rupture mechanism strongly depend on material and experimental conditions.

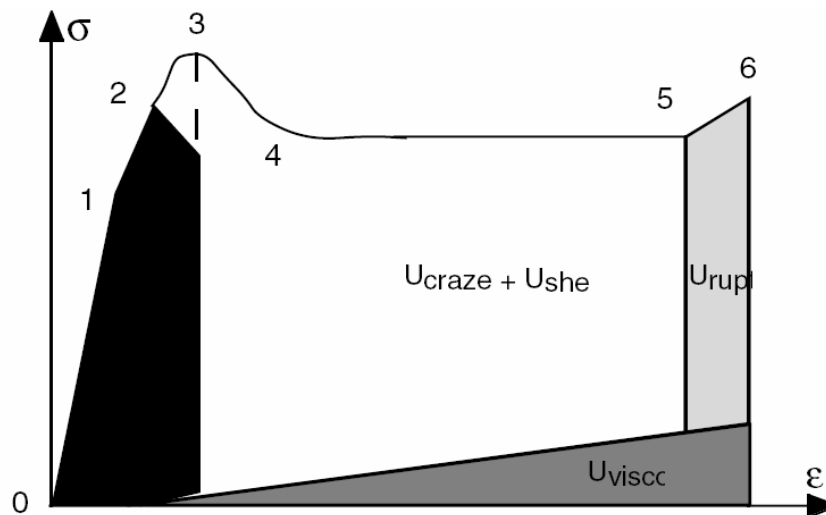


**Figure 2.16.** Typical stress-strain curve of an amorphous thermoplastic polymer [81].

## 2.2. PET nanocomposites

PET nanocomposites have attracted substantial academic and industrial interest. This section is reviewing the effect of nanofillers incorporation on the nanocomposites properties, in respect the method of preparation, up-to-date available, particularly: i) PET/MMT, ii) PET/TiO<sub>2</sub> nanocomposites and iii) PET/SiO<sub>2</sub> nanocomposites.

### 2.2.1. Montmorillonite

Silicates can be divided into several subclasses and one of them is the bentonite [82, 83]. Bentonite is a rock or ore, which belongs to the smectite group clays minerals. The smectite group consists of several minerals including [84]: i) vermiculite, ii) sauconite, iii) talc, iv) pyrophyllite, v) saponite, vi) nontronite and vii) MMT.

The most commonly used silicate for PNC preparation is the layered smectite clay silicate namely MMT. **Figure 2.17.** shows the typical structure of MMT, which is swellable with a proper polar solvent, for instance, water, since it contains an alkali metal. Talc and kaolin are not able to swell since they do not contain an alkali metal. Solvation of polar solvent can expand the basal spacing of MMT, measured by meaning of the basal peak (001) d-spacing, and finally separate the layers stack into individual layers, also called delamination.

The crystal lattice of MMTs (**Figure 2.17.**) is a sheet like structure consisting of two types of layers: i) the silica tetrahedral layer and ii) the alumina or magnesia octahedral layer.

The silica tetrahedral layer consists of  $\text{SiO}_4$  groups linked together to form a hexagonal network of repeating units of  $\text{Si}_4\text{O}_{10}$ . The alumina layer consists of two sheets of closely-packed oxygens or hydroxyls, between which octahedrally coordinated aluminum atoms are imbedded in such a position that they are equidistant from six oxygens or hydroxyls. These two layers are disposed like a sandwich with the tetrahedral layer on the outside and the octahedral layer in the middle, forming a clay sheet. [84]. The total layer thickness is about 1 nm, and the lateral dimensions of these layers may vary from  $300\text{\AA}$  to larger than several microns. Clay layers are stacked together with a van der Waals gap to form a gallery, or interlayer. Substitution of the lower valent metallic ions by Si, Al, or Mg in the layers generates negative charges that are counteracted by the alkali and alkaline cations within the galleries (**Figure 2.17.**). The surface charge of this layer structure is characterized by cation exchange capacity. The forces holding these stacks together are relatively weak, making intercalation possible [85].

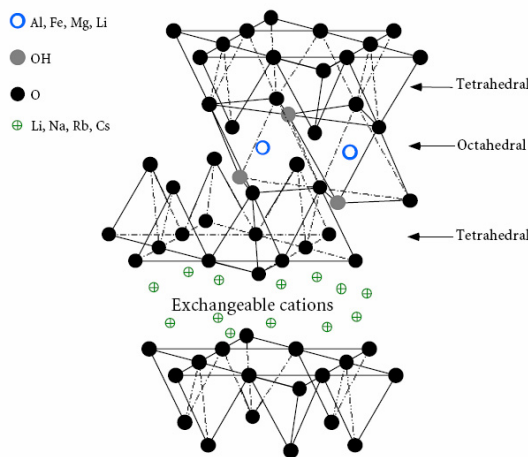


**Figure 2.17.** Structure of layered silicates [86].

The level of delamination of MMT into the polymer matrix can be used to define the morphology of the polymer/MMT nanocomposites. They can be: [87, 88] (**Figure 1.18**):

i) *tactoid morphology* (**Figure 1.18a**), it is obtained when the interlayer space of the MMT doesn't expand due to its poor affinity with the polymer, resulting in a microcomposite. As a consequence, MMT plays a little role in the property enhancement and is used only for cost reduction.

ii) *intercalated morphology* (**Figure 1.18b**), it is obtained when a small interlayer expansion of MMT is observed. In this case there is a well-ordered stacked multilayer structure as a result of some affinity between the polymer and the MMT. The interlayer spaces of the MMT are expanded as a few polymer chains penetrate the basal spacing of MMT, but the shape of layered stack maintains

iii) *exfoliated morphology* host MMT layers have lost their registry and are well separated into single layers within a continuous polymer matrix. This is due to very good affinity between the polymer and MMT (**Figure 1.18c**).

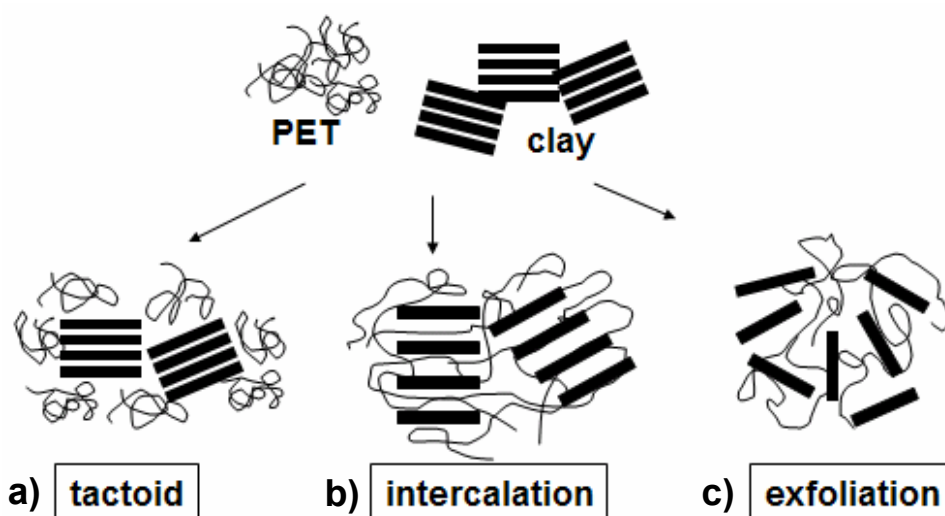


**Figure 2.18.** Three types of nanocomposite morphology: a) tactoid, b) intercalation, and c) exfoliation structure [87].

To render MMT hydrophobicity for higher compatibility with polymers, a cation exchange reaction is needed to replace sodium (or calcium or potassium) with cationic surfactants, such as:

- i) primary, secondary, tertiary and quaternary alkylammonium,
- ii) alkylphosphonium cations (onium).

When the MMT surface is chemically modified its surface energy is lowered and becomes more organophilic than natural MMT, which means that organic MMT, oMMT, can have more affinity with polymer than MMT. After an ion exchange reaction, the basal spacing of oMMT is expanded due to the bulkiness of the surfactants (alkylammonium or alkylphosphonium cations). Additionally these cations can provide functional groups reacting with polymer or initiate polymerization of monomers depend on sorts of surfactant [88-90].

A critical aspect of the surface modification of MMT is the surfactant degradation during preparation of PNCs. High temperature is needed to prepare the PNCs in order to obtain homogeneous mixing of MMT and polymer matrix or reaction of reactants, regardless of preparation methods. When the processing temperature or polymerization temperature is higher than the thermal decomposition temperature of oMMT's surfactant, thermal decomposition will occur and this cause interfacial force and affinity change between the MMT surface and the polymer matrix.

Decomposition of the surfactants is inevitable, especially in case of melt blending processing of PNCs with PET matrix, but it might be reduced by processing at a lower temperature between 255 - 265°C instead of 280°C, typical for PET processing. Recently, some works reported for preparation of PET/oMMT nanocomposites via melt blending at a temperature of 250 - 265°C with the commercial oMMT with virgin PET [91-93] and recycled PET, rPET [94-98]. All the commercial grades of oMMT dispersed in the PET matrix showed a similar final interlayer spacing, suggesting that the chemical structure of the surfactants slightly affects the degree of the PET chains intercalation into the MMT layers.

### 2.2.2. PET/MMT nanocomposites

There are several methods for preparation of PET/MMT nanocomposites. They are *in situ* polymerization, solvent blending and melt blending.

#### 2.2.2.1. In situ polymerization

*In situ* polymerization involves the swelling of oMMT by the insertion of monomers between the MMT layers then expanding and dispersing into the matrix by polymerization reaction. Four different *in situ* polymerization methods were recently used to produce PET/MMT nanocomposite:

i) *interlayer polymerization*. The growth of polymer chains separates the MMT particles into layers stacks or single layers.

Ke et al. [99] prepared PET/oMMT nanocomposite (0.5, 1.5, 3 and 5 wt%) with intercalated reagent through refinement and powdering of MMT, then reacted it with PET monomers in the reactor to form PET/oMMT nanocomposite. Exfoliation was not achieved for any of the formulations. Results of the non-isothermal crystallization, by DSC, showed that the nanocomposites had a three times greater crystallization rate than the neat PET. The tensile modulus of the PET/oMMT (5 wt%) nanocomposites increased three times compared with that of pure PET.

In more recent work, Ke et al. [100] using the same synthesis method of PET/oMMT (0.5, 1, 2.2, 3 and 5 wt%) nanocomposite. By TEM and atomic force microscopy analyses the have shown an exfoliated morphology for content less than 3 wt%, while in the range from 3 to 5 wt% a tactoid morphology of oMMT was detected. All nanocomposites exposed greater IV. DSC results proved that the nanocomposites have a higher crystallization rate than that of pure PET due to an exfoliated oMMT lamellae nucleation effect.

Chang et al. [101, 102] produced PET/oMMT (1, 2 and 3 wt%) nanocomposites which were melt-spun after. All concentrations of oMMT lead to slight increase of IV. Some of the oMMT particles were well exfoliated in the PET matrix, and some of them had a tactoid size

greater than approx. 10 nm. Improved thermal stability and tensile properties compared to the pure PET were registered for all nanocomposites. However, the values of the ultimate tensile strength and the initial modulus of the PET/oMMT fibers decreased markedly with increasing stretching ratio from 1 to 16.

ii) *polymerization with compatibilizer*. The polymerization process is initiated by the reaction between the compatibilizer and the PET monomer. By this method it is believed that the PET main chains are bonded to the oMMT surface, resulting in high mechanical performance.

Zhang et al. [103] reported for preparation of PET/oMMT (5 and 10 wt%) nanocomposites with surfactant (compatibilizer) hydroxypentyl trimethylammonium iodide, HPTA, and an ionically charged terminal monomer intercalated into the MMT. The PET/oMMT nanocomposites have an exfoliated morphology, enhanced tensile strength (58%) and better optical transparency than that of the neat PET.

Hao et al. [104] studied the effect of amount of compatibilizer used for preparation of PET/oMMT (2 wt%) nanocomposites with commercial oMMT. Delamination of MMT, as measured by TEM and XRD, was mainly in the form of tactoids. Compatibilizer results into the reduction of IV, that is proportional to its concentration, as compared to neat PET. DSC results revealed a nucleation effect, denoted by the decrease of  $T_{cc}$ , and reduction of  $T_m$ . Thermal stability evaluated by Thermal Gravimetric Analysis, TGA, showed a higher degradation temperature for nanocomposites than for PET. Dynamic Mechanical Analysis, DMA, experiments registered a decrease in  $T_g$  and an increase of storage modulus.

iii) *polymerization with a catalyst*. It is believed that the catalyst in the MMT layers increases the amount of the PET monomers between the MMT layers,

This method is used to overcome two disadvantages of using an oMMT: i) lack of a driving force between the oMMT during PET polymerization that would result in a tactoid and/or intercalated morphology, and ii) thermal degradation of the MMT's surfactants during polymerization.

Choi et al. [105] obtained PET/MMT (1, 2 and 5 wt%) nanocomposites via MMT-supported catalysts. Nanocomposites were characterized by a greater IV and TGA measurements registered much better thermal stability of PET/MMT nanocomposites, compared to neat PET. Mixed intercalated/exfoliated morphology was achieved, as detected by XRD and TEM. The oxygen permeability was gradually decreased with increase of MMT content.

iv) *polymerization with a catalyst and an organic modifier*. The MMT is further intercalated by the PET monomers, which is driven by the presence of the catalyst and facilitated by increased interlayer's space due to the surfactant. The polymerization process takes place



efficiently between the adjacent MMT layers.

Tsai et al. [106] synthesized via this method PET/oMMT (0.7, 1.2, 2.5 wt.%) nanocomposites with exfoliated morphology. IV is increased with MMT load. Nanocomposites showed a significant improvement in the flexural strength and modulus, with increase of MMT contents. Dramatic improvement of anti-UV properties and CO<sub>2</sub> gas barrier properties with MMT load increase was reported. PET/oMMT nanocomposite with 2.5 wt% was characterized by the reduction of clarity, while the other formulations were transparent.

#### 2.2.2.2. Solvent-assisted

In the solution assisted method, solvents are used to disperse the MMT and dissolve the polymers. Adequate solvents help to delaminate the MMT's layers held by the weak van der Waals forces. Polymer chains then can be absorbed onto the delaminated layers. Upon the removal of the solvents, the layers are reassembled to form the well-ordered intercalated MMT morphology.

Ou et al. [107, 108] produced PET/MMT (1, 5, 10 and 15 wt%) nanocomposite via solution assisted blending. MMT was modified with the an intercalation agent, such as: i) cetyltrimethylammonium chloride (CMC) [107] and ii) cetylpyridinium chloride (CPC) [108]. After that it was dispersed in the PET solution. They [107, 108] observed the same trends with both surfactants. TEM and WAXS results detected a mixed structure of intercalated/exfoliated morphology, for nanofiller content between 1 to 10 wt% and tactoid morphology of PET/oMMT from 10 to 15 wt%. DSC analysis shown that oMMT behaves as a nucleating agent and enhances the crystallization rate of PET, with maximum enhancement for oMMT content of 10 wt%. TGA investigation have shown that thermal stability of nanocomposites is enhanced for all concentrations of MMTs [108].

#### 2.2.2.3. Melt blending

The melt blending methods were extensively studied for preparation of PET/MMT nanocomposites, using: i) virgin PET and ii) recycled PET, rPET.

##### *PET/MMT nanocomposites with virgin PET*

Sanchez-Slois et al. [109] studied the effect of incorporation of MMT and different oMMTs (1 and 2 wt%), compounded into co-rotating twin-screw extruder under nitrogen atmosphere. Exfoliation was not observed in any of PET/MMT nanocomposites. Nevertheless significant reduction of T<sub>cc</sub>, and respective raise of degree of crystallinity with increase of MMT content was denoted. The mechanical properties were studied with specimens cut from injection blow moulded bottles. Improvement of 31% of Young's modulus and 30% of tension strength were attributed to the compatibility of MMT and the PET matrix, especially when pentarythrytol

was used as compatibilizer. The viscoelastic behaviour was affected by interaction between MMT and PET, due to polarity change.

Wang et al. [110] produced intercalated PET/oMMT (1, 3 and 5wt%) nanocomposites via extrusion in a twin-screw extruder. Best delamination was observed for the MMT content of 1wt%. Adding of MMT lead to  $T_m$  increase, decrease of  $T_{cc}$  and reduce half peak width of crystallization peak during cooling, as well as higher crystallization temperature. Nucleation rate of PET during cooling was achieved owing to nucleating effect of oMMT. PET/oMMT nanocomposite has the optimum comprehensive mechanical property when oMMTs content is 1wt%. While for 3wt% and 5wt% nanocomposites properties such as tensile strength, impact strength, flexural strength, and elongation at break are less than that of the neat PET. Thermal stability was improved for 1wt% content of MMT, as measured by TGA.

Barber et al. [111] investigated the effect of adding different content of ionomers in PET, as exfoliating agent, for the production of PET/oMMT (5 wt%) nanocomposite prepared via twin screw extruder. The nanocomposites were the injection moulded in tensile bars. TEM and XRD results show an exfoliated and/or highly intercalated morphologies due to the coupling of MMT's modification and PET ionomers content (1.8 – 5.8 mol%). The tensile modulus of nanocomposites prepared with PET with ionomers was greatly improved compared to nanocomposites made from the pure PET, as a result of the degree of exfoliation due to the strong interaction between the ionomers matrix and MMT. The higher tensile modulus corresponded to enhanced exfoliation. The DSC data revealed that the degree of MMT dispersion played an important role in the polymer crystallization process, namely: tactoids increase the crystallization rate while the exfoliated one decreased it.

Chung et al. [112] reported for PET/oMMT (8 wt%) nanocomposites prepared in a co-rotating twin-screw extruder using oMMTs with different surfactants. Exfoliated PET/oMMT nanocomposites excluding (MMT-PetLSNeom) or including (MMT-PetLSNiom) organic modifiers were prepared by melt processing via solution method with solvent-nonsolvent system and without solvent-nonsolvent system, respectively. Nanocomposite containing the commercial oMMT produced by direct melt blending had the tactoid morphology as observed by WAXS and TEM. All of the PET/oMMT nanocomposites exhibited faster crystallization kinetics and better thermal stability compared to neat PET, as measured by DSC and DMA. However, MMT-PetLSNiom and oMMT including organic modifier showed lower crystallization constant rates, longer crystallization half times, and poorer thermal properties than MMT-PetLSNeom. Mechanical characterization denoted enhanced modulus and maximum stress for all nanocomposites in respect to neat PET, while the elongation at break was reduced slightly by MMT-PetLSNeom incorporation and dramatically for the rest of the formulations. MMT-

PetLSNeom contributed for negligibly increase of yellowness of the nanocomposite, whereas other two formulations lead to 10 times greater, as compared to pure polymer sample. However, such results were ascribed to the thermal decomposition of the organic surfactants of MMT-PetLSNiom and oMMT during the melt processing.

Sanchez-Slois et al. [113] reported the investigation of PET/MMT (1, 2, and 3 wt%) nanocomposites, prepared using a twin-screw conical counter-rotating extruder, with natural MMT and with different surfactants. A series of modifiers were used, i.e. maleic anhydride (MAH), pentaerythritol (PENTA), and alkylammonium chlorides from amines of various chain lengths. Thereafter, the materials were ground and mould-injected to obtain samples for the rheological and tension tests. Significant PET thermomechanical degradation was observed by molecular weight measurements, performed by GPC, taking into account samples with the same thermomechanical history. A decrease in the viscoelastic properties (i.e. shear viscosity, storage and loss modulus) of injected samples with respect to the values of extruded PET was reported. The incorporation of MMT results in an enhancement of the elastic modulus together with deformability reduction as consequence of fillers concentration increase. Superior values were shown by all oMMT in respect to unmodified one.

Davis et al. [114] dispersed 5 wt% of two oMMTs with different thermal resistance surfactant into PET via a co-rotating mini twin-screw extruder, in a nitrogen atmosphere. Melt blending was carried out at various extruder settings. Higher surfactant temperature resistance enhanced the delamination, i.e. from intercalated PET/oMMT morphology to exfoliated one, as shown the WAXS and TEM analysis. A lower screw speed ( $21 \text{ rad.s}^{-1}$ ) and a shorter residence time (2 min) provided a better dispersion of oMMT, than a higher screw speed ( $31 \text{ rad.s}^{-1}$ ) and respectively a longer residence times (5 min).

Alyamac et al. [92] prepared PET/oMMT (1, 3, and 5 wt%) nanocomposites via reactive extrusion in a twin screw extruder. Various impact modifier of PET were added during melt blending. The characterization was performed on the injection moulded samples. In all formulations MMT decreased the MFI, since it acted as a filler. By WAXS analysis, all PET/MMT with 1 and 3 wt% MMT had an exfoliated morphology, whereas 5 wt% had tactoid morphology. The mechanical characterization revealed that: the modulus of PET/MMT nanocomposites increased with increasing MMT content; yield stress is slightly enhanced with MMT concentration; significantly improved deformability is observed at 1 wt% MMT content and decrease for 3 and 5 wt%. The impact strength of nanocomposites of 1 to 3 wt% was improved while of 5 wt% was reduced, due to stress concentration caused by the tactoid structure. DSC analysis showed that the highest  $T_g$  values were observed with 1 wt% MMT

concentration and for all nanocomposites having an exfoliated morphology. The  $T_{cc}$  decreased by the addition of the MMT, since MMT acted as a nucleating agent.

*PET/MMT nanocomposites with recycled PET*

Pegoretti et al. [94] studied extrusion blending and subsequent injection moulding of rPET/MMT nanocomposites with 1, 3, and 5 wt% of MMT and oMMT one. Better intercalation was observed in case of MMT than oMMT, according to the TEM and WAXS results. Incorporation of oMMT contributes for enhanced modulus as compared to PET/MMT. Increasing contents of both MMT result in enhanced modulus, while strain at break dramatically drops. The yield strength was not affected. The tensile compliance of the nanocomposites is only slightly lower than that of the neat rPET, the reinforcing effect of oMMT being somewhat stronger. Both MMTs have beneficial effect on the dimensional stability of the nanocomposites, in contrast to the neat rPET, the creep rate does not rise at long creep periods.

rPET/oMMT (1, 3, and 5 wt%) nanocomposites were compounded via co-rotating twin-screw extruder and subsequent injection moulded [95]. A large decrease of rPET matrix IV after extrusion-injection processing was detected. The combined WAXS and TEM results showed tactoid morphology with various tactoid sizes. Thermal analysis did not show significant changes in the thermal properties from those of rPET. The oMMT in this work did not act as an effective nucleating agent. Proportional to the nanofiller amount was reported improvement of modulus and mechanical strength (yield stress). This improvement was attributed to nanoscale effects and strong interaction between the rPET matrix and the MMT interface.

Kracalik et al. [96] compounded 5 wt% of various commercial available oMMT, which have dissimilar hydrophobicity, with rPET in a co-rotating twin-screw micro-extruder under nitrogen environment. Morphological investigations by WAXS and TEM revealed partial exfoliation of more hydrophobic oMMTs and intercalated for less one. The dynamic flow properties of the prepared composites related to structural changes associated both with the reinforcing effect (formation of physical network with oMMT loading) and degrading aspect (chain scission of rPET and oMMT decomposition tendency). Moderate matrix degradation caused by some oMMTs did not affect optical properties, mainly the transparency.

Kracalik et al. [115] additionally modified three commercial oMMTs, by solution assisted method, with [3-(glycidyoxy)propyl]trimethoxysilane, hexadecyltrimethoxysilane and (3-aminopropyl) trimethoxysilane. The 5 wt% of commercial oMMTs and additionally modified one were compounded with rPET and virgin PET via melt blending in the co-rotating twin-screw micro-extruder under nitrogen environment. The modification of oMMTs with [3-(glycidyoxy)propyl]trimethoxysilane increased the homogeneity of oMMT exfoliation in rPET with a melt viscosity reduction. Silanization of commercial oMMTs had remarkable impact on

crystallinity and melt temperature decrease accompanied by faster formation of crystalline nuclei during injection molding. Thermogravimetric analysis showed enhancement of thermal stability of additionally modified oMMTs. The tensile tests confirmed significant increase of rPET/oMMT nanocomposites stiffness with oMMT loading. On the other hand, the rPET/oMMT treated with [3-(glycidylloxy)propyl]trimethoxysilane revealed combination of high stiffness and extensibility.

In more recent work of Kracalik et al. [97] was using co-rotating twin-screw micro-extruder under nitrogen environment to prepare PET/oMMT (5 wt%) nanocomposites with virgin PET and rPET, and two types of surface modification of MMT, namely 1,2-dimethyl-3-octadecyl-1Himidazol-3-ium chloride (oMMT-IM) and additional treatment with [3-(glycidylloxy)propyl]trimethoxysilane (oMMT-IME). According to TEM and WAXS results indicated intercalated morphologies for both oMMT's where a slightly higher level of intercalation in case of PET/oMMT-IME. Rheological investigations revealed a typical shear thinning behavior with oMMT addition and a higher melt viscosity of nanocomposites in the whole measured range of shear rates compared with unfilled matrixes. In comparison with the neat polymers, the melt strength of all the nanocomposites was significantly enhanced by the formation of 3D physical network. The TGA results supported the valuation of thermal behaviour from rheological experiments. DSC analysis of nanocomposites prepared from rPET revealed a decrease in degree of crystallinity and  $T_m$ , a faster formation of crystalline nuclei, an increase in  $T_g$  and  $T_{cc}$  compared with the neat matrix. In the other hand, thermal characterization of nanocomposites with virgin PET showed similar level of  $\chi_c$ , a higher crystallization rate, and a lower  $T_g$  compared with the unloaded matrix. The rPET exhibited lower values of  $T_g$  and  $T_{cc}$  temperatures, a higher crystallization rate, and higher  $\chi_c$  than virgin PET. The results of tensile testing showed that all investigated nanocomposite increased modulus and decreased the material strength and deformability in similar range.

The effect of MMT incorporation on the properties of PET/MMT nanocomposites as compared to neat PET, is summarized here after:

- i) IV increase with the increase of MMT content,
- ii) MMT improve the degree of crystallinity due to its role as nucleation centres,
- iii) the thermal stability improves with content of MMT,
- iv) the increase of MMT's concentration strengthen the PET/MMT nanocomposites,
- v) exfoliated morphology improves yielding stress and deformability.

By far, most of the work to date on PET/oMMT nanocomposite is based on *in situ* polymerization and melt blending rather than solvent assisted method. PET/oMMT nanocomposites prepared via *in situ* polymerization in general give a higher degree of MMT

delamination than melt blending processing. Melt blending is, on the other hand, a convenient and flexible process. Both processes, however, are carried out at the processing temperature of 260-280°C for PET and this combined with a long residence time, consequently causes degradation of the MMT surfactants that resulted in a MMT's delamination.

### 2.2.3. Nanotitanium dioxide

Titanium dioxide occurs in nature as rutile, anatase and brookite. TiO<sub>2</sub> adopts at least 8 structures. Among them, rutile and anatase are mostly manufactured in the chemical industry as microcrystalline materials. The two polymorphs are based on interconnected TiO<sub>6</sub> octahedra, but their linkages and degree of edge and face sharing differ. Anatase can be regarded as a built-up of octahedrals that are connected by their vertices, whereas rutile is connected by the edges.

TiO<sub>2</sub> is widely applied as filler in polymers due to the improved physical and mechanical properties of the composites, while keeping the processability characteristics, light weight, and often ductile nature of neat polymer. Traditionally, the polymer composites are reinforced with micron-sized TiO<sub>2</sub>. Synthetic anatase and rutile are of prime importance as white pigments, colorants with application in coatings, cosmetic, foods and plastics. Because the optimal light scattering of titanium pigments occurs for particle diameter of 2.4 μm, most pigments are manufactured to have the majority of particles in the range of 1.5 to 0.3 μm, depending on the application and the undertone required.

Recently, processing techniques have been developed to allow the size reduction of TiO<sub>2</sub> to the nanoscale. Experiments have shown that nanoscale reinforcement brings new optical, electrical and physiochemical phenomena, which contribute to material properties and correspondingly extended applications. Ultrafine grades of TiO<sub>2</sub>, i.e. nanosized, typically have particle sizes in a range from 15 to 35 nm and, because of their small particle size, they are transparent to visible light, but absorb in the range of UV. Nanotitanium dioxide is manufactured by Degussa via high temperature hydrolysis process for extremely fine particle oxides [82, 116].

TiO<sub>2</sub> nanoparticles homogeneous dispersion in a polymeric matrix is a very difficult task due to the strong tendency of nanoparticles to agglomerate. The dispersability of TiO<sub>2</sub> can be strongly improved by surface modification or by the selection of the production method.

Surface modification aims to improve the hydrophobic/hydrophilic character of particles and to get better dispersability in polymers, to introduce new functional groups which can react with organic molecules and enhance their compatibility with organic polymers, to reduce the surface photoactivity in some cases. TiO<sub>2</sub> modifying methods can be divided into four main groups:

i) *chemisorption of small molecules*. Small molecules can be attracted to TiO<sub>2</sub> surface by van der Waals forces. These forces are so weak that small molecules may not be effectively

adsorbed, unless the molecule contains functional groups that can react with TiO<sub>2</sub> surface, resulting in chemisorption. The chemisorption processes include hydrogen bond formation, proton transfer, and coordination. The adsorbed species are organic acids, bases, salts and neutral compounds.

ii) *coupling agents*. This method involves the covalent bonding of adsorbed species and hydroxyl reactive groups present on TiO<sub>2</sub> surface. The O-H species on TiO<sub>2</sub> surface are used as anchor groups for the attachment of covalently bound surface modifiers. The “coupling agents” commonly used are organosilanes, metal alkoxides, epoxides, and isocyanates.

iii) *adsorption of polymers*. In contrast to small molecules modifiers, which only result in the thin adsorbed layers, use of polymers lead to forming of thick, solvatable and adsorbed layers on TiO<sub>2</sub> surface. Depending on their structures, the adsorbed polymers may act as dispersants or as processing aids.

iv) *grafting of polymers or monomers*. This method is another approach to avoid of phase-separation, where nanopowders are dispersed in the monomer or monomers solution, and the resulting mixture is polymerized. This process provides flexibility engineering the powder surface. Besides tailoring specific properties in composites via relatively strong interaction, the layer of polymer bonded to the nanopowders can control aggregation of the nanoparticles. Two principal approaches (**Figure 2.19**) for graft polymerization are [117]:

- *grafting to*, also termed "tethering", which consists of immobilization of polymerizable groups on the nanofiller surface for copolymerization,
- *grafting from*, also known as surface-initiated polymerization, which involves grafting an initiator onto the nanopowder surface to form polymer chains from the surface.

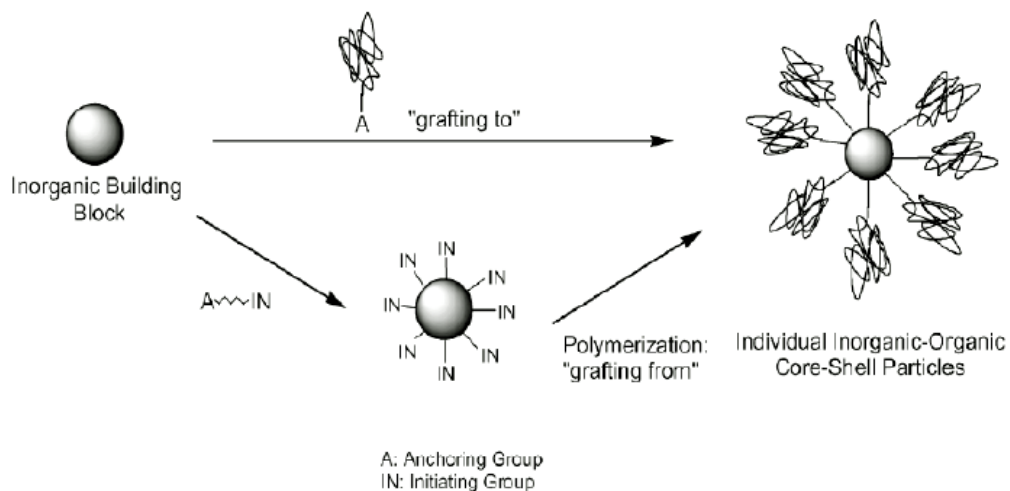


**Figure 2.19.** Two approaches of graft polymerization [117].

### 2.2.4. PET/TiO<sub>2</sub> nanocomposites

The focus of this section is according to compounding method how are altered by adding of nanosized TiO<sub>2</sub> effected the morphological, thermal, mechanical, and optical properties, in respect to preparation method.

i) *In situ polymerization method.* The PET/TiO<sub>2</sub> nanocomposites with content of 1 and 2 wt% were prepared via *in situ* polymerization, followed by melt-spinning process [118]. TiO<sub>2</sub> nanoparticles were modified with a silane coupling agent. Uniform dispersion of nanofillers in the nanocomposites was registered by TEM and scanning probe microscopy, SPM, measurements. The average particle diameter of the incorporated filler was typically below 100 nm. PET/TiO<sub>2</sub> fibres had slightly lower crystallinity in comparison with pure PET fibre, as calculated by WAXS. Polarizing light microscopy characterization revealed formation of small-sized crystals in PET/TiO<sub>2</sub> nanocomposites in comparison to the spherulites in neat PET sample. The mechanical behaviour of the fibres showed a strength and deformability reduction with the increase of the nanofiller concentration, in comparison to the neat polymer sample. The UV-blocking property of the PET/TiO<sub>2</sub> fibre improved remarkably with filler content.

ii) *Solvent-assisted method.* Frey et al. [119] prepared PET/DFA/TiO<sub>2</sub> by *in situ* polycondensation of multiblock poly(aliphatic/aromatic-ester), PET/DFA, and TiO<sub>2</sub> nanoparticles. A volume fraction of 0.13 vol% of inorganic nanofiller was used. It was observed by DSC that incorporation of TiO<sub>2</sub> particles reduces the melting point, as well as the glass transition temperature of the composite. Mechanical characterization results revealed nearly 100% tensile strength increase and 300% elongation at break increment with respect to the neat copolymer matrix due to incorporation of 0.13 vol% of TiO<sub>2</sub> nanoparticles. The surfaces of the composite samples were significantly rougher than those of the neat PET/DFA polymers according to the topographic measurements.

iii) *Melt blending method.* Taniguchi et al. [120] characterized PET/TiO<sub>2</sub> nanocomposites with 0.35 and 2.2 wt%. The nanocomposites were prepared by melt blending using a single screw extruder. Their results revealed slight decrease of IV with the increase of the inorganic filler. The thermal characterization revealed insignificant effect on the melting peak but enhance the thermally induced crystallization. A T<sub>g</sub> rise was measured by DMA with filler concentration. In the solid state, the presence of fillers increases the modulus and strength as compare to the neat PET sample.

### 2.2.5. Nanosilica

The structure of nanosilica shows a three-dimensional network. Silanol and siloxane groups are created on the silica surface, leading to the hydrophilic nature of the particles. The surfaces of the silica are typically terminated with three silanol types: free or isolated silanols,



hydrogen-bonded or vicinal silanols and geminal silanols (**Figure 2.20.**) [121]. The silanol groups residing on adjacent particles, in turn, form hydrogen bonds and lead to formation of aggregates, as shown in **Figure 2.21.** These bonds hold individual fumed silica particles together and the aggregates remain intact even under the best mixing conditions if stronger filler-polymer interaction is not present [122].

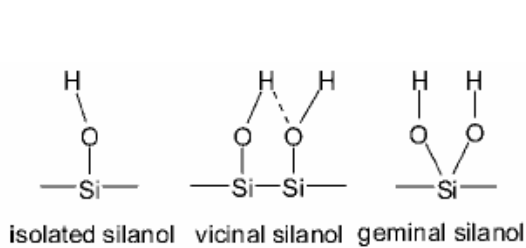


**Figure 2.20.** Schematic illustrations of three types of surface silanol [121].

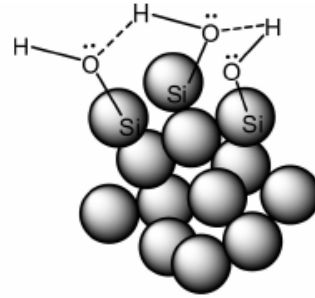


**Figure 2.21.** Schematic of aggregate formation between adjacent fumed silica particles through hydrogen bonding among the silanol groups [122].

Making a homogeneous dispersion of nanoparticles in a polymeric matrix is a very difficult task due to the strong tendency of nanoparticles to agglomerate. Consequently, the so-called nanoparticles filled polymers sometimes contain a number of loosened clusters of particles, agglomerates, (**Figure 2.22.**) and exhibit properties even worse than conventional particle/polymer systems [123].

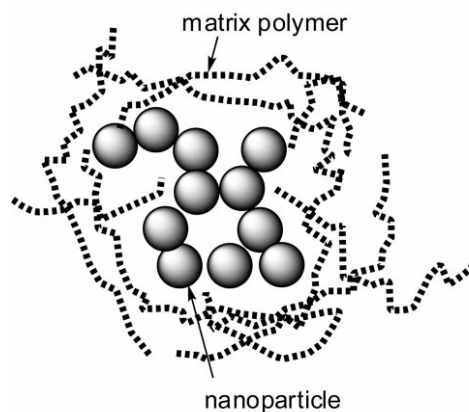


**Figure 2.22.** Schematic drawings of agglomerated nanoparticles within a polymer matrix [123].

In order to improve the dispersion/deagglomeration of SiO<sub>2</sub> nanofillers into the polymer matrix and to produce nanostructural composites, two main methods of surface modification can be used [124]:

i) *chemical modification*: methods involve modification either with a modifier agents or by grafting polymers.

As most used modifier agents are silane coupling agents. They generally have hydrolyzable and organofunctional ends. The general structure of the coupling agents can be represented as [121]  $\text{RSiX}_3$ , where the X represents the hydrolyzable groups, which are typically chloro, ethoxy, or methoxy groups. The organo, R, group can have a variety of functionalities chosen to meet the requirements of the polymer. The functional group X reacts with hydroxyl groups on the  $\text{SiO}_2$  surface, while the alkyl chain may react with the polymer. Hydrophobic silica can thus be obtained.

Grafting of polymer chains to silica nanoparticles is also an effective method to increase the hydrophobicity of the particles and to bring about tenable interfacial interactions in the nanocomposites. Generally, there are two main approaches to chemically attaching polymer chains to a surface (covalent attachment of end-functionalized polymers to the surface) as chemically presented in **Figure 2.19**. ways: i) *grafting to* and ii) *grafting from*.

It was found that modification of nanoparticles through graft polymerization was very effective to obtain nanocomposites because of: i) an increase in hydrophobicity of the nanoparticles that is beneficial to the filler/matrix miscibility, ii) an improved interfacial interaction yielded by the molecular entanglement between the grafting polymer on the nanoparticles and the matrix polymer, and iii) tailorable structure-properties relationship of the nanocomposites provided by change on the species of the grafting monomers and the grafting conditions since different grafting polymers might bring about different interfacial characteristics [121].

ii) *physical modification*: methods are based on physical interaction is usually implemented by using of surfactants or macromolecules adsorbed onto the surface of silica particles. The principle of surfactant treatment is the preferential adsorption of a polar group of a surfactant to the surface of silica by electrostatic interaction. A surfactant can reduce the interaction between the silica particles within agglomerates by reducing the physical attraction and can easily be incorporated into a polymer matrix.

### **2.2.6. PET/SiO<sub>2</sub> nanocomposites**

This section contains a retrospective review of work related to the PET/SiO<sub>2</sub> nanocomposites discussed by preparation method, i.e. i) *in situ* polymerization, ii) solvent-assisted, iii) melt blending, and iv) cryomilling blending.

#### **2.2.6.1. In situ polymerization**

PET/oSiO<sub>2</sub> (0.1, 0.5 and 2 wt%) nanocomposites were synthesized by *in situ*

polymerization and melt-spun into fibres [125]. A good dispersion of filler was obtained, i.e. agglomerated particles with average size of ranging from 10 to 20 nm for different formulations PET/SiO<sub>2</sub> nanocomposites as TEM investigation revealed. No reduction of IV of polymer matrix was observed. Fibres show nonlinear changes in the tensile strength and elongation at break, namely improvements for incorporations of 0.1 and of 0.5 wt% and a reduction for 2 wt %.

Yang et al. [126] prepared PET/oSiO<sub>2</sub> nanocomposites (0.1, 0.5, 1, 1.5, 2, 2.5 and 3 wt.%) by *in situ* polymerization. Approximately equal IVs of pure PET and PET/oSiO<sub>2</sub> samples due to control of polymerization by melt viscosities. TEM measurements show that oSiO<sub>2</sub> nanoparticles were well dispersed in the PET matrix at a size of 10–20 nm. The addition of SiO<sub>2</sub> results in an increase of T<sub>g</sub> proportional to the nanofiller content, as well as crystallization rate, by DSC. All the crystallization parameters were found to be sensitive to the content of nanosilica within the explored range. The crystallization kinetics constants of PET/SiO<sub>2</sub> nanocomposites are about 78–1770 times larger than those of the neat sample. On the other hand, reductions of the spherulite size and of the surface free energy for nucleus formation were observed by polarizing light microscopy.

PET/SiO<sub>2</sub> nanocomposites were fabricated by *in situ* polymerization, from PET monomer dispersed with oSiO<sub>2</sub>, with content of 0.5 and 2.5 wt% [127]. Relatively good dispersion of nanofiller was observed for concentration of 0.5 wt% and average agglomerate size about 30 nm were obtained at higher concentration of 2.5 wt% contributes for particle agglomeration respectively size about 60 nm. Approximately equal IVs were measured for nanocomposites and the neat PET because the polymerizations were controlled by melt viscosities. Addition of nanoparticles increases the T<sub>g</sub>, T<sub>cc</sub> and T<sub>m</sub> proportionally to the nanofiller content, as registered by DSC. Shifts to a higher temperature with increasing the inorganic filler amount was denoted by TGA experiments.

Tian et al. [128] prepared PET/SiO<sub>2</sub> (2 wt%) nanocomposites *in situ* polymerization. Nanocomposite sample has a slightly lower IV as compared to the pure PET. TEM micrographs revealed that the nanoparticles were well dispersed in the PET matrix and strong interaction between the particles and the polymer chains. DSC results indicated that the thermal properties of PET/SiO<sub>2</sub> are strongly enhanced as compared to pure PET, namely T<sub>g</sub> and T<sub>m</sub> increase evidencing nucleating agent effect. Both samples were spun in fibres at different velocities and after that stretched to the up to ratios in range the 3.6x – 4.4x. Mechanical test of fibres show that the tenacity and modulus of the nanocomposite sample were higher than those of neat one. Heat shrinkage of PET/SiO<sub>2</sub> was lower than that of pure PET. Those fibres properties were related to the increasing of crystallinity and the strong interface interaction of the nanocomposite.

Tian et al. [129] prepared PET/SiO<sub>2</sub> (0.5, 1, 2 and 4 wt%) nanocomposites were fabricated by *in situ* polymerization. The crystallization process of nanocomposites was investigated by DSC and then analyzed using the Avrami method. The results indicated that the crystallization of pure PET was fitted for thermal nucleation and three-dimensional spherical growth throughout the whole process, whereas the crystallization of nanocomposites exhibits two stages: i) first stage corresponds to athermal nucleation and three-dimensional spherical growth and ii) corresponds to re-crystallization caused by the earlier spherulites impingement. The crystallization rate increases remarkably and the activation energies decrease considerably when silica nanoparticles are added. The subsequent melting behaviour of the crystallized samples shows that the T<sub>m</sub> of nanocomposites is higher than that of pure PET. This was related to hypotheses: i) due to some hindrance to the PET chains caused by the nanoparticles at the beginning of the melting process and ii) it might also be the case that more perfect crystals can be formed due to the higher crystallization temperatures and lower activation energies of nanocomposites.

Yang et al. [130] synthesized by *in situ* polymerization PET/oSiO<sub>2</sub> (0.1, 0.5, and 2 wt%) nanocomposites which were melt-spun to fibres. According to the TEM, oSiO<sub>2</sub> nanoparticles were well dispersed in the PET matrix at a size level of 10–20 nm. Approximately equal to pure PET IV was obtained for the nanocomposites. PET/SiO<sub>2</sub> nanocomposite fibres showed a greater degree of weight loss as compared with that of pure PET fibres. Incorporation of nanofillers leads to formation more and tougher superfine structures, such as cracks, craters, and cavities which would facilitate the certain application like deep dyeing.

Zheng et al. [131] by *in situ* polymerization prepared PET/SiO<sub>2</sub> (0.1 wt%) nanocomposites which were spun in fibre further. Nanoparticles were uniformly dispersed in the process of polymerization by means of hot-stage polarization microscope. DSC results show that nanosilica does not behave as a nucleating agent in PET but postpones the appearance of crystallite. The investigation on melt spinning of nanocomposites has better spinnability than the pure PET.

Zheng et al. [132] by *in situ* polymerization prepared PET/SiO<sub>2</sub> (1, 3 and 5 wt%) nanocomposites. In focus of this work was investigation of thermal degradation measured by TGA and pyrolysis-gas chromatography/mass spectrometry. Main conclusions are: i) silica effect to on extend the decomposition process, ii) nanocomposites have better thermo stability as compared to pure PET and higher residual carbon content and activation energy. This is deduced that the increase of the activation energies and the residual carbon content result from the adsorption of the decomposed products on the surface of silica.

Zhang et al. [133] *in situ* polymerization was used for preparation of PET/SiO<sub>2</sub> (1 and 2 wt%) nanocomposites which were moulded in amorphous films by compression moulding. Such obtained films were annealed to different temperature for isothermal crystallization from the glassy state. Nanocomposite samples have the T<sub>cc</sub> shifted to a lower temperature as SiO<sub>2</sub> content increased which indicated that increasing silica favoured its role as a nucleating agent during the DSC tests. Effectiveness as nucleating agent of SiO<sub>2</sub> was confirmed by increased crystallinity of nanocomposite samples, in comparison to pure PET, measured via WAXS and FTIR.

Zhang et al. [134] synthesized by *in situ* polymerization PET/SiO<sub>2</sub> (1 wt%) nanocomposites which were melt-spun to fibres and after this stretched to ratios of 3.6x and 3.8x. Mechanical testing results showed improved mechanical properties of nanocomposites as correlated with the pure PET fibre, namely enhanced modulus. WAXS microstructure investigations suggested that the amorphous phase orientation was increased by presence of SiO<sub>2</sub> which was proposed as main factor contributing to the improvement of tensile properties of PET/SiO<sub>2</sub> fibres.

#### 2.2.6.2. Solvent-assisted

Bikiaris et al. [135] prepared using two-stages polycondensation method to prepare PET/oSiO<sub>2</sub> (1, 2.5 and 5 wt.%) nanocomposites. The PET/oSiO<sub>2</sub> cross-linked macromolecules of new type were obtained. TEM investigation show trend to increase size of SiO<sub>2</sub> particles agglomerates size with increase of their percentage. As the amount of oSiO<sub>2</sub> increased the rate of increase of the IV slow down because of the higher extent of branching. TGA results declared that upon addition of silica, the residue weight is increased. At 5 wt% SiO<sub>2</sub>, the extensive branching produced a cross-linked polymeric material. At concentrations lower than 2.5 wt%, these reactions are diminished and thus the IV appropriately increases. In all prepared samples the melt strength is substantially increased, which enhances the resins end properties. In more recent work of same group [136] the solid state polycondensation kinetics of PET/oSiO<sub>2</sub> (0.25, 0.5, 1, 2.5 and 5wt%) nanocomposites were thoroughly investigated.

Wu et al. [137] reported the preparation of PET/SiO<sub>2</sub> (0.5, 1, 2, 3 and 5 wt.%) nanocomposites films with unmodified, SiO<sub>2</sub>, and grafted with polystyrene, oSiO<sub>2</sub>. As production technique was used solution blending followed by compression moulding. Better dispersion and chemical connection between modified SiO<sub>2</sub> particles was revealed via TEM in respect to the unmodified ones. Adding of oSiO<sub>2</sub> particles to the PET matrix resulted in stronger barrier to water absorption than untreated nanoparticles.

Wu et al. [138] investigated the crystallization and optical behaviour of PET/SiO<sub>2</sub> (2 wt%) nanocomposites with SiO<sub>2</sub> and modified oSiO<sub>2</sub>. Nanocomposites were prepared by dispersion in solution and subsequently compression moulding. The addition of nanofillers has a

little effect on the  $T_m$  of PET, but an increasing effect on the  $T_{cc}$  from melt as measured by DSC, which was attributed to the better dispersion of oSiO<sub>2</sub> than the natural one, what results in multiple nucleation centres. The light transmittance was improved by adding of oSiO<sub>2</sub>.

### 2.2.6.3. Melt blending

Chung et al. [139] characterized PET/SiO<sub>2</sub> (0.5, 2 and 8 wt%) nanocomposites via direct melt blending in Haake twin roll counter rotating mixer with natural SiO<sub>2</sub> and with different surface modifications. The SEM images showed that oSiO<sub>2</sub> was better dispersed than the SiO<sub>2</sub> particles. DSC results show, regardless of the oSiO<sub>2</sub> modification and content, weak influence on the melting enthalpy and  $T_m$ , of PET/SiO<sub>2</sub> composites. The crystallinity of all nanocomposites increases rapidly until actual filler content of 2 wt%, but over this point it increase very slowly. Thus, this means that the crystallization rate and crystallinity of all nanocomposites are only proportional to the actual filler content, regardless of silica modification and there is critical filler content for them to act as nucleating agents. Tensile strength of PET/SiO<sub>2</sub> untreated nanocomposites increases until the filler content reaches 4.0 wt%, but the excessive filler loading induces the deterioration of the tensile strength for PET/oSiO<sub>2</sub> that it monotonously decreases from low filler content. In terms of elongation at break the PET/oSiO<sub>2</sub> nanocomposites shown higher than others formulations in the range of filler content of 1 - 4 wt%, although it decreases as filler content increase.

### 2.2.6.4. Cryomilling blending

Alternative method for preparation of PET/SiO<sub>2</sub> nanocomposites was proposed by Zhu et al. [140], namely the cryomilling. Initially, silica particles have an average size about 300 μm. A three-stage model to illustrate the formation mechanism of PET/SiO<sub>2</sub> nanostructures was deduced: i) *stage I*: the great reduction of particle size and the transformation of PET from big blocks into flakes; meanwhile the SiO<sub>2</sub> agglomerates were broken up and dispersed in PET flakes forming the primary composite particles, ii) *stage II*: the gradual dispersion of single SiO<sub>2</sub> nanoparticles into PET flakes, and the formation of the secondary composite particles due to the agglomerates of the refined PET/SiO<sub>2</sub> primary composite particles, iii) *stage III*: the constant size of the secondary composite particles and the further homogeneous dispersion of nanometer SiO<sub>2</sub> in the PET matrix.

It was shown that, upon cryomilling for 10 h, SiO<sub>2</sub> nanoparticles were well-separated into single particles, with size about 30 nm, that get homogeneously dispersed in PET matrix. The resulted PET/SiO<sub>2</sub> primary particles were flake-shaped with a size of 400 nm. These primary composite particles agglomerated to form secondary composite particles with an average size about 7.6 μm. The achieved dispersion ability of this method was far beyond the capability of

conventional melt blending carried out by HAAKE mixer, which was ascribed to solid processing, high mechanical energy of ball milling, and cryogenic temperature.

In more recent work of same authors [141] reported a structural characterization of PET/SiO<sub>2</sub> nanocomposites prepared by cryomilling. Cryomilling resulted in amorphization of crystalline PET matrix according to the WAXS results. Processing induced molecular chains scission and the decrease of the molecular weight. The DSC revealed that PET/SiO<sub>2</sub> nanocomposites dispersed nanoparticles play role of nucleating agent and improve the ability for crystallization during hot crystallization. On the other hand, nanocomposites have good size stability in the reheating process, which bifacial for in service conditions.

## 2.3. Deformation mechanism of PNC during uniaxial stretching

Very few reports can be found in the literature regarding the study of the deformation mechanisms of PNCs during uniaxial deformation. A review is made in this section, according to the type of nanoreinforcement used, namely: i) 1D as a MMT and ii) 3D particularly the SiO<sub>2</sub> and TiO<sub>2</sub> isodimensional nanofillers.

### 2.3.1. Polymer/1D nanocomposites deformation mechanism

The preparation of PNCs with MMT is greatly studied among the 1D reinforcements due to its availability and comparatively easy surface modification. As discussed previously, three types of MMT morphologies can appear in the PNCs, such as: i) tactoid, ii) intercalated and iii) exfoliated. Depending on that a variety and complex deformation mechanisms takes place during the uniaxial stretching of the composites.

Kim et al. [142, 143] proposed a models for the micromechanical deformation of PNCs with MMT tactoid [142] and morphology [143] upon uniaxial stretching PA/MMT samples were prepared by injection moulding. They recognized as main deformation mechanism microvoid formation inside tactoids or intercalated MMT particles, where large voids form around large inhomogeneities, based on the *in situ* high voltage electron microscope investigation. The formation of voids take place during the plastic deformation, since the individual MMT layers stacked in the polymer matrix are weakly bonded to each other. The nanoparticles are load-bearing because their surfaces in the microvoids are connected and hinder further growth of the microvoids, thus contributing for better deformability. As a consequence, the stiffness/strength/toughness balance has been synergistically improved. Three possible modes of deformation were identified depending on MMT's particles position toward the stretching direction, as depicted for the tactoid in **Figure 2.23** and for intercalated morphology in **Figure 2.24**. Modes can be summarized as follow:

i) *splitting*: perpendicular to stretching direction, deformation initiates at the middle region of the stacked MMT's particles (tactoid) or splitting of the platelets takes place in the middle of intercalated MMT particle,

ii) *opening*: at a certain angle in respect to stretching direction, opening of bundles of the stacked particles (tactoids) or bundles of the intercalated MMT layers,

iii) *slipping*: parallel with stretching direction, slipping bundles of the stacked MMT's particles in case of tactoid morphology and sliding of pallets of MMT particles for intercalated one.

The originated void size is directly related to the MMTs morphology: intercalated state results in smaller voids than the tactoid one.

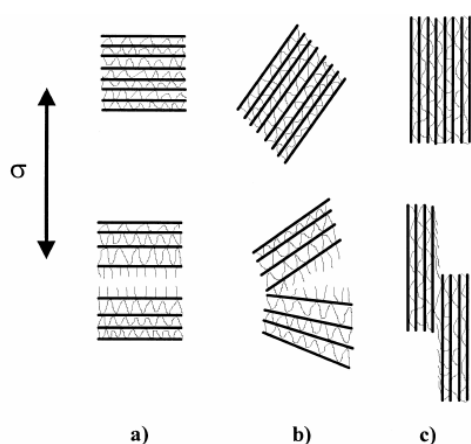


**Figure 2.23.** Schematic models of micromechanical deformation processes of the stacked MMT layers, tactoids, depending on the orientation (arrow indicates the load direction): a) splitting, b) opening and c) sliding mode [142].

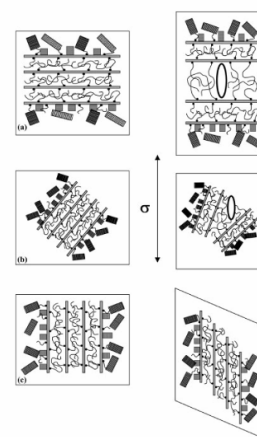


**Figure 2.24.** Schematic deformation processes in the intercalated morphology system (arrow indicates the load direction): (a) splitting, (b) opening and (c) sliding mode [143].

Kim et al. [143] via TEM investigation revealed microvoids in the range of micrometers are elongated in the stretching direction and homogeneously distributed in specimen with exfoliated morphology. Authors suggested that an exfoliated morphology is much more effective in transfer of the external applied stress from the polymer matrix to the MMT, as compared to the tactoid and intercalated one, due to the increased number of polymer/MMT interactions which results in the uniform formation of microvoids. Thus a higher increase in the Young's modulus is achieved. Furthermore, the uniform well-developed formation of microvoids throughout deformed specimens and their subsequent growth should enhance matrix shear yielding, which is directly associated with energy dissipation during deformation; that is, it is reflected in the enhancement of the toughness of the system of exfoliated morphology.



Renner et al. [144] investigated the deformation mechanism in PA/oMMT nanocomposites, with tactoids morphology, via *in situ* acoustic emission and volume strain measurements. Attention was paid to nanocomposites morphologies consisting of mixed MMT's morphology like tactoids, intercalated and exfoliated. They concluded that elastic deformation and shear yielding dominates during the elongation of the specimens. Also, the free volume increases due to voids occurrence, mainly generated mainly by the fracture of the tactoids and rarely owing to polymer/oMMT separation as based on the acoustic events. Authors claimed that the type and amount of the surfactant used for modification plays an important role in the determination of deformation processes and properties, since it influences both polymer/MMT interaction and the internal adhesion of MMT particles.

### **2.3.2. Polymer/3D nanocomposites deformation mechanism**

Kim et al. [145, 146] studied the toughening mechanisms occurring in PNC with semicrystalline polymer matrix. They proposed a three stage mechanism for describing the micromechanical deformation process of PNCs with inorganic spherical nanofillers during the uniaxial stretching. Two main modes micromechanical deformation processes, due to the dispersion of nanoparticles, of individual PNC systems can occur i) single debonding process in case of single particle (**Figure 2.25**) and ii) multiple debonding process when agglomerates are present (**Figure 2.26**). These stages are described as follow:

i) *Stage I: stress concentration.* The inorganic nanoparticles act as stress concentrators, because they have different elastic properties from the polymer matrix. The stress concentration leads to the development of a triaxial stress in the polar region of particles and in the equator of agglomerates that cause its dilatation.

ii) *Stage II: void and shear band formation.* Due to the stress concentration, a higher hydrostatic or triaxial stress builds up inside the particles, giving rise to void formation through debonding at the particle matrix interface on the poles (**Figure 2.25**) and within the agglomerates lead to developed craze-like structure (**Figure 2.26**). With continuous growth of voids, simultaneously, weak shear bands are formed in the matrix between the voids under an angle of about 45° to the direction of the maximum principal tensile stress.

iii) *Stage III: induced shear yielding.* When debonding occurred, the triaxial tension can be locally released in the surrounding of voids corresponding to an increase in the shear component. Thereby the yield strength is lowered. As a consequence, the further shear yielding is greatly induced in the matrix.

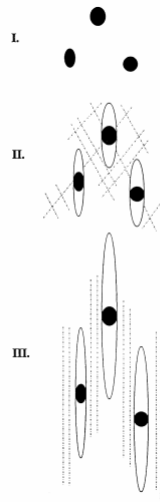


**Figure 2.25.** Single debonding process: PP/Al(OH)<sub>3</sub> polymer composite [146].

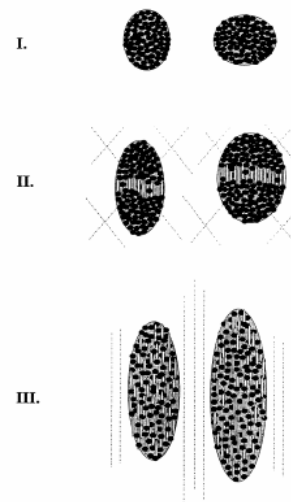


**Figure 2.26.** Multiple debonding process: PE/SiO<sub>2</sub> polymer composite [146].

Energy dissipation and stress state during uniaxial stretching of PNCs is schematically illustrated in **Figure 2.27** [145, 146]. Deformation process is divided into two regions:

i) *elastic region*: since uniaxial tensile stress is applied to the specimen, the stress concentrates around the nanoparticles due to the differences of modulus between the matrix and the dispersed nanoparticles. Consequently maximum stress concentration is placed at the poles of nanofiller. This stress concentration leads to the local transition from uniaxial to triaxial stress state. This triaxial stress causes a small volume dilatation in the surrounding area of inorganic rigid nanofiller particles, where some applied energy,  $E_D$ , is dissipated. Up to this point, these successive events take place within the elastic region, because on removal of the external load the specimen fully recovers.

ii) *plastic region*: is observed until the maximum triaxial stress is reached, the microvoid formation occurs in the specimen, which is caused by either debonding processes depending on the types of modifier particles. Through the initiation of microvoids, the extra additional applied energy,  $E_V$ , in the specimen is dissipated. Once the microvoids are formed in the matrix, the hydrostatic stress caused by stress concentration is released, with the stress state in the ligaments of matrix material between the voids being converted from a triaxial to more biaxial or uniaxial tensile stress state. This stress state is significant for the initiation of the shear bands. The microvoids gradually grow in the applied stress direction with increasing strain in the specimen. Through the continuous plastic growth of voids, the triaxial stress will be further released, by which the plastic deformation of the ligaments of matrix material is considerable accelerated. For these processes the applied energy through the growth of voids,  $E_{GV}$ , and the plastic deformation of matrix material,  $E_M$ , is dissipated.

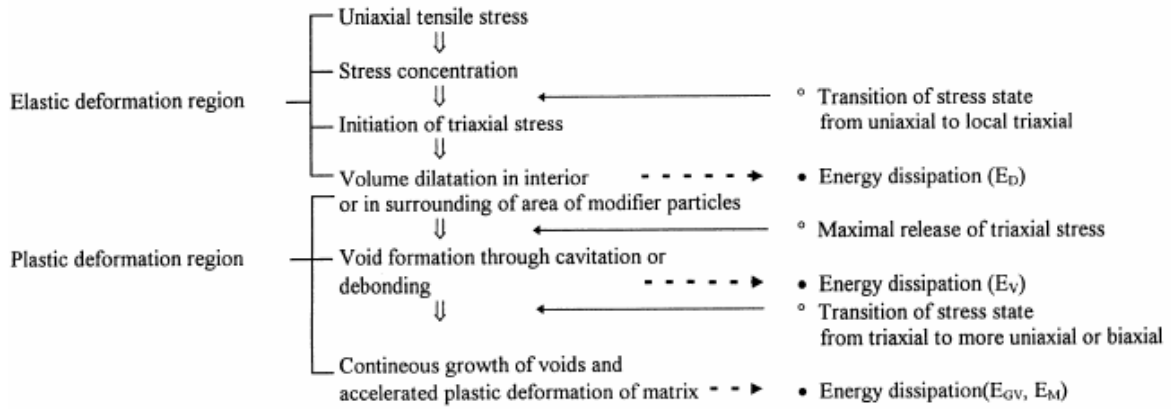


**Figure 2.27.** Schematic illustration of energy dissipation and stress state during uniaxial stretching [146].

Reynaud et al. [147] investigated the effect of SiO<sub>2</sub> nanoparticles (12 and 50 nm) on the deformation mechanism of PA6/SiO<sub>2</sub> (5wt%) nanocomposite prepared via *in situ* polymerization and subsequent injection moulding. Mechanical characterization revealed that nanocomposites have improved elastic modulus with a little variation with particle size as compared to neat PA6 sample. Nanocomposite yield stress increased with increasing filler concentration, and increased slightly as the size of the particles decreased. Ultimate strain decreased greatly, as concentration increased and particle size decreased. These differences in the mechanical properties of nanocomposites with different sizes of SiO<sub>2</sub> were explained by the debonding process (**Figure 2.28**), referring to the principles of deformation mechanism in [145, 146]. They suggest that: i) *small particles*: (12 nm) gather into smaller aggregates leading to a multiple debonding process resulting in multiple elliptical voids with sizes similar to the nanoparticle size and ii) *bigger particles*: (50 nm) forming bigger aggregates undergo a single debonding process causing voids of bigger size. The debonding process was also used to explain why the volume of the polymer nanocomposites increased, with the greatest increase occurring in systems with the smallest particles.

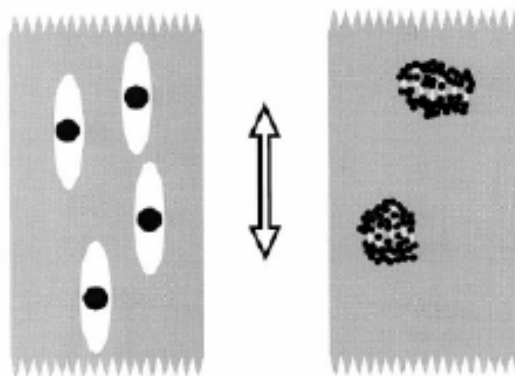


**Figure 2.28.** Schematic representations of the debonding process around 50 nm (left) and 12 nm (right) particles [147].

Recently, were also reported a few research works based on the *in situ* SAXS investigation of PET nanocomposites with: i) carbon nanotubes [148], ii) carbon black [149] and iii) multiwalled carbon nanotubes [149]. In case of incorporation of 3D nanoparticles, i.e. carbon black [149], in PET matrix increases the fracture toughness of the nanocomposite film by increasing the plastic work of fracture, during uniaxial stretching in the solid state. This prevented the localization of deformation upon the crazes formed at earlier stages of tensile deformation and to retard the growth of the fibrils in the crazes to a critical length.

## 2.4. References

1. Salem, D.R., *Crystallization during hot-drawing of poly(ethylene terephthalate) film: influence of temperature on strain-rate/draw-time superposition*. Polymer, 1994. **35**(4): p. 771-776.
2. Goschel, U., *Thermally stimulated structural changes in highly oriented glassy poly(ethylene terephthalate)*. Polymer, 1996. **37**(18): p. 4049-4059.
3. Salem, D.R., *Crystallization during hot-drawing of poly(ethylene terephthalate) film: influence of the deformation mode*. Polymer, 1995. **36**(18): p. 3605-3608.
4. Salem, D.R., *Crystallization kinetics during hot-drawing of poly(ethylene terephthalate) film: strain-rate/draw-time superposition*. Polymer, 1992. **33**(15): p. 3189-3192.
5. Salem, D.R., *Development of crystalline order during hot-drawing of poly(ethylene terephthalate) film: influence of strain rate*. Polymer, 1992. **33**(15): p. 3182-3188.
6. Clauss, B. and D.R. Salem, *Characterization of the non-crystalline phase of oriented poly(ethylene terephthalate) by chain-intrinsic fluorescence*. Polymer, 1992. **33**(15): p. 3193-3202.
7. Aiji, A., et al., *Amorphous orientation of poly(ethylene terephthalate) by X-ray diffraction in combination with Fourier transform infra-red spectroscopy*. Polymer, 1995. **36**(21): p. 4023-4030.
8. Hermanutz, F., D.R. Salem, and S.P. Wesson, *Influence of microstructure developed during drawing on surface properties of poly(ethylene terephthalate) film*. Polymer, 1994. **35**(21): p. 4611-4617.
9. le Bourvellec, G., L. Monnerie, and J.P. Jarry, *Amorphous orientation and induced crystallization in uniaxially stretched poly(ethylene terephthalate glycol)*. Polymer, 1986. **27**(6): p. 856-860.
10. le Bourvellec, G., L. Monnerie, and J.P. Jarry, *Kinetics of induced crystallization during stretching and annealing of poly(ethylene terephthalate) films*. Polymer, 1987. **28**(10): p. 1712-1716.
11. Nevalainen K, M.D., Everall NJ, Kuusipalo J, *The microstructure of a polyethylene terephthalate matrix near to a void under uniaxial draw*. Materials Chemistry and Physics, 2007(101): p. 103–111.
12. Ward, I.M., et al., *The Stress Optical Behavior of PET Fibers and Films*. Polymer Engineering and Science, 1999. **12**(39): p. 2335-2348.
13. Aiji, A., et al., *Orientation and structure of drawn poly(ethylene terephthalate)*. Polymer, 1996. **37**(16): p. 3707-3714.
14. Aiji, A., et al., *Orientation of Amorphous Poly(Ethylene Terephthalate) by Tensile Drawing, Roll-Drawing, and Die-Drawing*. Polymer Engineering and Science, 1997. **37**(11): p. 1801-1808.
15. Keum, J.K. and H.H. Song, *Thermal deformations of oriented noncrystalline poly(ethyleneterephthalate) fibers in the presence of mesophase structure*. Polymer, 2005(46): p. 939–945.
16. Matthews, R.G., et al., *The effects of stress relaxation on the structure and orientation of tensile drawn poly(ethylene terephthalate)*. Polymer, 2000. **41**(19): p. 7139-7145.
17. Pearce, R., et al., *Studies of Post Drawing Relaxation Phenomena in Poly(Ethylene Terephthalate) by Infrared Spectroscopy*. Polymer Engineering and Science 1997. **37**(11): p. 1795-1800.
18. Smith, M.R., et al., *Detailed mapping of biaxial orientation in polyethylene terephthalate bottles using polarised attenuated total reflection FTIR spectroscopy*. Polymer, 2006. **47**(15): p. 5691-5700.
19. Chevalier L, M.Y., *Identification of a strain induced crystallisation model for PET under uni- and bi-axial loading: Influence of temperature dispersion*. Mechanics of Material 2007(39):

p. 596–609.

20. Goschel, U., *Two-dimensional small-angle X-ray scattering studies on oriented poly(ethylene terephthalate) films*. *Polymer*, 1995. **36**(6): p. 1157-1165.
21. Goschel, U., K. Deutschert, and V. Abetzt, *Wide-angle X-ray scattering studies using an area detector: crystalline orientation in semisrystalline PET structures*. *Polymer*, 1996. **37**(1): p. 1-6.
22. Goschel, U. and G. Urban, *Supermolecular structure of oriented and semicrystalline poly(ethylene terephthalate) as revealed by the electron density correlation function from small-angle X-ray scattering studies*. *Polymer*, 1995. **36** (19): p. 3633-3639.
23. Adams, A.M., C.P. Buckley, and D.P. Jones, *Biaxial hot drawing of poly(ethylene terephthalate): measurements and modelling of strain-stiffening*. *Polymer*, 2000. **41**(2): p. 771-786.
24. Gowd, E.B., et al., *Effect of molecular orientation on the crystallization and melting behavior in poly(ethylene terephthalate)*. *Polymer*, 2004. **45**(19): p. 6707-6712.
25. Morawiec, J., et al., *High-Strength Uniaxially Drawn Tapes from Scrap Recycled Poly(ethylene terephthalate)*. *Journal of Applied Polymer Science* 2002. **86**: p. 1426–1435.
26. Vigny, M., et al., *Study of the Molecular Structure of PET Films Obtained by an Inverse Stretching Process. Part I: Constant Speed Drawing of Amorphous Films*. *Polymer Engineering and Science*, 1997. **11**(37): p. 1785-1794.
27. Gorlier, E., J.M. Haudin, and N. Billon, *Strain-induced crystallisation in bulk amorphous PET under uni-axial loading*. *Polymer*, 2001. **42**(23): p. 9541-9549.
28. Dargent, E., J. Grenet, and A. Dahoun, *Evolution of Hot Strain Induced Crystalline Texture of Poly(Ethylene Terephthalate) Films*. *Polymer Engineering and Science* 1997. **37**(11): p. 1853-1857.
29. Venkatesvaran, H. and M. Cakmak, *Kinetics of Structural Evolution During Crystallization of Preoriented PET as Followed by Dual Wavelength Photometric Birefringence Technique*. *Polymer engineering and science* 2001. **2**(41): p. 341-357.
30. Ajjji, A., et al., *Measurements of Absolute Birefringence of Biaxially Oriented Films and Sheets On-Line or Off-Line*. *Journal of Plastic Film and Sheeting*, 1999. **15**: p. 256-268.
31. Engelaere, J.C., J.P. Cavrot, and F. Rietsch, *Tensile drawing behaviour of polyethylene terephthalate: Influence of molecular weight and pre-orientation*. *Polymer*, 1982(23): p. 766-770.
32. Natu, A.A., E.A. Lofgren, and S.A. Jabarin, *Effect of Morphology on Barrier Properties of Poly(Ethylene Terephthalate)*. *Polymer engineering and science* 2005: p. 400-409.
33. Martins, C.I. and M. Cakmak, *Control the strain-induced crystallization of polyethylene terephthalate by temporally varying deformation rates: A mechano-optical study*. *Polymer*, 2007. **48**: p. 2109-2123.
34. Morawiec, J., et al., *High-Strength Uniaxially Drawn Tapes from Scrap Recycled Poly(ethylene terephthalate)*. *Journal of Applied Polymer Science* 2002(86): p. 1426–1435.
35. Mahendrasingam, A., et al., *Effect of draw ratio and temperature on the strain-induced crystallization of poly (ethylene terephthalate) at fast draw rates*. *Polymer*, 1999. **40**(20): p. 5553-5565.
36. Blundell, D.J., et al., *Orientation prior to crystallisation during drawing of poly(ethylene terephthalate)*. *Polymer*, 2000. **41**(21): p. 7793-7802.
37. Mahendrasingam, A., et al., *Influence of temperature and chain orientation on the crystallization of poly(ethylene terephthalate) during fast drawing*. *Polymer*, 2000. **41**(21): p. 7803-7814.
38. Blundell, D.J., et al., *Characterization of strain-induced crystallization of poly(ethylene terephthalate) at fast draw rates using synchrotron radiation*. *Polymer*, 1996. **37**(15): p. 3303-3311.
39. Chaari, F., M. Chaouche, and J. Doucet, *Crystallization of poly(ethylene terephthalate) under tensile strain: crystalline development versus mechanical behaviour*. *Polymer*, 2003.

- 44(2): p. 473-479.
40. Chaari, F. and M. Chaouche, *Rheoptical Investigation of the Crystallization of Poly(ethylene terephthalate) under Tensile Strain*. Journal of Polymer Science: Part B: Polymer Physics 2004(42): p. 1915–1927.
41. Kolb, R., et al., *Investigation of the high speed spinning process of poly(ethylene terephthalate) by means of synchrotron X-ray diffraction*. Polymer, 2000(41): p. 2931–2935.
42. Kawakami, D., et al., *Mechanism of Structural Formation by Uniaxial Deformation in Amorphous Poly(ethylene terephthalate) above the Glass Temperature*. Macromolecules, 2003(36): p. 9275-9280.
43. Middleton, A.C., et al., *Real-time FTIR and WAXS studies of drawing behavior of poly(ethylene terephthalate) films*. Journal of Applied Polymer Science, 2001. **79**(10): p. 1825-1837.
44. Gorlier, E., *Caractérisation multiaxiale du comportement et de la microstructure d'un semi-cristallin : Application au cas du PET*, . 2001: Ecole Nationale Supérieure des Mines de Paris.
45. Boyce, M.C., S. Socrate, and P.G. Llana, *Constitutive model for the finite deformation stress-strain behavior of poly(ethylene terephthalate) above the glass transition*. Polymer, 2000. **41**(6): p. 2183-2201.
46. Marco, Y., et al., *Induced crystallization and orientation of PET during uniaxial and biaxial elongation*. Macromolecular Symposia, 2002. **185**: p. 15-34.
47. Zaroulis, J.S. and M.C. Boyce, *Temperature, strain rate, and strain state dependence of the evolution in mechanical behaviour and structure of poly(ethylene terephthalate) with finite strain deformation*. Polymer, 1997. **38**(6): p. 1303-1315.
48. Llana, P.G. and M.C. Boyce, *Finite strain behavior of poly(ethylene terephthalate) above the glass transition temperature*. Polymer, 1999(40): p. 6729–6751.
49. Koenig, J.L., L. Wolfram, and J. Grasselli, *STRUCTURE AND PROPERTIES OF ORIENTED POLY(ACRYLONITRILE) FILMS*. Am Chem Soc-Div Polymer Chem, 1969. **10**(2 Papers for New York meeting): p. 959-964.
50. Varma, P., E.A. Lofgren, and S.A. Jabarin, *Properties and kinetics of thermally crystallized oriented poly(ethylene terephthalate) (PET). II: Physical and optical properties*. Polymer Engineering and Science, 1998. **38**(2): p. 245-253.
51. Oultache, A.K., et al., *Orientation and relaxation of orientation of amorphous poly(ethylene terephthalate)*. Polymer, 2001. **42**(21): p. 9051-9058.
52. Duchesne, C., et al., *Molecular orientation and relaxation of poly(ethylene terephthalate) by polarization Modulation infrared spectroscopy*. Macromolecules, 2002. **35**(23): p. 8768-8773.
53. Mahendrasingam, A., et al., *Observation of a transient structure prior to strain-induced crystallization in poly(ethylene terephthalate)*. Polymer, 2000(41): p. 1217–1221.
54. Ran, S., et al., *Mesophase as the Precursor for Strain-Induced Crystallization in Amorphous Poly(ethylene terephthalate) Film*. Macromolecules 2002(35): p. 10102-10107
55. Kawakami, D., et al., *Structural formation of amorphous poly(ethylene terephthalate) during uniaxial deformation above glass temperature*. Polymer, 2004. **45**(3): p. 905-918.
56. Marco, Y., L. Chevalier, and M. Chaouche, *WAXD study of induced crystallization and orientation in poly(ethylene terephthalate) during biaxial elongation*. Polymer, 2002. **43**(24): p. 6569-6574.
57. Kawakami, D., et al., *Superstructure Evolution in Poly(ethylene terephthalate) during Uniaxial Deformation above Glass Transition Temperature*. Macromolecules, 2006. **39**: p. 2909-2920.
58. Thompson, A.B., *Strain induced crystallization in PET*. Journal of polymer science, 1959. **34**: p. 741-760.
59. Seguela, R., *On the Natural Draw Ratio of Semi-Crystalline Polymers: Review of the Mechanical, Physical and Molecular Aspects* Macromolecular Material and Engineering 2007(292): p. 235–244.

60. Varma, P., E.A. Lofgren, and S.A. Jabarin, *Properties and kinetics of thermally crystallized oriented poly(ethylene terephthalate) (PET). I: Kinetics of crystallization*. Polymer Engineering and Science, 1998. **38**(2): p. 237-244.
61. Salem, D.R., *Microstructure development during constant-force drawing of PET film*. Polymer, 1998. **39**(26): p. 7067-7077.
62. Blundell, D.J., et al., *Orientation and crystallisation mechanisms during fast drawing of poly(ethylene terephthalate)*. Polymer Bulletin, 1999. **42**: p. 357-363.
63. Doi, M. and S.F. Edwards, *The Theory of Polymer Dynamics*. 1988: Oxford university press
64. Kawakami, D., et al., *Deformation-Induced Phase Transition and Superstructure Formation in Poly(ethylene terephthalate)*. Macromolecules, 2005. **38**: p. 91-103.
65. Kawakami, D., et al., *New Insights into Lamellar Structure Development and SAXS/WAXD Sequence Appearance during Uniaxial Stretching of Amorphous Poly(ethylene terephthalate) above Glass Transition Temperature*. 2008. p. 2859-2867.
66. Kawakami, D., et al., *Mechanism of Structural Formation by Uniaxial Deformation in Amorphous Poly(ethylene terephthalate) above the Glass Temperature*. Macromolecules, 2003. **36**: p. 9275-9280.
67. Huang, B., M. Ito, and T. Kanamoto, *Deformation mechanism of amorphous poly(ethylene terephthalate) as a function of molecular weight and entanglements*. Polymer, 1994. **35**(6): p. 1210-1215.
68. Gohil, R.M., *Morphology-property relationships in oriented PET films: A role of in-plane crystalline orientation distribution on the film properties*. Journal of Applied Polymer Science, 1993. **48**(9): p. 1635-1648.
69. Viana, J.C., N.M. Alves, and J.F. Mano, *Morphology and Mechanical Properties of Injection Molded Poly(Ethylene Terephthalate)*. Polymer engineering and science, 2004. **44**(12): p. 2174-2184.
70. Alves, N.M., et al., *Glass transition and structural relaxation in semi-crystalline poly(ethylene terephthalate): a DSC study*. Polymer, 2002. **43**(15): p. 4111-4122.
71. Ward, I.M. and J. Sweeney, *An Introduction to the Mechanical Properties of Solid Polymers*. 2004: John Wiley & Sons.
72. Bonart, R., *Paracrystalline structures in poly(ethylene terephthalate)*. Kolloid-zeitschrift and zeitschrift fur polymere, 1966. **213** p. 1-11.
73. Bonart, R., *Crystalline and colloidal structures during elongation and plastic deformations*. Kolloid Zeitschrift & Zeitschrift fuer Polymere, 1969. **231**( (1-2)): p. 438-458.
74. Auriemma, F., et al., *On the mesomorphic form of poly(ethylene terephthalate)*. Macromolecules, 1992. **25**(9): p. 2490-2497.
75. Asano, T., et al., *Crystallization of oriented amorphous poly(ethylene terephthalate) as revealed by X-ray diffraction and microhardness*. Polymer, 1999. **40**(23): p. 6475-6484.
76. Asano, T., et al., *Crystallization of oriented amorphous poly(ethylene terephthalate) as revealed by X-ray diffraction and microhardness*. Polymer, 1999. **40**(23): p. 6475-6484.
77. Parravicini, L., et al., *Crystallization of poly(ethylene terephthalate) (PET) from the oriented mesomorphic form*. Journal of Applied Polymer Science, 1994. **52**(7): p. 875-885.
78. Liu, Y., et al., *Characterization of stress-whitening of tensile yielded isotactic polypropylene*. Polymer, 1997. **38**(11): p. 2797-2805.
79. Viana, J.C., et al., *Nanostructure Evolution during Uni-axial Deformation of PET – a WAXS and SAXS Study using Synchrotron Radiation*. Materials Science Forum, 2006(514-516 ): p. 1583-1587.
80. Efimov, A.V., V.Y. Shcherba, and N.F. Bakeyev, *Effect of drawing conditions on structural parameters of crazes in crystalline poly(ethylene terephthalate)*. Polymer Science U.S.S.R., 1991. **33**(3): p. 568-574.
81. Michler, G.H. and F.J. Baltá-Calleja, *Mechanical Properties of Polymers Based on Nanostructure and Morphology*. 2005, Boca Raton, London, New York, Singapore: Taylor &



Francis Group.

82. Koo, J.H., *Polymer Nanocomposites Processing, Characterization, and Applications*. 2006, New York: McGraw-Hill.

83. Ray, S.S. and M. Okamoto, *Polymer/layered silicate nanocomposites: A review from preparation to processing*. Progress in Polymer Science (Oxford), 2003. **28**(11): p. 1539-1641.

84. Southern Clay Products Inc, <http://www.nanoclay.com/>.

85. Theng, B.K.G., *The Chemistry of Clay-Organic Reactions*. 1974, New York, : Wiley.

86. Giannelis, E.P., R.K. Krishnamoorti, and E. Manias, *Polymer-silica nanocomposites: model systems for confined polymers and polymer brushes*. Advances in Polymer Science, 1999. **118**: p. 108–147.

87. Liu, J., et al., *Intercalation and Exfoliation: A Review on Morphology of Polymer Nanocomposites Reinforced by Inorganic Layer Structures*. Materials and Manufacturing Processes, 2006. **21**(2): p. 143 - 151.

88. Alexandre, M. and P. Dubois, *Polymer-layered silicate nanocomposites: Preparation, properties and uses of a new class of materials*. Materials Science and Engineering R: Reports, 2000. **28**(1): p. 1-63.

89. Krishnamoorti, R., R.A. Vaia, and E.P. Giannelis, *Structure and Dynamics of Polymer-Layered Silicate Nanocomposites*. 1996. p. 1728-1734.

90. Gilman, J.W., et al., *Flammability Properties of Polymer/Layered-Silicate Nanocomposites. Polypropylene and Polystyrene Nanocomposites*. 2000. p. 1866-1873.

91. Calcagno, C.I.W., et al., *The effect of organic modifier of the clay on morphology and crystallization properties of PET nanocomposites*. Polymer, 2007. **48**(4): p. 966-974.

92. Alyamac, E. and U. Yilmazer, *Reactive extrusion of poly(ethylene terephthalate)-(ethylene/methyl acrylate/glycidyl methacrylate)-organoclay nanocomposites*. Polymer composites, 2007. **28**(2): p. 251-258.

93. Vidotti, S.E., et al., *Preparation of poly(ethylene terephthalate)/organoclay nanocomposites using a polyester ionomer as a compatibilizer*. Journal of Polymer Science: Part B: Polymer Physics, 2007. **45**(22): p. 3084-3091.

94. Pegoretti, A., et al., *Recycled poly(ethylene terephthalate)/layered silicate nanocomposites: morphology and tensile mechanical properties*. Polymer, 2004. **45**(8): p. 2751-2759.

95. Bizarria, M.T.M., et al., *Morphology and thermomechanical properties of recycled PET-organoclay nanocomposites*. Journal of Applied Polymer Science, 2007. **104**(3): p. 1839-1844.

96. Kracalik, M., et al., *Effect of 3D structures on recycled PET/organoclay nanocomposites*. Polymer Bulletin, 2007. **58**(1): p. 313-319.

97. Kracalik, M., et al., *Recycled PET-organoclay nanocomposites with enhanced processing properties and thermal stability*. Journal of Applied Polymer Science, 2007. **106**(3): p. 2092-2100.

98. Kracalik, M., et al., *Recycled PET nanocomposites improved by silanization of organoclays*. Journal of Applied Polymer Science, 2007. **106**(2): p. 926-937.

99. Ke, Y., C. Long, and Z. Qi, *Crystallization, Properties, and Crystal and Nanoscale Morphology of PET-Clay Nanocomposites*. Journal of Applied Polymer Science, 1999. **71**: p. 1139–1146.

100. Ke, Y.C., Z.B. Yang, and C.F. Zhu, *Investigation of properties, nanostructure, and distribution in controlled polyester polymerization with layered silicate*. Journal of Applied Polymer Science, 2002. **85**(13): p. 2677-2691.

101. Chang, J.H., et al., *Poly(ethylene terephthalate) nanocomposites by in situ interlayer polymerization: The thermo-mechanical properties and morphology of the hybrid fibers*. Polymer, 2004. **45**(3): p. 919-926.

102. Chang, J.H. and S.J. Kim, *Polyester nanocomposite fibers: comparison of their properties with poly(ethylene terephthalate) and poly(trimethylene terephthalate) (II)* Polymer Bulletin, 2004. **52**: p. 289-296.

103. Zhang, G., T. Shichi, and K. Takagi, *PET-clay hybrids with improved tensile strength*. Materials Letters, 2003. **57**(12): p. 1858-1862.
104. Hao, J., et al., *Synthesis of poly(ethylene terephthalate)/clay nanocomposites using aminododecanoic acid-modified clay and a bifunctional compatibilizer*. Journal of Applied Polymer Science, 2006. **101**(2): p. 1057-1064.
105. Choi, W.J., et al., *Preparation and barrier property of poly(ethylene terephthalate)/clay nanocomposite using clay-supported catalyst*. Journal of Applied Polymer Science, 2006. **100**(6): p. 4875-4879.
106. Tsai, T.Y., et al., *Preparation of Exfoliated Polyester/Clay Nanocomposites*. Advanced Materials, 2005. **17**(14): p. 1769-1773.
107. Ou, C.F., M.T. Ho, and J.R. Lin, *The Nucleating Effect of Montmorillonite on Crystallization of PET/Montmorillonite Nanocomposite*. Journal of Polymer Research, 2003. **10**(2): p. 127-132.
108. Ou, C.F., M.T. Ho, and J.R. Lin, *Synthesis and characterization of poly(ethylene terephthalate) nanocomposites with organoclay*. Journal of Applied Polymer Science, 2004. **91**(1): p. 140-145.
109. Sanchez-Solis, A., A. Garcia-Rejon, and O. Manero, *Production of nanocomposites of PET-montmorillonite clay by an extrusion process* Macromol. Symp., 2003. **192**: p. 281-292
110. Wang, Y., et al., *Study on mechanical properties, thermal stability and crystallization behavior of PET/MMT nanocomposites*. Composites Part B: Engineering, 2006. **37**(6): p. 399-407.
111. Barber, G.D., B.H. Calhoun, and R.B. Moore, *Poly(ethylene terephthalate) ionomer based clay nanocomposites produced via melt extrusion*. Polymer, 2005. **46**(17): p. 6706-6714.
112. Chung, J.W., et al., *Thermally stable exfoliated poly(ethylene terephthalate) (PET) nanocomposites as prepared by selective removal of organic modifiers of layered silicate*. Polymer Degradation and Stability, 2008. **93**(1): p. 252-259.
113. Sanchez-Solis, A., et al., *Mechanical and rheological studies on polyethylene terephthalate-montmorillonite nanocomposites*. Polymer Engineering and Science, 2004. **44**(6): p. 1094-1102.
114. Davis, H.R., et al., *Effects of melt-processing conditions on the quality of poly(ethylene terephthalate) montmorillonite clay nanocomposites*. Journal of Polymer Science: Part B: Polymer Physics, 2002. **40**(23): p. 2661-2666.
115. Kracalik, M., et al., *Recycled PET nanocomposites improved by silanization of organoclays*. Journal of Applied Polymer Science, 2007. **106**(2): p. 926-937.
116. Ettlinger, M., *Fine Particles, in Technical Bulletin Pigments, No. 80*. Inorganic Chemical Products Division ed. 1998, Düsseldorf: Degussa AG. 1-26
117. Kickelbick, G., *Concepts for the incorporation of inorganic building blocks into organic polymers on a nanoscale*. Progress in Polymer Science, 2003. **28**(1): p. 83-114.
118. Han, K. and M. Yu, *Study of the preparation and properties of UV-blocking fabrics of a PET/TiO<sub>2</sub> nanocomposite prepared by in situ polycondensation*. Journal of Applied Polymer Science, 2006. **100**(2): p. 1588-1593.
119. Fray, E., M. Boccaccini, and R. Aldo, *Novel hybrid PET/DFA-TiO<sub>2</sub> nanocomposites by in situ polycondensation*. Materials Letters, 2005. **59**(18): p. 2300-2304.
120. Taniguchi, A. and M. Cakmak, *The suppression of strain induced crystallization in PET through sub micron TiO<sub>2</sub> particle incorporation*. Polymer, 2004. **45**(19): p. 6647-6654.
121. Zou, H., W. Shishan, and J. Shen, *Polymer/Silica Nanocomposites: Preparation, Characterization, Properties, and Applications*. Chemical review, 2008. **108**: p. 3893-3957.
122. Jana, S.C. and S. Jain, *Dispersion of nanofillers in high performance polymers using reactive solvents as processing aids*. Polymer, 2001. **42**(16): p. 6897-6905.
123. Rong, M.Z., et al., *Structure-property relationships of irradiation grafted nano-inorganic particle filled polypropylene composites*. Polymer, 2001. **42**(1): p. 167-183.
124. Rong, M.Z., M.Q. Zhang, and W.H. Ruan, *Surface modification of nanoscale fillers for*

- improving properties of polymer nanocomposites: a review* Materials Science and Technology, 2006. **22**: p. 787-796.
125. Yang, Y. and H. Gu, *Preparation and properties of deep dye fibers from polyethylene terephthalate/SiO<sub>2</sub> nanocomposites by in situ polymerization*. Journal of Applied Polymer Science, 2007. **105**(4): p. 2363-2369.
126. Yang, Y., H. Xu, and H. Gu, *Preparation and crystallization of poly(ethylene terephthalate)/SiO<sub>2</sub> nanocomposites by in-situ polymerization*. Journal of Applied Polymer Science, 2006. **102**(1): p. 655-662.
127. Liu, W., et al., *Preparation and Characterization of PET/Silica Nanocomposites*. Journal of Applied Polymer Science, 2004. **91**(2): p. 1229-1232.
128. TIAN, X., et al., *Preparation and properties of poly(ethylene terephthalate)/silica nanocomposites*. Journal of macromolecular science, 2006. **45** (4 ): p. 507-513
129. Tian, X., et al., *Isothermal Crystallization and Subsequent Melting Behavior of Poly(ethylene terephthalate)/Silica Nanocomposites*. Journal of macromolecular science, 2006. **45**(5): p. 835 - 848.
130. Yang, Y. and H. Gu, *Superfine structure, physical properties, and dyeability of alkaline hydrolyzed poly(ethylene terephthalate)/silica nanocomposite fibers prepared by in situ polymerization*. Journal of Applied Polymer Science, 2006. **102**(4): p. 3691-3697.
131. Zheng, H. and J. Wu, *Preparation, crystallization, and spinnability of poly(ethylene terephthalate)/silica nanocomposites*. Journal of Applied Polymer Science, 2007. **103**(4): p. 2564-2568.
132. Zheng, J., et al., *Pyrolysis studies of polyethylene terephthalate/silica nanocomposites*. Journal of Applied Polymer Science, 2007. **104**(1): p. 9-14.
133. Zhang, X., et al., *The Suppression of Isothermal Cold Crystallization in PET Through Nano-Silica Incorporation*. 2008, Taylor & Francis. p. 166 - 173.
134. Zhang, X., et al., *Relationship between Microstructure and Tensile Properties of PET/Silica Nanocomposite Fibers*. Journal of macromolecular science, 2008. **47**(2): p. 368 - 377.
135. Bikiaris, D., V. Karavelidis, and G. Karayannidis, *A New Approach to Prepare Poly(ethylene terephthalate)/Silica Nanocomposites with Increased Molecular Weight and Fully Adjustable Branching or Crosslinking by SSP*. Macromolecular Rapid Communications, 2006. **27**(15): p. 1199-1205.
136. Achilias, D.S., et al., *Effect of silica nanoparticles on solid state polymerization of poly(ethylene terephthalate)*. European Polymer Journal, 2008. **44**(10): p. 3096-3107.
137. Wu, T. and Y. Ke, *The absorption and thermal behaviors of PET-SiO<sub>2</sub> nanocomposite films*. Polymer Degradation and Stability, 2006. **91**(9): p. 2205-2212.
138. Wu, T. and Y. Ke, *Melting, crystallization and optical behaviors of poly (ethylene terephthalate)-silica/polystyrene nanocomposite films*. Thin Solid Films, 2007. **515**(13): p. 5220-5226.
139. Chung, S.C., et al., *Poly(ethylene terephthalate)(PET) nanocomposites filled with fumed silicas by melt compounding* Macromolecular research, 2002. **10**(4): p. 221-229.
140. Zhu, Y.G., et al., *PET/SiO<sub>2</sub> nanocomposites prepared by cryomilling*. Journal of Polymer Science Part B: Polymer Physics, 2006. **44**(8): p. 1161-1167.
141. Zhu, Y.G., et al., *Thermal behaviors of poly(ethylene terephthalate)/SiO<sub>2</sub> nanocomposites prepared by cryomilling*. Journal of Polymer Science Part B: Polymer Physics, 2006. **44**(9): p. 1351-1356.
142. Kim, G.M., et al., *Influence of nanofillers on the deformation process in layered silicate/polyamide-12 nanocomposites*. Polymer, 2001. **42**(3): p. 1095-1100.
143. Kim, G.M., S. Goerlitz, and G.H. Michler, *Deformation mechanism of nylon 6/layered silicate nanocomposites: Role of the layered silicate*. Journal of Applied Polymer Science, 2007. **105**(1): p. 38-48.
144. Renner, K., et al., *Micromechanical deformation processes in PA/layered silicate nanocomposites: Correlation of structure and properties*. Polymer engineering and science,

2007. **47**(8): p. 1235-1245.

145. Kim, G.M. and G.H. Michler, *Micromechanical deformation processes in toughened and particle-filled semicrystalline polymers: Part 1. Characterization of deformation processes in dependence on phase morphology*. Polymer, 1998. **39**(23): p. 5689-5697.

146. Kim, G.M. and G.H. Michler, *Micromechanical deformation processes in toughened and particle filled semicrystalline polymers: Part 2. model representation for micromechanical deformation processes*. Polymer, 1998. **39**(23): p. 5699-5703.

147. Reynaud, E., et al., *Nanofillers in polymeric matrix: a study on silica reinforced PA6*. Polymer, 2001. **42**(21): p. 8759-8768.

148. Kobayashi, H., et al., *Synchrotron radiation small-angle X-ray scattering study on fracture process of carbon nanotube/poly(ethylene terephthalate) composite films*. Composites Science and Technology, 2007. **67**(15-16): p. 3209-3218.

149. Kobayashi, H., et al., *A comparative study of fracture behavior between carbon black/poly(ethylene terephthalate) and multiwalled carbon nanotube/poly(ethylene terephthalate) composite films*. Journal of Applied Polymer Science, 2007. **106**(1): p. 152-160.





# CHAPTER III

## Motivation, objectives and research approach

### 3.1. Motivation and objectives

The motivation of this work arises from the fact that the current state-of-the-art does not offer a complete understanding on the dependence of the stretching variables on the strain-induced structure development of PET during the uniaxial stretching, in the rubbery state. The stretching variables, typically temperature, rate and ratio, lead to significant difference in the structure development during the uniaxial deformation, which is from extreme importance for predicting the final properties. Contradictory and unclear results are found in the literature regarding the relevance and influence of the stretching parameters and the interactions among them on the strain-induced structure development. Moreover, it is also not well understood the structural mechanisms evolved during stretching. One can raise the question: what are the steps followed from amorphous to semicrystalline state? Is there any mesophase state? What is the effect of different initial morphological state - amorphous, mesophase or semicrystalline - working as a structure precursors, on further structure evolution? This last subject has never been addressed, however is of special importance to clarify the mechanisms of structural evolution during deformation and to predict the performance of the final product during its end use.

Another strong motivation leading to the present study is the fact that although PET has been widely used in the packaging industry, it does not completely fulfil the specific and rigorous requirements for its in-service application, such as barrier and thermal properties. As alternative material for substitution of neat PET in packaging's appears PET nanocomposites with different nanofillers: layered silicates, MMT, and different metal oxides i.e.: nanotitanium dioxide,  $\text{TiO}_2$ , and nanosilica,  $\text{SiO}_2$ . A key challenge in the preparation of nanocomposite materials is the establishment of good dispersion/delamination of nanosized inorganic phase into the polymer matrix. The direct melt blending techniques are an attractive pathway for production of PNC in industrial scale. PNC are remarkable for their enhanced thermal, mechanical and

optical properties. However their properties and deformation behaviour during uniaxial stretching is not deeply understood. In particular, the dependence of the nanofillers nature, size, shape and morphology on the deformation mechanism taking place during stretching and its influence on the structure evolution.

The main objectives of this PhD thesis can be summarized as follow:

- i) to reveal the importance and influence of each individual stretching variable - stretching temperature, stretching rate and stretching ratio, and the interactions between them, on the structure development of amorphous PET during the uniaxial stretching in the rubbery state;
- ii) to study the influence of different initial PET morphologies on the structure evolution during uniaxial stretching in the solid state;
- iii) to validate the adequate melt blending techniques for production of PNCs;
- iv) to investigate the effect of incorporation of different inorganic nanoreinforcements within PET matrix via melt blending techniques, on the thermal, mechanical and optical properties;
- v) to assess the effect of one and three dimensional nanoparticles on the structure evolution during the uniaxial stretching in the solid state;
- vi) to identify the deformation mechanisms responsible for enhancement of the mechanical properties of PET nanocomposites;
- vii) to propose multiscale model for the structure evolution of the PET nanocomposites in the solid state.

### **3.2. Research approach**

This section describes the research approach used to achieve the goals of this thesis. A scheme representing the research strategy is depicted in **Figure 3.1**. The study is divided into three main parts, following the study on the influence of the stretching variables, the effect of the initial morphology on further structural evolution upon uniaxial deformation of neat PET and the study of PET nanocomposites. All of these routes aim at understanding the multi-scale morphology evolution of PET and its nanocomposites under uniaxial deformation.

In order to have an overview of this research work, hereafter is presented the thesis outline including a brief chapter description and the followed research strategy.



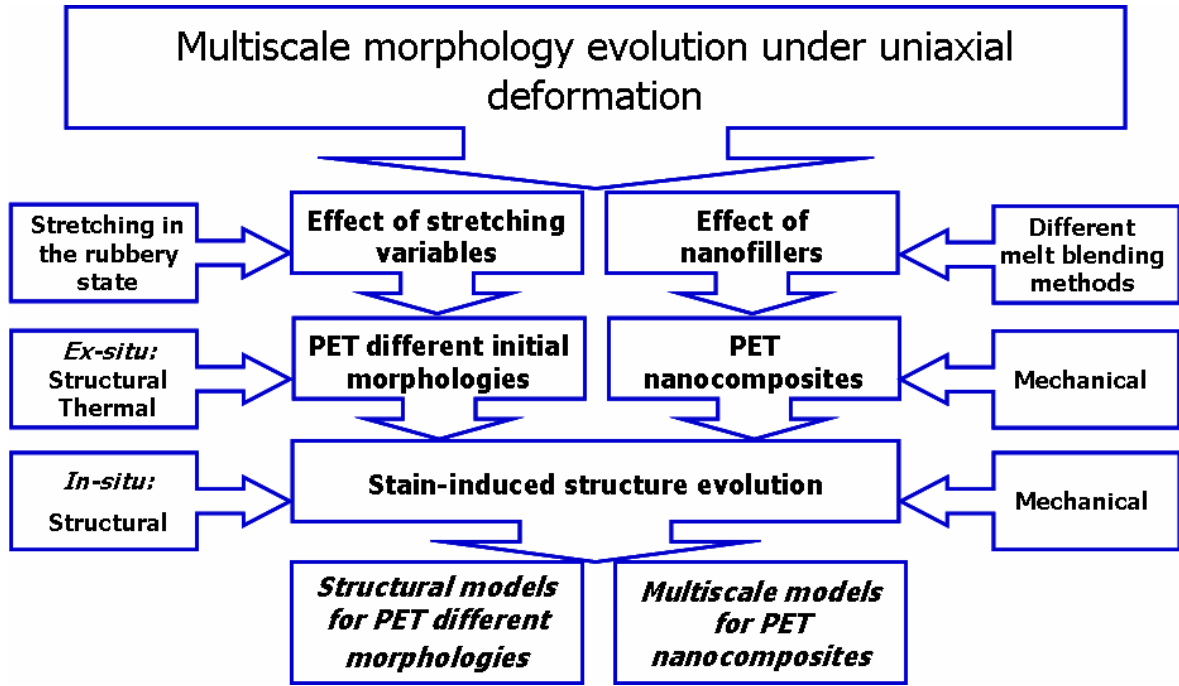


Figure 3.1. Scheme of thesis research strategy

### 3.2.1. Chapter V: Structure development of poly(ethylene terephthalate) during uniaxial stretching above the glass transition temperature: study of the statistical influence of the stretching variables

This chapter aims at exploring the effects of the stretching variables on the strain-induced structure development during uniaxial stretching in the rubbery state of initially amorphous PET samples, by applying an experimental protocol consisting on the variation of the stretching temperature,  $T_{st}$ , the stretching rate,  $\epsilon_{st}$ , and the stretching ratio,  $\lambda_{st}$ . A schematic representation of the research strategy applied in this study is depicted in the *Figure 3.2*.

To accomplish this task a design of experiments plan, DOE, with three selected variables (temperature, rate and ratio) at two levels, is followed. This investigation allows obtaining the relevance and the influence of each stretching variable and its interactions on the strain-induced structure development. For that amorphous PET stretched samples are rapidly quenched to freeze the morphology developed during the stretching process. The samples are then analyzed by WAXS, in-plane optical birefringence,  $BIR$ , and differential scanning calorimetry, DSC. The influences of the stretching variables on the structural and thermal properties are identified by the statistical tool called Analysis of Variance, ANOVA. The structural parameters are: i) phase's fraction (amorphous, meso and crystalline) calculated from 2D WAXS patterns and ii) molecular orientation level such as: average molecular orientation,  $f_{av}$ , and amorphous phase orientation,  $f_{am}$ , assessed by WAXS and optical anisotropy assessed by in-plane optical birefringence,  $BIR$  and iii) degree of crystallinity,  $\chi_c$ , by DSC. The thermal parameters like: i)

glass transition temperature,  $T_g$ , ii) cold crystallization temperature,  $T_{cc}$ , and iii) melting temperature,  $T_m$ , are evaluated by DSC experiments.

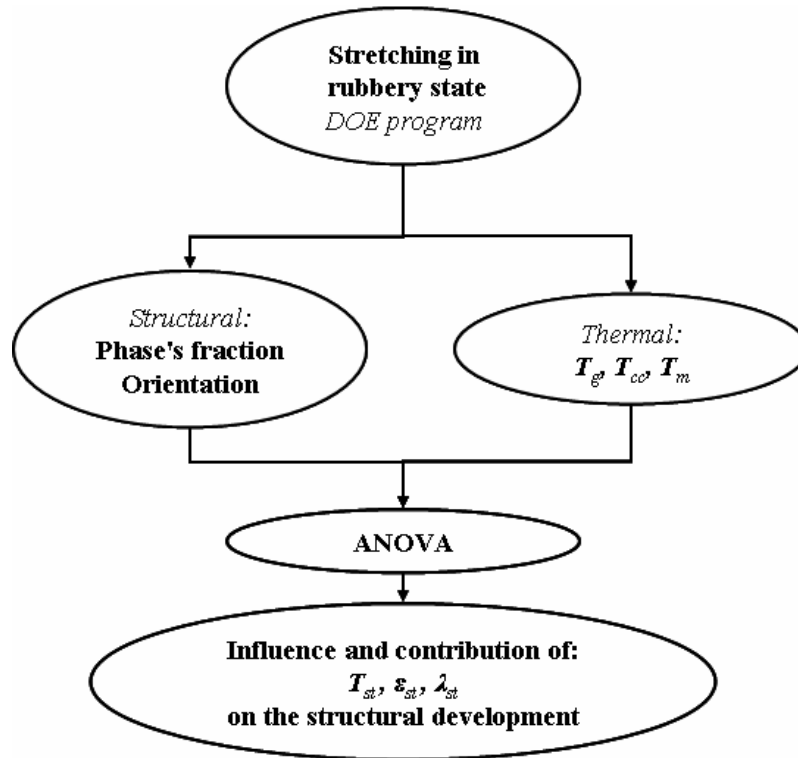


Figure 3.2. Scheme of the research approach used in Chapter V.

### 3.2.2. Chapter VI: Solid state structural evolution of poly (ethylene terephthalate) during step uniaxial stretching from different initial morphologies: an *in situ* WAXD study

This chapter aims at contributing for a deeper understanding of the PET structure evolution upon uniaxial step stretching in the solid state. An *in situ* WAXS characterization is applied to samples of distinct initial morphologies, i.e.: i) two quasi-amorphous samples of different orientation level and phase's fractions and ii) two semicrystalline samples, of different crystalline order, namely, one with 2D crystalline order and another with 3D order. The mechanism of structure evolution and effect of initial morphologies are discussed. A schematic representation of the research approach followed is depicted in the **Figure 3.3**.

The following steps are considered to complete this study: i) selection of the samples with different initial morphologies from the samples acquired in *Chapter V*; ii) solid state step uniaxial stretching of the selected sample, simultaneously to *in situ* WAXS experiments, carried out under synchrotron radiation source. From this set of experiments, the evolution of the phase's fraction (i.e amorphous, meso and crystalline), the average molecular orientation,  $f_{av}$ , and the amorphous phase orientation,  $f_{am}$ , are assessed for all morphologies. In the case of semi-

crystalline structure, the evolution of the crystallite orientation,  $f_c$ , and crystallite sizes is also evaluated. Structural models for each of the morphologies are proposed as well as the effect of the initial structural state on the strain-induced structure evolution.

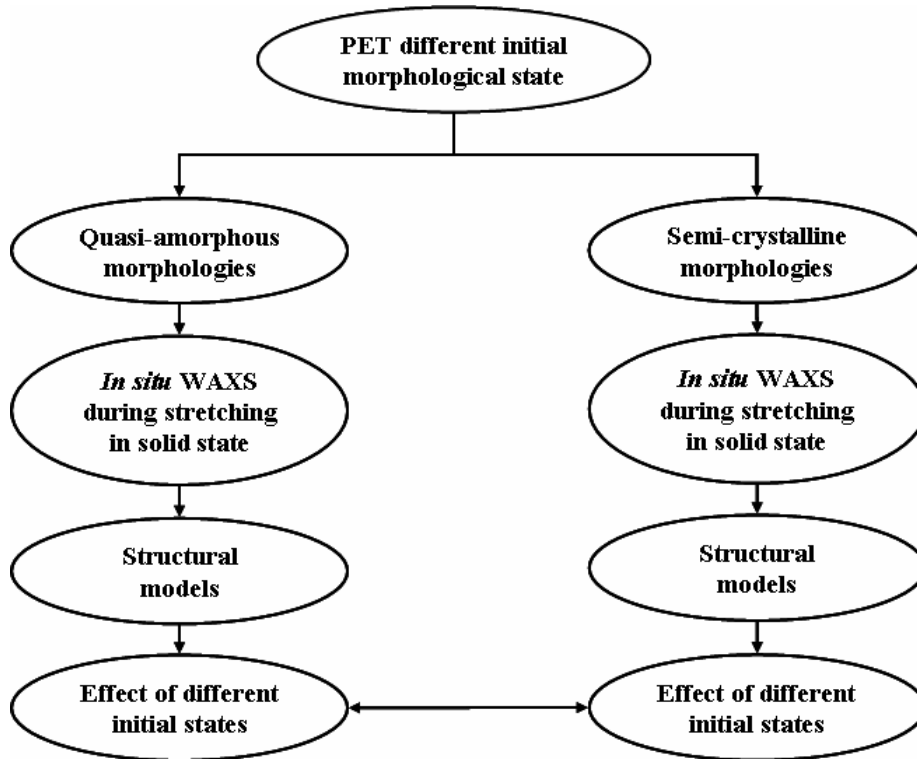


Figure 3.3. Scheme of the research approach used in Chapter VI.

### 3.2.3. Chapter VII: Characterization of PET nanocomposites produced by different melt blending techniques

The focus of *Chapter VII* is the preparation and characterization of PET nanocomposites with 1D and 3D nanoreinforcements prepared by different direct melt blending methods, namely: i) direct injection moulding and ii) extrusion with subsequent injection moulding. The steps followed to accomplish this study are summarized in the scheme presented in *Figure 3.4*. The goals of this Chapter can be summarized as follow: i) to study the efficiency of both melt blending methods and ii) to analyse the effect of the incorporation of inorganic nanofillers on the polymer degradation, thermal, mechanical and optical properties, as comparing to the processed neat PET.

To accomplish this study PET nanocomposites containing 3 wt% of different type of nanoparticles: i) organically modified montmorillonite, MMT5, and ii) nanotitanium dioxide,  $\text{TiO}_2$ , and iii) nanosilica dioxide,  $\text{SiO}_2$ , were incorporated via two independent procedures: i) direct injection moulding, DIM, and ii) extrusion blending followed by injection moulding, EIM. The efficiency of both methods on the dispersion/delamination of nanofillers into the polymer

matrix is estimated by SAXS and degradability of PET bulk via intrinsic viscosity (IV) measurements. The effect of different nanofillers on the thermal, mechanical and optical properties are assessed by DSC, tensile tests and gloss and haze measurements.

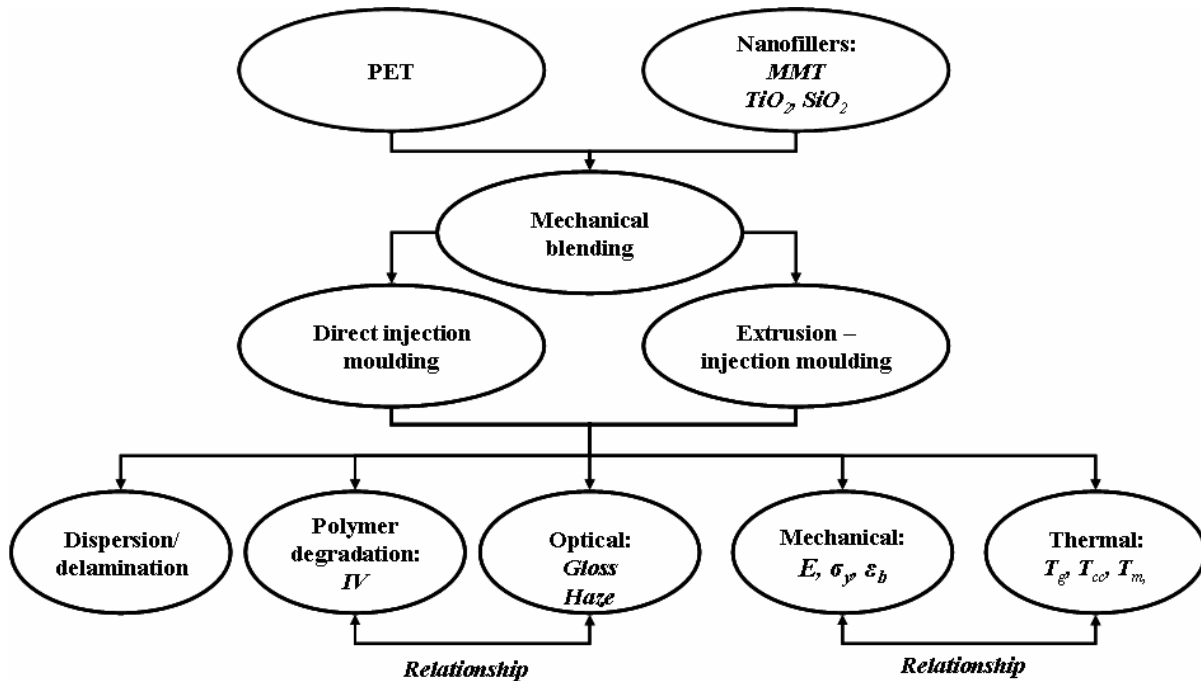


Figure 3.4. Scheme of the research approach used in Chapter VII.

### 3.2.4. Chapter VIII: Characterization of PET nanocomposites produced by asymmetric batch minimixer

The objective of this chapter is to characterize the PET nanocomposites, prepared by melt blending of neat PET with different nanofillers: MMT, TiO<sub>2</sub> and SiO<sub>2</sub>, in an asymmetric batch minimixer. The goals of this study are: i) to verify the efficiency of the asymmetric batch minimixer as a melt blending technique for production of PNCs; and ii) to characterize the effect of incorporation of the nanofillers on the polymer degradation, thermal, thermo-mechanical and mechanical properties as compared to the processed neat PET sample. The research strategy followed is depicted in the **Figure 3.5**.

Nanocomposites of PET and 0.3 wt% of the different types of nanofillers, namely: i) two types oMMTs, with equal particle size and different powder agglomerate size, and ii) 3D particles with similar powder agglomerate size and different nature and particle size respectively: a) nanotitanium dioxide, TiO<sub>2</sub>, and b) nanosilica, SiO<sub>2</sub>, will be produced in the asymmetric batch minimixer. The efficiency of the asymmetric batch minimixer upon the dispersion/deagglomeration of nanofillers is identified by TEM characterization. The degradation of the polymer bulk after processing is assessed by IV measurements. The effect of nanofillers addition on: i) the thermo-mechanical properties such as glass transition temperature,

$T_g$ , and the lost modulus,  $E'$ , are obtained by DMA, ii) the thermal parameters as the cold crystallization temperature,  $T_{cc}$ , and degree of crystallinity,  $\chi_c$ , are measured by DSC and iii) the mechanical properties as: elastic modulus,  $E$ , yield stress,  $\sigma_y$ , and deformation capability,  $\epsilon_b$  are obtained by mechanical testing.

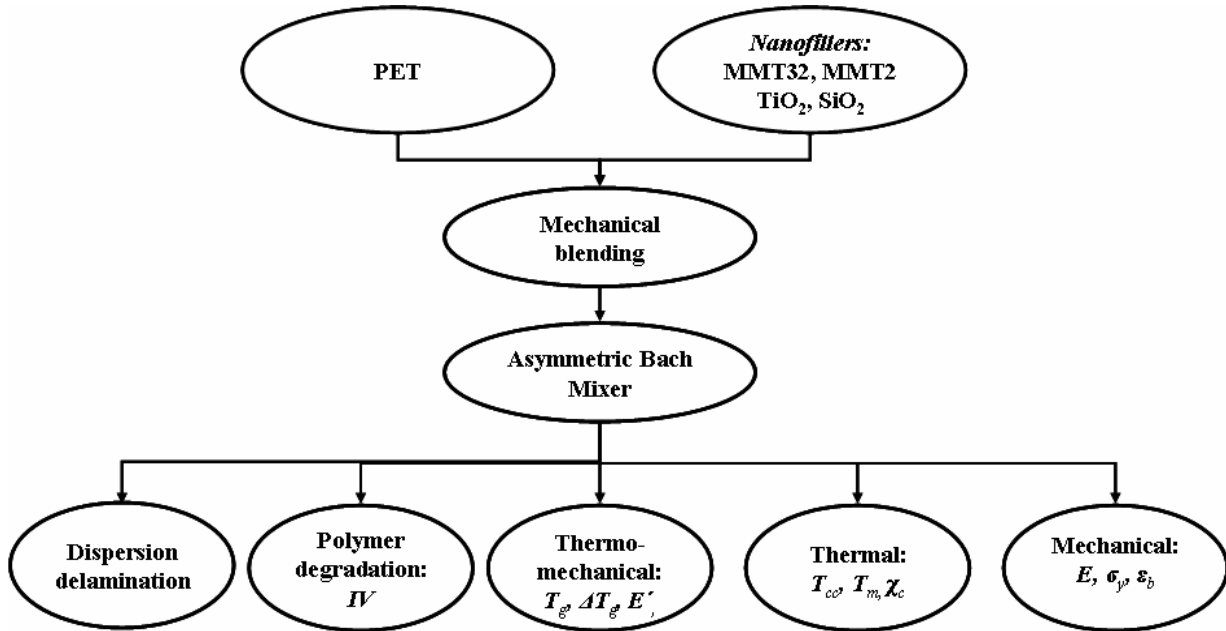


Figure 3.5. Scheme of the research approach used in Chapter VIII.

### 3.2.5. Chapter IX: In situ WAXS/SAXS structural evolution during uniaxial stretching of PET nanocomposites in solid state: PET/MMT nanocomposites

The main task of Chapter IX is to investigate the effect of different MMTs morphologies, i.e. tactoid and intercalated, on the multiscale structure evolution of PET/MMT nanocomposites and its deformation behaviour during uniaxial stretching in the solid state. In Figure 3.6. the research approach considered.

The PET/MMT nanocomposites prepared in chapter VIII are used in this study. In situ WAXS and SAXS investigations acquired under X-ray synchrotron source radiation are performed simultaneously to the uniaxial stretching process in the solid state. The influence of different MMTs morphologies on: i) the phase's fractions fraction (amorphous, mesophase and periodical mesophase), ii) the average molecular orientation,  $f_{av}$ , and iii) the amorphous phase orientation,  $f_{am}$ , are acquired by WAXS. In situ SAXS characterisation is used to assess the craze/voiding formation and evolution along the stretching process. The outcome of this study is a multiscale structural model defining the structural evolution during in solid state uniaxial stretching.

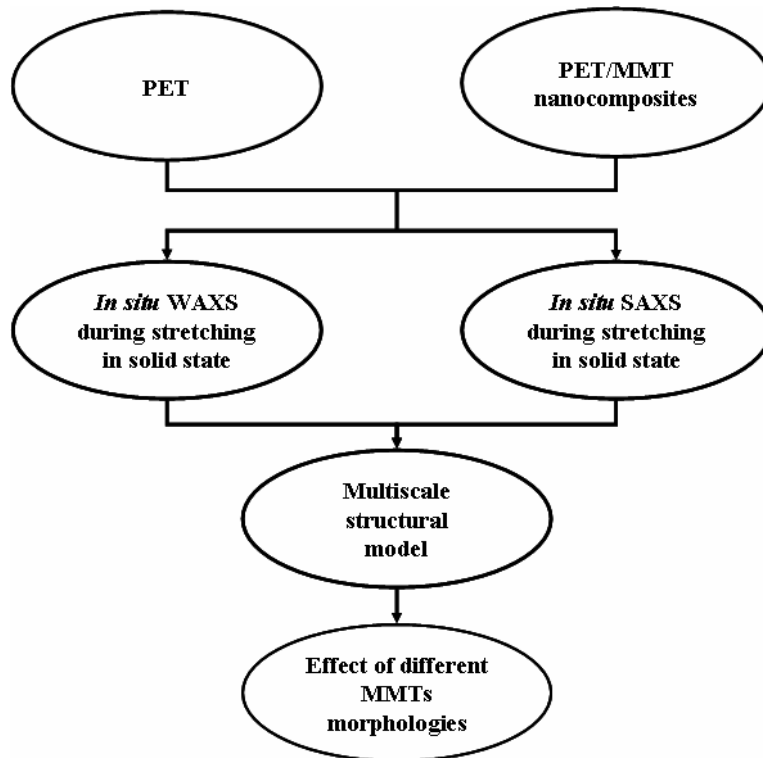


Figure 3.6. Scheme of the research approach used in Chapter IX

3.2.6. Chapter X: *In situ* WAXS/SAXS structural evolution during uniaxial stretching of PET nanocomposites in solid state: PET/TiO<sub>2</sub> and PET/SiO<sub>2</sub> nanocomposites

The intent of this chapter is to understand the effect of different spherical nanofillers, i.e. TiO<sub>2</sub> and SiO<sub>2</sub>, on the structure evolution. The research strategy applied is depicted in *Figure 3.7*.

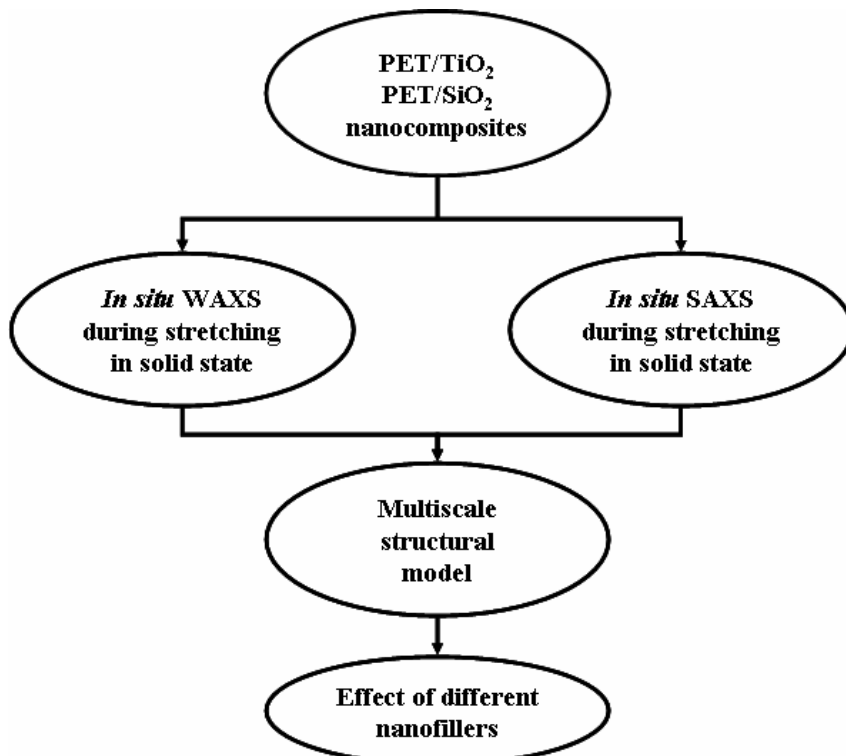


Figure 3.7. Scheme of the research approach used in Chapter X

PET nanocomposites are melt blended as described in Chapter VIII. X-ray synchrotron source radiation is used for *in situ* WAXS and SAXS investigations, simultaneously to mechanical stretching. The WAXS is used to reveal the influence of different nanofillers on the: i) phase's fractions (amorphous, mesophase and periodical mesophase), ii) the average molecular orientation,  $f_{av}$ , and iii) the amorphous phase orientation,  $f_{am}$ . *In situ* SAXS is used for the identification of craze/void evolution. To conclude, a deformation mechanism and multiscale structural model is proposed for each of the nanocomposites studied.





# CHAPTER IV

## Materials and methods

This chapter describes the materials, experimental protocols and characterization techniques used in this thesis.

### 4.1. Materials

#### 4.1.1. Poly (ethylene terephthalate), PET

Two type of neat PET were used. Their characteristics are summarized in **Table 4.1** and **4.2**, respectively. The materials are:

- i) *PET S41T*: supplied by Selenis S.A., Portugal (**Table 4.1**).
- ii) *PET T74 F9*: supplied by Tergal Fibers S.A., France (**Table 4.2**).

Detailed data sheets of virgin PET can be found in the *Appendixes (A.1 and A.2)* of this thesis.

**Table 4.1.** Technical specifications of *PET S41T*.

Parameter	Abbreviation	Values
Intrinsic viscosity [dl.g <sup>-1</sup> ]	IV	0.67 – 0.74
Degree of crystallinity [%]	$\chi_c$	40
Glass transition temperature [°C]	T <sub>g</sub>	78.3
Melting temperature [°C]	T <sub>m</sub>	235.6
Melt flow index [g.10min <sup>-1</sup> ]	MFI	63.6 ± 5.2

**Table 4.2.** Technical specifications of *PET T74 F9*.

Parameter	Abbreviation	Values
Intrinsic viscosity [dl.g <sup>-1</sup> ]	IV	0.74 ± 0.02
Solid density [g.cm <sup>-3</sup> ]	P	1.40
Glass transition temperature [°C]	T <sub>g</sub>	81.2
Melting temperature [°C]	T <sub>m</sub>	252
Average molar mass [g.mol <sup>-1</sup> ]	M <sub>n</sub>	≈ 20000

#### 4.1.2. Nanoparticles

For the preparation of PET nanocomposites, two types of nanoreinforcements were used, namely *one-dimensional*, 1D, nanoparticles such as MMT and *three-dimensional*, 3D,

nanoparticles, such as SiO<sub>2</sub> and TiO<sub>2</sub>.

#### 4.1.2.1. 1D nanoparticles

The 1D nanoparticles used in this study are the montmorillonite supplied by Süd-Chemie AG, Germany. Three kinds of organo-modified MMTs were supplied, namely:

- i) *Nanofil 5*: ion exchanged bentonite modified with distearyl-dimethyl-ammonium, MMT5,
- ii) *Nanofil 32*: ion exchanged bentonite modified with stearylbenzyl-dimethyl-ammonium chloride, MMT32,
- iii) *Nanofil 2*: ion exchanged bentonite modified with stearylbenzyl-dimethyl-ammonium chloride, MMT2.

Detail technical data of the MMTs used, as provided by the supplier [1], is listed in the **Table 4.3**. The corresponding technical data sheets can be found in the *Appendixes (A.4, A.5 and A.6)* of the thesis. The chemical structure of the surfactants is schematically represented in **Figure 4.1**.

**Table 4.3.** MMTs technical specifications.

Nanofiller	D <sub>av</sub>		t <sub>pl</sub> [nm]	d <sub>(001)</sub> [nm]	UTBD [g l <sup>-1</sup> ]	Surfactant
	Aggl.* [μm]	Platelet [nm]				
MMT5	8 - 12	≈200	1	2.8	150	long chain hydrocarbon
MMT32	30 - 80	≈200	1	1.8	350	long chain hydrocarbon / benzyl group
MMT2	8 - 12	≈200	1	1.8	150	long chain hydrocarbon / benzyl group

(D<sub>av</sub> – main average diameter, Aggl.\* – powder agglomerates, t<sub>pl</sub> – approx. platelet thickness, d<sub>(001)</sub> – interlayer distance by basal plane (001); UTBD - untamped bulk density)

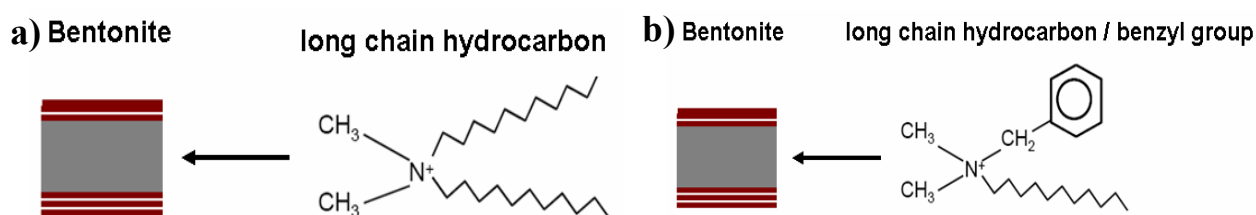


**Figure 4.1.** Chemical functionalization of MMTs: a) MMT5 and b) MMT32 and MMT2 [1].

#### 4.1.2.2. 3D nanoparticles

The following 3D nanofillers were supplied by Degussa AG, Germany:

- i) *AEROXIDE P25*: nanotitanium dioxide, TiO<sub>2</sub>, consisting of 80% anatase and 20% rutile
- ii) *AEROSIL 200*: nanosilica, SiO<sub>2</sub>.

The main technical data of the 3D nanofillers is listed in the **Table 4.4**. The detailed technical data sheets as provided by the supplier can be found in the *Appendixes (A.7 and A.8)* of

this thesis.

**Table 4.4.** 3D nanoparticles technical specifications

Nanofiller	$D_{av}$ [nm]		Surface area* [m <sup>2</sup> g <sup>-1</sup> ]	Bulk density [g l <sup>-1</sup> ]
	Aggl.*	Particles		
TiO <sub>2</sub>	≈100	≈ 21	50 ± 15	≈ 130
SiO <sub>2</sub>	≈100	≈ 12	200 ± 25	≈ 50

( $D_{av}$  – main average diameter, Aggl. – powder agglomerate, \* - Specific surface according to BET).

## 4.2. PNC preparation techniques

Three different melt blending techniques were employed in the production of the polymer nanocomposites, respectively: i) direct injection moulding, DIM, ii) extrusion and subsequent injection moulding, EIM, and iii) asymmetric batch minimixer, ABM.

Prior to the direct melt blending of nanocomposites, a predefined amount of nanofillers (i.e. 3 and 0.3 wt %) were added to the dried PET pellets (drying conditions: 170°C for 4 ÷ 7 h in dry air atmosphere with dew point of -20°C) and were then mechanically blended in a tumbler mixer for 15 min.

### 4.2.1. Direct injection moulding, DIM

The preparation of the nanocomposites by injection moulding was carried in an ENGEL T45 injection moulding machine. The processing conditions applied are listed in the **Table 4.5**.

**Table 4.5.** Processing conditions of DIM.

Parameter	Setting
Plasticizing speed [%]	50
Back pressure [bar]	30
Holding pressure [bar]	35
Barrel temperature [°C]	280 – 280 – 280 - 220
Injection velocity [mm.s <sup>-1</sup> ]	40
Holding time [s]	10
Cooling time [s]	20

These processing conditions resulted from a series of preliminary experiments done to optimize the dispersion of the nanofillers within the polymer matrix. For that a relatively high backpressure ( $P_b = 30$  bar) has been used to increase the shearing actions during the plasticizing phase. Also a high injection velocity ( $V_p = 68$  mm.s<sup>-1</sup>) has been used (corresponding to a injection flow rate of 28.3 cm<sup>3</sup>.s<sup>-1</sup>). Other processing conditions were: the screw rotation velocity of 240 rpm, the total plasticizing time of 3.4 s and a total cycle time of 32 s. The dried pellets and mechanical blends of PET/nanofillers were directly supplied to the hopper of the injection moulding machine by a vacuum transport system, in order to avoid contact with room atmosphere. Nanocomposites were moulded according to *section 4.3.3*.

### **4.2.2. Extrusion blending followed by injection moulding, EIM**

The blends were processed in a counter rotating twin-screw extruder Carvex. The temperature profile of the extruder ranged from 220°C (at the feeder) to 245°C (at the die). The screws speed was set at 15 rpm. The extruded material has been cooled from the die temperature to room temperature at air ambient. Such prepared blends were further injection moulded according to *section 4.3.3*.

### **4.2.3. Asymmetric Batch Minimixer, ABM**

The ABM employed for the preparation of PET nanocomposites via direct melt blending has a geometry and construction similar to the one described in [2]. The mixer consists on a cylindrical cup (with the following dimensions: diameter of 26 mm and height of 50 mm), a rotor with asymmetric geometry (with dimensions: length of 50 mm and alternating diameter along the length) similar to a roller blade, heating band placed around the mixer cup and a thermocouple mounted in the cup wall allowing the control and monitoring of the temperature. The ABM design is presented in the **Figure 4.2.** and the asymmetric rotor is shown in the **Figure 4.3.**

The ABM attempts to achieve the complex flow patterns observed in a standard two-rotor laboratory internal batch mixer (Haake batch mixer), in a simple one-rotor configuration similar to that of the MiniMAX<sup>TM</sup> mixer [3], and therefore combines design concepts from both [2]. Such rotor profile is similar to the structure of a standard rotor used in a batch mixer, but it is asymmetrical around the central axis, resulting in different clearances between the tips of the rotor and the wall (**Figure 4.2.**). The altering clearance enables the material to be squeezed, stretched and kneaded in a manner similar to the processes occurring between the two rotors of the standard internal batch mixer or in the kneading blocks of a twin-screw extruder. As the small gaps are important for generating high shear zones and obtain a good mixing efficiency, larger gaps are also important, to enable the passage of more material and for relaxation and breakup of the stretched domains. The small clearances, combined with a range of rotation speeds, allow the user to obtain shear rates ranging from 1 s<sup>-1</sup> to 550 s<sup>-1</sup> [4].

The following procedure was used: i) initially, the entire mixer assembly was heated to the desired temperature, ii) then, the polymers and nanofillers were loaded into the cup, and the rotor inserted onto it, iii) after the complete melting of the material the rotor was moved down to the base of the cup, squeezing the molten material upwards into the cavity between the rotor and the cylindrical cup, and iv) finally, the motor turns the rotor at the desired rpm to perform the mixing operation.

The experimental protocol used for preparation of PET nanocomposites (same for *Chapters VIII, IX and X*) was: i) the mechanically blended PET and nanoparticles were melted (for 10 min) and mixed at 280°C for 5 min into the ABM. The PET/nanoparticles melts were

casted on a preheated stainless steel plate (280°C) covered with a Teflon foil and used to prepare plaques with dimensions 200x200x0.3 mm by compression moulding, according to the protocol described in *Section 4.3.1*. The same procedure was applied to the neat PET.

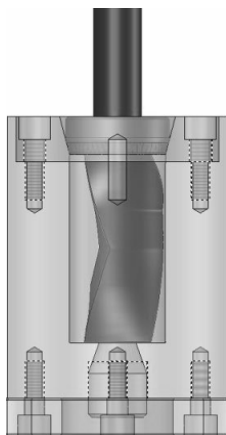


**Figure 4.2.** *ABM design.*



**Figure 4.3.** *Asymmetrical rotor of ABM.*

## **4.3. Processing techniques**

### **4.3.1. Compression moulding, CM**

The CM was performed on a MOORE hydraulic press in combination with rapid quenching (i.e. in the cold water). This technique was employed for the production of amorphous plaques of neat PET and its nanocomposites.

Compression moulded plaques with dimensions 200x200x0.3 mm were prepared from the prior dried PET pellets, (drying conditions: 170°C for 4 ÷ 7 h in dry air atmosphere with dew point of -20°C). The mouldings were prepared using the following procedure: the material was heated up at 280°C for 5 min with no pressure. The pressure was increased to 774 MPa and then released; this cycle was repeated three times to ensure that the samples were air bubbles free. Finally, the material was held at 774 MPa for 5 min and rapidly quenched in a vessel with controlled water temperature at  $5 \pm 0.5^\circ\text{C}$  by a chillier PIOVAN, in order to obtain completely amorphous samples.

### **4.3.2. Stretching in rubbery state, SRS**

The SRS was used to produce PET samples of different morphologies: quasi-amorphous, QA, and semi-crystalline, SC, from the initially amorphous PET samples (samples used in *Chapter V* and *Chapter VI*).

Dumbbell-like specimens with dimensions: length 95 mm and cross-section 42x0.3 mm (**Figure 4.4.**) were cut from the compression moulded plaques (produced according to *section 4.3.1.*)

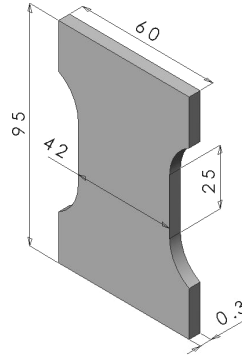


**Figure 4.4.** Geometry of the rectangular tensile bar specimen (dimensions in mm).

The tensile bars were stretched in a universal testing machine (Instron 4505) equipped with an environment chamber, using the stretching programme presented in **Table 4.6.** The stretching procedure included variations of the stretching variables: temperature,  $T_{st}$ , rate,  $\dot{\epsilon}_{st}$ , and ratio,  $\lambda_{st}$ , (in the limits of the laboratory equipment). They were varied accordingly to a L8 Taguchi orthogonal 2-level array. The dumbbell-like specimens were clamped at room temperature at gauge length of 55 mm, after which they were heated up by hot air to the programmed temperature. Prior to stretching, the samples were allowed to thermally equilibrate for 2 min.

**Table 4.6.** Stretching program according to a L8 Taguchi orthogonal array.

Variable		Condition							
		C1	C2	C3	C4	C5	C6	C7	C8
Temperature [°C]	$T_{st}$	90	110	90	110	90	110	90	110
Rate* [s <sup>-1</sup> ]	$\dot{\epsilon}_{st}$	0.003	0.003	0.03	0.03	0.003	0.003	0.03	0.03
Ratio**	$\lambda_{st}$	1.6	1.6	1.6	1.6	2.1	2.1	2.1	2.1

(\*stretching rate,  $\dot{\epsilon}_{st} = V/l_0$ , where  $V$  is the stretching velocity and  $l_0$  is the initial length of rectangular part of tensile bar; \*\*Stretching ratio,  $\lambda_{st} = l/l_0$ , where:  $l$  is actual and  $l_0$  is initial length of rectangular part of the tensile bar)

At the end of the deformation process, the tensile bars were cooled down by high pressure CO<sub>2</sub> at -70°C introduced into the environmental chamber volume. Such cooling protocol was chosen in order to achieve a fast and uniform cooling of the sample and the entire testing equipment (clamps and chamber), with the intention of diminish the heat transfer among the hot (metallic) grips and the polymeric sample.

### 4.3.3. Injection moulding, IM

Neat PET and its nanocomposites were injection moulded in an ENGEL T45 machine with the processing conditions listed in the *Table 4.5*. Dried pellets of neat PET or PET/nanofillers were directly supplied to the injection moulding machine hopper (by a vacuum transport system) in order to avoid contact with room atmosphere. Two different types of mouldings were produced:

- i) *laterally gated rectangular plaques*: 64x64x2 mm, used for optical studies (*Figure 4.5*),
- ii) *dumbbell-like standard specimens*: length of 50 and cross-section of 4x2 mm, used for mechanical testing (*Figure 4.6*).

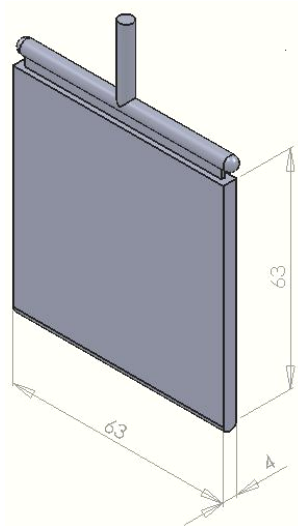


**Figure 4.5.** Geometry of the laterally gated rectangular plaques specimen (dimensions mm).

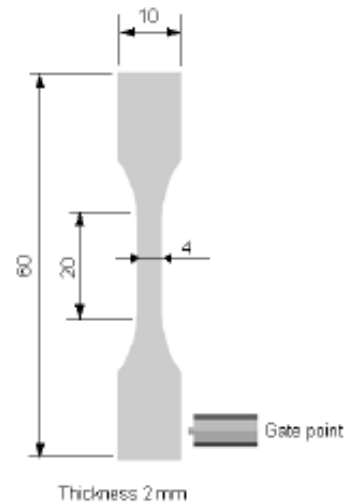


**Figure 4.6.** Geometry of the rectangular tensile bar specimen (dimensions in mm).

## 4.4. Statistical tools

The experimental stretching program was defined following a DOE approach. Analysis of variance, ANOVA, was performed on all assessed structural and thermal parameters [5]. The use of a DOE and data analysis by ANOVA allows the independent assessment of the influence of each individual factor and its interactions (that can not be assured by the traditional approaches of variation of stretching parameters once at one time). Results presented were significant upon 95% of confidence limit. The statistical significance of the stretching parameters (factors) was evaluated by the F-ratio, translated into a percentage of contribution of the individual factor and factor interactions. The influence of the stretching variables and their interactions is presented in effect graphs. Statistical treatment results were used to identify the percent of contribution and effect of different stretching variables on the morphological parameters, as reported in *Chapter V*.

## **4.5. Characterization techniques**

### **4.5.1. X-ray scattering techniques**

*In situ* X-ray scattering experiments were carried under synchrotron X-ray radiation at HASYLAB, DESY, Hamburg in the A2 soft condensed matter beamline. A Ge (111) radiation beam with  $\lambda=0.15$  nm was used. The 2D patterns were acquired by a MARCCD camera. The intensity was normalized with respect to the incident X-ray intensity, accumulation time and specimen thickness. The specimens were positioned perpendicular to the incident X-ray beam, with its stretching direction pointing upwards.

The synchrotron X-ray radiation experiments were performed at two setups:

- i) Wide Angle X-ray Scattering, WAXS,
- ii) Small Angle X-ray Scattering, SAXS.

#### **4.5.1.1. Wide Angle X-ray Scattering, WAXS**

Solid state stretching was carried simultaneously with WAXS characterization, at high-angle region ( $10^\circ < 2\Theta < 35^\circ$ ), by two modes: i) step stretching, SS, and ii) continuous stretching, CS and iii) low-angle region  $2\Theta < 10^\circ$ . For all experiments the WAXS was calibrated with the different diffractions of a crystalline PET sample.

##### ***i) Step stretching, SS***

This characterization was carried out using rectangular tensile test specimens with dimensions: length 50 mm and cross-section of 4x0.3 mm, shown in **Figure 4.7.**, cut longitudinal from the middle of the stretched in rubbery state tensile bars (**Figure 4.4.**), according to procedure described in *section 4.3.2*. The specimens were positioned at distance sample-to-detector 135 mm. A Microtester, micro-universal testing apparatus, developed by our group [6], was used to perform the uniaxial stretching. The PET samples were clamped between jaws of the Microtester (distance between tie bar 25 mm) with its centre positioned perpendicularly to the X-ray beam, at a sample-to-detector distance of 135 mm and the stretching direction pointing upward. The Microtester was employed in tensile mode at a constant velocity of 2 mm.min<sup>-1</sup> (stretching rate 0.001 s<sup>-1</sup>) with simultaneous movement of the grips apart from each other to the maximum stretching ratio of 1.5x. In order to allow the acquisition of WAXD patterns simultaneously to the stretching procedure, the stretching protocol followed the steps: (i) clamp the sample in the stretching machine and start the deformation process; (ii) after some deformation the stretching was ceased and allowed a 2 min pause at constant strain, (iii) acquire the 2D WAXS pattern with an accumulation time of 20 s; (vi) restore the stretching procedure. The WAXS was calibrated with the different diffractions of a crystalline PET sample. Background scattering was subtracted and all plots were normalized with respect to the incident



X-ray intensity, accumulation time and specimen thickness. Actual specimen's thickness was obtained by the first approximation of a homogeneous deformation, in which actual sample thickness,  $t$ , changes with the stretching ratio,  $\lambda$ , according to the following equation [7]:

$$t = t_0 \lambda^{-1/2} \quad (4.1)$$

where  $t_0$  – initial sample thickness. This protocol was used in *Chapter VI*.

**ii) Continuous stretching, CS**

Under this mode were obtained results reported in *Chapter IX* and *Chapter X*. The specimens were positioned at distance sample-to-detector 145 mm. The uniaxial stretching was carried out with a curved axisymmetric shape, with dimensions: length 35 mm, minimum cross-section 13.9x0.3 mm of deformation part length 14 mm and curvature radius 10.44 mm (**Figure 4.8.**), was used at constant velocity of 2 mm.min<sup>-1</sup> (stretching rate 0.002 s<sup>-1</sup>) with simultaneous grips movement in converse directions. The 2D WAXS patterns were acquired every 60 s during which 20 s accumulation time. Stretching apparatus output (force and displacement) was converted into as called homogeneous stress-strain curves ( $\sigma_N$  versus  $\ln\lambda$ ). It was assumed that the curved axisymmetric tensile specimen deforms through rectangular neck. The stretching ratio,  $\lambda$ , was defined as:

$$\lambda = \frac{l}{l_0} \quad (4.2)$$

where  $l$  is actual tensile specimen length and  $l_0$  the grip distance in mm. Also the homogeneous stress was calculated as follows:

$$\sigma_N = \frac{F}{A_0} \lambda \quad (4.3)$$

where  $F$  is the force and  $A_0$  the initial minimum tensile specimen cross-section area.

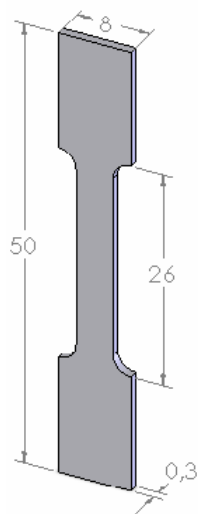


**Figure 4.7.** Geometry of the rectangular tensile bar specimen (dimensions in mm).

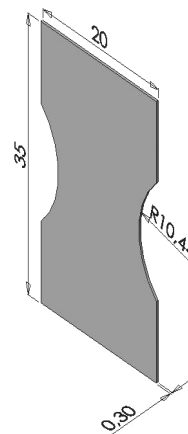


**Figure 4.8.** Geometry of curved axisymmetric shape tensile bar specimen (dimensions in mm).

**iii) Low-angle region**

As-moulded plaques were characterized at low-angle region of  $2\Theta < 10^\circ$  by WAXS, performed at AXS NanoStar Bruker equipment working with  $\text{CuK}\alpha$  radiation ( $\lambda=0.154 \text{ nm}$ ). Equipment was setup at sample-to-detector distance of 99 mm and 2D WAXS patterns were acquired with 2D HI-STAR Area Detector with accumulation time of 600 s. The WAXS patterns were investigated in range of  $2\Theta = 1.6 - 10^\circ$ , in order to study delamination of the MMTs, in *Chapter IX*.

**4.5.1.2. WAXS data analysis**

The 2D WAXS patterns were treated in different ways according to the morphology of the PET samples: i) *quasi-amorphous*, QA, and ii) *semi-crystalline*, SC. The methodology used for the determination of the phases mass fraction, orientation and crystalline dimension are described in this section.

**i) Phase mass fraction**

The linear intensity profiles taken from the 2D WAXD patterns along the equatorial and meridional directions were used to estimate the mass fraction of each phase (amorphous, mesophase and crystalline). A peak-fitting program was used to deconvolute the peaks of the intensity- $2\theta$  profiles which were then fitted by a Gaussian function. Considering the different morphologies observed for PET, a specific data analyses for the calculation of district phase's mass fractions was adopted.

**- Quasi-amorphous morphologies, QA**

Initially QA samples morphologies were assumed to consist of two main phases: i) amorphous – isotropic and ii) mesophase - anisotropic phase with degree of packing and order between the crystalline and the amorphous phases. The mass fraction of each individual phase was taken as the ratio of the area for each phase to the total area of the equatorial profile. The amount of amorphous phase was assumed to be proportional to the area of the linear meridional profile (**Figure 4.9**), calculated by equation 4.4. The subtraction of the amorphous fractions from the total area in the equatorial profile was proportional to the amount of the mesophase as calculated by equation 4.5.

$$Amor[\%] = \frac{A_{iso}^{mer}}{A_{anis}^{eq}} \cdot 100 \quad (4.4)$$

$$Meso[\%] = \frac{A_{anis}^{eq} - A_{iso}^{mer}}{A_{anis}^{eq}} \cdot 100 \quad (4.5)$$

where  $A$  is the area convoluted under meridional and equatorial intensity profiles.

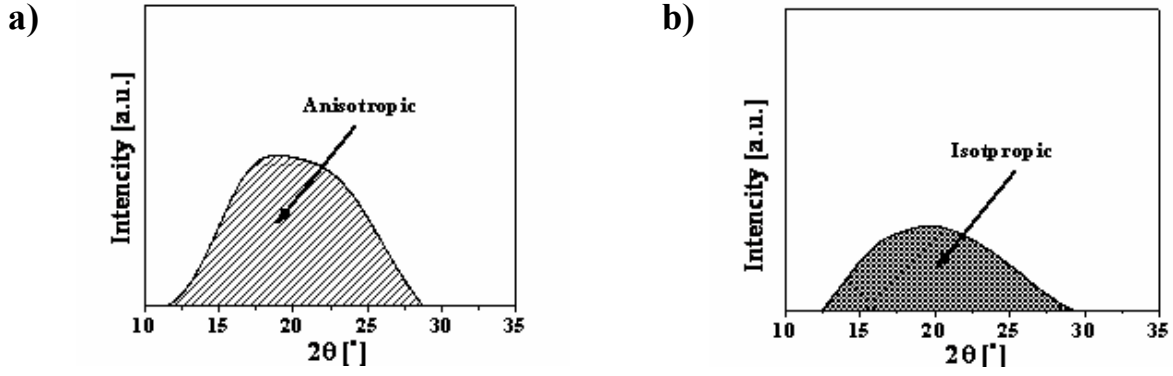


**Figure 4.9.** Intensity profiles extracted from the 2D WAXD patterns used for mass fraction calculation of QA samples at low strains: a) equatorial and b) meridional.

At high strains the 2D WAXS patterns exhibit a meridional mesomorphic reflection (10-3) at about  $2\Theta = 25.8^\circ$ , indicating conformational regularity called periodical mesophase. At this stage of deformation the QA samples morphologies were considered to be composed of three phases: (i) amorphous (ii) mesophase and (iii) periodical mesophase – mesophase with conformational periodicity perpendicular to the stretching direction. The mass fractions of the individual phase were taken as the ratio of the area for each phase to the total area, whereas a total area was assumed to be the sum of the area deconvoluted under the equatorial intensity profile and under the meridional (10-3) peak (**Figure 4.10.**), as calculated by equation 4.6. Each phase fraction was obtained as follow: i) the amount of amorphous phase was assumed to be proportional to the area deconvoluted by isotropic meridional peak in the linear meridional profile, calculated by equation 4.7.; ii) the amount of mesophase corresponds to the subtraction of the amorphous fractions from the total area in the equatorial profile and the area deconvoluted under peak (10-3), as obtained by equation 4.8.; and iii) periodical mesophase portions was estimated by equation 4.9., i.e. the ratio between the deconvoluted area under the peak (10-3) of the meridional profile and the total area.

$$A_{total}[\%] = A_{anis}^{eq} + A_{(10-3)}^{mer} \quad (4.6)$$

$$Amor[\%] = \frac{A_{iso}^{mer}}{A_{total}} \cdot 100 \quad (4.7)$$

$$Meso[\%] = \frac{A_{total} - A_{iso}^{mer} - A_{(10-3)}^{mer}}{A_{total}} \cdot 100 \quad (4.8)$$

$$PeriodicalMeso[\%] = \frac{A_{(10-3)}^{mer}}{A_{total}} \cdot 100 \quad (4.9)$$

where  $A$  is area deconvoluted under meridional and equatorial intensity profiles.

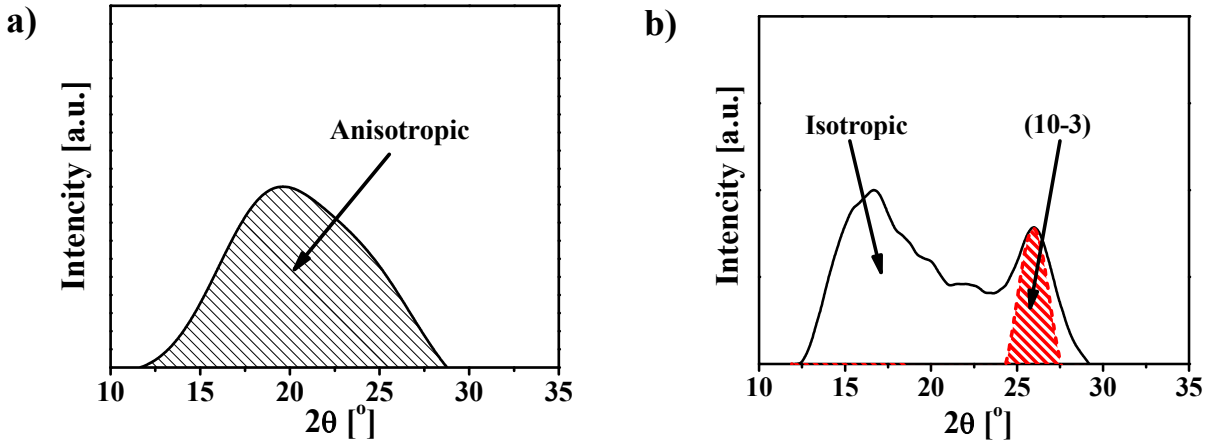


**Figure 4.10.** Peak fitting with Gaussian peaks of intensity profiles extracted from the 2D WAXD patterns used for mass fraction calculation of QA samples at high strains: a) equatorial and b) meridional.

- Semi-crystalline morphologies, SC

SC samples morphologies were assumed to contain three distinct phases [8]: i) amorphous – isotropic, ii) mesophase - which has a degree of packing order between the crystalline and the amorphous phase, and iii) a crystalline (triclinic) phase. The mass fraction of the individual phases was taken as the ratio of the area for each phase to the total area of the equatorial profile (**Figure 4.11**). The amount of crystalline phase was assumed to be proportional to the total area of the convoluted (010) at  $2\theta = 17.3^\circ$ , (-110) at  $2\theta = 22.5^\circ$ , and (100) at  $2\theta = 25.7^\circ$  peaks from the linear equatorial profile (equation 4.12), whereas the amount of the amorphous phase was assumed to be proportional to the area of the linear meridional profile (equation 4.10). When a crystal diffraction peak was detected in the meridional profile, i.e. at the (-103) at  $2\theta = 26.6^\circ$  reflection (**Figure 4.11**) [8], the subtraction of the crystalline and the amorphous fractions, from the total area of the equatorial profile was considered to be proportional to the amount of the mesophase (equation 4.11). Phases were obtained by the following equations:

$$Amor[\%] = \frac{A_{iso}^{mer}}{A_{total}^{eq}} \cdot 100 \quad (4.10)$$

$$Meso[\%] = \frac{A_{total}^{eq} - A_{iso}^{mer} - A_{(010)}^{eq} - A_{(100)}^{eq} - A_{(-110)}^{eq}}{A_{total}^{eq}} \cdot 100 \quad (4.11)$$

$$Cryst[\%] = \frac{A_{(010)}^{eq} + A_{(100)}^{eq} + A_{(-110)}^{eq}}{A_{total}^{eq}} \cdot 100 \quad (4.12)$$

where  $A$  is area deconvoluted under meridional and equatorial intensity profiles.

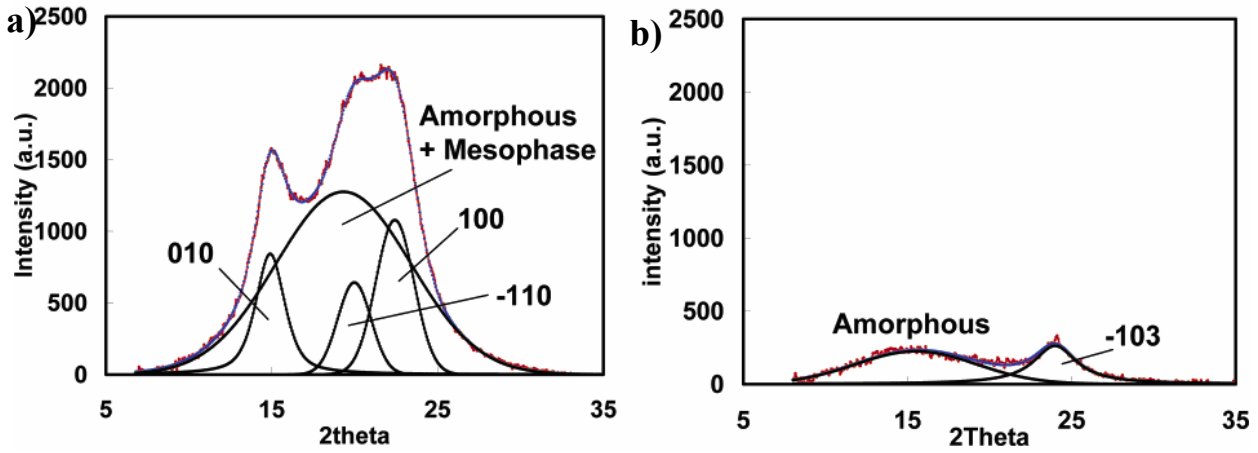


**Figure 4.11.** Peak fitting with Gaussian peaks of intensity profiles extracted from the 2D WAXD patterns used for mass fraction calculation of SC samples at high strains: a) equatorial and b) meridional [9].

## ii) Orientation level

Three different orientation parameters were determined:

- i) *average polymer orientation,  $f_{av}$* , - representing the global bulk orientation,
- ii) *amorphous phase orientation,  $f_{am}$* , - describing the amorphous phase orientation,
- iii) *crystallite orientation,  $f_c$* , - defining the orientation level of the crystalline sites.

### Average polymer orientation, $f_{av}$

The WAXS patterns were integrated along an azimuthal angle of  $\phi = 0 \div \pi/2$  ( $\phi = 0$  equator), over a section with a  $2\Theta = 13 \div 28^\circ$ , in order to calculate the average polymer orientation,  $f_{av}$ . That sector encloses all possible crystal reflections of crystallographic planes, isotropic amorphous phase and mesophases [10]. The Hermans' orientation function was used to evaluate the average polymer orientation,  $f_{av}$ , calculated by the following equation [11]:

$$f = \frac{3\langle \cos^2 \phi \rangle - 1}{2} \quad (4.13)$$

where the  $\langle \cos^2 \phi \rangle$  is defined as:

$$\langle \cos^2 \phi \rangle = \frac{\int_0^{\pi/2} I(\phi) \cos^2 \phi \sin \phi d\phi}{\int_0^{\pi/2} I(\phi) \sin \phi d\phi} \quad (4.14)$$

where  $\phi$  is the azimuthal angle,  $I$  the diffracted intensity and  $\langle \cos \phi \rangle$  the average angle that the normal makes with principal deformation direction.

### Amorphous phase orientation, $f_{am}$

Amorphous phase orientation,  $f_{am}$ , was determined from azimuthal scans obtained over  $\phi = 2\pi$  ( $\phi = 0$  equator) between  $2\Theta$  values of  $19.3^\circ$  and  $20.8^\circ$  [12]. This annular ring is located between the (010) at  $2\theta = 17.3^\circ$  and (-111) at  $2\theta = 21.2^\circ$  crystalline reflections, that is an angular

range where the amorphous peak is reasonably intense and has least overlap from the crystalline reflections, when such are present. The profiles were fitted to Gaussian peaks and a horizontal baseline. The width of the peak was used to calculate the  $f_{am}$  using Herman's equations (equation 4.13 and 4.14). The  $\langle \cos^2 \phi \rangle$  was evaluated by the full-width at half maximum ( $\Delta\phi$ ) of the Gaussian peak intensity distribution by  $\langle \cos^2 \phi \rangle$  integrated between  $\pi/2$  and  $-\pi/2$  for each value of  $\Delta\phi$  from the relation:

$$I(\phi) = \exp\left(\frac{-4\phi^2 \ln 2}{\Delta\phi^2}\right) \quad (4.15)$$

*Crystallite orientation,  $f_c$*

Crystallite orientation,  $f_c$ , of PET in terms of the angle  $\sigma$  between the c-axis of the unit cell and the stretching direction can be characterized by the normal to the (-105) lattice plane as well as by using the three equatorial reflexes (010), (-110) and (100) according to the Wilchinsky's method [13]. The (-105) reflex is found to occur at a large scattering angle,  $2\Theta = 43^\circ$  [10] which is out of the characterized sector. Using Wilchinsky's method [10, 13] to determine the crystallite orientation of PET, the  $\langle \cos^2 \sigma \rangle$  can be calculated from the experimental  $\langle \cos^2 \phi_{hko} \rangle$  (equation 4.14) of the three equatorial reflexes by the following equation:

$$\langle \cos^2 \sigma \rangle = 1 - A\langle \cos^2 \phi_{010} \rangle - B\langle \cos^2 \phi_{-110} \rangle - C\langle \cos^2 \phi_{100} \rangle \quad (4.16)$$

where the parameters  $A = 0.8786$ ,  $B = 0.7733$  and  $C = 0.3481$  are derived from the triclinic crystal system [32]. The  $f_c$  values were calculated by from equation 4.13 by meaning of  $\langle \cos^2 \sigma \rangle$  equation 4.16.

**iii) Crystallite dimensions**

The apparent crystal sizes normal to the three crystal reflections: (100), (010) and (-103), which are almost orthogonal to each other, were estimated by the analysis of the linear intensity profiles taken across the reflection peaks. The vector normal (100) is coincided with that of benzene stacking, (010) vector normal is approximately parallel the benzene ring and appearance of the (-103) peak indicating the ordering along the stretching axis. Thus making the average lateral of the crystal [8, 14, 15] which was estimated using the Scherer equation:

$$D_{hkl} = K\lambda/(\beta_{1/2} \cos\Theta) \quad (4.17)$$

where  $D_{hkl}$  represents the apparent lateral crystallite size of the hkl reflection plane,  $\beta_{1/2}$  is the full width at the half height of the diffraction peak hkl in radians, the shape factor  $K$  is set at 0.9 for polymer systems,  $\lambda$  is the X-ray wavelength ( $\lambda = 1.54 \text{ \AA}$ ), and  $\Theta$  is half of the diffraction angle. There is the possibility of lattice distortion, which would broaden the line width, leading to the underestimation of the crystal size. According to Kawakami et al. [14], based on work of Salem [16, 17] the contribution of the lattice distortion is likely to be small.

#### 4.5.1.3. Small angle X-ray scattering, SAXS

Investigation by SAXS was performed in two approaches: i) *static* and ii) *continuous stretching*.

##### i) *Static*

The specimens were positioned perpendicular to the incident X-ray beam with the flow (injection) direction pointing upward. The  $2\Theta$  scale was calibrated by means of rattail cornea. For all conditions the equipment was setup as follow: sample to detector distance 1765 mm and 2D SAXS patterns were acquired with accumulation time was of 20 s. The 2D SAXS patterns were integrated along the equator, being plotted Intensity- $2\Theta$  curves. These experiments were evolved in the *Chapter VII*, in order to study dispersion/delamination of nanofillers. The angular and layer spacing values are related through the Bragg's law:

$$\lambda = 2d \sin \Theta \quad (4.18)$$

where  $d$  is spacing between diffraction lattice planes and  $\Theta$  is the measured diffraction angle. Characterization by SAXS was performed in a  $2\Theta$  range of 1 to  $4^\circ$ , corresponding to a lattice spacing range between 8.79 and 2.12 nm.

##### ii) *Continuous stretching, CS*

Under this mode were obtained results reported in *Chapter IX* and *Chapter X*. The specimens were positioned at distance sample-to-detector 3025 mm. The uniaxial stretching was carried out with a curved axisymmetric shape, with dimensions: length 35 mm, minimum cross-section 13.9x0.3 mm of deformation part length 14 mm and curvature radius 10.44 mm (**Figure 4.8.**), was used at constant velocity of 5 mm.min<sup>-1</sup> (stretching rate 0.006 s<sup>-1</sup>) with simultaneous grips movement in converse directions. The 2D SAXS patterns were acquired every 60 s during which 30 s accumulation time. Stretching apparatus output (force and displacement) was converted into as called homogeneous stress-strain curves ( $\sigma_N$  versus  $\ln\lambda$ ), calculated by equation 4.2 and 4.3.

#### 4.5.2. In-plane optical birefringence, BIR

In-plane optical birefringence, BIR, measurements were obtained using a commercially available Spectrophotometer (Shimadzu UV – 2401PC - UV-VIS Spectrophotometer) modified to accommodate the polarizer-sample-analyzer system. The measurements were performed within the wavelength range of 350 ÷ 800 nm. The polarizer – sample – analyzer sandwich was interposed in the spectrophotometer system and transmittances,  $T$ , versus wavelength,  $\lambda$ , graphs were obtained. The methodology used to determining the birefringence was the following [18]: the phase difference,  $\delta$ , as a function of wavelength,  $\lambda$ , is defined as:

$$\delta = \frac{2 \cdot \pi \cdot \Gamma}{\lambda} \quad (4.19)$$

where,  $\Gamma$  is the retardation, and can be written as:

$$\Gamma = m \cdot \lambda = d \cdot \Delta n \quad (4.20)$$

In this equation,  $m$  is an integer when the condition of constructive interference is met and the emergent light is plane polarized and  $d$  is the thickness of the specimen. If one defines  $m = \frac{\delta}{2\pi}$ , then equation 4.20 becomes:

$$m = \frac{d \cdot \Delta n}{\lambda} \quad (4.21)$$

Thus, by plotting  $m$  versus  $1/\lambda$ ,  $(d \Delta n)$  can be readily determined by the slope in the linear portion of the curve. Since  $d$  is known,  $\Delta n$ , BIR, can be calculated.

### **4.5.3. Intrinsic viscosity measurement**

The intrinsic viscosity measurements were performed according to the ASTM D4603-03 standard. This method allows determining the intrinsic viscosity of polymers by measuring the flow time of a solution with a single concentration using the Billmeyer equation (equation 4.22). An Ubbelohde type viscometer U 4944 2KRK was used. A solvent mixture composed of 60/40 phenol/1,1,2,2- tetrachloroethane was needed to prepare the PET solutions. The PET samples were previously ground in order to accelerate solubilization. Grounded materials were dried in an oven for 4 h at 170°C to avoid polymer hydrolytic degradation. The humidity presence causes rapidly decrease of equilibrium molar mass  $M_{ne}$  [19], which explains the need for careful polymer drying prior preparing of solutions. The polymer composites, prepared with corrected concentration (with 0.3 and 3 wt.%) after complete dissolution, were centrifuged for 30 min at 3500 rpm and filtered in order to remove the formed nanofiller sediment. From the flow time of the pure solvent mixture and the known concentration of polymer solutions, it is possible to obtain intrinsic viscosity,  $\eta$ , as follow:

$$\eta = \frac{0.25 \left( \left( \frac{t}{t_0} \right) - 1 + 3 \ln \left( \frac{t}{t_0} \right) \right)}{c} \quad (4.22)$$

where  $t$  is the flowing time of polymer solution (s),  $t_0$  is the flow time of pure solvent mixture (s), and  $c$  is the polymer solution concentration (g.dl<sup>-1</sup>).

### **4.5.4. Differential scanning calorimetry, DSC**

A Perkin Elmer DSC7 and DIAMOND PYRIS running in standard mode were used. The nitrogen purge gas flow rate was 20 cm<sup>3</sup>.min<sup>-1</sup>. Temperature and enthalpic calibrations were carried out using indium and lead standards. Heating experiments were performed over all samples, from 30 to 270 °C, at a heating rate of 20 °C.min<sup>-1</sup>. The sample weight was around 9 mg.

The glass transition temperature,  $T_g$ , cold crystallization and melting parameters were obtained from the heating scans. Melting,  $T_m$ , and cold crystallization,  $T_{cc}$ , temperatures were



considered to be the maximum value of the endothermic and the exothermic peaks, respectively. The fusion,  $\Delta H_m$ , and the cold crystallization,  $\Delta H_{cc}$ , enthalpies were determined from the areas of the melting peaks and crystallization peaks, respectively. Calculation of the degree of crystallinity,  $\chi_c$ , was based on a two-phase (crystalline–amorphous) method, using the following equation:

$$\chi_c = \frac{\Delta H_m - \Delta H_{cc}}{\Delta H_f} \quad (4.23)$$

where  $\Delta H_f$  is the enthalpy of fusion of pure PET crystals, taken to be equal to 120 Jg<sup>-1</sup> [20]. The reported results are the average of the measurements obtained in three different samples.

#### **4.5.5. Dynamic mechanical analysis, DMA**

The DMA analyses were carried out using Triton Tritec 2000 from Triton Technology Ltd. All samples were measured in a tension mode over -140 to 240°C temperature range, at a heating rate of 4°C.min<sup>-1</sup> and at a frequency of 1 Hz. Samples were cut into rectangular shapes 3x20x0.3 mm from the compression moulded plaques. An average of three samples values were used: i) glass transition temperature,  $T_g$ , calculated by the peak position of loss factor,  $\tan\delta$  curve and ii) breadth of the glass transition by means of half width of full maximum of loss factor,  $\tan\delta$ , peak fitted by Gaussian function.

#### **4.5.6. Tensile testing**

The mechanical properties were assessed using a universal testing machine - Zwick/Roell Z005. The experiments were carried at the controlled room temperature of 23°C. Since different samples geometries and test velocities were applied along the studies accomplished in this work, it is worth to summarize the stretching conditions and sample geometries used in here:

- i) *Chapter VII*: injection moulded rectangular tensile specimen with dimensions: length 50 mm and cross-section of 4x2 mm (**Figure 4.6.**) at a test velocity of 1.5 mm.min<sup>-1</sup> (stretching rate of 0.0013 s<sup>-1</sup>),
- ii) *Chapter VIII*: curved axisymmetric shape tensile specimens with dimension of length 35 mm and minimum cross-section of 14x0.3 mm (**Figure 4.8.**) at a test velocity of 2 mm.min<sup>-1</sup> (stretching rate of 0.002 s<sup>-1</sup>).

At least five specimens were tested for each condition and the average value was considered for the following mechanical properties: initial modulus,  $E$ , yield stress,  $\sigma_y$ , and strain at break,  $\epsilon_b$ .

#### **4.5.7. Transmission electron microscopy, TEM**

Ultramicrotome cuts made through the thickness sections of the compressed moulded samples, with approx. thickness of 60 nm, were used. TEM observation was carried out under an

operation voltage of 100 kV on a JEOL JEM 1010. Three micrographs per nanocomposite were used for agglomerates measurement from randomly transversal cuts. All nanofillers agglomerates shape was assumed to be elliptical and two main diameters were measured in order to obtain average agglomerate size.

The average agglomerates diameter,  $D_{av}$ , was calculate by following formula:

$$D_{av} = \frac{\sum_{i=1}^n [(d_1 + d_2)_i / 2]}{n} \quad (4.24)$$

where  $d_1$  and  $d_2$  are main diameters of each particle and  $n$  is the number of considered particles. At least partials of five micrographs were considered to obtain average particle diameter.

#### **4.5.8. Optical properties**

##### **4.5.8.1. Gloss**

The gloss was measured according to the ASTM D-523 standard [21], in a flat surface glossmeter Micro TRI-gloss (Gardner, Germany). Measurements were taken in triplicate for each sample from three mouldings of each formulation. All results are expressed as gloss units, relative to a highly polished surface of black glass standard with a value equal to 100.

##### **4.5.8.2. Haze**

Haze was measured as per ASTM D1003 [22] using a Hazemeter XL-211 Hazegard (Gardner), in three samples of moulded material systems.

## 4.6. References

1. *Thechnical datasheet* B.U.P.A. Süd-Chemie AG, Germany, Editor. 2003.
2. Breuer, O., U. Sundararaj, and R.W. Toogood, *The design and performance of a new miniature mixer for specialty polymer blends and nanocomposites*. Polymer Engineering and Science, 2004. **44**(5): p. 868-879.
3. Maric, M. and C.W. Macoskot, *Improving Polymer Blend Dispersions in Mini-Mixers*. Polymer Engineering and Science, 2001. **41**.
4. Breuer, O., et al., *Simulation and visualization of flow in a new miniature mixer for multiphase polymer systems*. Journal of Applied Polymer Science, 2005. **97**(1): p. 136-142.
5. Roy, R.K., *Design of experiments using the Taguchi approach*. . 2001, USA: Wiley.
6. Teixeira, D.S., et al., *Microtesting of micro-injection molded parts*, in *Micro Mechanics Europe 2007* University of Minho: Guimarães, Portugal. p. 345-352.
7. Oultache, A.K., et al., *Orientation and relaxation of orientation of amorphous poly(ethylene terephthalate)*. Polymer, 2001. **42**(21): p. 9051-9058.
8. Kawakami, D., et al., *Mechanism of Structural Formation by Uniaxial Deformation in Amorphous Poly(ethylene terephthalate) above the Glass Temperature*. Macromolecules, 2003(36): p. 9275-9280.
9. Kawakami, D., et al., *Mechanism of Structural Formation by Uniaxial Deformation in Amorphous Poly(ethylene terephthalate) above the Glass Temperature*. Macromolecules, 2003. **36**: p. 9275-9280.
10. Goschel, U., K. Deutschert, and V. Abetz, *Wide-angle X-ray scattering studies using an area detector: crystalline orientation in semisrystaline PET structures*. Polymer, 1996. **37**(1): p. 1-6.
11. Stribeck, N., *X-Ray Scattering of Soft Matter*. 2007: Springer Berlin Heidelberg New York.
12. Gowd, E.B., et al., *Effect of molecular orientation on the crystallization and melting behavior in poly(ethylene terephthalate)*. Polymer, 2004. **45**(19): p. 6707-6712.
13. Wilchinsky, Z.W., *Measurement of orientation in polypropylene film*. Journal of Applied Physics, 1960. **31**(11): p. 1969-1972.
14. Kawakami, D., et al., *Structural formation of amorphous poly(ethylene terephthalate) during uniaxial deformation above glass temperature*. Polymer, 2004. **45**(3): p. 905-918.
15. Kawakami, D., et al., *Deformation-Induced Phase Transition and Superstructure Formation in Poly(ethylene terephthalate)*. Macromolecules, 2005. **38**: p. 91-103.
16. Salem, D.R., *Crystallization kinetics during hot-drawing of poly (ethylene terephthalate) film: strain-rate/draw-time superposition*. Polymer, 1992. **33**(15): p. 3189-3192.
17. Salem, D.R., *Development of crystalline order during hot-drawing of poly(ethylene terephthalate) film: influence of strain rate*. Polymer, 1992. **33**(15): p. 3182-3188.
18. Yang, H.H., M.P. Chouinard, and W.J. Lingg, *Birefringence of highly oriented fibers*. Journal of polymer science. Part A-2, Polymer physics, 1982. **20**(6): p. 981-987.
19. Assadi, R., X. Colin, and J. Verdu, *Irreversible structural changes during PET recycling by extrusion*. Polymer, 2004. **45**(13): p. 4403-4412.
20. Viana, J.C., N.M. Alves, and J.F. Mano, *Morphology and Mechanical Properties of Injection Molded Poly(Ethylene Terephthalate)*. Polymer engineering and science, 2004. **44**(12): p. 2174-2184.
21. *ASTM standard D523–85 Standard test method for specular gloss*, in *Annual Book Of ASTM Standards*. 1985, West Conhohocken, PA. p. 104.
22. *ASTM Standard D1003–63 Standard test method for haze and luminous transmittance of transparent plastics* in *Annual Book Of ASTM Standards*. 1961, West Conhohocken, PA. p. 365.





# CHAPTER V

## Structure development of poly(ethylene terephthalate) during uniaxial stretching above the glass transition temperature: study of the statistical influence of the stretching variables

This Chapter presents an investigation about the structure development of poly(ethylene terephthalate), PET, during uniaxial stretching above  $T_g$ , following a statistical design of experiment approach in order to understand the influence of the stretching variables on the structural development. Amorphous PET was submitted to a stretching programme considering variations of the stretching temperature,  $T_{st}$ , rate,  $\dot{\epsilon}_{st}$ , and ratio,  $\lambda_{st}$ . Stretched samples were rapidly quenched and characterized by wide angle X-ray scattering, WAXS, optical birefringence, BIR, and differential scanning calorimetry, DSC. The relevance and influence of stretching variables on the obtained parameters: (i) phase's fraction, (ii) orientation and (iii) thermal parameters were analyzed. Strain induced crystallinity is controlled by the  $T_{st}$ ,  $\lambda_{st}$  and the interaction between them. Mesophase development is not dependant on the  $T_{st}$  but on the interaction between the  $\dot{\epsilon}_{st}$  and  $\lambda_{st}$ . The molecular orientation is almost proportionally dependent upon the  $T_{st}$ ,  $\lambda_{st}$  and their interaction.

*This chapter is adapted from the following publication:*

Todorov L.V., Martins C.I., Viana J.C.; *Structure development of poly(ethylene terephthalate) during uniaxial stretching above the glass transition temperature: study of the statistical influence of the stretching variables*; Journal of Applied Polymer Science, Online

## 5.1. Introduction

Poly(ethylene terephthalate), PET, is a thermoplastic polyester of important commercial significance due to its enhanced mechanical, thermal and barrier properties. It is a slowly crystallizing material that can have different degrees of crystallinity when cooled from the melt, depending on the cooling rate applied. Therefore, it can be either in a semi-crystalline state or in an amorphous state, the last when it is rapidly quenched from the melt. Amorphous PET can be further crystallized if deformed in the rubbery state i.e. above its glass transition temperature,  $T_g$  [1]. The distinguishing feature of PET to develop a specific semi-crystalline microstructure under uniaxial stretching in the rubbery state, plays an important role for the performance and characteristics of the final products.

PET's structure development is directly related to the thermo-mechanical environment used during the uniaxial stretching. Many studies have been conducted to characterize this material under different stretching conditions and to relate those to its structure development. Such studies were focused on the: (i) constant stretching rate and at various temperatures [2]; (ii) different stretching rates and constant temperature [3, 4]; (iii) fast stretching rates ( $\approx 10 \text{ s}^{-1}$ ) at diverse temperatures [5-7] and (iv) multi-step stretching at different stretching ratios and temperatures [8-11]. Different techniques were used to access the structure development of PET from post mortem techniques based on densimetric measurements [4, 12, 13]; fluorescence spectroscopy [3, 13-16]; raman spectroscopy [17, 18]; infra-red spectroscopy [14, 19-24]; X-ray diffraction [8-12, 14, 19, 20, 24-32]; optical birefringence [8, 11, 13, 18, 19, 32-36] and differential scanning calorimetry [11, 22, 27, 32, 37, 38], to *in situ* characterization using: (i) synchrotron X-ray diffraction [5-7, 22, 39-43]; (ii) online optical birefringence [37] and real time Fourier transform infra-red, FTIR [44], allowing significant progress on the understanding of the structural formation in PET films and fibres. The mechanical response and structure development was correlated by Salem [4, 12] which divided this process into two stages: (i) initial stage where stress increased slowly with stretching ratio but crystallinity increased relatively fast (up to 15% of crystallinity) and (ii) second stage where the stress increased rapidly (strain-hardening) and crystallinity increased slowly. Gorlier et al.[31] investigated the rubbery state deformation of initially amorphous PET by WAXS. They suggested three stages of Structure Development Mechanisms, SDM, consisting of: (i) "orientation" – molecular orientation occurs due to strong molecular interactions, (ii) "nucleation" - nuclei appear as a result of molecular orientation. At a given level of strain, the number of nuclei is fixed, forming a network structure that is responsible for strain hardening and (iii) "growth" stage – crystallization develops through the growth process. Kawakami et al. [43] [45] by *in situ* WAXS and SAXS gave new incites to the SDM. According to the authors, the first stage, also called

“orientation” stage, takes place until strain hardening region is initiated (plastic deformation region) and involves the formation of a mesophase with highly oriented chain segments. In this stage, the oriented mesophase was found to increase continuously with applied strain without the actual formation of crystals. Stretching is accompanied by the appearance of an equatorial streak in SAXS patterns at the later phase of the stage, which indicates the formation of a microfibrillar structure. The second stage, “nucleation” involves the initiation of crystallisation from the mesophase through nucleation and growth processes. This stage occurs during the strain-hardening region. Imperfect crystals (2D crystals) were observed for strains up to the initiation of strain-hardening. Increasing strain was followed by further chain orientation and crystal perfection. SAXS analysis showed the existence of two sub-stages within the nucleation stage, consisting of: (i) formation of titled lamellar structure within the microfibrils in conjunction with lamellar insertion; (ii) lamellar insertion which occurred at a slower rate. The last stage, “growth” corresponds to the stable crystal (3D crystals) growth phase, where the lamellar superstructure is responsible for the linear load increase with strain, which enables a good lattice PET triclinic unit cell to be registered in the WAXS patterns. However, at very high strains, some lamellar domains become fragmented, resulting in microfibrillar spinning and the prelude for catastrophic disruption of the crystalline phase.

Martins et al. [37] proposed a three stages stress-optical behaviour, SOB, for the structural development of amorphous PET above  $T_g$  based on *in situ* optical birefringence measurements simultaneous to the mechanical stretching of PET films and *ex situ* WAXS and DSC analyses. At early stages of deformation it was observed a linear increase of birefringence with stress, following the stress-optical rule, while the material remained in the amorphous stage. Then, a fast increase of birefringence was observed at almost constant stress. Here, there was the formation of crystalline structures with the establishment of long-range connected network. With further deformation, the chains connected through the network approach their finite extensibilities (third stage). In this stage the birefringence achieved a plateau while the stress increased, corresponding the strain hardening.

The phase's matter was defined by Ajji et al. [19, 20] using FTIR as: (i) amorphous - composed solely of *gauche* conformers; (ii) mesophase - consisting of *gauche* and highly oriented *trans* conformers; and (iii) crystalline – consisting only of *trans* conformers. Mesophase have been the focus of many works. Blundell et al. by *in situ* WAXS [6, 7, 46] concluded that when fast rates are applied the crystallization do not appear during the stretching process. Instead a mesomorphic structure appears which is the precursor of the crystalline structures appearing upon stretching has been finished. These observations are based on the disappearance of the meridional (00-1) peak at  $2\theta = 8.56^\circ$  and simultaneous appearance of the triclinic crystalline



peak at the equator. Ran et al. [47] via *in situ* WAXS indicated that mesophase was developed during deformation as detected by the intensity increase, upon stretching, of the meridian peak (00-1) ( $d=10.32 \text{ \AA}$ ) corresponding to inclined smectic C structure. This peak would drastically decrease when crystalline structure started to appear. Asano et al. [48] suggested the formation of oriented nematic structures upon solid state stretching of amorphous PET, with alternate position of the phenylene rings on neighbouring molecules. After annealing to  $60^\circ\text{C}$ , the nematic phase transforms into smectic, with the neighbouring rings aligned on the plane perpendicular to the stretching direction and a slight tilt of the molecules. Kawakami et al. [49], proposed the formation of a mesophase in the early stages of deformation. The mesophase phase has a degree of packing order between the crystalline phase and the amorphous phase. According to the authors the mesophase is responsible for the nucleation and the formation of imperfect crystals (with 2D order), forming a network and causing strain-hardening to occur.

Some works [16, 31, 50] dealing particularly with the influence of stretching variables on the molecular orientation referred that the orientation level increased with increasing stretching rate and decreasing temperature. Others investigations focused on the influence of the stretching variables on the crystallinity suggested that crystallinity develops above the stretching ratio of 2.0 [4, 19, 22, 51, 52], but its appearance can occur at higher strains with increasing stretching temperature and/or decreasing stretching rate [4, 12, 16, 31, 53].

Despite the abundant amount of investigations in this area, there is still the lack of understanding of the contribution and influence of each stretching parameter on the structure development of PET during uniaxial stretching in the rubbery state. The present investigation aims at going further in this subject by applying an experimental protocol consisting on the variations of stretching temperature, rate and ratio, and analysing its statistical contribution on the strain induced structure of PET. The relevance and influence of the stretching variables on the development of: phase fraction, orientation and thermal parameters are discussed.

## **5.2. Experimental**

### **5.2.1. Material**

Poly(ethylene terephthalate) with intrinsic viscosity of  $0.74 \pm 0.02 \text{ dl.g}^{-1}$  (bottle grade), solid density of  $1.40 \text{ g.cm}^{-3}$  and approximate average molar mass,  $M_n$ , of  $20000 \text{ g.mol}^{-1}$  was used in this study.

### **5.2.2. Samples preparation**

Compression moulded plaques with dimensions  $200 \times 200 \times 0.3 \text{ mm}^3$  were prepared from the dried PET pellets (dried at  $170^\circ\text{C}$  for 4 h, in dry air atmosphere, according to the producer recommendation), using the following conditions: the material was heated up at  $285^\circ\text{C}$  for 5 min

with no pressure. The pressure was increased to 774 MPa and then released; this cycle was repeated three times to ensure that the samples were air bubbles free. Finally, the material was held at 774 MPa for 5 min and rapidly quenched in a water vessel adapted with a cooling device in order to control the temperature at  $-5 \pm 0.5^\circ\text{C}$  and to obtain amorphous PET samples. Along the text these samples are designated by as-moulded samples.

Dumbbell-like specimens with dimensions: length 95 mm and cross-section  $42 \times 0.3 \text{ mm}^2$  were cut from the compression moulded plaques. These samples were stretched in a universal tensile testing machine (Instron 4505) equipped with an environment chamber, using the stretching programme presented in Table 1. The stretching procedure included variations of the  $T_{st}$  – stretching temperature;  $\dot{\epsilon}_{st}$  - stretching rate and  $\lambda_{st}$  – stretching ratio, within the limits of the stretching equipment, accordingly to a L8 Taguchi orthogonal 2-level array [54].

**Table 5.1.** Stretching program according to a L8 Taguchi orthogonal array.

Variable		Condition							
		C1	C2	C3	C4	C5	C6	C7	C8
Temperature [ $^\circ\text{C}$ ]	$T_{st}$	90	110	90	110	90	110	90	110
Rate [ $\text{s}^{-1}$ ]	$\dot{\epsilon}_{st}$	0.003	0.003	0.03	0.03	0.003	0.003	0.03	0.03
Ratio*	$\lambda_{st}$	1.6	1.6	1.6	1.6	2.1	2.1	2.1	2.1

(\*Stretching ratio –  $\lambda_{st} = (l_o + d)/l_o$ , where:  $l_o$  – initial length of rectangular part of the tensile bar and  $d$  – displacement).

Samples were clamped at room temperature at gauge length of 55 mm and then heated up to the programmed temperature by circulating hot air in the environmental chamber. Prior to stretching, samples were allowed to thermally equilibrate for 2 min. After stretching, samples were maintained clamped while high pressure  $\text{CO}_2$  at  $-70^\circ\text{C}$  was introduced into the chamber volume, in order to uniformly cool down the sample and the entire testing equipment (clamps and chamber), with the intention of diminishing the heat transfer among the hot metallic grips and the polymeric sample.

### 5.2.3. Wide angle X-ray scattering, WAXS

WAXS patterns were obtained using X-ray synchrotron radiation beam monochromized by reflection of a bent Ge (111) single crystal ( $\lambda=0.15 \text{ nm}$ ). These experiments were carried at HASYLAB, DESY, Hamburg on the A2 soft condensed matter beam-line. The specimens were positioned perpendicularly to the incident X-ray beam with the stretching direction pointing vertically. For all experiments the sample-to-detector distance was set at 13.5 cm. The 2D WAXS patterns were acquired by a MARCCD camera with accumulation time of 20s. The WAXS was calibrated with the different diffractions of a crystalline PET sample. Background scattering was subtracted and all plots were normalized with respect to the incident X-ray intensity.

A peak-fitting program was used to deconvolute the crystalline peaks and amorphous halo from the intensity profiles extracted from the 2D WAXS patterns. The patterns treatment was adapted from that proposed by Kawakami et al. [49]. The equatorial and meridional profiles of the 2D WAXS patterns were used to estimate the mass fractions of the three phases: amorphous phase, mesophase (which has a degree of packing between the crystalline and amorphous) and crystalline phase. The amount of crystalline phase was assumed to be proportional to the total area of the deconvoluted peaks: (010) at  $2\theta = 17.3^\circ$ , (-110) at  $2\theta = 22.5^\circ$ , and (100) at  $2\theta = 25.7^\circ$  taken from the linear equatorial profile, whereas, the amount of the unoriented amorphous phase was assumed to be proportional to the area of the linear meridional profile. When a crystal diffraction peak was detected in the meridional profile (e.g. at the (-103) at  $2\theta = 26.6^\circ$  reflection), its area contribution was excluded (e.g. C7) [43]. The subtraction of the crystalline and amorphous fractions from the total area of the equatorial profile was considered to be proportional to the amount of the mesophase. The mass fraction of the individual phases was taken as the ratio of the area for each phase to the total area of the equatorial profile.

In order to calculate the average polymer orientation,  $f_{av}$ , WAXS patterns were integrated along an azimuthal angle of  $\phi = 0 \div \pi/2$  over a section with a  $2\Theta = 13 \div 28^\circ$ . This sector encloses all possible crystal reflections of crystallographic planes, isotropic amorphous phase and mesophase of PET [10]. The Herman's orientation function was used to evaluate the average polymer orientation,  $f_{av}$ , calculated by the following equation [55]:

$$f = \frac{3\langle \cos^2 \phi \rangle - 1}{2} \quad (5.1)$$

where the  $\langle \cos^2 \phi \rangle$  is defined as:

$$\langle \cos^2 \phi \rangle = \frac{\int_0^{\pi/2} I(\phi) \cos^2 \phi \sin \phi d\phi}{\int_0^{\pi/2} I(\phi) \sin \phi d\phi} \quad (5.2)$$

Additionally, amorphous phase orientation,  $f_{am}$ , was determined from azimuthal scans obtained over  $\phi = 2\pi$  between  $2\Theta$  values of  $19.3^\circ$  and  $20.8^\circ$  [27]. This annular ring is located between the (010) at  $2\theta = 17.3^\circ$  and (-111) at  $2\theta = 21.2^\circ$  crystalline reflections, that is an angular range where the amorphous peak is reasonably intense and has least overlap from the crystalline reflections, when such are present. The profiles were fitted to Gaussian peaks and a horizontal baseline. The width of the peak was used to calculate the  $f_{am}$  using Herman's equations (equation 1 and 2). The  $\langle \cos^2 \phi \rangle$  was evaluated by the full-width at half maximum ( $\Delta\phi$  of the Gaussian peak intensity distribution by  $\langle \cos^2 \phi \rangle$  integrated between  $\pi/2$  and  $-\pi/2$  for each value of  $\Delta\phi$  from the relationship:

$$I(\phi) = \exp\left(\frac{-4\phi^2 \ln 2}{\Delta\phi^2}\right) \quad (5.3)$$

#### 5.2.4. Optical birefringence, BIR

In-plane optical birefringence, BIR, measurements were obtained using a commercially available Spectrophotometer (Shimadzu UV – 2401PC - UV-VIS Spectrophotometer) modified to accommodate the polarizer-sample-analyzer system. The measurements were performed within the wavelength range of 350 ÷ 800 nm. The polarizer – sample – analyzer sandwich was interposed in the spectrophotometer system and transmittances, T, versus wavelength,  $\lambda$ , graphs were obtained. The methodology used to determining the birefringence was the following [56]: the phase difference,  $\delta$ , as a function of wavelength,  $\lambda$ , is defined as:

$$\delta = \frac{2 \cdot \pi \cdot \Gamma}{\lambda} \quad (5.4)$$

where,  $\Gamma$  is the retardation, and can be written as:

$$\Gamma = m \cdot \lambda = d \cdot \Delta n \quad (5.5)$$

In this equation,  $m$  is an integer when the condition of constructive interference is met and the emergent light is plane polarized and  $d$  is the thickness of the specimen. If one

defines  $m = \frac{\delta}{2\pi}$ , then equation 5 becomes:

$$m = \frac{d \cdot \Delta n}{\lambda} \quad (5.6)$$

Thus, by plotting  $m$  versus  $1/\lambda$ , ( $d \Delta n$ ) can be readily determined by the slope in the linear portion of the curve. Since  $d$  is known,  $\Delta n$ , BIR, can be calculated.

#### 5.2.5. Differential scanning calorimetry, DSC

A Perkin Elmer DSC-7 running in standard mode was used. The temperature of the cold block was kept at 5°C and the nitrogen purge gas flow rate was 20 cm<sup>3</sup>.min<sup>-1</sup>. Temperature and enthalpic calibrations were carried out using indium and lead standards. Heating experiments were performed over all samples, from 30 to 270 °C, at a heating rate of 20 °C.min<sup>-1</sup>. The sample weight was around 9 mg.

The glass transition temperature,  $T_g$ , cold crystallization and melting parameters were obtained from the heating scans. Melting,  $T_m$ , and cold crystallization,  $T_{cc}$ , temperatures were considered to be the maximum value of the endothermic and the exothermic peaks, respectively. The fusion,  $\Delta H_m$ , and the cold crystallization,  $\Delta H_{cc}$ , enthalpies were determined from the areas of the melting peaks and crystallization peaks, respectively. Calculation of the degree of

crystallinity,  $\chi_c$ , was based on a two-phase (crystalline–amorphous) method, using the following equation:

$$\chi_c = \frac{\Delta H_m - \Delta H_{cc}}{\Delta H_f} \quad (5.7)$$

where  $\Delta H_f$  is the enthalpy of fusion of pure PET crystals, taken to be equal to  $120 \text{ Jg}^{-1}$  [57]. The reported results are the average of the measurements obtained in three different samples.

### 5.2.6. Statistical data treatment

The experimental stretching program was defined following a DOE approach. Analysis of variance, ANOVA, was performed on all assessed structural and thermal parameters [58]. The use of a DOE and data analysis by ANOVA allows the independent assessment of the influence of each individual factor and its interactions (that can not be assured by the traditional approaches of variation of stretching parameters once at one time). Results presented were significant upon 95% of confidence limit. The statistical significance of the stretching parameters (factors) was evaluated by the F-ratio, translated into a percentage of contribution of the individual factor and factor interactions. The influence of the stretching variables and their interactions is presented in effect graphs.

## 5.3. Results and Discussion

### 5.3.1. As-moulded PET

As-moulded PET samples were characterized in terms of WAXS, BIR and DSC to access the structural state of the material. The results are summarized in Table 2. The analyses of the 2D WAXS patterns, indicates a content of 96.5% of amorphous material. The average polymer orientation and the amorphous phase orientation are, respectively,  $f_{av}$  of -0.15 and  $f_{am}$  of -0.30, indicating that polymer chains tends to orient perpendicularly to the stretching (equatorial) direction. This result is caused by the compression moulding procedure. The optical birefringence measurement shows a birefringence level of 0.008; this value is recognized to belong to a fully isotropic state [8]. DSC shows a residual crystallinity level less than 5%, typical for amorphous PET [59]. It is conclude from these results that the compression moulded samples obtained are amorphous.

**Table 5.2.** Structural parameters of as-moulded PET.

Sample	Amor. [%]	Meso. [%]	$f_{av}$	$f_{am}$	BIR
as-moulded	96.5	3.5	-0.15	-0.30	0.008

(Amor. – amorphous phase fraction, Meso. – mesophase fraction;  $f_{av}$ – average polymer orientation;  $f_{am}$  – amorphous phase orientation, BIR – birefringence)

### 5.3.2. Stretched PET samples

#### 5.3.2.1. Structural characterization by WAXS and BIR

2D WAXS patterns of the stretched samples are presented in **Figure 5.1**. Only two sets of conditions are developing a crystalline pattern, corresponding to conditions C5 and C7, respectively. These samples were stretched at the lowest temperature (90°C) and at the highest stretching ratio applied (2.1x), at both studied stretching rates. All of the other conditions used gave rise to an amorphous halo, although in some cases the intensity profile seems to concentrate at the equator region, suggesting the existence of some polymer chain orientation in the stretching direction and presence of some content of mesophase, as reported elsewhere [39, 43, 45, 47, 49]. Although it is expectable to have an amorphous halo in C1, C2, C3 and C4 conditions, since the material is stretched to only 1.6x, C6 and C8, are stretched to much higher stretching level (2.1x) and still present an amorphous halo. This result shows that the temperature has an important role on the structure development of the sample, and in these cases, it hindered the strain induced crystallization mechanism of PET due to a possible competing mechanism between chain elongation due to mechanical deformation and chain relaxation due to the elevated temperature.

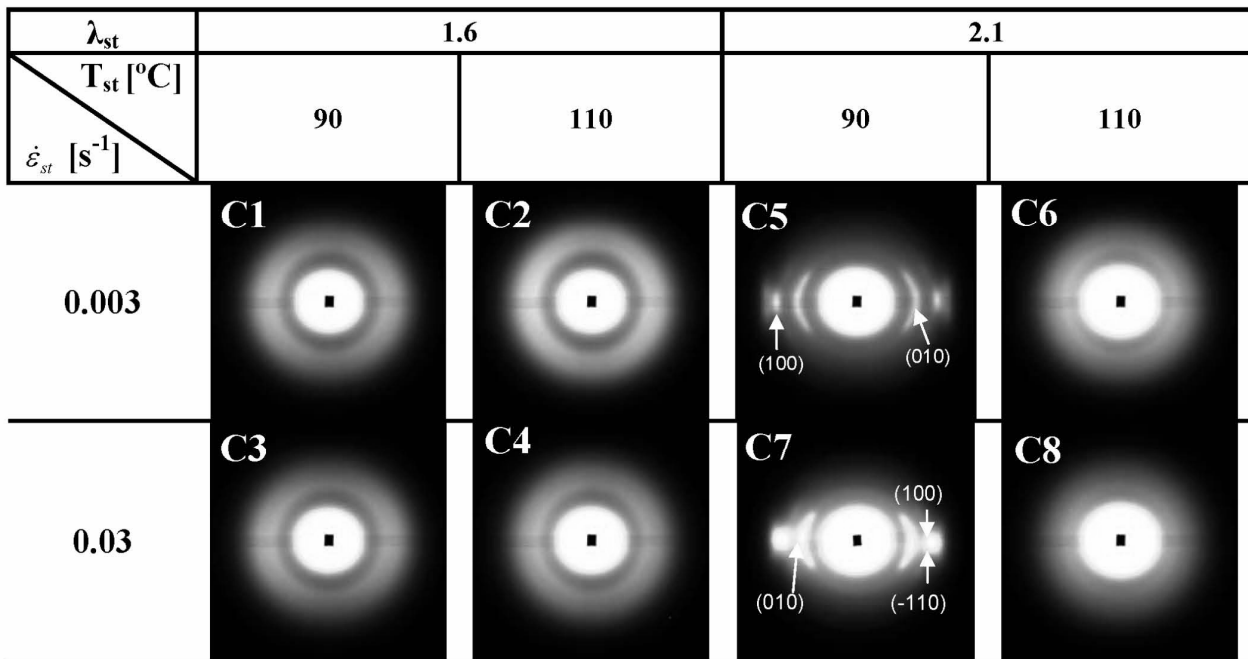


**Figure 5.1.** WAXS patterns of PET samples stretched in the rubbery state.

In order to detail the morphological state of the samples obtained in each condition, the equatorial and the meridional intensity vs.  $2\theta$  profiles extracted from the 2D WAXS patterns, were analysed. These results are shown in **Figure 5.2**. In **Figure 5.2(a)** three distinct equatorial reflection peaks are identified for samples C5 and C7, namely (010) at  $2\theta = 17.3^\circ$ , (-110) at  $2\theta = 22.5^\circ$ , and (100) at  $2\theta = 25.7^\circ$ . These peaks corresponds to the lattice planes parallel to the

molecular c-axis of PET triclinic unit cell [10]. In the case of C7, (-110) is overlapping with (100) reflection, and therefore it is difficult to identify it. When looking at the meridional intensity profiles (**Figure 5.2(b)**), a small crystalline reflection, assigned to the crystalline unit cell reflection (-103) at about  $2\Theta = 26.3^\circ$ , appears in C7 sample only. According to Kawakami et al. [49] this peak is visible during the so called “nucleation” stage but it is not located in the meridional position until the beginning of the “growth” stage. Increase of orientation and crystal perfection causes the shifting of (-103) peak to the meridian, as a result of 3D crystalline order formation. This peak was not observed for C5 sample, therefore indicating that imperfect 2D crystalline order is obtained with these conditions (lower strain rate comparing to C7).

All of the other cases are showing typical broad amorphous peak. Nevertheless, the dissimilarities in shape and area of the meridional intensity vs.  $2\Theta$  profiles (**Figure 5.2(b)**) indicate the presence of unlike amorphous mass fraction.

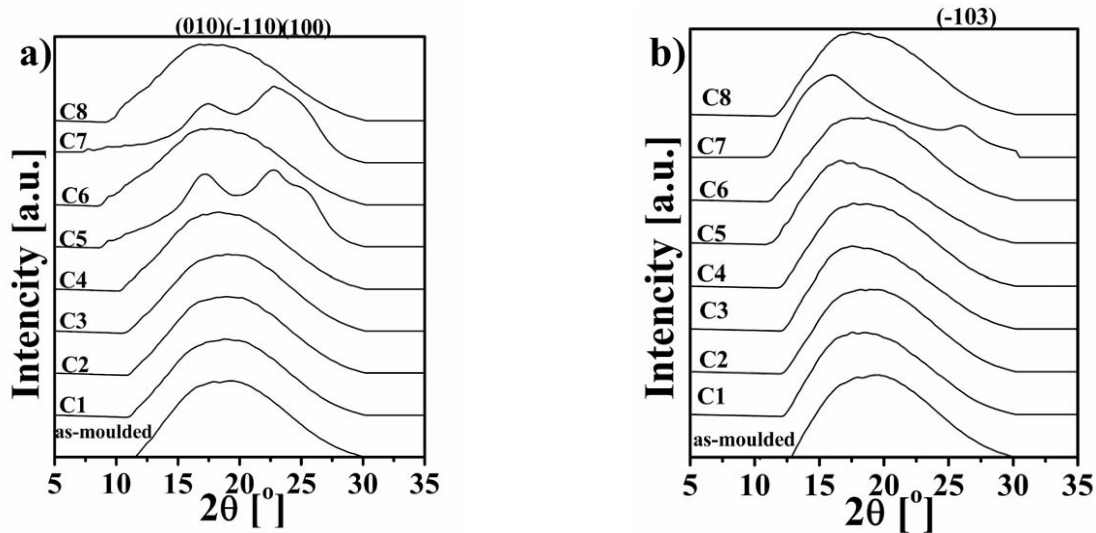


**Figure 5.2.** a) equatorial and b) meridional linear intensity profiles extracted from 2D WAXS patterns

From the 2D WAXS patterns shown previously, the mass fractions of the amorphous, mesophase and crystalline phases were estimated. Results are presented in **Figure 5.3(a)**. In **Figure 5.3(b)** it is shown the amorphous phase orientation and the average polymer orientation calculated through the use of the Herman’s orientation function. In the same plot the polymer orientation obtained through optical birefringence measurements is shown.

In **Figure 5.3(a)**, the samples deformed at lower stretching ratio ( $\lambda_{st} = 1.6$ ) and lower stretching rate ( $\dot{\epsilon}_{st} = 0.003s^{-1}$ ), respectively, C1 and C2, have the highest amount of amorphous phase fraction among the studied conditions. They show around 90% of amorphous phase fraction and 10% of the mesophase fraction, for both temperatures used. The increase of stretching rate (C3 and C4) causes the decrease of amorphous phase and the increase of mesophase fraction that is slightly more pronounced if low temperature is used (C3). According

to the results shown in **Figure 5.3(b)**, samples stretched to low stretching ratios – C1 to C4 – have similar levels of orientation, increasing slightly when the stretching rate increases (i.e. C1 and C3) or the stretching temperature decreases (i.e. C2 and C1 or C4 and C3). For instance, sample C3 stretched at high rate and lower temperature has 11.5% less amorphous phase and it is better oriented according to  $f_{am}$  results than C4 sample (**Figure 5.3(b)**).

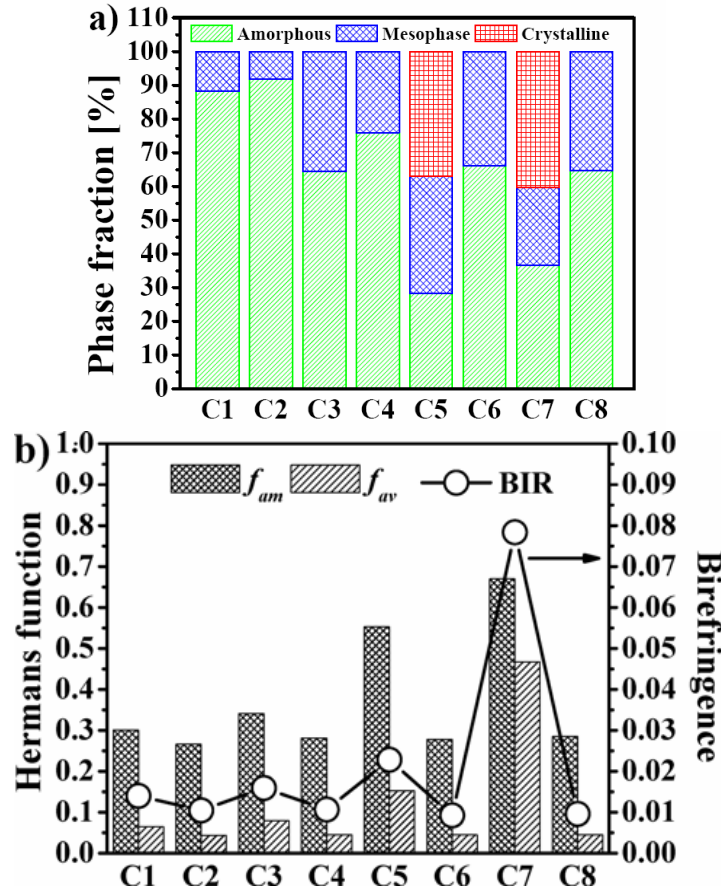


**Figure 5.3.** (a) Percentage of mass fractions and (b) amorphous phase,  $f_{am}$ , and average polymer,  $f_{av}$ , orientations calculated from 2D WAXS patterns and polymer chains orientation determined by birefringence measurements, BIR.

When high stretching ratios are applied (C5 to C8), two different morphologies can be detected. For high temperatures (C6 and C8), the material is composed by around 65% amount of amorphous phase fraction and 35% mesophase phase fraction, independently of the strain rate applied (**Figure 5.3(a)**). For low temperatures, the material crystallizes, showing a reduction of amorphous and mesophase phase fractions and the appearance of crystalline phase. These two conditions (C5 and C7) are showing the highest levels of amorphous and average orientation function among all the conditions. The effect of strain rate is mostly observed in here, where C7, corresponding to a deformation with higher stretching rate, appears with much higher levels of amorphous orientation and average polymer orientation, comparing to C5.

From the results shown in **Figure 5.3(a)** it is also possible to observe the importance of strain ratio on the development of crystalline structures. This processing variable has pronounced



influence on the strain-induced crystalline phase when low temperatures are applied, for both stretching rates used, as observed when comparing the samples (C1 and C5) obtained at low  $\dot{\epsilon}_{st}$  and (C3 and C7) obtained at high  $\dot{\epsilon}_{st}$ . The results are suggesting that decreased stretching temperature facilitates the strain-induced structure development and identical but minor effect is given to elevated stretching rates. This conclusion was also withdrawn by other authors [60].

In general, low stretching ratio results in low average polymer chain orientation, as observed by the birefringence measurements and by the average orientation function, presented in **Figure 5.3(b)**. Regarding the amorphous phase, some level of orientation is observed, which is slightly higher for the samples stretched at lower temperature (C1 and C3).

The combination of high stretching ratio and high temperature results in samples with similar orientation levels as the previously described samples. Although the orientation level is the same, the elevated stretching ratio seems to have a positive influence on the transformation of the amorphous phase fraction into mesophase (compare C2-C6 and C4-C8). At high temperatures polymer orientation and polymer relaxation are competing mechanisms [60], thus hindering the samples from crystallizing. For low stretching temperatures (C5 and C7), the samples are showing less amorphous phase, dissimilar amount of mesophase and presence of crystalline phase. Although C7 uses faster stretching rate it appears with less mesophase mass fraction than that of C5 (**Figure 5.3(a)**). This might be explained as follow: the applied fast rate causes the increase of mesophase, but since this phase is responsible for nucleation and formation of imperfect crystals (2D order crystallites) starting forming a network, this mesophase is easily converted into the crystalline phase. As observed, this sample has slightly higher crystalline phase than sample C5. It is noteworthy that crystalline phase of C7 has 3D order while in C5 it consists of imperfect crystalline phase with 2D order. In terms of orientations (**Figure 5.3(b)**), the results presented much higher levels of  $f_{am}$ ,  $f_{av}$  and BIR comparing to the other studied conditions.

### 5.3.2.2. Thermal characterization by DSC

**Figure 5.4** depicts the DSC thermograms of the as-moulded sample and the stretched counterparts. As observed, different structural states are evidenced by the DSC thermograms. Samples stretched at high temperatures (C2, C4, C6 and C8) have identical DSC curves as the as moulded plate. They are showing a broad  $T_{cc}$  peak, with its maximum at around 147°C. These samples have a percentage of crystallinity bellow 5%, as it can be seen by the **Table 5.3**, therefore one can consider that they are in the amorphous state. When lower stretching temperature is applied, two different results are appearing depending on the stretching ratio. For low stretching ratio, i.e, C1 and C3, the  $T_{cc}$  peak narrows and slightly moves towards  $T_g$ , appearing at around 135°C. In this case the percentage of crystallinity increases slightly to values

between 5-12%, also considered a quasi-amorphous state. The biggest change is observed for C5 and C7, where high stretching ratio is applied. In this case,  $T_{cc}$  peak overlaps with  $T_g$ , appearing at around 100°C. These samples have around 28% and 32% of crystallinity. The movement of  $T_{cc}$  towards  $T_g$  indicates that chains are more oriented as comparing to the other samples. This result is also confirming the WAXS results shown previously.

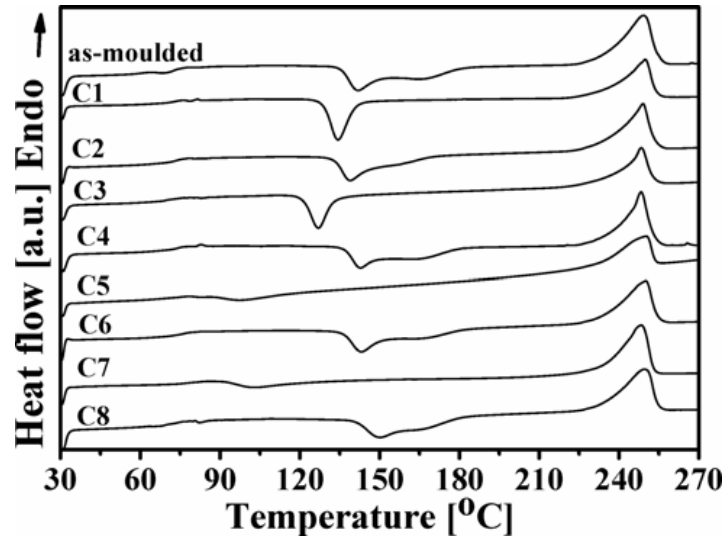


Figure 5.4. DSC thermograms obtained at  $20\text{ }^{\circ}\text{C}\cdot\text{min}^{-1}$  heating rate

Table 5.3 is showing the results acquired from the DSC thermographs. Regarding  $T_g$ , its minimum and maximum values are observed in the range of 70 to 80°C, respectively. These results are expected for PET samples having different percentage of crystallinity, the lowest corresponding to amorphous samples and the highest corresponding to a more crystalline sample. The highest  $T_g$  is observed for samples C5 and C7, those samples presenting the highest level of crystallinity. As Viana et al. [57] suggests crystalline phase geometrically constrains the amorphous phase, inhibiting the amorphous phase motion and increasing  $T_g$ . Regarding  $T_m$ , it remained constant at around 249°C, for all the conditions studied.

The different structural states of the samples are mainly evidenced in the position and the area of cold crystallization peak. Generally, the movement of the cold crystallization peak is a sensitive measure of the state of the polymer chains. If amorphous chains are oriented but not crystallized during the stretching process, the  $T_{cc}$  decreases toward  $T_g$  as the amorphous phase orientation increases [27, 61]. Decrease of  $T_{cc}$  and enthalpy in respect to the as-moulded PET was shown by all samples stretched at lower stretching temperature (90°C), respectively, C1, C3, C5 and C7 and opposite effect is denoted for all condition submitted to higher stretching temperatures (110°C). This suggests an important influence of the stretching temperature on the  $T_{cc}$ , consequently on orientation of amorphous phase. Developed crystalline structure caused strongly shift of the cold crystalline peak position toward the  $T_g$ , as observed for C5 (e.g. 99.5°C)

and C7 (e.g. 102.3°C). The more perfect crystalline structure of C7 contributes for slightly higher value  $T_{cc}$  than the C5, attributed to more oriented amorphous phase.

**Table 5.3. DSC results.**

Sample	$T_g$ [°C]	$T_{cc}$ [°C]	$\Delta H_{cc}$ [Jg <sup>-1</sup> ]	$T_m$ [°C]	$\Delta H_m$ [Jg <sup>-1</sup> ]	$\chi_c$ [%]
as-moulded	72.4±0.2	139.9±2.4	37.4±1.0	248.6±0.5	41.4±0.7	3.3±0.3
C1	73.5±0.7	135.0±1.4	32.5±1.0	249.3±0.6	41.4±0.9	7.4±0.7
C2	72.3±0.4	140.9±3.3	35.7±2.0	249.3±0.6	41.5±1.0	5.4±0.0
C3	70.8±0.6	132.6±3.3	28.1±0.0	248.9±0.6	42.3±0.1	11.8±0.1
C4	73.2±0.9	142.0±0.6	28.9±1.8	248.7±0.4	38.3±1.1	7.9±0.8
C5	75.5±0.4	99.5±0.8	16.8±2.4	249.6±0.5	50.2±0.4	27.9±1.7
C6	74.0±0.5	145.1±2.4	30.3±0.3	249.4±0.7	39.1±0.3	7.4±0.4
C7	80.3±1.6	102.3±1.1	10.6±2.3	248.4±0.0	49.5±2.7	32.4±2.8
C8	72.7±1.2	147.7±2.4	28.9±0.9	249.5±0.5	40.9±0.2	10.0±0.7

( $T_g$  - glass transition temperature,  $T_{cc}$  - cold crystallization peak temperature,  $\Delta H_{cc}$  - enthalpy of cold crystallization,  $T_m$  - melting peak temperature,  $\Delta H_m$  - enthalpy of melting,  $\chi_c$  - degree of crystallinity)

### 5.3.2.3. Structural interpretation

From the results analysed previously, the following remarks can be withdrawn:

(i) Conditions C1 to C4, and C6 and C8, gave rise to amorphous oriented structures, as well called quasi-amorphous. Although C6 and C8 were deformed to higher stretching ratio, the use of high temperatures (almost 40°C above  $T_g$ ), might have promoted a process of strain relaxation faster than the strain orientation of the chains. This competing mechanism is also reported in the literature, by other authors [7]. Absent of crystalline phase, detected by WAXS, assigning those condition to the orientation stage of SDM [31].

(ii) Condition C5 resulted in a semi-crystalline structure, with crystallite characterized with 2D order. Although a high level of crystallinity (~28% detected by DSC) is achieved, the average polymer chains orientation remains low, therefore indicating network is already formed but not yet reached its fully extensibility. Thus this condition might belong to the so called nucleation stage of SDM [31].

(iii) Among all, C7 is the condition presenting the highest crystallinity, with 3D crystallite order, and highest orientation level. The reason for that is the conjugation of stretching conditions: lower temperature, higher strain rate and higher stretching ratio, respectively. This result might indicate that a crystalline network has been formed and full extensibility of the chains was attained, since the levels of orientation are very high for the amorphous phase, the average polymer orientation and birefringence (comparing to C5). C7 might be assigned to the growth stage of SDM [31].

### 5.3.3. Statistical influence of the stretching variables on the structure developed

The statistical influences of the stretching variables on the structure and thermal parameters studied are shown in terms of percentage of contribution and effect graphs: **Figure**

5.5 shows the effect of processing variables on the amorphous, mesophase and crystalline phase mass fractions; *Figure 5.6* presents the effects on the orientation functions; and *Figure 5.7* depicts the effects on the percentage of crystallinity,  $T_g$  and  $T_{cc}$ .

### 5.3.3.1. Phase mass fractions

The most relevant variables on the amount of amorphous phase are the stretching ratio and the stretching temperature, with percentage of contributions of 54 and 23%, respectively (*Figure 5.5(a)*). However, mesophase phase fraction is influenced mainly by the stretching ratio and its interaction with stretching rate (with contributions of 33 and 37%, respectively). The crystalline phase is determined mainly by the stretching temperature, ratio and interaction between them (33% each), although only two conditions revealed a crystalline structure. These results reveal the complex effect of stretching variables upon the development of the different phases. Interestingly, the influence of the stretching ratio is common to all phase mass fractions. Chain extensibility seems to govern the development of phase fractions, mainly the amount of amorphous material, which is also influenced by chain relaxation (stretching temperature effect). Same phenomena determine the amount of crystalline phase, but a higher interaction between these factors is present.

*Figure 5.5(b)* presents the graphs corresponding to the effects of stretching variables upon the phases development. Higher stretching temperature favours a high amount of amorphous phase, but reduces the amount of crystalline one. This may be caused by the domination of polymer chain relaxation during stretching [4, 16, 19, 28, 40]. On the other hand,  $T_{st}$  affects negligibly the mesophase development. The opposite effect of chain extensibility and relaxation seems to govern the development of amorphous and crystalline phases. High stretching rates leads to a slight decrement of the amount of amorphous phase, a small increment of the mesophase, but no changes upon the amount of crystalline phase. In fact, for low stretching rates, when the stretching rate becomes comparable with chain reptation rate, the crystallization is prevented.[7, 62]. Furthermore, the transformation of amorphous into mesophase is favored by the increment of stretching rate. But this stretching variable shows the lower effect on structure development (considering the selected range of variation). Increasing the stretching ratio results in a low amount of amorphous phase, higher mesophase content and higher degree of crystallinity. The transformation of amorphous into mesophase is positively affected by the increment of stretching ratio [40, 53]. It has been also observed that the initiation of “nucleation” stage, where crystalline structure occurs, is anticipated for decreasing stretching temperature and that a greater amount of strain-induced crystallinity was observed at elevated stretching ratios [4, 16, 19, 28]. Interaction between stretching parameter  $T_{st} \times \lambda_{st}$  supports the effect of temperature and even amplifies it, but in different way. At low stretching ratio, the

effect of  $T_{st}$  on the development of amorphous phase is enhanced. At high stretching ratio, an increase of  $T_{st}$  reduces significantly the amount of crystalline phase. In fact, a sufficient level of molecular orientation, imposed by a high stretching ratio, is necessary to start the crystallization process, that competes with a higher chain relaxation with increased temperature [5, 16, 39]. Statistically important interaction between the  $\dot{\epsilon}_{st}$  and  $T_{st}$  was found only for amorphous and mesophase development, which confirms negligible effect of stretching rate on the crystalline phase development. At low stretching ratio, the increase of  $\dot{\epsilon}_{st}$  facilitates the transformation of amorphous into mesophase, the opposite effect being observed at elevated  $\lambda_{st}$ .

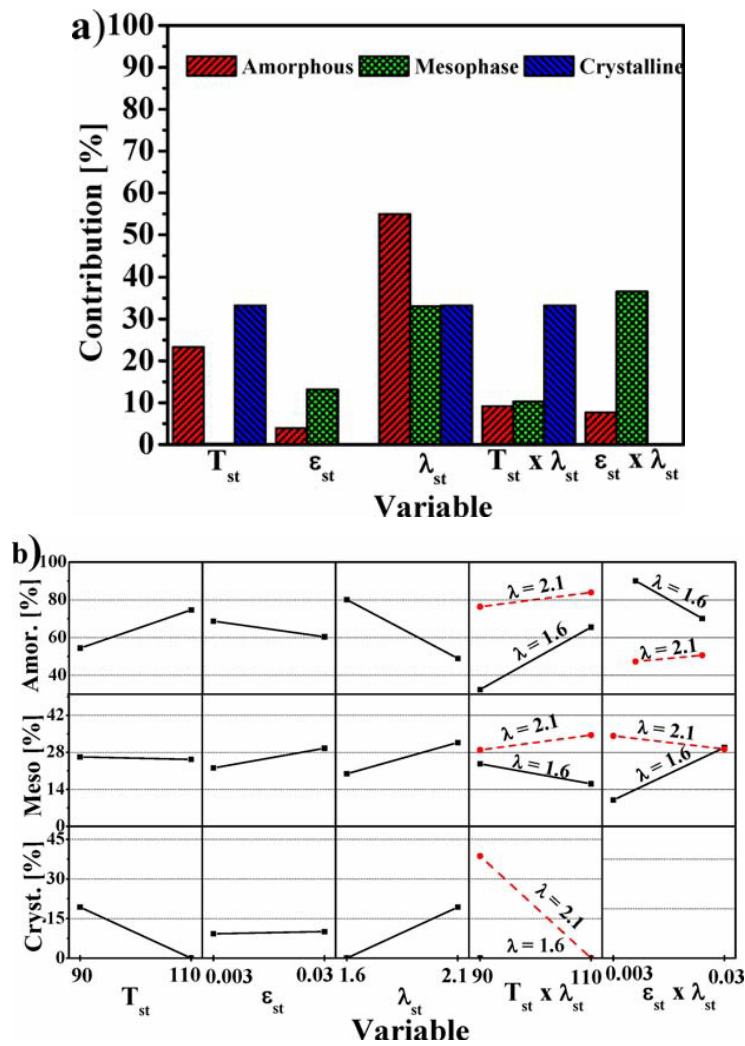
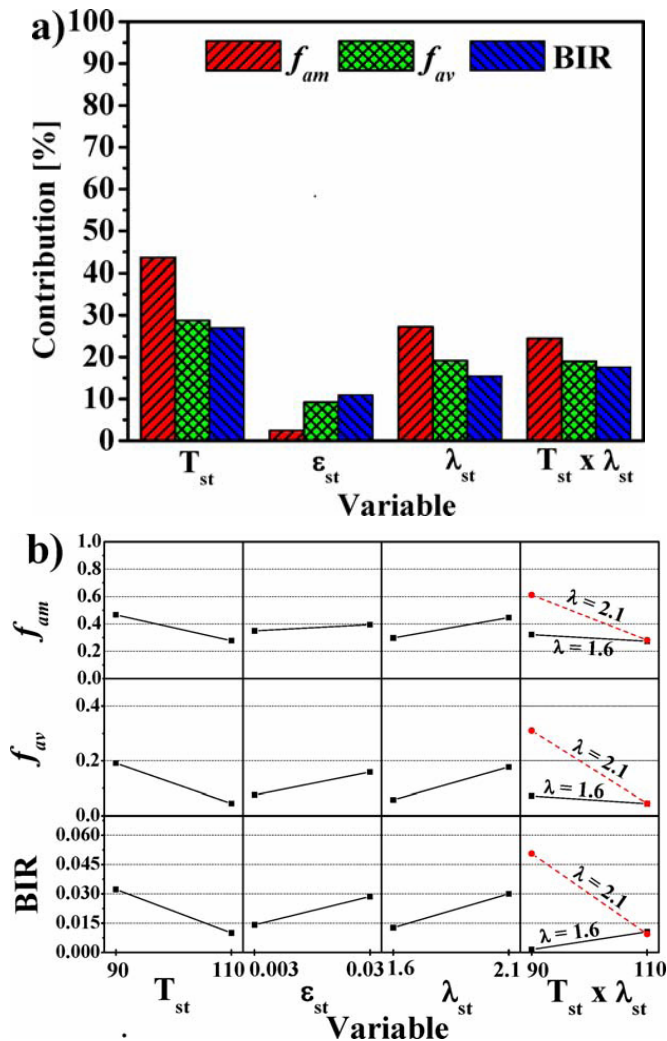


Figure 5.5. Effect of stretching variables on the amorphous; mesophase and crystalline phase mass fractions: a) percent of contribution and b) effects graph.

### 5.3.3.2. Molecular orientation

Figure 5.6 depicts the relevance of the stretching variables on the polymer orientation, namely, on the amorphous phase orientation, on the average polymer orientation, and on the birefringence. In descending order of their statistical significance are: the stretching temperature, the stretching ratio, the interaction of  $T_{st} \times \lambda_{st}$  and, in a less importance, the stretching rate (Figure 5.6a). It is very interesting to observe the relevant contribution of the interaction

$T_{st}\lambda_{st}$ , meaning that the effect of the stretching temperature depends upon the level of the stretching ratio.



**Figure 5.6.** Effect of stretching variables on the level of amorphous phase orientation,  $f_{am}$ , level of average polymer orientation,  $f_{av}$ , and birefringence, BIR,: a) percent of contribution and b) effects graph.

**Figure 5.6b)** depicts the dependence of molecular orientation measurements upon the significant stretching parameters and interactions. The variations are similar for all the molecular orientation data. Raising of  $T_{st}$  causes a decrement upon the molecular orientation, which could be attributed a higher macromolecular relaxation. An increment of the stretching rate leads to a slight increase upon the orientation level. In fact, low  $\dot{\epsilon}_{st}$  promotes the enhancement of relaxation process due to longer time scale of the deformation [16, 31, 50]. An increase of  $\lambda_{st}$  causes the orientation level to rise, conversely to the effect for  $T_{st}$ . The influence of  $T_{st}$  upon orientation level is intensified for high  $\lambda_{st}$  values. Stretching at high  $\lambda_{st}$  and at low  $T_{st}$  is favourable for obtaining a highly oriented PET, due to the reduction of chain relaxation and

increased chain extension level. Nevertheless, it is widely believed that orientation level increases with increasing stretching rate and decreasing temperature [16, 31, 50].

### 5.3.3.3. Transition temperatures and degree of crystallinity

**Figure 5.7(a)** shows the percentage of contribution of the stretching variables upon the transition temperatures (glass transition and cold crystallization temperatures,  $T_g$  and  $T_{cc}$ , respectively), as obtained by DSC.  $T_g$  is mainly influenced by the stretching ratio and the  $T_{st} \times \lambda_{st}$  interaction, while  $T_{st}$  has a relatively small effect (of 15%). The amount of amorphous phase is determined largely by the stretching ratio (**Figure 5.5(a)**) and the level of orientation of the amorphous phase  $T_{st}$ ,  $\lambda_{st}$  and their interactions (**Figure 5.6(a)**). The net result of the opposed effects of these variables (**Figures 5.5(b)** and **5.6(b)**) makes  $T_g$  mainly dependent upon  $\lambda_{st}$  and  $T_{st} \times \lambda_{st}$ , highlighting the contribution of the amount of amorphous phase on  $T_g$ .  $T_{cc}$  is mainly determined by  $T_{st}$ , and with less effect by the interaction  $T_{st} \times \lambda_{st}$  and  $\lambda_{st}$ . This reflects the contribution of molecular orientation and degree of crystallinity upon  $T_{cc}$ . The degree of crystallinity is mainly determined, in descent order of importance, by  $T_{st}$ ,  $\lambda_{st}$  and  $T_{st} \times \lambda_{st}$  interaction. The contribution of the stretching variables is similar to those assessed by X-ray (**Figure 5.5(a)**), as would be expected. As a general trend,  $\dot{\epsilon}_{st}$  has no statistical importance on the variations of these thermal parameters.

According to **Figure 5.7(b)**, higher stretching temperature decreases  $T_g$ , and the increment of  $\lambda_{st}$  shifts  $T_g$  toward higher temperatures. These variations are similar to those of  $f_{am}$  (**Figure 5.6(b)**) and opposed to that of the degree of crystallinity (**Figure 5.5(b)** or **Figure 5.7(b)**, respectively). Imposition of a low  $T_{st}$  and high  $\lambda_{st}$  leads to an increment of  $T_g$ , due to a high restraint of the molecular mobility originated by a high degree of crystallinity and high level of molecular orientation [57].  $T_{cc}$  increases with raising of  $T_{st}$ , in a well known effect, concomitant with the decrease of the cold crystallization enthalpy [32, 37]. Furthermore, at high  $\lambda_{st}$  the influence of  $T_{st}$  is amplified. The same variation of the stretching parameters causes a decrement upon  $T_{cc}$  (as opposed to the changes on  $T_g$ ). The effect of the level of amorphous molecular orientation (non crystallised samples) upon  $T_{cc}$  is reported elsewhere:  $T_{cc}$  decreases toward  $T_g$  as the amorphous phase orientation increases [27, 61]. Again, at high  $\lambda_{st}$  the influence of  $T_{st}$  on  $T_{cc}$  is enhanced strongly. The effect of the stretching parameters on the  $\chi_c$  is similar to the above discussed for **Figure 5.5(b)**: higher stretching temperature reduces  $\chi_c$ , because of the predomination of polymer chain relaxation; at high  $\lambda_{st}$  this variation is enhanced (interaction effect); increased stretching ratio increases the degree of crystallinity.

On **Table 5.4** are summarised the main effects of the stretching variables upon all assessed parameters. In general,  $T_{st}$  and  $\lambda_{st}$  are the main influencing variables; together with the interaction  $T_{st} \times \lambda_{st}$ .  $\dot{\epsilon}_{st}$  has a negligible effect.

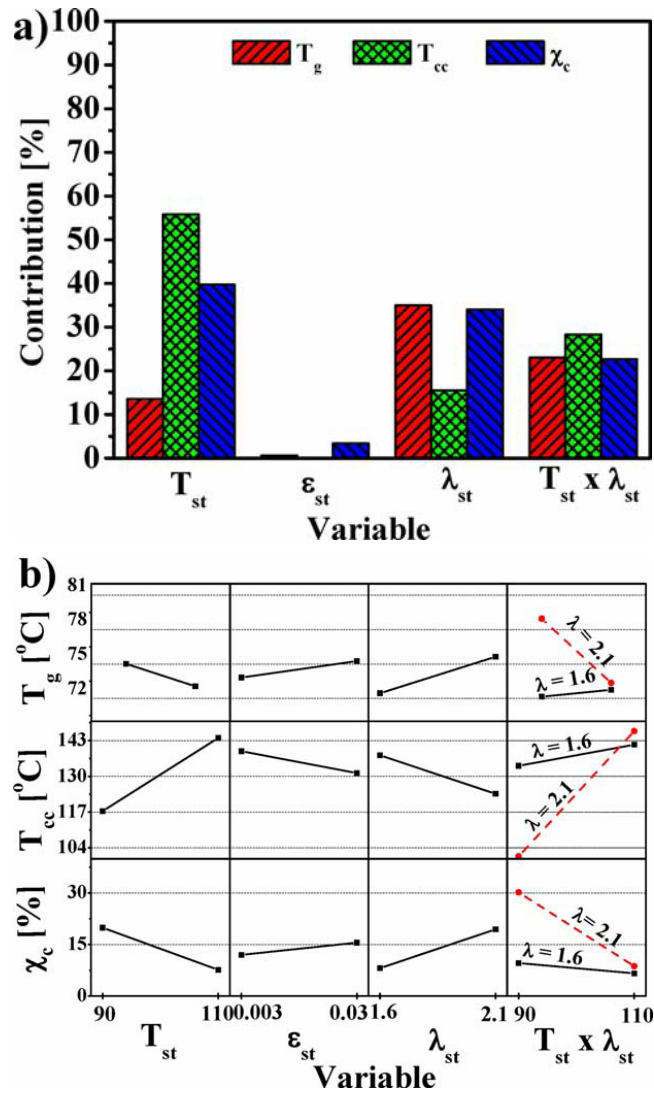


**Figure 5.7.** Effect of stretching variables on the glass transition temperature,  $T_g$ ; the cold crystallization temperature,  $T_{cc}$ ; and the degree of crystallinity,  $\chi_c$  (calculated from DSC): a) percent of contribution and b) effects graph.

**Table 5.4.** Effect of stretching variables upon all assessed parameters (in bold are the main contributing factors; double arrows in factors means strong effect; for interactions the arrow size is related to the importance of the variation; horizontal arrows means no influence).

Variable	Parameter								
	Amor [%]	Meso [%]	Cryst [%]	$f_{am}$	$f_{av}$	BIR	$T_g$ [°C]	$T_{cc}$ [°C]	$\chi_c$ [%]
$T_{st}$	↑↑	↔	↓↓	↓↓	↓↓	↓↓	↓	↑↑	↓↓
$\dot{\epsilon}_{st}$	↓	↑	↔	↔	↑	↑	↔	↔	↔
$\lambda_{st}$	↓↓	↑↑	↑	↑	↑↑	↑	↑	↓	↑↑
$T_{st} \times \lambda_{st}$	↑↑	↓↑	↓	↓	↓	↑↓	↓	↑↑	↓↓
$\dot{\epsilon}_{st} \times \lambda_{st}$	↓↑	↑↓	--	--	--	--	--	--	--

(Stretching variables:  $T_{st}$  – temperature,  $\dot{\epsilon}_{st}$  – rate,  $\lambda_{st}$  – ratio,  $T_{st} \times \lambda_{st}$  – temperature–ratio interaction,  $\dot{\epsilon}_{st} \times \lambda_{st}$  – rate–ratio interaction; Parameters: Amor. – amorphous phase fraction, Meso. – mesophase fraction, Cryst. – crystalline fraction,  $f_{am}$  – amorphous phase orientation,  $f_{av}$  – average polymer orientation, BIR – optical birefringence,  $T_g$  – glass transition temperature,  $T_{cc}$  – cold crystallization peak temperature,  $\chi_c$  – degree of crystallinity)



## 5.4. Conclusions

Upon variations of the stretching variables, different PET morphologies were developed, ranging from quasi-amorphous to semi-crystalline states. Stretching temperature and stretching ratio have both an important role on the structure development. High temperatures may hinder strain induced crystallization mechanism of PET. This is the result of two possible competing mechanisms: chain elongation due to mechanical deformation and chain relaxation due to the elevated temperature. Stretching ratio has a pronounced influence on the strain-induced crystalline phase, mainly when low temperatures are applied. In this way, deformation at low stretching ratio and high temperatures give rises to the highest amount of amorphous phase fraction. Or, on the opposite way, decreasing stretching temperature facilitates the strain-induced structure development. Structural characterization had shown that semi-crystalline morphology was developed only in condition which combined the high stretching ratio and low temperature. The combination of low stretching temperature, higher strain rate and higher stretching ratio, leads to a high degree of crystallinity.

In general, low stretching ratio results in low average polymer chain orientation, and hence low birefringence. The combination of high stretching ratio and high temperature results in samples with similar low orientation levels. Using high stretching ratio seems to have a positive influence on the transformation of the amorphous phase fraction into mesophase.

The highest crystalline PET shows the highest  $T_g$  suggesting that the crystalline phase geometrically constrains the amorphous phase, inhibiting the amorphous phase motions. There is an important effect of the stretching temperature on the  $T_{cc}$ , and consequently on orientation of amorphous phase.

Statistical analysis indicated the following main influences of the stretching variables on the structural and thermal parameters: (i) transformation of amorphous phase into mesophase is mainly controlled by stretching ratio and interaction between the stretching ratio and rate; (ii) strain-induced crystallization, measured by WAXS and DSC, governed by stretching temperature and ratio and interaction among them; (iii) level of molecular orientation, average and birefringence, is influenced mainly by stretching temperature, assisted by stretching ratio and the interaction between them with similar portions; (iv) glass transition temperature depends on the orientation level of amorphous phase, which is governed by the stretching ratio and its interaction with temperature, while the solely temperature influence is statistically small; (v) dominating influence over cold crystallization temperature is associated to the stretching temperature, followed by the stretching ratio and interaction among them.

## 5.5. References

1. Fakirov, S., *Handbook of Thermoplastic Polymers: Homopolymers, Copolymers, Blends, and Composites*. 2002: WILEY-VCH Verlag GmbH, Weinheim.
2. Salem, D.R., *Crystallization during hot-drawing of poly(ethylene terephthalate) film: influence of the deformation mode*. *Polymer*, 1995. **36**(18): p. 3605-3608.
3. le Bourvellec, G., L. Monnerie, and J.P. Jarry, *Amorphous orientation and induced crystallization in uniaxially stretched poly(ethylene terephthalate glycol)*. *Polymer*, 1986. **27**(6): p. 856-860.
4. Salem, D.R., *Development of crystalline order during hot-drawing of poly(ethylene terephthalate) film: influence of strain rate*. *Polymer*, 1992. **33**(15): p. 3182-3188.
5. Mahendrasingam, A., et al., *Effect of draw ratio and temperature on the strain-induced crystallization of poly (ethylene terephthalate) at fast draw rates*. *Polymer*, 1999. **40**(20): p. 5553-5565.
6. Blundell, D.J., et al., *Orientation prior to crystallisation during drawing of poly(ethylene terephthalate)*. *Polymer*, 2000. **41**(21): p. 7793-7802.
7. Mahendrasingam, A., et al., *Influence of temperature and chain orientation on the crystallization of poly(ethylene terephthalate) during fast drawing*. *Polymer*, 2000. **41**(21): p. 7803-7814.
8. Goschel, U., *Two-dimensional small-angle X-ray scattering studies on oriented poly(ethylene terephthalate) films*. *Polymer*, 1995. **36**(6): p. 1157-1165.
9. Goschel, U. and G. Urban, *Supermolecular structure of oriented and semicrystalline poly(ethylene terephthalate) as revealed by the electron density correlation function from small-angle X-ray scattering studies*. *Polymer*, 1995. **36** (19): p. 3633-3639.
10. Goschel, U., K. Deutschert, and V. Abetzt, *Wide-angle X-ray scattering studies using an area detector: crystalline orientation in semicrystalline PET structures*. *Polymer*, 1996. **37**(1): p. 1-6.
11. Goschel, U., *Thermally stimulated structural changes in highly oriented glassy poly(ethylene terephthalate)*. *Polymer*, 1996. **37**(18): p. 4049-4059.
12. Salem, D.R., *Crystallization kinetics during hot-drawing of poly (ethylene terephthalate) film: strain-rate/draw-time superposition*. *Polymer*, 1992. **33**(15): p. 3189-3192.
13. Clauss, B. and D.R. Salem, *Characterization of the non-crystalline phase of oriented poly(ethylene terephthalate) by chain-intrinsic fluorescence*. *Polymer*, 1992. **33**(15): p. 3193-3202.
14. Ajji, A., et al., *Amorphous orientation of poly(ethylene terephthalate) by X-ray diffraction in combination with Fourier transform infra-red spectroscopy*. *Polymer*, 1995. **36**(21): p. 4023-4030.
15. Hermanutz, F., D.R. Salem, and S.P. Wesson, *Influence of microstructure developed during drawing on surface properties of poly(ethylene terephthalate) film*. *Polymer*, 1994. **35**(21): p. 4611-4617.
16. le Bourvellec, G., L. Monnerie, and J.P. Jarry, *Kinetics of induced crystallization during stretching and annealing of poly(ethylene terephthalate) films*. *Polymer*, 1987. **28**(10): p. 1712-1716.
17. Nevalainen K, M.D., Overall NJ, Kuusipalo J, *The microstructure of a polyethylene terephthalate matrix near to a void under uniaxial draw*. *Materials Chemistry and Physics*, 2007(101): p. 103–111.
18. Ward, I.M., et al., *The Stress Optical Behavior of PET Fibers and Films*. *Polymer Engineering and Science*, 1999. **12**(39): p. 2335-2348.
19. Ajji, A., et al., *Orientation and structure of drawn poly(ethylene terephthalate)*. *Polymer*, 1996. **37**(16): p. 3707-3714.

20. Ajji, A., et al., *Orientation of Amorphous Poly(Ethylene Terephthalate) by Tensile Drawing, Roll-Drawing, and Die-Drawing*. Polymer Engineering and Science, 1997. **37**(11): p. 1801-1808.
21. Keum, J.K. and H.H. Song, *Thermal deformations of oriented noncrystalline poly(ethyleneterephthalate) fibers in the presence of mesophase structure*. Polymer, 2005(46): p. 939-945.
22. Matthews, R.G., et al., *The effects of stress relaxation on the structure and orientation of tensile drawn poly(ethylene terephthalate)*. Polymer, 2000. **41**(19): p. 7139-7145.
23. Pearce, R., et al., *Studies of Post Drawing Relaxation Phenomena in Poly(Ethylene Terephthalate) by Infrared Spectroscopy*. Polymer Engineering and Science 1997. **37**(11): p. 1795-1800.
24. Smith, M.R., et al., *Detailed mapping of biaxial orientation in polyethylene terephthalate bottles using polarised attenuated total reflection FTIR spectroscopy*. Polymer, 2006. **47**(15): p. 5691-5700.
25. Chevalier L, M.Y., *Identification of a strain induced crystallisation model for PET under uni- and bi-axial loading: Influence of temperature dispersion*. Mechanics of Material 2007(39): p. 596-609.
26. Adams, A.M., C.P. Buckley, and D.P. Jones, *Biaxial hot drawing of poly(ethylene terephthalate): measurements and modelling of strain-stiffening*. Polymer, 2000. **41**(2): p. 771-786.
27. Gowd, E.B., et al., *Effect of molecular orientation on the crystallization and melting behavior in poly(ethylene terephthalate)*. Polymer, 2004. **45**(19): p. 6707-6712.
28. Salem, D.R., *Crystallization during hot-drawing of poly(ethylene terephthalate) film: influence of temperature on strain-rate/draw-time superposition*. Polymer, 1994. **35**(4): p. 771-776.
29. Morawiec, J., et al., *High-Strength Uniaxially Drawn Tapes from Scrap Recycled Poly(ethylene terephthalate)*. Journal of Applied Polymer Science 2002. **86**: p. 1426-1435.
30. Vigny, M., et al., *Study of the Molecular Structure of PET Films Obtained by an Inverse Stretching Process. Part I: Constant Speed Drawing of Amorphous Films*. Polymer Engineering and Science, 1997. **11**(37): p. 1785-1794.
31. Gorlier, E., J.M. Haudin, and N. Billon, *Strain-induced crystallisation in bulk amorphous PET under uni-axial loading*. Polymer, 2001. **42**(23): p. 9541-9549.
32. Dargent, E., J. Grenet, and A. Dahoun, *Evolution of Hot Strain Induced Crystalline Texture of Poly(Ethylene Terephthalate) Films*. Polymer Engineering and Science 1997. **37**(11): p. 1853-1857.
33. Venkatesvaran, H. and M. Cakmak, *Kinetics of Structural Evolution During Crystallization of Preoriented PET as Followed by Dual Wavelength Photometric Birefringence Technique*. Polymer engineering and science 2001. **2**(41): p. 341-357.
34. Ajji, A., et al., *Measurements of Absolute Birefringence of Biaxially Oriented Films and Sheets On-Line or Off-Line*. Journal of Plastic Film and Sheeting, 1999(15): p. 256-268.
35. Engelaere, J.C., J.P. Cavrot, and F. Rietsch, *Tensile drawing behaviour of polyethylene terephthalate: Influence of molecular weight and pre-orientation*. Polymer, 1982(23): p. 766-770.
36. Natu, A.A., E.A. Lofgren, and S.A. Jabarin, *Effect of Morphology on Barrier Properties of Poly(Ethylene Terephthalate)*. Polymer engineering and science 2005: p. 400-409.
37. Martins, C.I. and M. Cakmak, *Control the strain-induced crystallization of polyethylene terephthalate by temporally varying deformation rates: A mechano-optical study*. Polymer, 2007. **48**: p. 2109-2123.
38. Morawiec, J., et al., *High-Strength Uniaxially Drawn Tapes from Scrap Recycled Poly(ethylene terephthalate)*. Journal of Applied Polymer Science 2002(86): p. 1426-1435.

39. Blundell, D.J., et al., *Characterization of strain-induced crystallization of poly(ethylene terephthalate) at fast draw rates using synchrotron radiation*. *Polymer*, 1996. **37**(15): p. 3303-3311.
40. Chaari, F., M. Chaouche, and J. Doucet, *Crystallization of poly(ethylene terephthalate) under tensile strain: crystalline development versus mechanical behaviour*. *Polymer*, 2003. **44**(2): p. 473-479.
41. Chaari, F. and M. Chaouche, *Rheoptical Investigation of the Crystallization of Poly(ethylene terephthalate) under Tensile Strain*. *Journal of Polymer Science: Part B: Polymer Physics* 2004(42:): p. 1915–1927.
42. Kolb, R., et al., *Investigation of the high speed spinning process of poly(ethylene terephthalate) by means of synchrotron X-ray diffraction*. *Polymer*, 2000(41): p. 2931–2935.
43. Kawakami, D., et al., *Mechanism of Structural Formation by Uniaxial Deformation in Amorphous Poly(ethylene terephthalate) above the Glass Temperature*. *Macromolecules*, 2003(36): p. 9275-9280.
44. Middleton, A.C., et al., *Real-time FTIR and WAXS studies of drawing behavior of poly(ethylene terephthalate) films*. *Journal of Applied Polymer Science*, 2001. **79**(10): p. 1825-1837.
45. Kawakami, D., et al., *Superstructure Evolution in Poly(ethylene terephthalate) during Uniaxial Deformation above Glass Transition Temperature*. *Macromolecules*, 2006. **39**: p. 2909-2920.
46. Mahendrasingam, A., et al., *Observation of a transient structure prior to strain-induced crystallization in poly(ethylene terephthalate)*. *Polymer*, 2000(41): p. 1217–1221.
47. Ran, S., et al., *Mesophase as the Precursor for Strain-Induced Crystallization in Amorphous Poly(ethylene terephthalate) Film*. *Macromolecules* 2002(35): p. 10102-10107
48. Asano, T., et al., *Crystallization of oriented amorphous poly(ethylene terephthalate) as revealed by X-ray diffraction and microhardness*. *Polymer*, 1999. **40**(23): p. 6475-6484.
49. Kawakami, D., et al., *Structural formation of amorphous poly(ethylene terephthalate) during uniaxial deformation above glass temperature*. *Polymer*, 2004. **45**(3): p. 905-918.
50. Oultache, A.K., et al., *Orientation and relaxation of orientation of amorphous poly(ethylene terephthalate)*. *Polymer*, 2001. **42**(21): p. 9051-9058.
51. Varma, P., E.A. Lofgren, and S.A. Jabarin, *Properties and kinetics of thermally crystallized oriented poly(ethylene terephthalate) (PET). II: Physical and optical properties*. *Polymer Engineering and Science*, 1998. **38**(2): p. 245-253.
52. Varma, P., E.A. Lofgren, and S.A. Jabarin, *Properties and kinetics of thermally crystallized oriented poly(ethylene terephthalate) (PET). I: Kinetics of crystallization*. *Polymer Engineering and Science*, 1998. **38**(2): p. 237-244.
53. Llana, P.G. and M.C. Boyce, *Finite strain behavior of poly(ethylene terephthalate) above the glass transition temperature*. *Polymer*, 1999. **40**: p. 6729–6751.
54. Roy, R.K., *Design of experiments using the Taguchi approach*. 2001, USA: Wiley.
55. Stribeck, N., *X-Ray Scattering of Soft Matter*. 2007: Springer Berlin Heidelberg New York.
56. Yang, H.H., M.P. Chouinard, and W.J. Lingg, *Birefringence of highly oriented fibers*. *Journal of polymer science. Part A-2, Polymer physics*, 1982. **20**(6): p. 981-987.
57. Viana, J.C., N.M. Alves, and J.F. Mano, *Morphology and Mechanical Properties of Injection Molded Poly(Ethylene Terephthalate)*. *Polymer engineering and science*, 2004. **44**(12): p. 2174-2184.
58. Roy, R.K., *Design of experiments using the Taguchi approach*. . 2001, USA: Wiley.
59. Arnoult, M., E. Dargent, and J.F. Mano, *Mobile amorphous phase fragility in semi-crystalline polymers: Comparison of PET and PLLA*. *Polymer*, 2007. **48**(4): p. 1012-1019.
60. Martins, C.I. and M. Cakmak, *Large deformation mechano-optical and dynamical phase behavior in uniaxially stretched poly(ethylene naphthalate)*. *Macromolecules*, 2005. **38**(10): p. 4260-4273.

61. Alves, N.M., et al., *Glass transition and structural relaxation in semi-crystalline poly(ethylene terephthalate): a DSC study*. *Polymer*, 2002. **43**(15): p. 4111-4122.
62. Blundell, D.J., et al., *Orientation and crystallisation mechanisms during fast drawing of poly(ethylene terephthalate)*. *Polymer Bulletin*, 1999. **42**: p. 357-363.

## CHAPTER VI

# Solid state structural evolution of PET during step uniaxial stretching from different initial morphologies: an *in situ* WAXS study

This work reports an *in situ* Wide-Angle X-ray Scattering, WAXS, study of the structural evolution of PET with distinct initial morphologies during step uniaxial stretching in the solid state. Two types of samples were analyzed under synchrotron X – ray radiation, namely quasi-amorphous, QA, and semi-crystalline, SC (with 2D and 3D order). Results are showing that initially different QA morphologies evolves following the same stages: i) stage I (before neck), at almost constant orientation level the amorphous phase evolves into mesophase; ii) stage II (neck formation), there is a rapid increase of polymer orientation and the appearance of a periodical mesophase from the highly oriented mesophase; iii) stage III (necking propagation), there is a levelling off of the average polymer orientation together with partial conversion of the periodical mesophase and mesophase into highly oriented amorphous. The behaviour of the two SC morphologies are completely distinct. A 2D order crystalline morphology evolves with stretching likewise the QA through three stages: i) at early stages of deformation the polymer orientation remains unchanged while the amorphous phase amount increases slightly, stage I; ii) in stage II, a fast increase of polymer orientation is accompanied by large formation of mesophase; and iii) in stage III there is the level off of polymer orientation as the chains approach their finite extensibility and the 3D crystalline order is achieved. Evolution of SC sample with 3D crystalline order mainly features constant orientation increase together with mesophase increment. Structure deformation models are suggested based on the WAXS results obtained.

*This chapter is adapted from the following publication:*

Todorov L.V., Martins C.I., Viana J.C. *Solid state structural evolution of poly (ethylene terephthalate) during step uniaxial stretching from different initial morphologies: an in situ WAXS*; Journal of Polymer Science Part B: Polymer Physics, Submitted

## 6.1. Introduction

PET is the unquestioned leader among thermoplastic polyesters regarding its industrial applications [1]. PET is a slowly crystallizing thermoplastic polyester that can be obtained with different morphologies, either an amorphous or a semi-crystalline when cooled from the melt, depending on the cooling rate applied. Once rapidly quenched into its amorphous state, PET structure can be developed by: i) stretching in the rubbery state (above  $T_g$ ), which leads to high polymer orientation and strain-induced triclinic crystalline structure development [2, 3] and/or by ii) stretching in the solid state (at room temperature) resulting in extraordinarily large chain orientation without actual crystallization, but developing a strain-induced mesomorphic phase, the mesophase [4, 5]. Both pathways lead to strain-induced structural development that improves mechanical and physical properties, determined by the imposed thermo-mechanical environment during stretching [6-8]. The structural evolution mechanisms taking place during the stretching requires *in situ* characterization techniques as synchrotron X-ray diffraction. The structure evolution is of academic and industrial interest and from extreme importance under processing and in-service conditions.

*Ex situ* [2, 6, 7, 9-23] and *in situ* [24-34] synchrotron X-ray scattering have been used to characterize the PET structural evolution during the uniaxial stretching in the rubbery state. Gorlier et al. [21] proposed a three stages structure development mechanism, SDM. More recently, the SDM was correlated to the superstructure by *in situ* SAXS/WAXS [35, 36], by stages: i) first stage, called “orientation”, involves the formation of mesophase from oriented chain segments and formation of microfibrillar structure; ii) second, “nucleation” stage, involves the initiation of crystallisation from the mesophase through nucleation and growth processes, forming imperfect crystals with 2D order; and iii) third, “growth” stage, corresponds to the stable crystal growth phase with 3D order. The lamellar superstructure is responsible for the linear load increase, enabling a good lattice PET triclinic unit cell to be registered. PET’s triclinic unit cell is described with  $a = 4.62 \text{ \AA}$ ,  $b = 5.92 \text{ \AA}$ ,  $c = 10.68 \text{ \AA}$ ,  $\alpha = 99.8^\circ$ ,  $\beta = 127.6^\circ$ , and  $\gamma = 104.9^\circ$  [37].

During stretching in the solid state, amorphous PET develops in a mesophase without crystallization to occur. Mesophase was first reported by the pioneer studies of Bonart [4, 5]. Auriemma et al. [38] associated the meridional peak (00-1), corresponding to  $d = 10.3 \text{ \AA}$ , to the mesophase, which has a smaller monomer length than the typical PET unit cell ( $c = 10.7 \text{ \AA}$ ). Asano et al. [39] reported that stretching of amorphous PET in the solid state results in the formation of an oriented nematic phase, with alternating position of the phenylene rings on neighbouring molecules. After annealing at  $60^\circ\text{C}$  nematic transforms into smectic phase (00-1)  $2\theta = 8.56^\circ$  ( $d = 10.7 \text{ \AA}$ ) with neighbouring rings aligned on the plane perpendicular to the stretching direction and slightly tilted on the molecule axis. Other works reported the meridional

peak (10-3) appearance at  $2\Theta = 25.8^\circ$  [7, 40]. Ran et al. [41] interpreted the emergence of this peak to the mesophase formation with similar packing symmetry to the crystalline phase with 3D crystalline order [35, 42] that is described by meridional crystalline unit cell reflection (-103) at  $2\Theta = 26.6^\circ$  [40].

The present study aims at contributing for a deeper understanding on the PET structure evolution upon uniaxial step stretching in the solid state by *in situ* WAXS characterization from distinct initial morphologies. For that purpose two types of morphologies were studied: i) two quasi-amorphous samples with different orientation level and phase's fractions and ii) two semi-crystalline samples, one with 2D crystalline order and the other with 3D order. The mechanism of structure evolution and effect of initial morphologies are discussed.

## 6.2. Experimental

### 6.2.1. Material

Poly(ethylene terephthalate) with intrinsic viscosity of  $0.74 \pm 0.02 \text{ dl.g}^{-1}$  – bottle grade, solid density of  $1.40 \text{ g.cm}^{-3}$  and approximate average molar mass,  $M_n$ , of  $20000 \text{ g.mol}^{-1}$  was used in this study.

### 6.2.2. Samples

The samples used in this work were prepared following the procedure described in a previous work [43]. In summary, PET pellets were compression moulded and quenched in order to obtain amorphous plaques. The plaques were cut with a dumbbell-like shape and uniaxially deformed in the rubbery state following a stretching programme, where stretching rate ( $\epsilon_{st} = 0.003$  and  $0.03 \text{ s}^{-1}$ ), stretching temperature ( $T_{st} = 90$  and  $110^\circ\text{C}$ ) and stretching ratio ( $\lambda_{st} = 1.6x$  and  $2.1x$ ) were varied. Different morphologies were obtained through this procedure: two quasi-amorphous, QA, and two semi-crystalline, SC, samples. These samples were then cut into rectangular tensile bars with the dimensions of: length of rectangular part of 25 mm and cross-section of  $4 \times 0.3 \text{ mm}$ , to perform the solid state deformation simultaneous to the *in situ* X-ray characterization.

Structural parameters of the initial samples, as revealed by WAXS analyses, are listed in **Table 6.1**. For clear identification of the samples, the following nomenclature has been adopted:

(i) quasi-amorphous samples, QA1 and QA2. The main differences between them are the orientation level and content of phase's mass fractions, in which QA1 has a greater amount of mesophase and slightly lower orientation level than the QA2.

(ii) semicrystalline samples, SC1 and SC2. The SC2 sample is more oriented than SC1, and shows a crystalline phase with 3D order, indicated by the meridional crystalline peak reflection (-103), while in case of SC1 this peak is absent, showing a 2D crystalline order.



**Table 6.1.** Structure parameters calculated from the 2D WAXS patterns.

Samples	Parameter								
	$f_{av}$	$f_{am}$	$f_c$	Amor [%]	Meso [%]	Cryst [%]	Crystallite size		
							(100) [Å]	(010) [Å]	(-103) [Å]
QA1	0.05	0.28	-	64.7	35.3	0.0	-	-	-
QA2	0.07	0.30	-	88.3	11.7	0.0	-	-	-
SC1	0.18	0.55	0.58	28.4	34.6	37.0	24	38	-
SC2	0.47	0.67	0.65	36.5	23.2	40.3	20	36	26

( $f_{av}$  - average polymer orientation;  $f_{am}$  - amorphous phase orientation;  $f_c$  - crystallite orientation; Amor – amorphous phase, Meso – mesophase, Cryst – crystalline mass fraction, (100), (010) and (-103) crystalline plains)

### 6.2.3. Solid state stretching and *in situ* WAXS characterization

Solid state stretching was carried simultaneously to *in situ* WAXS experiments under synchrotron radiation at HASYLAB, DESY, Hamburg (A2 soft condensed matter beam-line) with incident X-ray beam, monochromatized by reflection from a bent Ge (111) single crystal ( $\lambda=0.15$  nm). A Microtester, micro-universal testing apparatus, developed by our group [44] was used to perform the uniaxial stretching. The PET samples were clamped between jaws of the Microtester (distance between tie bar 25 mm) with its centre positioned perpendicularly to the X-ray beam, at a sample-to-detector distance of 135 mm and the stretching direction pointing upward. The Microtester was employed in tensile mode with simultaneous movement of the grips apart from each other to the maximum stretching ratio of 1.5x, the limit of apparatus. The stretching protocol was as follows:

- (i) clamp the sample in the stretching machine and start the deformation process (typical stretching rate of  $10^{-3}$  s $^{-1}$ );
- (ii) after some deformation the stretching was ceased and allowed a 2 min pause at constant strain,
- (iii) in meanwhile acquire the 2D WAXS pattern with an accumulation time of 20 s,
- (iv) restore the stretching procedure.

This step wise procedure results in some molecular relaxation that affects the morphology development. The comparison between the continuous and step wise protocols was reported elsewhere [45]. The use of step wise result in higher level of amorphous phase orientation, in case of both morphologies, as related to a better rearrangement of the mesophase during the relaxation over the interrupted deformation period. On the other hand stretching stopping contributes for better defined 2D WAXS patterns.

The WAXS was calibrated with the different diffractions of a crystalline PET sample. Background scattering was subtracted and all plots were normalized with respect to the incident X-ray intensity, accumulation time and specimen thickness. Actual specimen's thickness was obtained by first approximation of a homogeneous deformation, in which sample thickness changes with the stretching ratio,  $\lambda$ , according to the following equation [46]:

$$t = t_0 \lambda^{-1/2} \quad (6.1)$$

where  $t$  – actual sample thickness and  $t_0$  – initial sample thickness.

#### **6.2.4. WAXS data analysis**

##### **6.2.4.1. Phase mass fraction**

The two linear intensity profiles, taken along the equatorial and meridional directions from the 2D WAXD patterns were used to estimate mass fractions of the phases. A peak-fitting program using a Gaussian function was used to deconvolute the phase's peaks. Studied samples have two different particular morphologies: a) quasi-amorphous and b) semi-crystalline. Therefore, two specific data analyses procedures were adopted for the calculations of the phase's mass fractions. These methodologies are described below:

##### *a) quasi-amorphous morphologies, QA*

The morphology of QA samples was assumed to consist of two main phases: (i) amorphous – isotropic phase and (ii) mesophase - anisotropic phase with degree of packing and order between the crystalline and the amorphous. The amount of amorphous phase was assumed to be proportional to the area of the linear meridional profile. The subtraction of the amorphous fractions from the total area in the equatorial profile was proportional to the amount of the mesophase. The mass fractions of the individual phase were taken as the ratio of the area for each phase to the total area of the equatorial profile. As the strain increases, the WAXS patterns can exhibit a pair of meridional mesomorphic reflection (10-3) at about  $2\Theta = 25.8^\circ$  [7, 40], indicating conformational regularity, and called periodical mesophase, PM. At this stage of deformation the QA samples morphologies were considered to be composed of three phases: (i) amorphous (ii) mesophase and (iii) periodical mesophase – mesophase with conformational periodicity perpendicular to the stretching direction. The area of fitted (10-3) peak profile was used to determine the mass fraction of the PM. The sum of the area convoluted under the equatorial intensity profile and the meridional (10-3) peak was assumed to be the total area. The

mass fractions of the individual phase were taken as the ratio of the area for each phase to the total area.

*b) semi-crystalline morphologies, SC*

The morphology of initially SC samples was assumed to contain three distinct phases [31]: (i) amorphous – isotropic phase, (ii) mesophase - which has a degree of packing order between the crystalline and the amorphous phase, and (iii) a crystalline (triclinic) phase. The amount of crystalline phase was assumed to be proportional to the total area of the deconvoluted peaks: (010) at  $2\theta = 17.3^\circ$ , (-110) at  $2\theta = 22.5^\circ$ , and (100) at  $2\theta = 25.7^\circ$  from the linear equatorial profile, whereas, the amount of the unoriented amorphous phase was assumed to be proportional to the area of the linear meridional profile. When a crystal diffraction peak was detected in the meridional profile, i.e. (-103) at around  $2\theta = 26^\circ$ , its area contribution was excluded [31]. The subtraction of the crystalline and amorphous fractions from the total area of the equatorial profile was considered to be proportional to the amount of the mesophase. The mass fraction of the individual phases was taken as the ratio of the area for each phase to the total area of the equatorial profile.

**6.2.4.2. Polymer molecular orientation**

*a) average polymer molecular orientation*

The WAXS patterns were integrated along an azimuthal angle of  $\mu = 0 \div \pi/2$  ( $\mu = 0$  at equator), over a section with a  $2\Theta = 13 \div 28^\circ$ , in order to calculate the average polymer molecular orientation,  $f_{av}$ . That sector encloses all possible crystal reflections of crystallographic planes, isotropic amorphous phase and mesophases of PET [14]. The Hermans' orientation function was used to evaluate the  $f_{av}$  [47]:

$$f = \frac{3\langle \cos^2 \phi \rangle - 1}{2} \tag{6.2}$$

where the  $\langle \cos\phi \rangle$  is defined as:

$$\langle \cos^2 \phi \rangle = \frac{\int_0^{\pi/2} I(\phi) \cos^2 \phi \sin \phi d\phi}{\int_0^{\pi/2} I(\phi) \sin \phi d\phi} \tag{6.3}$$

where  $\phi$  is the azimuthal angle, I is the diffracted intensity and  $\langle \cos\phi \rangle$  is the average angle that the normal makes with the principal deformation direction.

*b) amorphous phase molecular orientation*

Amorphous phase molecular orientation,  $f_{am}$ , was determined from the azimuthal scans obtained over  $\mu = 2\pi$  ( $\mu = 0$  at equator) between  $2\Theta$  values of  $19.3^\circ$  and  $20.8^\circ$  [18]. This annular ring is located between the (010) at  $2\theta = 17.3^\circ$  and (-111) at  $2\theta = 21.2^\circ$  crystalline reflections, that is an angular range where the amorphous peak is reasonably intense and has least overlap from the crystalline reflections, when such are present. The profiles were fitted to Gaussian peaks and a horizontal baseline. The width of the peak was used to calculate the  $f_{am}$  using (equation 6.2 and 6.3). The  $\langle \cos \phi \rangle$  was evaluated by the full-width at half maximum ( $\Delta\phi$ ) of the Gaussian peak intensity distribution, by  $\langle \cos \phi \rangle$  integrated between  $\pi/2$  and  $-\pi/2$  for each value of  $\Delta\phi$  from the relation:

$$I(\phi) = \exp\left(\frac{-4\phi^2 \ln 2}{\Delta\phi^2}\right) \quad (6.4)$$

*c) crystalline phase orientation*

Crystalline phase orientation,  $f_c$ , of PET in terms of the angle  $\sigma$  between the c-axis of the unit cell and the stretching direction can be characterized by the normal to the (-105) lattice plane as well as by using the three equatorial reflections (010), (-110) and (100) according to the Wilchinsky's method [48]. The (-105) reflection is found to occur at a large scattering angle,  $2\Theta = 43^\circ$  [14], which is out of the characterized sector. Using Wilchinsky's method [14, 48] to determine the crystallite orientation of PET, the  $\langle \cos \sigma \rangle$  can be calculated from the experimental  $\langle \cos \phi_{hkl} \rangle$  (equation 6.3) of the three equatorial reflections, by the following equation:

$$\langle \cos \sigma \rangle = 1 - A\langle \cos \phi_{010} \rangle - B\langle \cos \phi_{-110} \rangle - C\langle \cos \phi_{100} \rangle \quad (6.5)$$

where the parameters  $A = 0.8786$ ,  $B = 0.7733$  and  $C = 0.3481$  are derived from the triclinic crystal system [32]. The  $\langle \cos \phi_{hkl} \rangle$  values were obtained by equation 6.3 for each peak reflection and substituted in equation 6.5, in order to obtain  $\langle \cos \sigma \rangle$ , which was used to calculate the  $f_c$  by means of equation 6.2.

**6.2.4.3. Crystallite dimensions**

The apparent crystal sizes normal to the three crystalline reflections: (100), (010) and (-103), which are almost orthogonal to each other, were estimated by the analysis of the linear intensity profiles taken across the reflection peaks. The vector normal (100) is coincided with that of benzene stacking, the vector normal (010) is approximately parallel the benzene ring and the appearance of the (-103) peak indicates ordering along the stretching axis. Thus crystalline dimensions [31, 49, 50] was estimated using the Scherrer equation:

$$D_{hkl} = K\lambda/(\beta_{1/2} \cos\Theta) \quad (6.6)$$

where  $D_{hkl}$  represents the apparent lateral crystallite size of the  $hkl$  reflection plane,  $\beta_{1/2}$  is the full width at the half height of the diffraction peak  $hkl$  in radians, the shape factor  $K$  is set at 0.9 for polymer systems,  $\lambda$  is the X-ray wavelength ( $\lambda = 1.54 \text{ \AA}$ ), and  $\Theta$  is half of the diffraction angle. There is the possibility of lattice distortion, which would broaden the line width, leading to the underestimation of the crystal size. According to Kawakami et al. [49], based on work of Salem [2, 3], the contribution of the lattice distortion is likely to be small.

## 6.3. Results and discussion

### 6.3.1. Structural evolution from quasi-amorphous morphologies

**Figure 6.1** shows the evolution of the average polymer orientation,  $f_{av}$ , as a function of the strain applied, together with the 2D WAXS patterns acquired along the stretching process of QA samples. Both samples are following similar pathways on the  $f_{av}$  – strain curve and show similar 2D WAXS patterns. The curve follows a trend of three stages. In the first stage the average polymer orientation remains almost constant as the strain increases. Suddenly, there is a fast increase of the average polymer orientation, at relatively low change in strain, remarking the stage II. Finally, in stage III, a plateau on the orientation is reached, that is maintained till the end of the deformation process. These stages are identified in the **Figure 6.1** by I, II and III, respectively. Along the stage I there is no change in 2D WAXD patterns, remaining as a typical amorphous diffraction ring, which becomes with an elliptic like shape during the stage II and transforms into two diffused spots on the equator, which intensifies and reduces in area, during the stage III. In this stage, it is observed the emerging of the mesomorphic meridional reflection (10-3) peak. The results are suggesting an analogous way of structural evolution of QA morphology, despite the slightly greater orientation attained by QA2 in the stage III, perhaps due to the slightly higher initial orientation of this sample (see **Table 6.1**).

Equatorial and the meridional intensity vs.  $2\Theta$  profiles extracted from the 2D WAXS patterns are depicted in **Figure 6.2**. Distinct equatorial reflection peaks of amorphous PET, at about  $2\theta \approx 19^\circ$ , is observed for both QA samples till the end of stage I (**Figure 6.2(a)** and **(c)** for QA1 and QA2, respectively). As the stretching is progressing, in stage II, this peak intensifies and concentrates at an angle of  $2\theta \approx 20^\circ$ . During the stage III only an increase in intensity is observed. The meridional profiles, shown in **Figure 6.2 (b)** and **(d)**, undergoes an intensification of the isotropic (amorphous) meridional peak at about  $2\Theta \approx 18^\circ$  during stage I. In the stage II this peak shifts to a smaller angle around  $2\Theta \approx 16^\circ$ , following the appearance of the mesomorphic peak (10-3) at about  $2\Theta \approx 26^\circ$ . It is important to note that the shift observed in the equatorial profile from  $2\theta \approx 19^\circ$  to  $2\theta \approx 20^\circ$  is coincident with the appearance of the mesomorphic peak, in the meridional profile. The I- $2\theta$  profiles do not show any new feature along stage III.

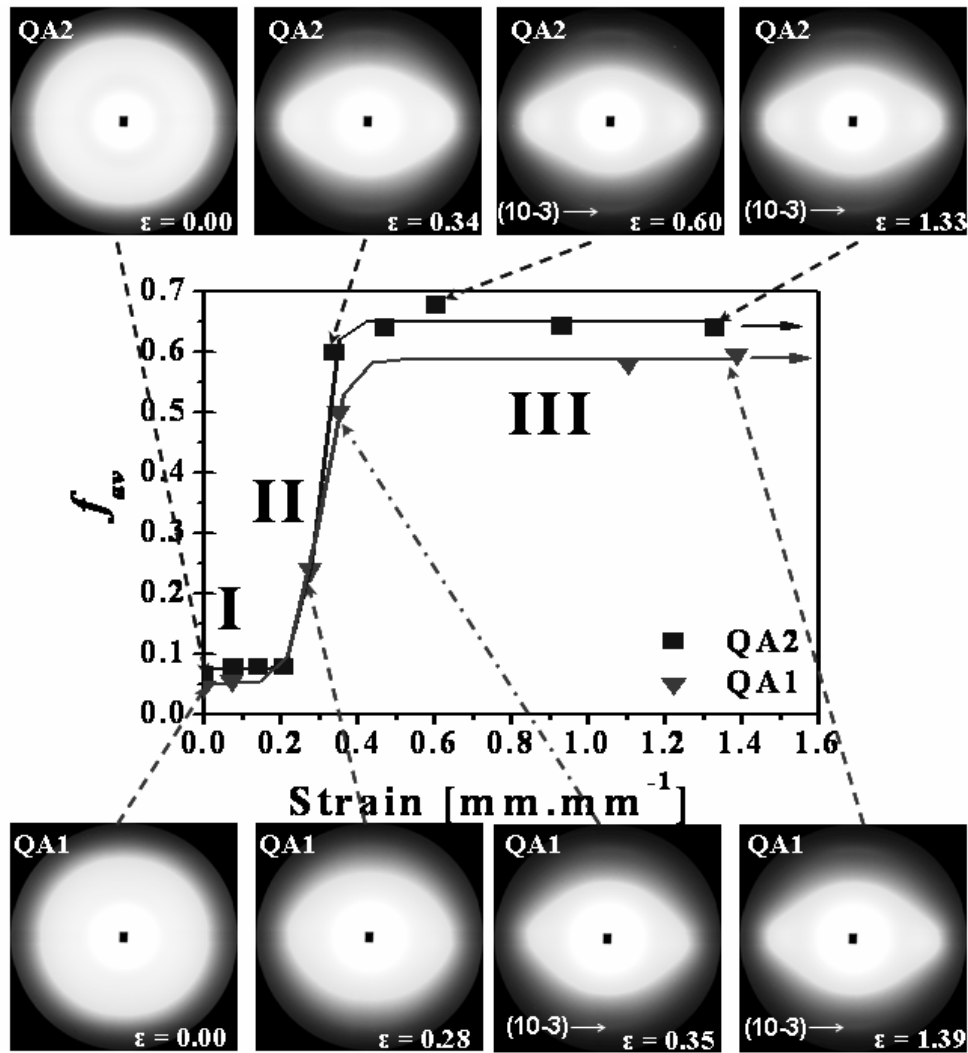


**Figure 6.1.** Average polymer orientation,  $f_{av}$ , evolution with strain and selected 2D WAXS patterns of samples QA1 and QA2. (fitted by Boltzmann function,  $R^2 = 0.99$ ).

Phase's mass fractions and amorphous phase orientation evolution as function of strain are plotted in the **Figure 6.3**, **Figure 6.3 (a)** corresponds to QA1 and **(b)** to QA2, respectively. As can be seen, the amorphous phase orientation evolution curves have identical shape with the average polymer orientation ones (**Figure 6.1**). The main features of phase's evolution are as follow: in stage I, there is a small decrease of amorphous phase due to its transformation into mesophase. In stage II, rapid transformation of great amount of amorphous phase into mesophase is observed and part of the mesophase is organized into periodical mesophase. Such fast phase transformations are taking place simultaneously to the rapid increase of amorphous phase orientation. Finally, in stage III, a higher content of ordered phases is observed, i.e. mesophase and periodical mesophase that reduce steadily in amount during strain, at constant maximum amorphous phase orientation level. This anticipates some destruction/conversion of the ordered phases during deformation (eventually by chain slippage).

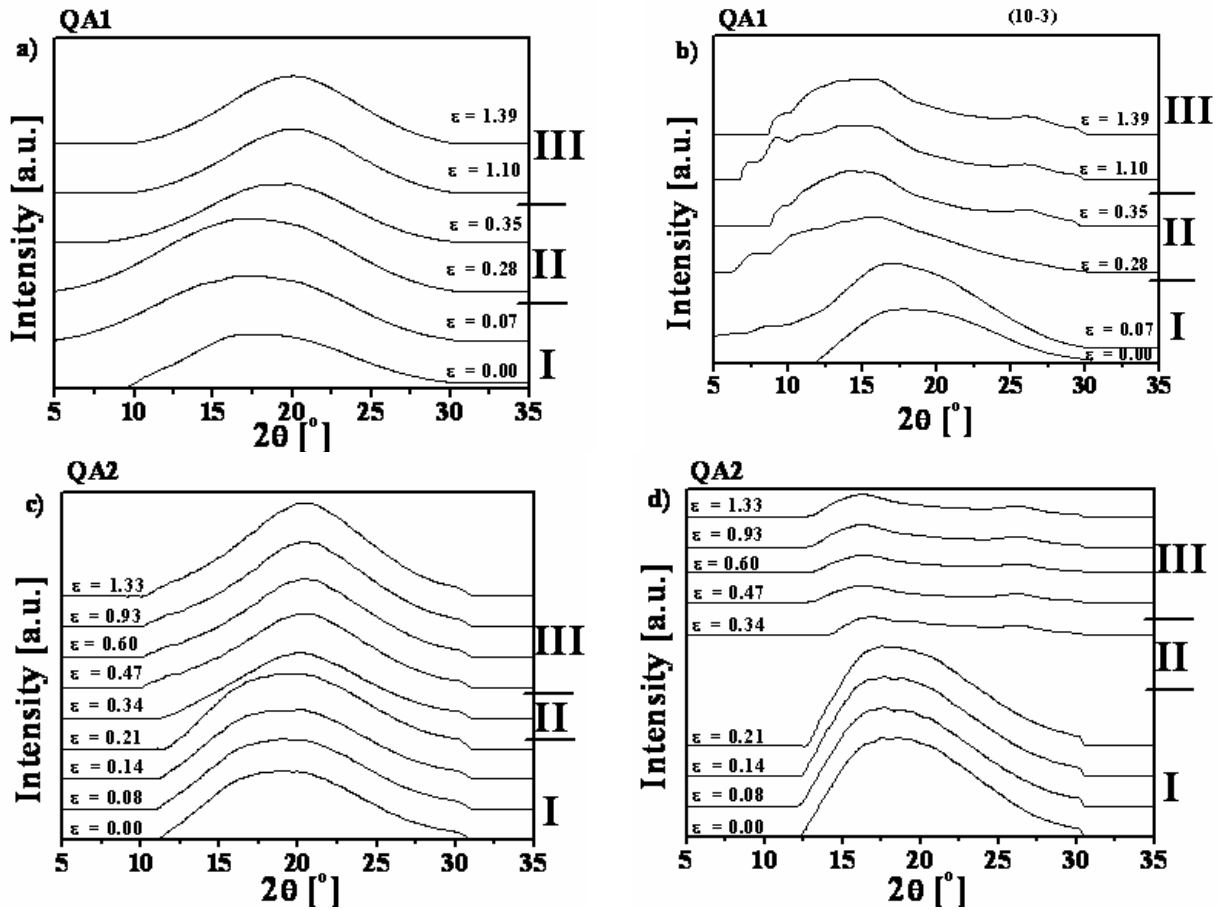


Figure 6.2. Linear intensity profiles extracted from 2D WAXS patterns: a) equatorial and b) meridional of QA1; c) equatorial and d) meridional of QA2.

The two QA samples are following the same trends, as described previously; nevertheless, since the initial portion of mesophase in QA1 was greater than in QA2 sample, it originated a greater amount of periodical mesophase, during stretching. In solid state, the deformation of QA morphologies did not lead to crystallization, but only to periodical mesophase formation, due to the low mobility of the polymeric chains.

The structural evolution during stretching in solid state of quasi-amorphous precursors can be summarized as follows: (i) Stage I, starts when the deformation is initiated and is characterized by a constant level of  $f_{am}$ , and no notable changes in the 2D WAXD patterns, remaining as a typical amorphous hallow. Only a small intensification of the equatorial and the meridional intensity profiles, at constant peak position, is observed together with a negligible amount of amorphous phase fraction transforming into mesophase. At the strain level applied in stage I, it would be expected an earlier transition of the stage I to stage II, due to neck formation. Thus the lack of structural evolution at such strains might be interpreted by the neck formation somewhere along the tensile dumbbell-like bar, out of the region where the 2D WAXS patterns were acquired. Nevertheless, it is expected the neck formation to lead to a slight polymer orientation, however that could be completely recovered when the stretching is stopped,

suggesting the absence of a long range network, which could constrain the amorphous chains from relaxing at this strain level in QA morphology. (ii) Further, stretching leads to the beginning of the second stage, stage II, which is characterized by a sharp increase of the amorphous orientation and by the appearance of two spots on the equator in the 2D WAXD patterns. The beginning of this stage is marked by the shift of the meridional peak position to minor angles, followed by the appearance of the meridional peak at about  $26^\circ$ , corresponding to the appearance of the periodical mesophase and by the simultaneous shift of the equatorial peak at  $2\theta \approx 19^\circ$  to  $2\theta \approx 20^\circ$  (marking already the end of this stage and the beginning of stage III) [10 40, 51]. The rapid increment of polymer chain orientation leads to a rapid phase transformation from amorphous to mesophase and the appearance of the first signs of organization of the mesophase into periodical one. This fast structural evolution can be attributed to the neck propagation along the centre of the tensile bar, where WAXS investigation was carried out. Thus the tensile bar lateral shrinkage induces a considerable polymer chains alignment into the stretching direction, resulting into much oriented/entangled amorphous phase, which is able to transform into mesophase. On the other hand, in consequence of neck propagation, a part of oriented mesophase evolves into periodical one, as result of its orientation and ordering. At this strain level, the polymer chains relaxation is hindered, during the stops of the stretching protocol, due to greater orientation of polymer bulk. The stage III starts when the polymeric chains achieve a plateau on the molecular orientation, which is maintained till the end of the stretching process. This stage is characterized by the presence of an equatorial peak at about  $2\theta \approx 20^\circ$ , and two meridional peaks corresponding to the isotropic and mesomorphic phases that are maintained with no position alterations in the intensity scans. Typical of this stage is ordered phases transformation into less ordered one, namely periodical mesophase into mesophase and respectively mesophase into highly oriented amorphous one. This may be the result of relaxation that is taking place during stretching stops or of the destruction of ordered phases during the progress of deformation (e.g., by chain slippage). In terms of macro deformation, this stage is related to the tensile bar homogeneous deformation through necking propagation.



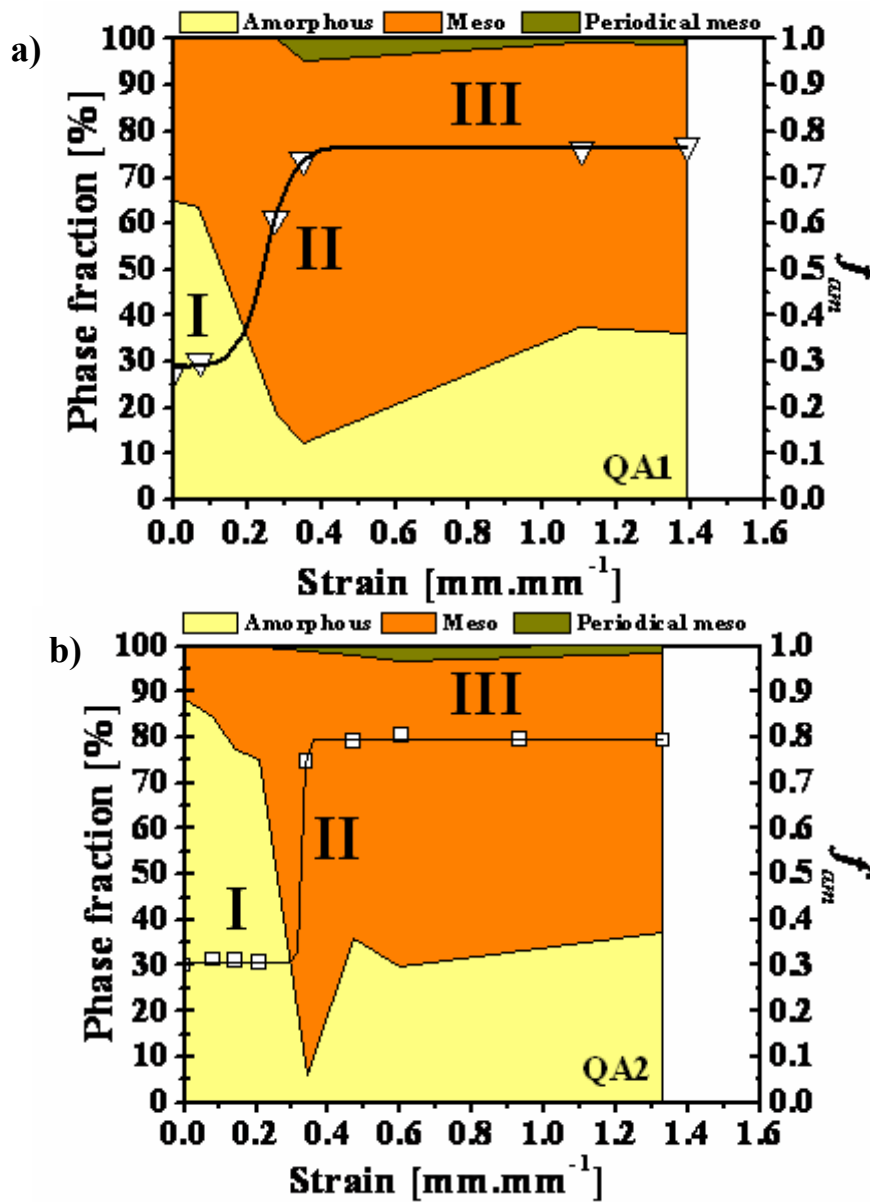


**Figure 6.3.** Phase's mass fractions and amorphous phase orientation,  $f_{am}$ , evolution of samples: a) QA1 and b) QA2. (fitted by Boltzmann function amorphous phase orientation curves,  $R^2 = 0.99$ ).

### 6.3.2. Structural evolution from semicrystalline morphologies

The average polymer orientation evolution with strain, for both SC specimens, is depicted in **Figure 6.4**, with respective 2D WAXD patterns. As observed, there is a considerable difference in the behaviour of both samples that is caused by the difference in the initial morphological state of each one (see **Table 6.1**). For SC1, originally having a 2D crystalline order, the average polymer orientation evolves through three distinct stages, likewise to QA ones. On the other hand, in specimen SC2 with 3D crystalline order, the average polymer orientation increases linearly as the deformation is applied.

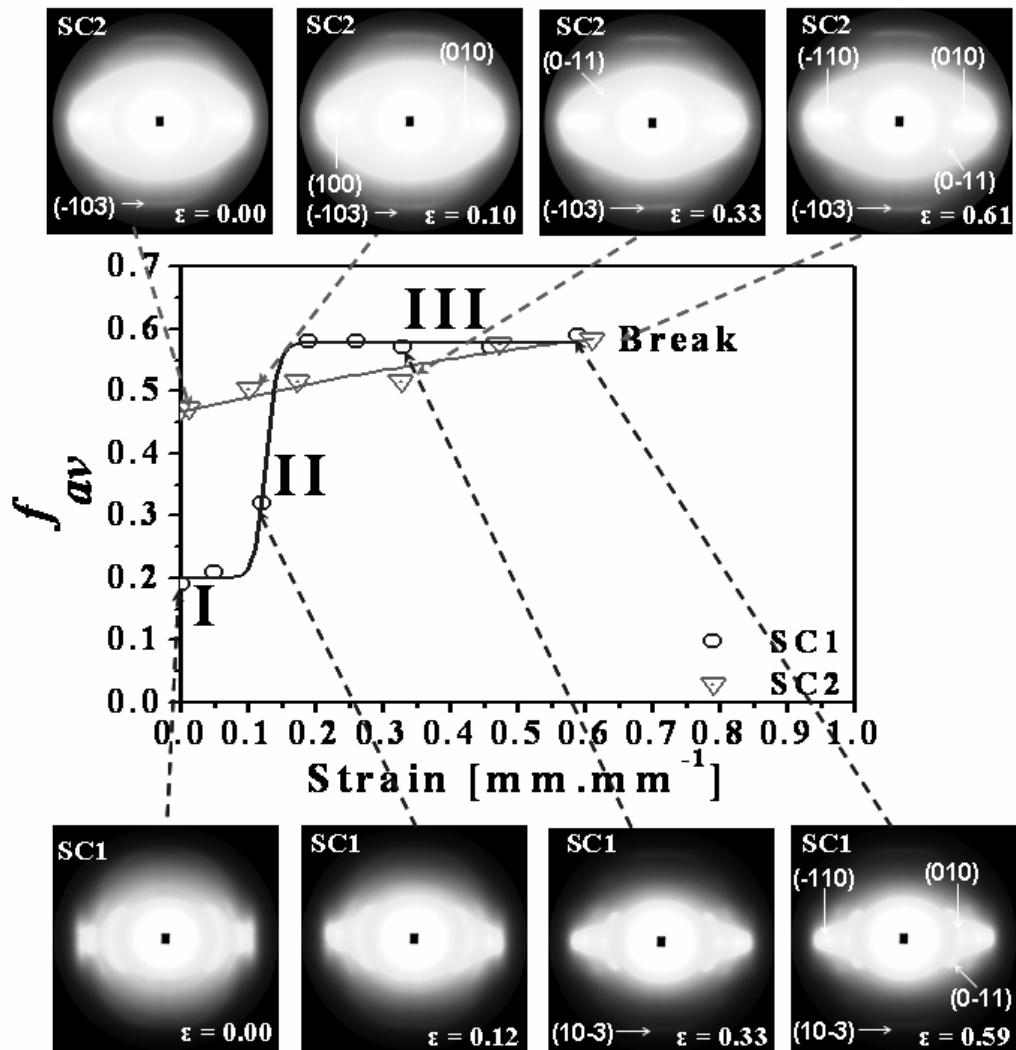


**Figure 6.4.** Average polymer orientation,  $f_{av}$ , and selected 2D WAXS patterns collected during the stretching of SC1 (fitted by Boltzmann function,  $R^2 = 0.99$ ) and SC2.

SC1 stages can be defined as follow: i) stage I, occurring at initial part of deformation, features a constant level of orientation, with no notable change in the 2D WAXS patterns, ii) stage II follows with a sharp increase of orientation level, for small changes of deformation. In addition there is the intensification of the three main equatorial crystalline reflections, i.e. (010), (-110), (100), of 2D WAXS patterns, and iii) finally, stage III, begins when the sample reaches the plateau of maximum level of orientation along with the intensification of the principal PET peak reflections, and the emergence of the (-103) meridional peak. This meridional peak is referred as descriptive of the 3D crystalline order [42, 49].

SC2 sample average polymer orientation rises continuously with the strain till breakage of the tensile bar occurs. The 2D WAXS patterns show intensification of PET reflections as well as the appearance and definition of other reflections.

Different initial morphologies of SC1 and SC2 lead to unequal pathway of evolution, but to similar final level of average polymer orientation. Moreover, SC1 develops a 3D crystalline order likewise SC2.

Equatorial and meridional intensity profiles of SC1 and SC2 are shown in **Figure 6.5**. In SC1, three distinct PET unit cell reflections are visible, i.e. (010) at  $2\theta = 17.3^\circ$ , (-110) at  $2\theta = 22.5^\circ$ , and (100) at  $2\theta = 25.7^\circ$ . These peaks correspond to the lattice planes parallel to the molecular c-axis of PET triclinic unit cell [14]. SC2 shows (010), (-110) and (100) reflection, however (-110) and (100) reflections appear overlapping as a result of the tendency of the crystallographic plane (100) to align preferentially to the stretching direction [51]. Observing the meridional intensity profiles, it might be noted that SC2 (**Figure 6.5 d**) exposed a small peak reflection assigned to the (-103) plane of unit cell (at  $2\theta = 26^\circ$ ) indicative for 3D crystalline order, which is only appearing in stage III of SC1's I-  $2\theta$  profiles. In common for both SC I- $2\theta$  profiles evolution is the intensification of the equatorial and meridional profiles with stretching progress.

Evolution of I- $2\theta$  profiles of the SC1 sample is described by stages as follows: the main characteristics of stage I is shift of the meridional peak to the lower angle and its narrowing; further stretching leads to start of stage II, where meridional peak narrows and alters to about  $2\theta=16^\circ$ ; along the last stage, stage III, its beginning is marked by appearance in the meridional profiles of (-103) crystalline peak reflection, at about  $2\theta = 26.8^\circ$ , while the isotropic peak narrows without alteration of its position. Further stretching, along stage III, leads to slight alteration of both meridional peaks positions, i.e. isotropic to angle of about  $2\theta=16.3^\circ$  and crystalline one respectively to around  $2\theta=26.3^\circ$ .

SC2 equatorial profiles evolution (**Figure 6.5c**) is distinguished by amplification of the (-110) peak at strain of  $0.47 \text{ mm.mm}^{-1}$ . On the other hand, the meridional profile features a broad isotropic peak around  $2\theta=16^\circ$  and a weak crystalline peak (-103) at about  $2\theta=26.2^\circ$  (see also **Figure 6.4**). This peak moves during the stops of stretching protocol, evidencing the crystallite longitudinal order changes and its sensibility to macromolecular chains extension/relaxation.

Phase's mass fraction, as well as the amorphous and crystalline phases orientation evolution with deformation, for both semicrystalline samples are shown in **Figure 6.6**. During stage I, SC1 sample features an increase of the amorphous phase mass fraction as a result of some mesophase relaxation concomitant with a decrease upon the crystalline phase orientation is also observed. Thereafter, both amorphous and crystalline phases orientation increase until the end of stage II, being accompanied by the reduction of the amorphous phase mass fraction and the increase of mesophase. Along Stage III, the amorphous and crystalline phase's orientations are maintained constant at its maximum level. A small decrement of the mesophase mass fraction is observed due to its transformation into amorphous phase at alike crystalline phase content, similar to the QA morphologies

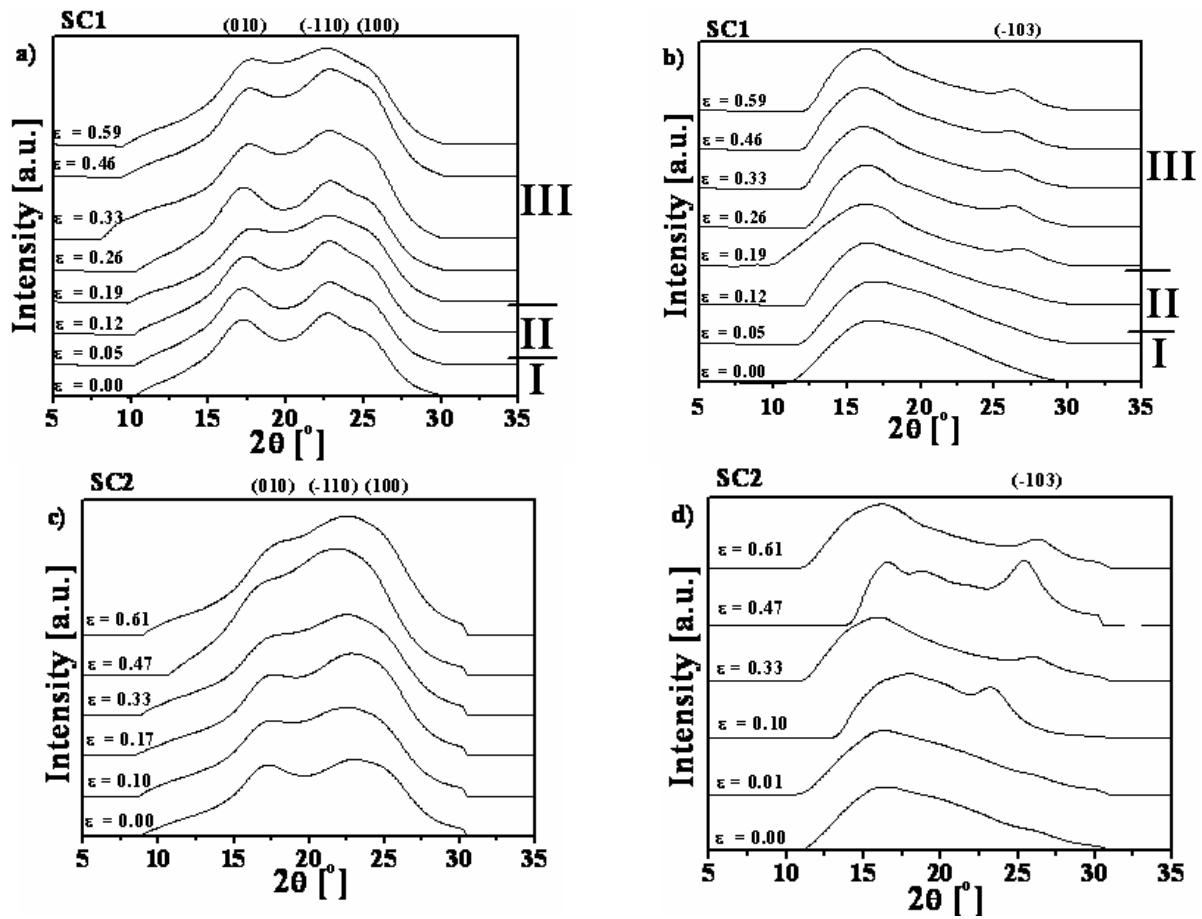


**Figure 6.5.** Linear intensity profiles extracted from 2D WAXS patterns: sample SC1 a) equatorial and b) meridional, and sample SC2 c) equatorial and d) meridional.

In the case of SC2 (**Figure 6.6b**), it is observed the continuous increase of mesophase content with strain due to amorphous phase fraction reduction and some crystalline phase relaxation, which is concomitant to the steady increase of amorphous and crystalline phase orientation levels until sample breakage. At ultimate strain levels, just before rupture, minor increase of crystalline phase is observed, as a result of a mesophase reduction; also some mesophase relaxation into amorphous phase is taking place. The 3D crystalline order of SC2 hinders chains relaxation, leading to a linear increase of the polymer bulk orientation (both amorphous and crystalline phases) levels with strain progress. In contrast, for sample SC1, such behaviour is only observed during stage III, when the crystalline phase reaches the 3D order.

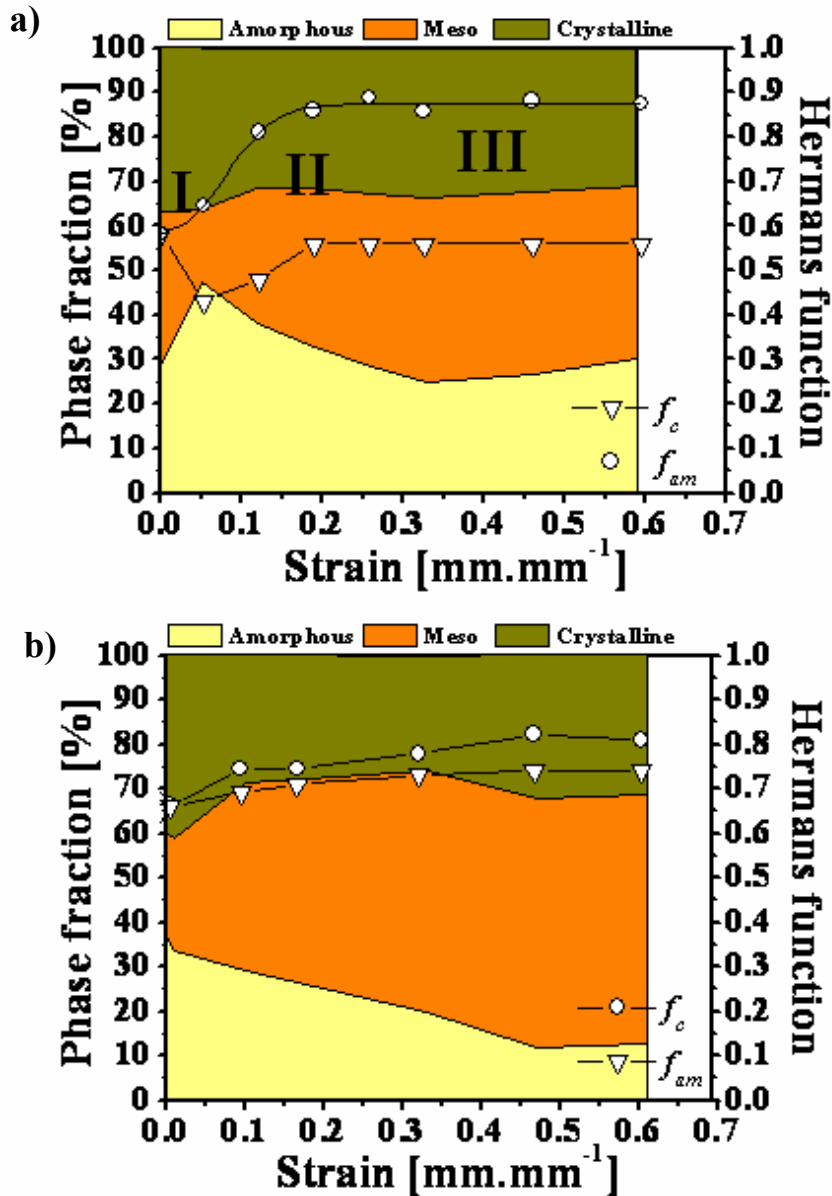


**Figure 6.6.** Phase's mass fractions and amorphous,  $f_{am}$ , and crystalline,  $f_c$ , phases orientations evolution for samples: a) SC1 ( $f_{am}$  results fitted by Boltzmann function,  $R^2 = 0.99$ ) and b) SC2

The apparent crystal sizes normal to the three crystal reflections planes (100), (010) and (-103), were estimated by the analysis of the linear intensity profiles taken across the reflection peaks, using the Scherrer equation (eq. (6.6)). These results are shown in **Figure 6.7 (a)** and **(b)** for SC1 and SC2 samples, respectively. The three chosen reflections planes are almost orthogonal to each other, thus marking the average lateral sizes of the crystallites induced by deformation.

The SC1 samples crystallites sustain the following directional changes along the stages (**Figure 6.7a**): Stage I - the crystallites show two dimensional order with no change on its dimensions. Crystallites become slightly larger along the stage II. This may be attributed to some rotation of the benzene rings within the crystallites. The start of stage III is marked by appearance of (-103) peak corresponding to longitudinal order (3D crystalline order), which

causes shrinkage of frontal plane (100) at stable lateral size (010), due to rearrangement of the benzene stacking. Along the stage III, the crystallites undergo reorganization by a slight frontal enlargement, followed by longitudinal contraction, till sample breakage.

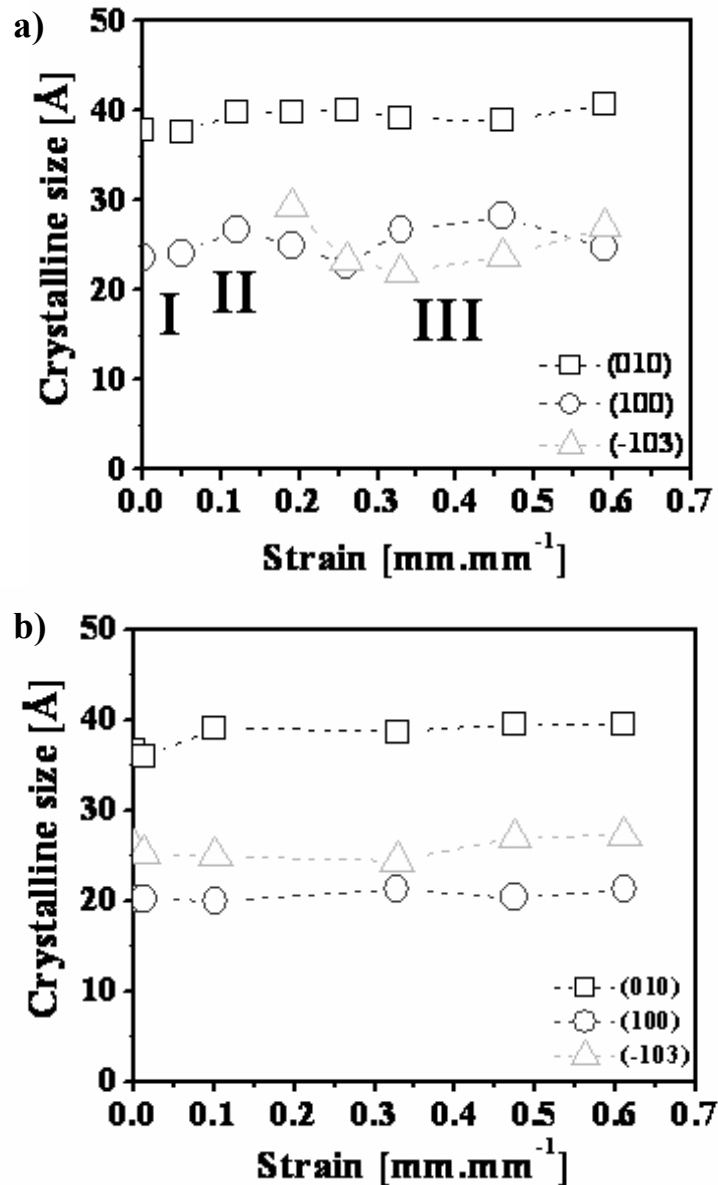


**Figure 6.7.** Changes of estimated crystal size from three nearly orthogonal planes (010), (100) and (-103) calculate by Scherer equation during uniaxial deformation of: a) SC1 and b) SC2.

The SC2 has a crystalline phase with three dimensional order, from the start, defined by the crystalline reflection (-103). In this case, there is a slight laterally enlargement of (010) during the first steps of stretching protocol, followed by stable crystallite sizes till sample breakage (**Figure 6.7b**).

Crystallites with 2D order prior to deformation (samples SC1) result in significant variation of its size along stretching protocol, whereas with 3D crystalline order (SC2 morphology) shows only slight change of its size.

The solid state structural evolution of semicrystalline morphologies that have not reached the 3D crystalline order (SC1) can be summarized as follows:

Stage I corresponds to a stable average polymer orientation level, while the amorphous phase orientation rapidly increases and orients. This behaviour is occurring during the first stop of deformation of the step deformation applied and is associated to the mesophase relaxation. The crystalline orientation level declines along the stage I, but the crystalline phase content does not change, as well as the crystallite sizes. This might be related to a taut polymer bulk, causing a decrement of the crystallite orientation. In terms of macroscopic deformation, during stage I, neck forms somewhere along the tensile bar, out of incident point of X-ray beam, contributing to the relatively poor structural evolution. During stage II, neck propagates and the X-ray beam coincides on that region. The average of amorphous and crystalline phase orientation rises rapidly, causing a decrease of amorphous phase due to its transformation into mesophase. Crystallites with 2D order, enlarge slightly in the frontal (010) and lateral (100) sides. Stage III is characterized by a plateau of maximum orientation level, i.e. average, amorphous and crystalline phases orientation, at alike crystalline phase content. The mesophase fraction improves as a result of amorphous phase consumption. Such structure evolution is suggestive for deformation of tensile bar through necking. At the beginning of stage III, (-103) peak reflection appears, showing the formation of longitudinal order associated with frontal enlargement of the crystallites. At the last part of the stage III, crystallites feature longitudinal shrinkage till sample rupture.

The morphology of SC2 specimen with strain progress evolves by constant increase of the level of orientation (i.e. average polymer, amorphous and crystalline) promoting the evolution of intermediate mesophase as result of decline of amorphous phase at almost invariable crystalline phase content. Such behaviour might be attributed to immediate neck propagation and following homogeneous lengthening through necking.

### **6.3.3. Structural models**

Based on the experimental observations mentioned above, some structural models depicting the structural hierarchy or structural evolution mechanism from different initial morphologies, in the solid state, are proposed. In **Figure 6.8** it is represented the structural evolution mechanism for QA morphologies, whereas in **Figure 6.9** and **6.10**, the models for the SC precursors with 2D and 3D crystalline order are shown, respectively.

#### **6.3.3.1. Structural evolution from quasi-amorphous morphologies**

**Figure 6.8** represents the structural evolution of QA samples. At the initiation of deformation QA samples consist of slight oriented amorphous phase and mesophase, and their

proportion changes into more mesophase throughout stage I at constant orientation level. Stage I ends and stage II begins when the polymer chain orientation rapidly increases and a large amount of amorphous phase is transformed into mesophase. Since the orientation has increased, a small fraction of mesophase is developed into periodical mesophase, as a result of the overlapping of the mesophase chains perpendicular to the stretching direction. As deformation further proceeds, the polymer chains approach their extensibility limit, leading to levelling off of the average polymer orientation. This is called stage III. Here, a part of the periodical mesophase relaxes into mesophase and further into amorphous one, maintaining the same level of orientation. This can be explained by the untying of mesophase polymer chains surrounded by tight polymer bulk, which transforms them into highly oriented amorphous phase. These samples are not able to crystallize during deformation.

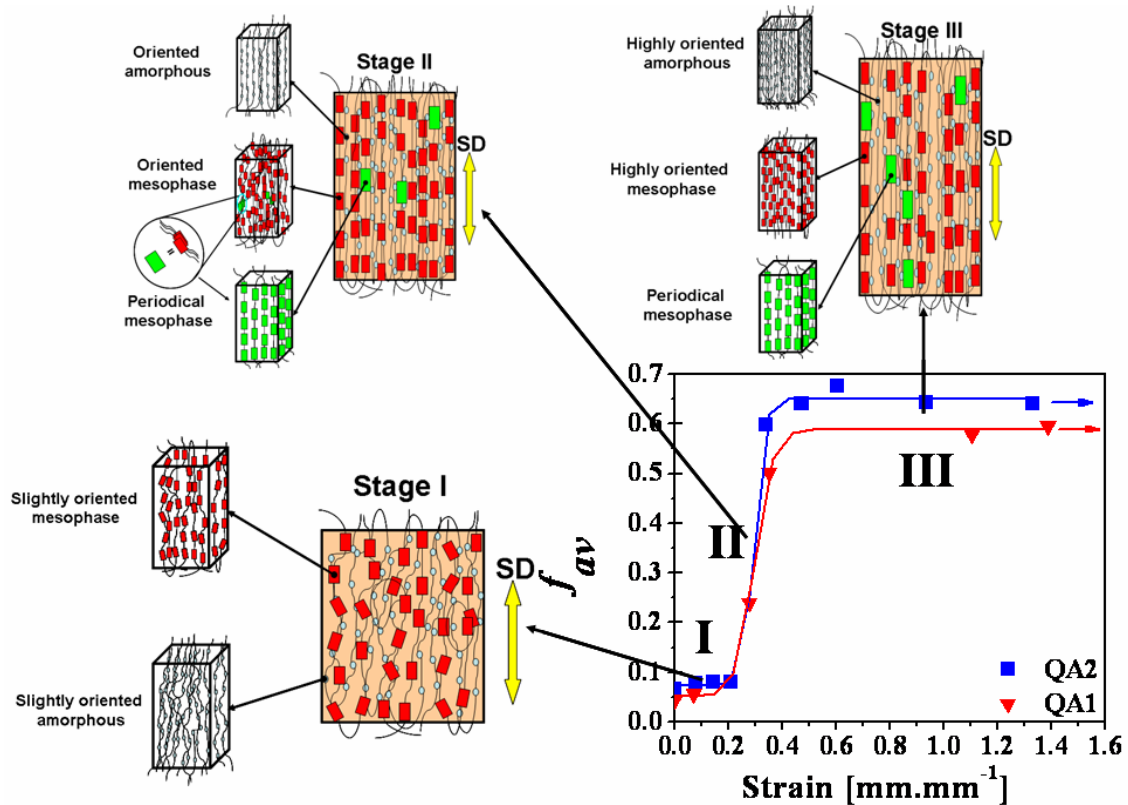


**Figure 6.8.** Schematic diagrams to illustrate the structure evolution during in solid state stop uniaxial stretching of PET with QA morphology.

### 6.3.3.2. Structural evolution from semi-crystalline morphology with 2D crystalline order

The mechanism responsible for the strain-induced structural changes in the solid state of the SC sample with 2D crystalline order can be summarized using the structural model illustrated in **Figure 6.9**. Stage I is described by initially constant average polymer molecular orientation level, out of the necking region. As the stretching progresses, initially slightly oriented polymer bulk evolves by increasing amorphous phase portion due to some mesophase relaxation. A small



amount of crystalline phase also relax into mesophase. A raise in the average polymer orientation, leading to mesophase increase is observed in stage II, at necking. Along this stage crystallites feature enlargement of frontal and lateral sides parameters, owing to tightening of polymer amorphous matrix. Further stretching causes the polymer chains orientation approaching its extensibility limits that results in a plateau of maximum polymer orientation, recognized as stage III. This orientation level contributes for the development of 3D ordered crystalline phase and increment of mesophase, mainly because of amorphous phase transformation. Along, this stage the crystallites with 3D order grow into the stretching direction.

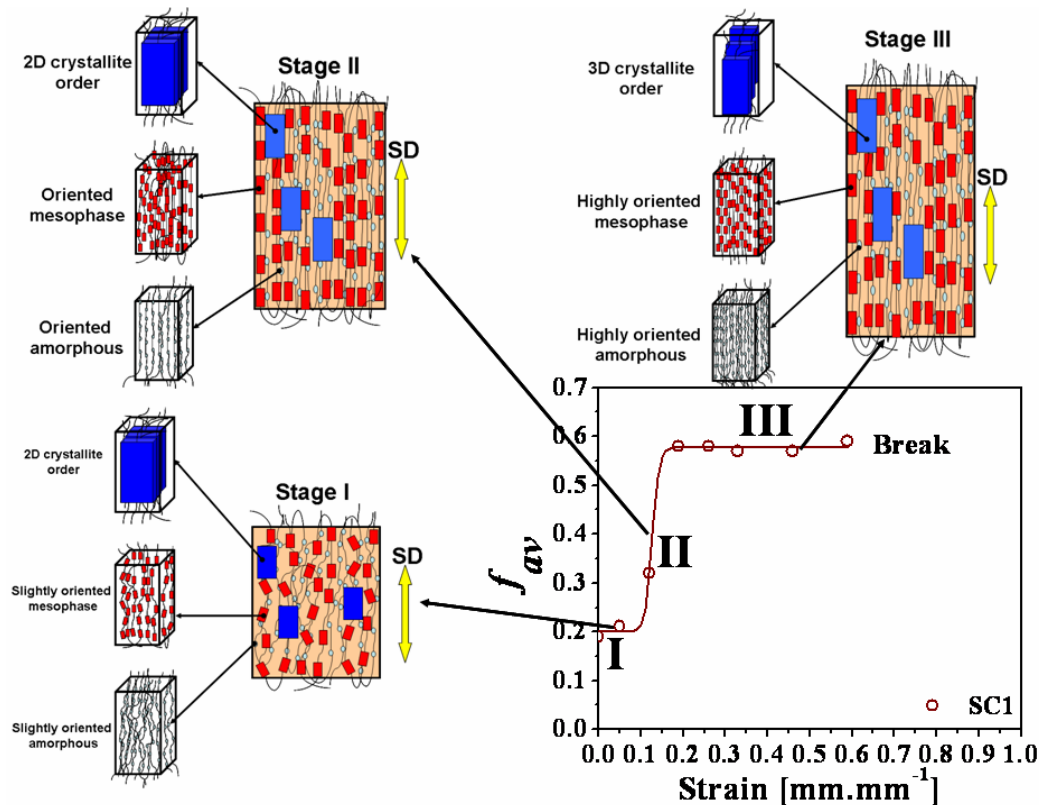


**Figure 6.9.** Schematic diagrams to illustrate the structure evolution during in solid state stop uniaxial stretching of PET with SC morphology with 2D crystalline order.

### 6.3.3.3. Structural evolution from semi-crystalline morphology with 3D crystalline order

For SC2 samples with 3D crystalline order, the structure evolution and average polymer orientation with strain progress is illustrated in **Figure 6.10**. The strain-induced phase transitions involved mainly mesophase formation from oriented amorphous phase and some from crystalline phase relaxation. Average polymer orientation increases with the increase of strain, until maximum chain extensibility is reached. During the first steps of the stretching protocol crystallites laterally enlarge, where after feature a stable crystallite size till sample rupture.

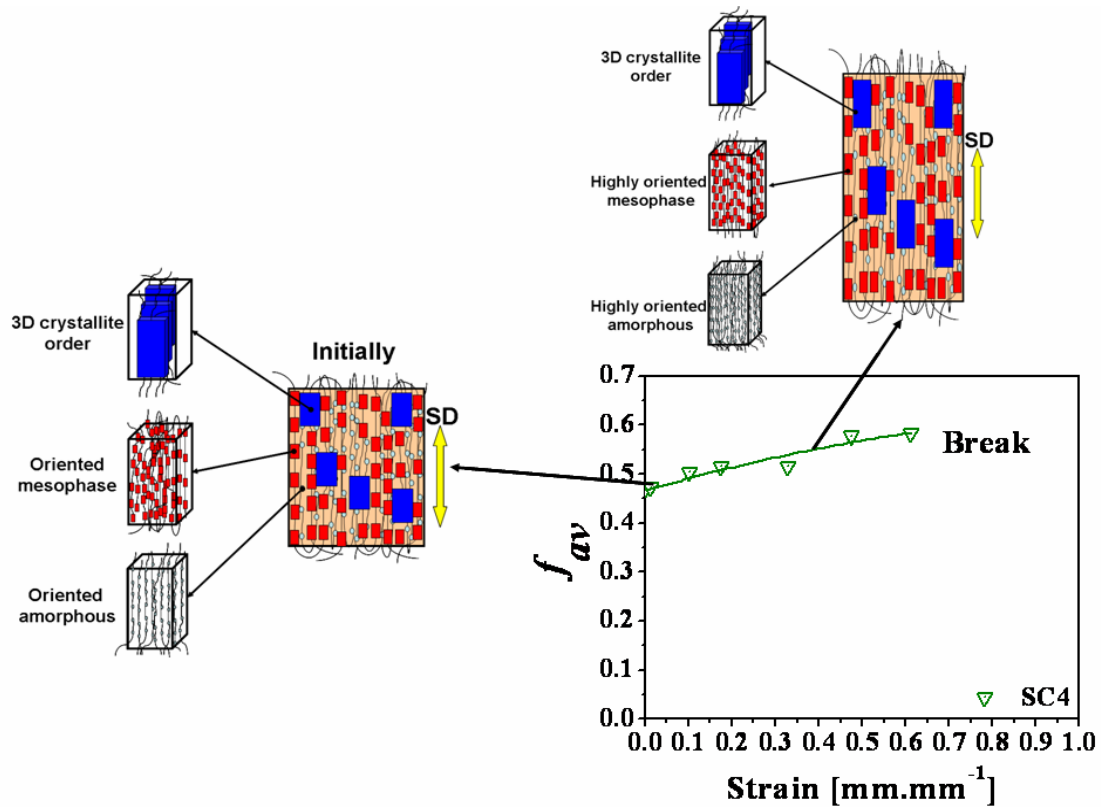


**Figure 6.10.** Schematic diagrams to illustrate the structure evolution during in solid state stop uniaxial stretching of PET with SC morphology with 3D crystalline order.

## 6.4. Conclusions

The evolution of strain-induced phase transition and average polymer molecular orientation with strain increment was investigated for different initial morphological states of PET. Quasi-amorphous, QA, and semicrystalline, SC, morphologies show distinct structure evolutions during stretching. Distinct structural models were proposed for each type of initial morphology, interpreting the obtained experimental results.

Solid state structural evolution upon deformation is strongly dependent on the initial state of the material. Initially amorphous samples evolve into highly oriented ones that are not able to crystallize, although a high level of average polymer molecular orientation is achieved. They are formed of highly oriented chains in different phases (amorphous, mesophase and periodical mesophase) whose mass fractions evolve during stretching, as a result of subsequent chain stretching/slippage and relaxation phenomena. A semicrystalline precursor gives rise to a final structure where a 3D crystalline order is attained, even when starting with 2D crystalline order. In all cases, the final average molecular orientation level attained is independent of the initial morphological state. Its evolution follows three stages, for any kind of samples that has not achieved a 3D crystalline order: firstly there is a small plateau of constant molecular orientation (stage I) until neck formation; followed by quick rise (stage II), that then stabilizes in a new plateau of maximum molecular orientation during necking propagation through the specimen

(stage III). For 2D crystalline precursor, crystallite size enlarges during initial deformation stages, and then evolves due to rearrangements of benzene ring stacking during stretching. A 3D crystalline precursor (SC2) leads to a continuous evolution of the average molecular orientation with strain until break, without almost no crystalline phase evolution.

Initially morphological distinct PET samples show different structural evolutions during stretching and also markedly distinct mechanical behaviours.

## 6.5. References

1. Fakirov, S., *Handbook of Thermoplastic Polymers: Homopolymers, Copolymers, Blends, and Composites*. 2002: WILEY-VCH Verlag GmbH, Weinheim.
2. Salem, D.R., *Crystallization kinetics during hot-drawing of poly(ethylene terephthalate) film: strain-rate/draw-time superposition*. *Polymer*, 1992. **33**(15): p. 3189-3192.
3. Salem, D.R., *Development of crystalline order during hot-drawing of poly(ethylene terephthalate) film: influence of strain rate*. *Polymer*, 1992. **33**(15): p. 3182-3188.
4. Bonart, R., *Paracrystalline structures in poly(ethylene terephthalate)*. *Kolloid-zeitschrift and zeitschrift fur polymere*, 1966. **213** p. 1-11.
5. Bonart, R., *Crystalline and colloidal structures during elongation and plastic deformations*. *Kolloid Zeitschrift & Zeitschrift fuer Polymere*, 1969. **231**( (1-2)): p. 438-458.
6. Salem, D.R., *Crystallization during hot-drawing of poly(ethylene terephthalate) film: influence of temperature on strain-rate/draw-time superposition*. *Polymer*, 1994. **35**(4): p. 771-776.
7. Goschel, U., *Thermally stimulated structural changes in highly oriented glassy poly(ethylene terephthalate)*. *Polymer*, 1996. **37**(18): p. 4049-4059.
8. Salem, D.R., *Crystallization during hot-drawing of poly(ethylene terephthalate) film: influence of the deformation mode*. *Polymer*, 1995. **36**(18): p. 3605-3608.
9. Chevalier L, M.Y., *Identification of a strain induced crystallisation model for PET under uni- and bi-axial loading: Influence of temperature dispersion*. *Mechanics of Material* 2007(39): p. 596–609.
10. Ajji, A., et al., *Amorphous orientation of poly(ethylene terephthalate) by X-ray diffraction in combination with Fourier transform infra-red spectroscopy*. *Polymer*, 1995. **36**(21): p. 4023-4030.
11. Ajji, A., et al., *Orientation and structure of drawn poly(ethylene terephthalate)*. *Polymer*, 1996. **37**(16): p. 3707-3714.
12. Ajji, A., et al., *Orientation of Amorphous Poly(Ethylene Terephthalate) by Tensile Drawing, Roll-Drawing, and Die-Drawing*. *Polymer Engineering and Science*, 1997. **37**(11): p. 1801-1808.
13. Goschel, U., *Two-dimensional small-angle X-ray scattering studies on oriented poly(ethylene terephthalate) films*. *Polymer*, 1995. **36**(6): p. 1157-1165.
14. Goschel, U., K. Deutschert, and V. Abetz, *Wide-angle X-ray scattering studies using an area detector: crystalline orientation in semisrystaline PET structures*. *Polymer*, 1996. **37**(1): p. 1-6.
15. Goschel, U. and G. Urban, *Supermolecular structure of oriented and semicrystalline poly(ethylene terephthalate) as revealed by the electron density correlation function from small-angle X-ray scattering studies*. *Polymer*, 1995. **36** (19): p. 3633-3639.
16. Adams, A.M., C.P. Buckley, and D.P. Jones, *Biaxial hot drawing of poly(ethylene terephthalate): measurements and modelling of strain-stiffening*. *Polymer*, 2000. **41**(2): p. 771-786.
17. Smith, M.R., et al., *Detailed mapping of biaxial orientation in polyethylene terephthalate bottles using polarised attenuated total reflection FTIR spectroscopy*. *Polymer*, 2006. **47**(15): p. 5691-5700.
18. Gowd, E.B., et al., *Effect of molecular orientation on the crystallization and melting behavior in poly(ethylene terephthalate)*. *Polymer*, 2004. **45**(19): p. 6707-6712.
19. Morawiec, J., et al., *High-Strength Uniaxially Drawn Tapes from Scrap Recycled Poly(ethylene terephthalate)*. *Journal of Applied Polymer Science* 2002. **86**: p. 1426–1435.
20. Vigny, M., et al., *Study of the Molecular Structure of PET Films Obtained by an Inverse Stretching Process. Part I: Constant Speed Drawing of Amorphous Films*. *Polymer Engineering and Science*, 1997. **11**(37): p. 1785-1794.

21. Gorlier, E., J.M. Haudin, and N. Billon, *Strain-induced crystallisation in bulk amorphous PET under uni-axial loading*. Polymer, 2001. **42**(23): p. 9541-9549.
22. Dargent, E., J. Grenet, and A. Dahoun, *Evolution of Hot Strain Induced Crystalline Texture of Poly(Ethylene Terephthalate) Films*. Polymer Engineering and Science 1997. **37**(11): p. 1853-1857.
23. Martins, C.I. and M. Cakmak, *Control the strain-induced crystallization of polyethylene terephthalate by temporally varying deformation rates: A mechano-optical study*. Polymer, 2007. **48**: p. 2109-2123.
24. Mahendrasingam, A., et al., *Effect of draw ratio and temperature on the strain-induced crystallization of poly (ethylene terephthalate) at fast draw rates*. Polymer, 1999. **40**(20): p. 5553-5565.
25. Blundell, D.J., et al., *Orientation prior to crystallisation during drawing of poly(ethylene terephthalate)*. Polymer, 2000. **41**(21): p. 7793-7802.
26. Mahendrasingam, A., et al., *Influence of temperature and chain orientation on the crystallization of poly(ethylene terephthalate) during fast drawing*. Polymer, 2000. **41**(21): p. 7803-7814.
27. Blundell, D.J., et al., *Characterization of strain-induced crystallization of poly(ethylene terephthalate) at fast draw rates using synchrotron radiation*. Polymer, 1996. **37**(15): p. 3303-3311.
28. Chaari, F., M. Chaouche, and J. Doucet, *Crystallization of poly(ethylene terephthalate) under tensile strain: crystalline development versus mechanical behaviour*. Polymer, 2003. **44**(2): p. 473-479.
29. Chaari, F. and M. Chaouche, *Rheoptical Investigation of the Crystallization of Poly(ethylene terephthalate) under Tensile Strain*. Journal of Polymer Science: Part B: Polymer Physics 2004(42): p. 1915-1927.
30. Kolb, R., et al., *Investigation of the high speed spinning process of poly(ethylene terephthalate) by means of synchrotron X-ray diffraction*. Polymer, 2000(41): p. 2931-2935.
31. Kawakami, D., et al., *Mechanism of Structural Formation by Uniaxial Deformation in Amorphous Poly(ethylene terephthalate) above the Glass Temperature*. Macromolecules, 2003(36): p. 9275-9280.
32. Matthews, R.G., et al., *The effects of stress relaxation on the structure and orientation of tensile drawn poly(ethylene terephthalate)*. Polymer, 2000. **41**(19): p. 7139-7145.
33. Mahendrasingam, A., et al., *Observation of a transient structure prior to strain-induced crystallization in poly(ethylene terephthalate)*. Polymer, 2000(41): p. 1217-1221.
34. Mahendrasingam, A., et al., *Observations of structure development during crystallisation of oriented poly(ethylene terephthalate)*. Polymer, 2003. **44**(19): p. 5915-5925.
35. Kawakami, D., et al., *Superstructure Evolution in Poly(ethylene terephthalate) during Uniaxial Deformation above Glass Transition Temperature*. Macromolecules, 2006. **39**: p. 2909-2920.
36. Kawakami, D., et al., *New Insights into Lamellar Structure Development and SAXS/WAXD Sequence Appearance during Uniaxial Stretching of Amorphous Poly(ethylene terephthalate) above Glass Transition Temperature*. 2008. p. 2859-2867.
37. Daubley, R., C.W. Bunn, and B. C.J., *The crystal structure of polyethylene terephthalate*. Proceeding of the royal Society of London, Series A, Mechanical and Physical Science, 1954. **226**: p. 531-542.
38. Auriemma, F., et al., *On the mesomorphic form of poly(ethylene terephthalate)*. Macromolecules, 1992. **25**(9): p. 2490-2497.
39. Asano, T., et al., *Crystallization of oriented amorphous poly(ethylene terephthalate) as revealed by X-ray diffraction and microhardness*. Polymer, 1999. **40**(23): p. 6475-6484.
40. Parravicini, L., et al., *Crystallization of poly(ethylene terephthalate) (PET) from the oriented mesomorphic form*. Journal of Applied Polymer Science, 1994. **52**(7): p. 875-885.

41. Ran, S., et al., *Mesophase as the Precursor for Strain-Induced Crystallization in Amorphous Poly(ethylene terephthalate) Film*. *Macromolecules* 2002(35): p. 10102-10107
42. Kawakami, D., et al., *Mechanism of Structural Formation by Uniaxial Deformation in Amorphous Poly(ethylene terephthalate) above the Glass Temperature*. *Macromolecules*, 2003. **36**: p. 9275-9280.
43. Todorov, L.V., C.I. Martins, and J.C. Viana, *Structure development of poly(ethylene terephthalate) during uniaxial stretching above the glass transition temperature: study of the statistical influence of the stretching variables* *Journal of Applied Polymer Science*, 2010. **Online**.
44. Teixeira, D.S., et al., *Microtesting of micro-injection molded parts*, in *Micro Mechanics Europe 2007* University of Minho: Guimarães, Portugal. p. 345-352.
45. Todorov, L.V. and J.C. Viana, *Structure evolution of PET under step-wise and continuous deformation modes: the effect of stress relaxation on the strain-induced morphology*. *International Journal of Material Forming*, 2008. **Online**
46. Oultache, A.K., et al., *Orientation and relaxation of orientation of amorphous poly(ethylene terephthalate)*. *Polymer*, 2001. **42**(21): p. 9051-9058.
47. Stribeck, N., *X-Ray Scattering of Soft Matter*. 2007: Springer Berlin Heidelberg New York.
48. Wilchinsky, Z.W., *Measurement of orientation in polypropylene film*. *Journal of Applied Physics*, 1960. **31**(11): p. 1969-1972.
49. Kawakami, D., et al., *Structural formation of amorphous poly(ethylene terephthalate) during uniaxial deformation above glass temperature*. *Polymer*, 2004. **45**(3): p. 905-918.
50. Kawakami, D., et al., *Deformation-Induced Phase Transition and Superstructure Formation in Poly(ethylene terephthalate)*. *Macromolecules*, 2005. **38**: p. 91-103.
51. Alvarez, C., et al., *Structure-dynamics relationship in crystallizing poly(ethylene terephthalate) as revealed by time-resolved X-ray and dielectric methods*. *Polymer*, 2004. **45**(11): p. 3953-3959.



## CHAPTER VII

# Characterization of PET nanocomposites produced by different melt blending techniques

PET, based nanocomposites containing 3 wt.% of different nanoparticles (MontMorilloniTe - MMT; titanium dioxide -  $\text{TiO}_2$  and silica dioxide -  $\text{SiO}_2$ ) were prepared via two independent procedures: mechanical mixing with subsequent direct injection moulding, DIM, and mechanical mixing, followed by extrusion blending and injection moulding, EIM. The different contributions of three nanofillers at applied production procedures with respect to pure PET were evaluated. The incorporation of nanofillers reduces significantly the intrinsic viscosity of the polymer matrix when processed by DIM and EIM. SAXS results showed that: MMT layers were intercalated for both processing procedures, but slightly higher for EIM; a better dispersion in the polymer matrix with smaller agglomerates size is achieved for  $\text{TiO}_2$  and  $\text{SiO}_2$  nanoparticles for EIM than for DIM. According to the results of DSC analysis, all fillers behave as nucleating agents for PET except  $\text{SiO}_2$  that acts as inhibitor in case of DIM procedure. The mechanical behaviour was assessed in tensile testing at  $1.5 \text{ mm}\cdot\text{min}^{-1}$  (nominal strain-rate of  $0.0013 \text{ s}^{-1}$ ) and  $23 \text{ }^\circ\text{C}$ . The mechanical test revealed that the addition of nanoparticles have a slight influence on the elastic modulus and yield stress, but a drastic negative influence on the deformation capabilities of the mouldings. The measured optical properties of the mouldings gloss and haze are also strongly affected by the presence of nanoparticles agglomerates.

*This chapter is adapted from the following publication:*

Todorov L.V., Viana J.C. *Characterization of PET nanocomposites produced by different melt-based production methods*. Journal of Applied Polymer Science, Vol. 106, 1659–1669 (2007)



## **7.1. Introduction**

Nowadays one of the most widely used polyester as material for plastic packing (e.g. beverage bottles, cosmetic containers, food, pharmaceutical packaging) is poly(ethylene terephthalate), PET, because of their good mechanical, barrier and optical properties. PET is considered a high consumption polymer of important commercial interest. PET is a slowly crystallizing polymer that can be obtained with different degrees of crystallinity (0% to 50%) as a result of specific thermal and/or mechanical treatment to which it is submitted [1]. However, there is some tasting and quality problems of packaged products resulted from daylight exposure [2, 3]. Therefore, there is still room for improvement of the optical, barrier and mechanical properties of PET. One possible and very attractive alternative for this is the replacement of conventional unfilled materials with nanosized particle-filled PET (nanocomposites).

Nanocomposites are a new class of composites that are particle-filled polymers for which at least one dimension of the dispersed particles is in the nanometer range (less than 100 nm). One can distinguish three types of nanocomposites, depending on how many dimensions of the fillers are in the nanometer range. When the three dimensions are in the order of nanometers, we are dealing with isodimensional nanoparticles, such as fumed spherical silica, titanium dioxide nanoparticles and others [4-7]. Particles with two dimensions in the nanometer range form elongated structures, such as in the case of carbon nanotubes or cellulose whiskers [4, 5]. The third type of nanoparticles is characterized by only one nanosized dimension, the filler being in the form of platelets of one to a few nanometers thick of hundreds to thousands nanometers long (e.g. nanoclays such as MMT [8-12]. These materials are almost exclusively obtained by the intercalation of the polymer inside the galleries of layered host crystals or preferably by fully exfoliation of the layered crystals.

The macroscopic effects of the incorporation of nanoparticles to the polymer matrix are quite remarkable. For example, the mechanical properties, optical, barrier and fire resistant properties [4] of these new material systems are strongly enhanced depending upon the filler type, its level of concentration, its size, and the polymer production method [5].

Making good samples of polymer matrix nanocomposites is a challenging area that draws considerable efforts in the last years. Researchers have tried a variety of processing techniques to make polymer matrix nanocomposites. These include: exfoliation-adsorption; in situ interactive polymerization; template synthesis and other approaches [4, 8]. All listed production methods are complicated, rather difficult for industrial implementation and costly. A chosen route is melt blending techniques for direct preparation of polymer nanocomposites, such as extrusion and injection moulding, both well known industrial methods with vast practical use. But, if in one side the mixing capability in injection moulding is limited, subjecting the polymer at several

processing stages (extrusion then injection moulding) may induce polymer degradation, which may have a drastic effect on the properties and behaviour of the polymer based nanocomposite. However, injection moulding as direct processing method for production of polymer nanocomposites allow avoiding previous compounding stages (e.g. extrusion), which brings polymer degradation and additional production expenses.

In this work, the melt processing of PET nanocomposites based in different types of nanoparticles and processing methods is investigated. The selected nanoparticles were: nanoclay (MontMorillonite, MMT), fumed silica ( $\text{SiO}_2$ ) and fumed titanium dioxide ( $\text{TiO}_2$ ). Two production processes are used to mould the different types of PET nanocomposites: direct injection moulding and extrusion with subsequent injection moulding. Processing induced PET degradation is analysed. The thermal, mechanical and optical properties of the differently moulded PET nanocomposites are also compared.

## **7.2. Experimental**

### **7.2.1. Materials**

The PET – (reference S41T from Selenis S.A.) has a melt flow index of  $63.6 \pm 5.2$  g.10min<sup>-1</sup>. Different types of nanosized fillers were used:

- i) an organic modified nanodispersed layered silicate (MMT5) with a primary particle size 100x500x1 nm and interlayer distance of 2.8 nm (NANOFIL 5, distearyl-dimethyl-ammonium ion exchanged bentonite, from SUD-CHEMIE AG, Germany);
- ii) a highly dispersed hydrophilic fumed titanium dioxide ( $\text{TiO}_2$ ) with an average primary particle size of 21 nm (AEROXIDE  $\text{TiO}_2$  P25, from Degussa AG, Germany). The nanoparticles consist of approximately 80% anatase and 20% rutile [13].
- iii) a hydrophilic fumed silica ( $\text{SiO}_2$ ) with an average primary particle size of 12 nm (AEROSIL 200, from Degussa AG, Germany).

### **7.2.2. Preparation of PET nanocomposites**

The three PET nanocomposites, with contents of 3 wt.% of MMT5,  $\text{TiO}_2$  and  $\text{SiO}_2$ , respectively, were prepared via two independent preparation procedures:

- i) mechanical mixing with subsequent direct injection moulding, DIM,
- ii) mechanical mixing, followed by extrusion blending and injection moulding, EIM.

The nanofillers were independently added to PET dried pellets (with dry air at 170 °C for 5h) and were mechanical blending in a tumbler mixer for 15 min. The PET is very sensitive to thermal, oxidative degradation [14]. In order avoiding or reduction degradation during extrusion, some authors applied  $\text{N}_2$  atmosphere during extrusion, which is not applicable for IM process. In

this work we did not use, because we aimed at objective comparison (at same conditions) of both production procedures.

### 7.2.2.1. Extrusion blending

The blends were processed in a counter rotating twin-screw extruder. They were dried in a dry air dehumidifier at 170 °C for 5h before extruding. The temperature profile of the extruder ranged from 220 °C (at the feeder) to 245 °C (at the die). The screws speed was set at 15 rpm. The extruded material has been cooled from die temperature to room temperature at air ambient. Obtained blends were milled in conventional milling equipment.

### 7.2.2.2. Injection moulding

The PET nanocomposites were injection moulded in an ENGEL T45 machine. Before injection moulding PET blends were dried in a dehumidifier with dry air at 170 °C for 5h. The dried pellets were directly supplied to the injection moulding machine hopper (by a vacuum transport system) in order to avoid contact with room atmosphere. Two different types of mouldings were used:

- i) laterally gated rectangular plaques of 64x64x2 mm for optical studies,
- ii) dumbbell-like standard specimens of length of 50 and cross-section of 4x2 mm for mechanical testing.

All specimens were injection moulded with fixed processing conditions listed in **Table 7.1**.

**Table 7.1.** Injection moulding processing parameters.

$T_{inj}$ [°C]	$T_w$ [°C]	$P_h$ [bar]	$P_b$ [bar]	$V_{inj}$ [mm.s <sup>-1</sup> ]
280	15	35	30	40

( $T_{inj}$  - injection temperature,  $T_w$  - water temperature,  $P_h$  - holding pressure,  $P_b$  - back pressure and  $V_{inj}$  - injection speed)

These conditions have been chosen after series of preliminary experiments, and found to be as most appropriate in order to get a good dispersion of nanofillers. Relatively high backpressure ( $P_b = 30$  bar) has been used, increasing shearing actions during the plasticizing phase. A high injection velocity ( $V_p = 68$  mm.s<sup>-1</sup>) was also set up (corresponding to a injection flow rate of 28.3 cm<sup>3</sup>.s<sup>-1</sup>). Other process parameters were set as follow: screw rotation velocity (240 rpm), total plasticizing time (3.4 s) and total cycle time (32 s).

### 7.2.3. Determination of PET intrinsic viscosity

The intrinsic viscosity measurements were performed in order to evaluate polymer degradation caused by the several processing steps, according to ASTM D4603 standard [15]. This method allows the determination of the intrinsic viscosity of a PET sample by measuring the flow time of the solution with a single concentration using the Billmeyer equation (Eq. 1). An Ubbelohde type viscometer U 4944 2KRK was used. A solvent mixture composed of 60/40

phenol/1,1,2,2- tetrachloroethane was needed to prepare the PET solutions. The PET samples were previously ground in order to accelerate solubilization. Grounded materials were dried in an oven for 4 h at 170°C to avoid polymer hydrolytic degradation. The humidity presence causes rapidly decrease of equilibrium molar mass  $M_{ne}$  [14], which explains the need for careful polymer drying prior preparing of solutions. The polymer composites, prepared with corrected concentration (with 3wt.%) after complete dissolution, were centrifuged for 30 min at 3500 rpm and filtered in order to remove the formed nanofiller sediment. From the flow time of the pure solvent mixture and the known concentration of polymer solutions, it is possible to obtain the intrinsic viscosity,  $\eta$ , as follows:

$$\eta = \frac{0.25 \left( \left( \frac{t}{t_0} \right) - 1 + 3 \ln \left( \frac{t}{t_0} \right) \right)}{c} \quad (7.1)$$

where  $t$  is the flowing time of polymer solution (s),  $t_0$  is the flow time of pure solvent mixture (s), and  $c$  is the polymer solution concentration (g.dl<sup>-1</sup>).

#### **7.2.4. Characterization techniques**

##### **7.2.4.1. Small angle X-ray scattering, SAXS**

Injection moulded and extruded injection moulded samples were characterized by small angle X-ray scattering (SAXS). These experiments were performed under synchrotron X-ray radiation a X-ray synchrotron radiation (Ge (111)  $\lambda=0.15$  nm) at HASYLAB, DESY, Hamburg (A2 soft condensed matter beam-line). The specimens were positioned perpendicular to the incident X-ray beam with the flow direction pointing upward. For all conditions the distance between the sample and detector was at 1765 mm. Accumulation time was of 20 s. The two-dimensional SAXS patterns were acquired by a MARCCD camera. These patterns were integrated along the equatorial, being plotted Intensity- $2\Theta$  curves. Intensities were normalized with respect to the incident X-ray intensity, accumulation time and specimen thickness. The  $2\Theta$  scale was calibrated by means of rattail cornea. The angular and layer spacing values are related through the Bragg's law:

$$\lambda = 2d \sin \Theta \quad (7.2)$$

where  $d$  is spacing between diffraction lattice planes and  $\Theta$  is the measured diffraction angle. Characterization by SAXS was performed in a  $2\Theta$  range of 1 to 4°, corresponding to a lattice spacing range between 8.79 and 2.12 nm.

##### **7.2.4.2. Differential scanning calorimetry, DSC**

A Perkin Elmer DSC-7 running in standard mode was used. The temperature of the cold block was kept at 5°C and the nitrogen purge gas flow rate was 20 cm<sup>3</sup>.min<sup>-1</sup>. Temperature and enthalpic calibrations were carried out according to the DSC7 manual procedures (with indium and lead). The sample weight was around 9 mg for all materials analyzed and 50 ml aluminium

pan with holes were used. For evaluating the melting range, heating experiments were performed over all samples, from 30 to 270°C, at a heating rate of 20 °C.min<sup>-1</sup>. For these experiments, a base line was obtained with two empty pans, in the same working temperature range and with the same scanning rate.

Both cold crystallization and melting parameters were obtained from the heating scans. The glass transition temperature ( $T_g$ ) was identified too. Melting ( $T_m$ ) and cold crystallization ( $T_{cc}$ ) temperatures were considered to be the maximum of the endothermic and of the exothermic peaks of the thermographs, respectively. The fusion ( $H_m$ ) and the cold crystallization ( $H_{cc}$ ) enthalpies were determined from the areas of the melting peaks and crystallization peaks, respectively. The calculation of the relative percentage of crystallinity ( $\chi_c$ ) was based on a two-phase (crystalline–amorphous) peak area method [1], being given by:

$$\chi_c = \frac{\Delta H_m - \Delta H_{cc}}{\Delta H_f} \quad (7.3)$$

where  $\Delta H_{cc}$  is the enthalpy released during cold crystallization,  $\Delta H_m$  is the enthalpy required for melting and  $\Delta H_f$  is the enthalpy of fusion of 100% crystalline PET, taken to be equal [1] to 120 J.g<sup>-1</sup>. The reported results are the average of three samples.

#### 7.2.4.3. Mechanical characterization

The injection moulded dumbbell-like specimens were tested in a universal testing machine Zwick/Roell Z005 in tensile mode. The tests were performed at controlled room temperature of 23°C at a test velocity of 1.5 mm.min<sup>-1</sup> (nominal strain-rate of 0.0013 s<sup>-1</sup>). At least five specimens of each sample were tested. The mechanical properties envisaged were the elastic modulus (E), yield stress ( $\sigma_y$ ) and strain at break ( $\epsilon_b$ ).

#### 7.2.4.4. Optical properties

The optical properties measured were the gloss and haze. The gloss was measured at 20, 60, and 85° angles from the normal to the moulding surface, according to the ASTM D-523 standard [16], in a flat surface glossmeter Micro TRI-gloss (Gardner, Germany). Measurements were taken in triplicate for each sample from three mouldings of each formulation. All results are expressed as gloss units, relative to a highly polished surface of black glass standard with a value equal to 100. Haze was measured as per ASTM D1003 [17] using a Hazemeter XL-211 Hazegard (Gardner), in three samples of moulded material systems.

## 7.3. Results and discussion

### 7.3.1. Intrinsic viscosity

The effect of the processing route of the different PET nanocomposites on the intrinsic viscosity,  $\eta$ , are presented in **Table 7.2**. in terms of the percentage of reduction of  $\eta$  of the processed samples with respect to the virgin PET pellets.

**Table 7.2.** Percentage reduction of the intrinsic viscosity of the processed PET composite samples with respect to the pristine PET pellets.

Processing	Material	Percentage of reduction (%)*
Extruded	PET	5.18
	PET/MMT5	14.16
	PET/TiO <sub>2</sub>	14.40
	PET/SiO <sub>2</sub>	9.28
Injection moulded; DIM	PET	2.76
	PET/MMT5	11.80
	PET/TiO <sub>2</sub>	5.84
	PET/SiO <sub>2</sub>	17.68
Extruded injection moulded; EIM	PET	10.90
	PET/MMT5	12.09
	PET/TiO <sub>2</sub>	18.92
	PET/SiO <sub>2</sub>	21.98

(Percentage of reduction:  $[(\eta_{pristine} - \eta_x)/\eta_{pristine}] \times 100$ ; where  $\eta_x$  is the intrinsic viscosity of each of the processed specimens and  $\eta_{pristine}$  of pristine PET granules)

The intrinsic viscosity values are related to the average molecular weight by means of the Mark-Houwink equation. In case of extrusion and injection moulding of pure PET, the most important polymer degradation mechanism proposed was the oxidation process leading to chain scission [18]. During extrusion, as more complex melt-blending technique, the following processes may occur simultaneously: 1) hydrolysis and condensation (the predominating process depends on the water content); 2) trans-esterification, cycle formation; 3) thermal degradation by ethylene-ester rearrangement; 4) thermal degradation by decomposition of weak points (diethylene glycol); 5) chain scission resulting of oxidation at high oxygen concentration and 6) crosslinking resulting of oxidation at low oxygen concentration. On other hand, oxidation was drastically diminished in the case of injection moulding: the polymer was totally confined, but the anaerobic thermal degradation could also occur [18]. As can be observed in **Table 7.2.**, for the selected processing setup, the extrusion of PET resulted in higher reduction of  $\eta$  as compared to DIM (a difference of 2.42%). Similar results have also been already reported [14, 19]. The EIM samples are revealing the highest degradation, as would be expectable due to the extended processing history. Additional to degradation caused by processing could be adjoin moisture coming from the specific surface of the milled material being much greater than that of pellets which could cause some hydrolytic degradation [20].

The PET nanocomposites show greater reduction on  $\eta$  for all the studied samples as compared to pure PET for same production procedure. This means that PET nanocomposites are more sensitive to degradation than pure PET. In literature could be find works confirming decreasing of viscosity with increasing concentration of inorganic contents in filled polymers [9,

14]. From the results of **Table 7.2.**, it might be evaluated the different contribution of three nanofillers type at applied production procedures. Sanches-Solis et al. [9] had suggested that slip between the polymer and filler due to low friction of smooth plates and high shear heating during the melt-compounding process are reasons for elevated degradation. On one hand, MMT5 is causing higher degradation for extrusion rather than in EIM and DIM procedures. On the other hand, TiO<sub>2</sub> showed the lowest reduction on the intrinsic viscosity for DIM and respectively similar but significant higher variations for the extrusion and EIM process. Similar trend was obtained for MMT5, but seems that TiO<sub>2</sub> is less sensitive to the thermal degradation taking part during injection moulding. The decreasing of the intrinsic viscosity of the polymer with increasing TiO<sub>2</sub> concentration after extrusion was already reported elsewhere [21]. SiO<sub>2</sub> based nanocomposites are revealing similar behaviour as pure PET but showing greater percentage variation values. In case of SiO<sub>2</sub> based PET nanocomposites, the lowest  $\eta$  variation occurs for extrusion and the highest belongs to EIM. For all the cases EIM samples show a higher variation of  $\eta$ , and then higher polymer degradation, as already above mentioned. PET degradation seems to be a complex process strongly dependent upon the processing history and filler type (e.g., nature, size).

### 7.3.2. X-ray diffraction studies

**Figure 7.1.** shows the SAXS patterns for the PET systems produced by both production procedures. For the directly injected MMT5 samples, a peak appear at approximately  $2\Theta = 2.72^\circ$  ( $d = 3.25$  nm) (**Figure 7.1.a**), corresponding to the basal interlayer spacing of the (001) plane of MMT5. Pristine MMT5 shows a basal gallery distance of 2.8 nm ( $2\Theta = 3.15^\circ$ ). This slight increase in the intergallery spacing indicates that intercalation of MMT5 occurred, and that the interlayer space of clay increased by 0.45 nm. Therefore obtained nanocomposite is intercalated. Applying of EIM procedure causes slight improved intercalation of MMT5, which is confirmed by shift of a peak at  $2\Theta = 2.69^\circ$  ( $d = 3.28$  nm). The relative intensity provides information on the number of scattering structures, regardless of whether they are oriented aggregates or individual sheets. Peak broadness provides information on the scattering domain size distribution (by Scherrer equation). Broader peaks correspond to smaller scattering domains, sharper peaks to larger domains. The SAXS pattern for MMT5 composite processed by EIM presents a relative intensity decrease and a 4.8% broader intercalation peak with respect to the DIM's one, which indicates higher number of exfoliated clay plates [21]. However, any of used production procedures was sufficient to produce completely exfoliated MMT5 polymer nanocomposites (lattice spacing higher than 8 nm) [8].

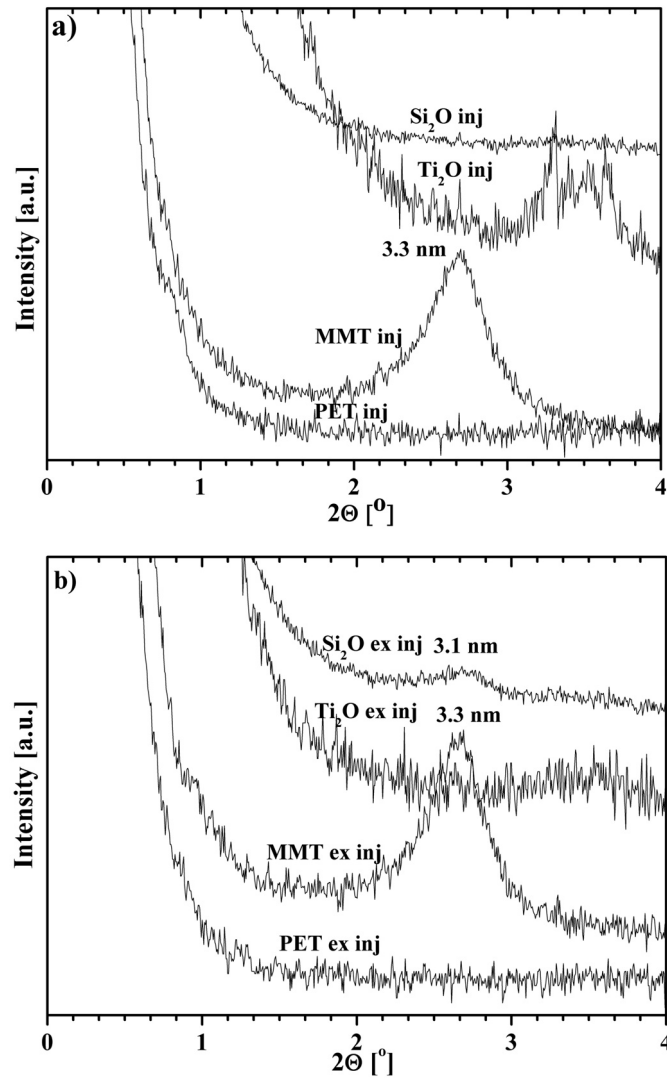


**Figure 7.1.** SAXS patterns for PET and PET composites processed by: a) direct injection moulding (*inj*) and b) by extrusion-injection moulding (*ex inj*).

The SAXS patterns of the TiO<sub>2</sub> filled injection moulded nanocomposites shows crystalline peaks at  $2\Theta = 3.5^\circ$  and  $2\Theta = 3.8^\circ$ , this peaks in belongs to the anatase structure of titania nano powder and a smaller quantity of rutile, which qualitatively agrees with the crystallographic composition (80% anatase, 20% rutile) of the nanopowder [13]. These peaks are narrower in the case of EIM (**Figure 7.1**) due to the decreased size of scattering domains.

For the SiO<sub>2</sub> filled injection moulded samples (**Figure 7.1.a**), X-ray diffraction pattern did not registered any visible peak in the studied scattering vector range. However, in the case of EMI of SiO<sub>2</sub> based PET composites (**Figure 7.1.b**) a peak may be observed at approximately  $2\Theta = 2.68^\circ$  (3.1 nm). This peak could be attributed to the formation of periodic agglomerates of small SiO<sub>2</sub> crystals that are separated by circa 3.1 nm, as a result of better filler dispersion and orientation inducing during processing.



### 7.3.3. Differential scanning calorimetry, DSC

Figure 7.2. presents the DSC thermograms of the pure PET and its nanocomposites processed by the different methods.

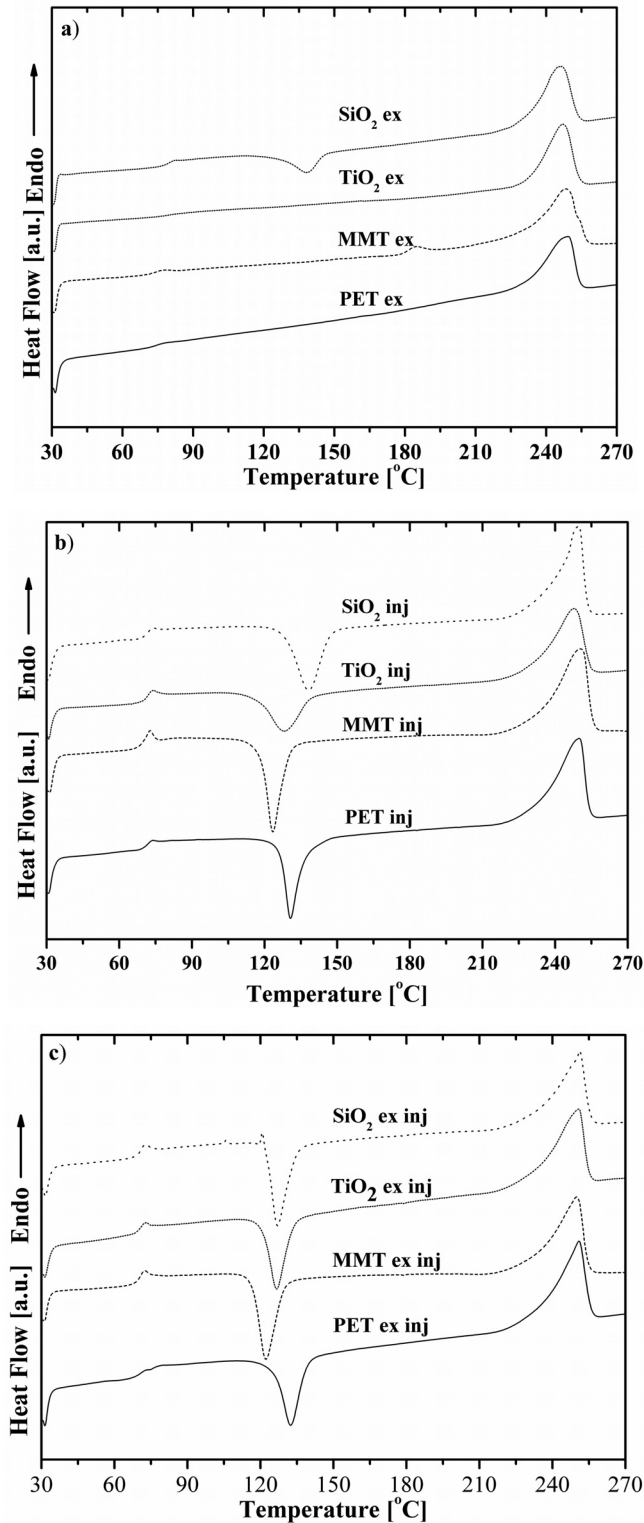


**Figure 7.2.** DSC thermograms at  $20\text{ }^{\circ}\text{C}\cdot\text{min}^{-1}$  for PET and PET composites processed by: a) extrusion (ex); b) injection moulding (inj) and c) by extrusion-injection moulding (ex inj).

The values of the glass transition temperature,  $T_g$ , cold crystallization peak temperature,  $T_{cc}$ , enthalpy of cold crystallization,  $H_{cc}$ , melting peak temperature,  $T_m$ , enthalpy of melting,  $H_m$  and degree of crystallinity,  $\chi_c$  (calculated from eq. 3) are listed in **Table 7.3**.

As observed in **Figure 7.2a)** and also in **Table 7.3.**, the thermograms of extruded material show no presence of cold crystallization peak. This reveals that these specimens are already crystallised as a result of the lower cooling rates to which they have been subjected.

A decrement on  $T_g$  could be traced in all used production procedures (in average about  $1^\circ\text{C}$ ) relatively to pure PET.  $T_g$  tends also to decrease with the decrement on the size of nanoparticles for amorphous polymers [5]. This tendency is more visible for the extrusion process. Adding of MMT5 decreases  $T_g$  by  $1.1^\circ\text{C}$ ; use of  $\text{TiO}_2$  by  $-1.6^\circ\text{C}$  and use of  $\text{SiO}_2$  by  $-2.2^\circ\text{C}$ . These variations are less expressive when materials are injected or extrusion-injection moulded. On the other hand, MMT5 composites have lower  $T_g$ :  $-1.9^\circ\text{C}$  and  $-2.6^\circ\text{C}$  in the case of DIM and EIM with respect to pure polymer for the same production techniques, which could be explained by the presence of intercalated MMT5. Difference influence on the  $T_g$  may be caused by dissimilar amount of intercalated phase which is lower for DIM. Other works also report that MMT5 concentration larger than 2 wt.% cause a decrease on  $T_g$  [5, 10]. Moreover, the role of nanofillers should be considered as complex involving shape, nature, particle size effects and interactions between those.

**Table 7.3.** DSC calculated parameters.

Processing	Material	$T_g$ [ $^\circ\text{C}$ ]	$T_{cc}$ [ $^\circ\text{C}$ ]	$\Delta H_{cc}$ [ $\text{J}\cdot\text{g}^{-1}$ ]	$T_m$ [ $^\circ\text{C}$ ]	$\Delta H_m$ [ $\text{J}\cdot\text{g}^{-1}$ ]	$\chi_c$ [%]
Extruded	PET	74.6	-	-	249.2	39.2	32.7
	PET/MMT5	73.5	-	-	248.3	44.8	37.4
	PET/ $\text{TiO}_2$	73.0	-	-	248.1	39.2	32.7
	PET/ $\text{SiO}_2$	72.4	-	-	248.8	44.3	37.0
	Var. (%)	3.1	-	-	0.4	14.3	14.3
Injection moulded. DIM	PET	71.4	130.7	23.6	249.9	42.6	15.8
	PET/MMT5	69.5	123.5	25.6	250.3	45.8	16.8
	PET/ $\text{TiO}_2$	71.0	128.2	20.8	247.7	39.4	15.5
	PET/ $\text{SiO}_2$	71.0	138.2	24.0	249.7	39.9	13.2
	Var. (%)	2.6	11.9	23.2	1.1	16.3	27.2
Extruded injection moulded. EIM	PET	72.0	132.4	26.1	250.9	42.9	14.0
	PET/MMT5	69.4	122.2	29.8	249.9	45.4	13.0
	PET/ $\text{TiO}_2$	70.0	126.7	25.8	250.7	45.5	16.4
	PET/ $\text{SiO}_2$	70.2	127.1	27.1	251.2	44.2	14.3
	Var. (%)	3.9	8.3	15.6	0.5	6.2	26.7

( $T_g$  – glass transition temperature,  $T_{cc}$  - cold crystallization peak temperature,  $H_{cc}$  - enthalpy of cold crystallization,  $T_m$  - melting peak temperature,  $H_m$  - enthalpy of melting,  $\chi_c$  - degree of crystallinity (equation 1 with  $H_f = 120 \text{ J/g}$  [1]); Var - percentage of variation [(max - min)/min]).

The presence of nanofillers strongly affects  $T_{cc}$ . In DIM the use of MTT5 decreases  $T_{cc}$  by  $7.2^\circ\text{C}$ , magnitude also reported by other authors [10]; the use of  $\text{TiO}_2$  decreases  $T_{cc}$  by  $2.5^\circ\text{C}$ . These decrements upon  $T_{cc}$  mean that these nanofillers act as nucleating agents for the crystallization process [19]. Single increasing effect on  $T_{cc}$  was evidenced by adding  $\text{SiO}_2$

nanoparticles with subsequent DIM, with an increment of 7.5 °C, corresponding to a crystallization inhibitor activity. On the other side, for the PET SiO<sub>2</sub> composite produced by EIM the filler acts as nucleating agent, decreasing  $T_{cc}$ . This may be attributed to the presence of smaller nanoparticle agglomerate size and its better dispersion in polymer matrix achieved during extrusion [11, 19, 22], and supported by the SAXS data (**Figure 7.1.**). In fact, this nucleating agent effect was observed in all EIM moulded PET nanofilled composites leading to a decrease on  $T_{cc}$ . For EIM samples, MMT5 is again the filler with main contribution, decreasing  $T_{cc}$  by 10.2 °C [10]; TiO<sub>2</sub> reduces  $T_{cc}$  by 5.7 °C and SiO<sub>2</sub> by 5.3 °C. Published results manifest also a close relation between nucleation effect and the filler particles nature and dimensions [10, 11, 19].

The different morphological states of the specimens are mainly evidenced in the area of cold crystallization peak, which is characterized by a significant percent of variation (**Table 7.3.**). In a comparison at a fixed processing method, DIM of MMT5 and SiO<sub>2</sub> filled PET leads to an increment in  $\Delta H_{cc}$  of 8.7 % and 1.8 %, respectively. Ou et al. [11] also reported an increment of  $\Delta H_{cc}$  with increasing organonano clay concentration in PET nanocomposites. An augmentation of  $\Delta H_{cc}$  means that the material was initially less crystalline. It appears that adding MMT5 filler accelerates the crystallization kinetics but the developed crystalline structure is less crystalline, and on the other side SiO<sub>2</sub> acts as a crystallization inhibitor also reducing the degree of crystallinity. Conversely, the addition of TiO<sub>2</sub> decreases  $\Delta H_{cc}$  by 11.8 %, meaning an initially higher degree of crystallinity of the processed samples. On the other hand, EIM of MMT5 and SiO<sub>2</sub> increase  $\Delta H_{cc}$  by 13.4 % and 3.9 %, respectively. Adding of TiO<sub>2</sub> has almost no influence on  $\Delta H_{cc}$ .

Negligible variations on the melting peak position were detected in all production methods and nanofillers used. Exception is the incorporation in PET of TiO<sub>2</sub> that leads to a decrease on  $T_m$  of 2.2 °C in the case of EIM and of 1.1 °C for extruded samples. Fray et al.<sup>7</sup> also observed a decrement of  $T_m$  with using similar nanofiller; but with a different amount of filler was used.

The absence of the cold crystallization peak corresponds to a higher degree of crystallinity ( $\chi_c$ ) of extruded PET nanocomposite. MMT5 and SiO<sub>2</sub> fillers increase  $\chi_c$  [10] by 4.7 %, but not affecting the TiO<sub>2</sub> based nanocomposite. Injection moulding samples present always a lower  $\chi_c$ . MMT5 composites show a slight increasing of  $\chi_c$  for DIM, but a reduction in the case of EIM. The intercalation of MMT5 produces an obstacle on the mobility of the macromolecular chains that is, the lamellar space of clay confines the molecular chains movements, which may reduce the ability to crystallize [23]. In fact, our results also point out to decrement of  $\chi_c$  with a greater amount of intercalated phase (e.g., EIM). DIM production of TiO<sub>2</sub> reflects no changes of

$\chi_c$ , but EIM causes an increment of 17.4 % that could be related to the decrease on the filler agglomerate size. The lowest  $\chi_c$  value (13.2%) for DIM processed samples belongs to SiO<sub>2</sub> nanofiller, that might be related to their crystallization inhibitor character. In the case of EIM, the presence of SiO<sub>2</sub> fillers does not change  $\chi_c$ .

#### **7.3.4. Mechanical Characterization**

**Figure 7.3.** presents stress-strain curves for DIM (**Figure 7.3a**) and EIM (**Figure 7.3.b**) specimens of PET and their nanocomposites. Assessed mechanical properties are listed in **Table 7.4**. Negligible influence on the pure PET initial modulus by production procedures is observed. The initial modulus, E, of PET/MMT5 composites processed by DIM and EIM also do not vary unlike pure PET. In literature, many works reported about a drastic increasing of E with increasing amount of MMT5 for exfoliated nanocomposites [8-10]. This similar contribution of both production procedures may be due to the lack of exfoliation of nanofiller in the polymer matrix, to a change on the morphological state of the mouldings induced by the nanoclay and/or to a high degradation of the PET matrix. Another reason for the improvement of E has been attributed to a strong interaction between matrix and silicate layers via formation of hydrogen bonds<sup>4</sup>. The values in **Table 7.4** do not present such strong interaction. In fact, in our case, it is possible that these interactions are reduced due to the organo-modified treatment of the nanoclay (modification by distearyl-dimethyl-ammonium chloride).

The tensile test results for DIM and EIM processed SiO<sub>2</sub> nanocomposites exhibit insignificant diminishing of the stiffness in comparison with pure PET. Some authors refer slightly higher modulus by preparing various silica polymer nanocomposites and little difference between composites with different particle sizes and production methods<sup>5</sup>. This was not confirmed in the present work might be because of the different production procedures, particle sizes and polymer nature. TiO<sub>2</sub> injection moulded nanocomposite exhibit the lowest modulus from all compared nanocomposites. The decreasing of agglomerate size by applying EIM improves the initial modulus of TiO<sub>2</sub>-PET in comparison with DIM procedure. Straightforward relation between initial modulus and nature, shape and particle size was not distinguished in attained results. The filler concentration could be suggested as most important parameter controlling the material stiffness, and not the production technique, neither the filler nature.

The yield stress of pure PET shows also no dependence upon the used processing techniques. In respect to pure polymer, MMT5 composites moulded by DIM show a reduction of  $\sigma_y$  of -16.2 % and EIM of -10.7%. The addition of SiO<sub>2</sub> particles also decreases the yield stress by comparison with pure polymer matrix for the same production technique, respectively -10.8% for DIM and -8.5% for EIM. Injection moulded TiO<sub>2</sub> composite do not show a yield point, showing a highly brittle behavior. EIM of TiO<sub>2</sub> composite reduces by 8.8% the yield stress

compared to pure PET. All type of nanofillers used in this study induce a decrease of the yield stress with respect to pure PET. The bad dispersion of the nanofillers, the presence of agglomerated particles that act as stress concentrators and the lack of interaction between particles and polymer matrix may contribute to this [5]. The higher values of  $\sigma_y$  of PET/MMT5 composite moulded by EIM procedure could be attributed to an higher amount of exfoliated MMT as compared to the DIM. Furthermore, in some studies the yield stress was found to increase slightly with decreasing size of the nanoparticles [5].

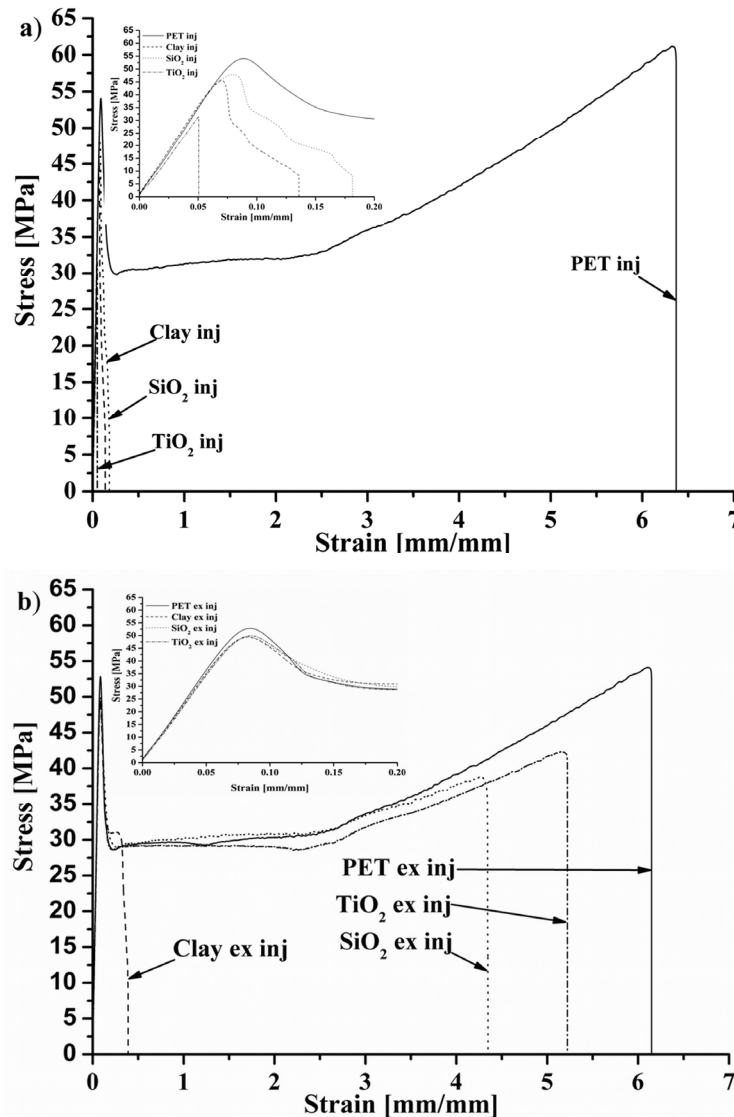


**Figure 7.3.** Experimental stress-strain curves for pure PET and its nanocomposites processed by: a) direct injection moulding (inj); and b) extrusion followed by injection moulding (ex inj).

The results shown in **Table 7.4.** for pure PET reveal a strong influence of the production procedures on the strain at break values. Injection moulded PET has 61.1 % higher  $\epsilon_b$  than the EIM of poly(ethylene terephthalate) that may be due to the significant degradation caused by this production procedure, as already abovementioned. The influence of nanofillers on the deformation capabilities of the mouldings is clearly evidenced by the distinct strain at break

shown by the mouldings. The strain at break diminishes drastically with respect to that of PET in both moulded MMT nanocomposites (**Figure 7.3.**). Sanches-Solis et al. has shown that strain at break diminishes drastically for clay composites with their contents of 1, 2 and 3% for organo-modified and non-modified MMT [9]. The improvement with 24.9 % of  $\epsilon_b$  for MMT5 - EIM in comparison with DIM moulded composite may be related to the higher amount of exfoliated inorganic nanoparticles. The SiO<sub>2</sub> and TiO<sub>2</sub> nanocomposites produced by DIM show a marked decreasing of deformation capability with respect to PET moulded with identical thermomechanical conditions. EIM nanocomposites present also a decrease on  $\epsilon_b$ . Fray et al. [7] have reported an improvement on the strain at break with 300% for 0.13 vol% of TiO<sub>2</sub> nanofiller content in PET matrix. The strain at break seems to be very sensitive to the dispersion satte and size of the nanoparticles agglomerates, as would be expected.

The possible reasons for different influence of the production procedure on mechanical properties could be explained by the lack of dispersion and agglomeration formation in case of DIM, and better dispersion for two step procedure (EIM) as a result of applied higher shearing levels. Besides, this will be also accompanied expectantly by strong matrix degradation that may significantly reduces their mechanical properties.

**Table 7.4. Mechanical test values.**

Processing	Material	E [MPa]	$\sigma_y$ [MPa]	$\epsilon_b$ [%]
<b>Direct injection moulded. DIM</b>	PET	889.2±19.3	55.2±0.8	524.1±15.8
	PET/MMT5	871.4±12.8	47.1±1.3	11.2±0.7
	PET/TiO <sub>2</sub>	803.1±9.9	37.2±2.4*	5.2±0.3
	PET/SiO <sub>2</sub>	861.3±21.3	49.5±0.2	16.7±2.4
	Var. (%)	10.7	17.3	10056.6
<b>Extruded injection moulded. EIM</b>	PET	892.4±6.8	55.8±1.1	475.2±56.5
	PET/MMT5	865.5±20.1	49.8±0.9	31.0±4.6
	PET/TiO <sub>2</sub>	866.1±5.4	51.0±1.1	421.9±35.9
	PET/SiO <sub>2</sub>	866.2±16.6	50.9±1.2	355.9±10.7
	Var. (%)	3.1	12.1	1434.4

(E – initial modulus,  $\sigma_y$  - Yeild Stres,  $\sigma_{max}$  - Maximum Stress,  $\epsilon_b$  – Strain at break, Var - percentage of variation [(max - min)/min]); \*fracture stress)

#### 7.3.4.1. Structure-mechanical property relationships

Relationship between yield stress,  $\sigma_y$ , and the glass transition temperature,  $T_g$ , and the temperature of cold crystallization,  $T_{cc}$  was established (**Figure 7.4.**). The  $\sigma_y$  value for DIM TiO<sub>2</sub>-PET composite was excluded because of not presence of yielding phenomena in this case. The yield stress increases with  $T_g$  and the decrement of  $T_{cc}$ . This reflects, for this particular case, a strong dependence of  $\sigma_y$  on the amount and molecular orientation of amorphous phase. This reveals the importance of the amorphous phase for the yielding phenomena. Furthermore, the

relative high coefficient of multiple correlation,  $R^2$ , means that other morphological parameters are insignificant for the yield stress.

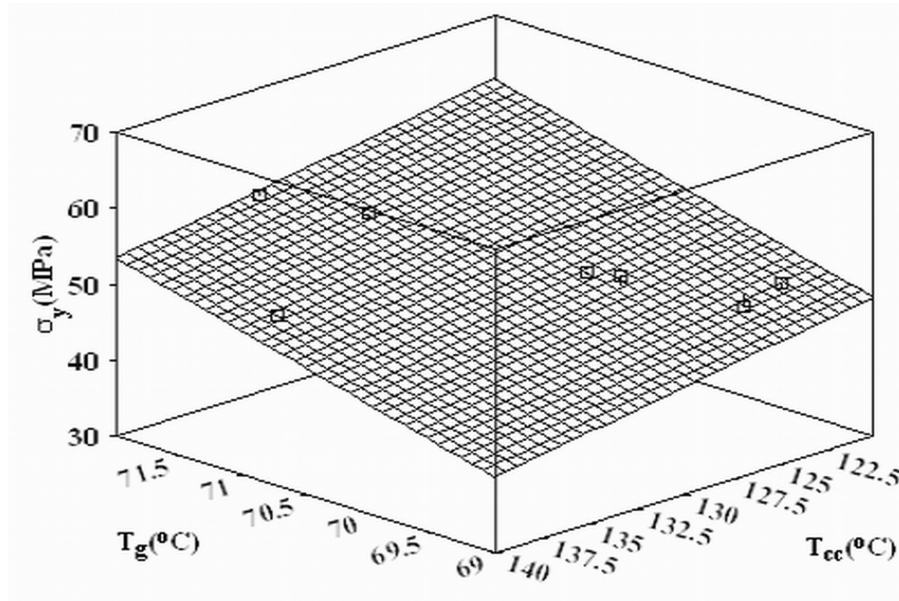


**Figure 7.4.** Variation of yield stress,  $\sigma_y$ , glass transition temperature,  $T_g$ , and cold crystallization temperature,  $T_{cc}$ . (the plane is a linear fit to the data:  $E = -210,05 + 4,46T_{cc} - 0,41T_g$ ;  $R^2 = 0,89$ )

### 7.3.5. Optical properties

#### 7.3.5.1. Gloss characterization

The gloss of the moulded samples was measured at 20 and 60 and 85° as a function of processing technique and type of nanofiller. According to ASTM standard [16] the values further considered values will be the measured at 20° because of the high gloss (greater than 70 gloss units) of the samples exposed at 60°. The measured glosses are depicted in **Figure 7.5.**, for both processing procedures and filler type. The glosses of the samples are related with the surface topology developed during the processing. From **Figure 7.5.** could be judged that all nanofillers cause a reduction in gloss with respect to pure PET for both processing procedures. EIM pure PET reduces significantly the specimen gloss as compared to DIM and their relatively higher level of degradation becomes apparent in samples yellowishing. For both processing procedures, the lowest gloss is achieved by the use of SiO<sub>2</sub> nanoparticles, which for DIM decrease gloss of pure PET 59.2% and for EIM by 61.8%. The gloss is almost independent of processing technique for MMT5 and TiO<sub>2</sub> PET composites.

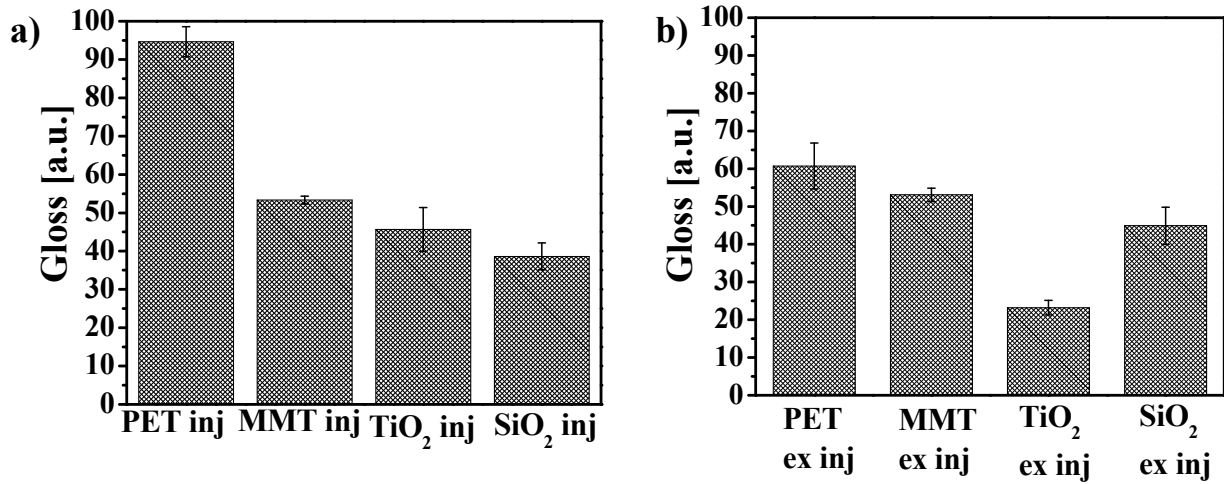


Figure 7.5. Gloss measurements of pure PET and its nanocomposites processed by: a) injection moulding (inj); and b) extrusion injection moulding (ex inj).

In this sense, the polymer properties (e.g., viscosity), the type of nanofiller and the processing technique all play an important role in the surface roughness, thus determining the specular reflectance characteristics of the air–sample interface: the higher the surface roughness, the lower the gloss [24]. **Figure 7.6.** shows the variation of the gloss with the degradation ratio as measured by the variations on the intrinsic viscosity, both being related by a straight line. An increment of polymer degradation results in a decrease on the glossiness, as shown in **Figure 7.6.**

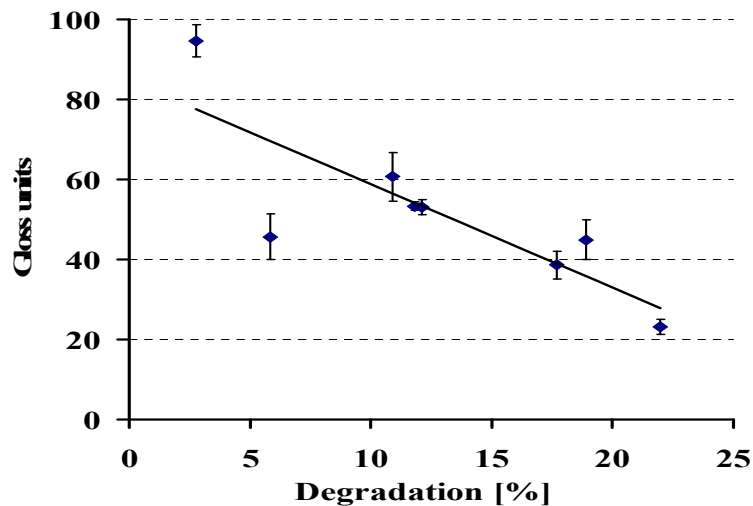


Figure 7.6: Dependence of gloss and degradation ratio (solid line is a linear fit to the data:  $Gloss = -2,59 Degradation; R^2 = 0,67$ )

### 7.3.5.2. Haze

Haze describe the transparency of a material and can be defined as the percentage of the total transmitted light that, in passing through the specimen, is scattered from the incident beam



by an angle greater than [24]  $2.5^\circ$ . In practice, a reduction in the contrast of an object viewed through a specimen could be due to an increase of haze. Detected haze for pure PET directly injection moulded was of  $8.7 \pm 1.0\%$ , this being the unique condition having a haze value lower than 30% (limit value associated with a transparent polymer). The rest of conditions, both DIM and EIM, have a haze value greater than 30%, which respond to diffusing or translucent samples (following the ASTM standard [17]). According to proposed microstructure models used for calculation of transparency [24] the elevated haze of EIM pure PET material is the result of appearance of degraded particles in bulk polymer, which are originating more scattering. Nanofillers in general are increasing slightly haziness, that is directly related to filler size and sample thickness [19].

## **7.4. Conclusions**

The structure of the polymer was varied by two production procedures (direct injection moulding, DIM, and extrusion blending followed by injection moulding, EIM) and different types of nanofillers. The PET nanocomposites are more sensitive to degradation than virgin PET, caused by presence of the nanofillers, which are inducing chain scission process leading to a reduction on the average molecular weight and respectively on the intrinsic viscosity. All the EIM samples show a higher variation of  $\eta$ , and then higher polymer degradation during processing.

Both production procedures are suitable for production intercalated MMT5, but slightly higher amount of intercalated phase for EIM is detected. Better dispersion in the polymer matrix of  $\text{TiO}_2$  and  $\text{SiO}_2$  nanoparticles was also obtained for EIM as compared with DIM, as would be expected. The different processing procedures represented slight influence on  $T_g$  and negligible upon  $T_m$ . In case of DIM, MMT and  $\text{TiO}_2$  are acting as nucleating agents, but  $\text{SiO}_2$  particles behave as crystallization inhibitor. This nucleating effect was exposed by all used inorganic fillers for EIM procedure that is originated by the better nanofillers dispersion.  $\sigma_y$  increases with  $T_g$  and respectively decrease with the raise of the cold crystallization peak position. The strain at break is related mainly with dispersion: better dispersion result in improved  $\epsilon_b$ . Gloss is affected mainly by filler presence and small processing influence is reported. All nanofillers strongly increasing sample haziness.

## 7.5 References

1. Viana, J.C., N.M. Alves, and J.F. Mano, *Morphology and mechanical properties of injection molded poly(ethylene terephthalate)*. Polymer Engineering and Science, 2004. **44**(12): p. 2174-2184.
2. Moysiadi, T., et al., *Effect of light transmittance and oxygen permeability of various packaging materials on keeping quality of low fat pasteurized milk: Chemical and sensorial aspects*. International Dairy Journal, 2004. **14**(5): p. 429-436.
3. Jenkinsand, W.A. and J.P. Harrington, *Packing foods with plastics*. 1991: Technomic Publishing Co. Inc.
4. Ray, S.S. and M. Okamoto, *Polymer/layered silicate nanocomposites: A review from preparation to processing*. Progress in Polymer Science (Oxford), 2003. **28**(11): p. 1539-1641.
5. Jordan, J., et al., *Experimental trends in polymer nanocomposites - A review*. Materials Science and Engineering A, 2005. **393**(1-2): p. 1-11.
6. Petrovic, Z.S., et al., *Effect of silica nanoparticles on morphology of segmented polyurethanes*. Polymer, 2004. **45**(12): p. 4285-4295.
7. Fray, E., M. Boccaccini, and R. Aldo, *Novel hybrid PET/DFA-TiO<sub>2</sub> nanocomposites by in situ polycondensation*. Materials Letters, 2005. **59**(18): p. 2300-2304.
8. Alexandre, M. and P. Dubois, *Polymer-layered silicate nanocomposites: Preparation, properties and uses of a new class of materials*. Materials Science and Engineering R: Reports, 2000. **28**(1): p. 1-63.
9. Sanchez-Solis, A., et al., *Mechanical and rheological studies on polyethylene terephthalate-montmorillonite nanocomposites*. Polymer Engineering and Science, 2004. **44**(6): p. 1094-1102.
10. Sanchez-Solis, A., A. Garcia-Rejon, and O. Manero, *Production of nanocomposites of PET-montmorillonite clay by an extrusion process* Macromol. Symp., 2003. **192**: p. 281-292
11. Ou, C.F., M.T. Ho, and J.R. Lin, *Synthesis and characterization of poly(ethylene terephthalate) nanocomposites with organoclay*. Journal of Applied Polymer Science, 2004. **91**(1): p. 140-145.
12. Nam, P.H., et al., *A hierarchical structure and properties of intercalated polypropylene/clay nanocomposites*. Polymer, 2001. **42**(23): p. 9633-9640.
13. Boccaccini, A.R., et al., *Fabrication, characterisation and assessment of bioactivity of poly(D,L lactid acid) (PDLLA)/TiO<sub>2</sub> nanocomposite films*. Composites Part A: Applied Science and Manufacturing, 2005. **36**(6): p. 721-727.
14. Assadi, R., X. Colin, and J. Verdu, *Irreversible structural changes during PET recycling by extrusion*. Polymer, 2004. **45**(13): p. 4403-4412.
15. *ASTM standard D4603-96, Standard test method for determining inherent viscosity of Poly(ethylene terephthalate) (PET) by glass capillary viscosimeter*, in *Annual Book Of ASTM Standards*. 2000, West Conhohocken, PA. p. 104.
16. *ASTM standard D523-85 Standard test method for specular gloss*, in *Annual Book Of ASTM Standards*. 1985, West Conhohocken, PA. p. 104.
17. *ASTM Standard D1003-63 Standard test method for haze and luminous transmittance of transparent plastics* in *Annual Book Of ASTM Standards*. 1961, West Conhohocken, PA. p. 365.
18. Colin, X. and J. Verdu, *Polymer degradation during processing*. Comptes Rendus Chimie, 2006. **9**(11-12): p. 1380-1395.
19. Torres, N., J.J. Robin, and B. Boutevin, *Study of thermal and mechanical properties of virgin and recycled poly(ethylene terephthalate) before and after injection molding*. European Polymer Journal, 2000. **36**(10): p. 2075-2080.
20. Taniguchi, A. and M. Cakmak, *The suppression of strain induced crystallization in PET through sub micron TiO<sub>2</sub> particle incorporation*. Polymer, 2004. **45**(19): p. 6647-6654.
21. Tolle, T.B. and D.P. Anderson, *Morphology development in layered silicate thermoset nanocomposites*. Composites Science and Technology, 2002. **62**(7-8): p. 1033-1041.

22. Esteves, A.C.C., et al., *Crystallization behaviour of new poly(tetramethyleneterephthalamide) nanocomposites containing SiO<sub>2</sub> fillers with distinct morphologies*. *Composites Part B: Engineering*, 2005. **36**(1): p. 51-59.
23. Ou, C.F., M.T. Ho, and J.R. Lin, *The Nucleating Effect of Montmorillonite on Crystallization of PET/Montmorillonite Nanocomposite*. *Journal of Polymer Research*, 2003. **10**(2): p. 127-132.
24. Meeten, G.H., *Optical Properties of Polymers*. 1986, London and New York: Elsevier Applied Science.

## CHAPTER VIII

# Characterization of PET nanocomposites produces by asymmetric batch minimixer

This chapter reports an investigation of the incorporation of different size and shape nanofillers on the properties of PET nanocomposites. PET was reinforced with 0.3 wt.% of four different shape/size nanoreinforcements, namely: 1D platelet-like shape organo-modified layered silicates MMT with average initial particle sizes (i) 30  $\mu\text{m}$  and other with (ii) 8  $\mu\text{m}$ ; (iii) 3D spherical shape titanium oxide with average particle size of 21 nm and (iv) 3D spherical shape silica with average particle size of 12 nm. PET nanocomposites were prepared by melt blending in an asymmetric batch minimixer followed by compression moulding process for sample preparation. The effect of nanofillers upon thermal, mechanical and structural properties in comparison to the neat PET are discussed.

*This chapter is adapted from the following publication:*

Todorov L.V., Martins C.I., Viana J.C.; *Characterization of PET nanocomposites with different nanofillers*; Solid State Phenomena, 151, 113-117, 2009

## 8.1. Introduction

Polymer nanocomposite properties are affected by the nature and concentration of the nanoreinforcement used and by their characteristics such as shape and size, specific surface area (surface-to-volume ratio) and surface treatment functionality [1]. In terms of shape and size, nanoparticles used for polymer reinforcement can be classified as follow: (i) 1D, when they have only one dimension in the nanometer range, such as the platelet-like shaped MontMorillonite (nanoclays), MMT: one to a few nanometers thick and hundreds to thousands nanometers long; (ii) 2D, when two dimensions are on the nanometer scale, such as elongated structures, in the case of carbon nanotubes or cellulose whiskers; and 3D, that are those having three dimensions in the nanometer scale, such as spherical silica, SiO<sub>2</sub>, and titanium oxide, TiO<sub>2</sub> [1].

The macroscopic effects of the incorporation of nanoparticles onto the polymer matrix are generally the enhancement of mechanical performance, barrier properties, thermal stability, fire retardancy, etc. Very low incorporation of nanoparticles, typically less than 5%, is needed to observe such properties improvements [1].

The production of polymer nanocomposites and primarily the incorporation of nanofillers in the polymer matrix can be made either by in situ polymerization, by solvent-assisted techniques, or by melt blending techniques. The melt blending techniques are the most attractive pathway to produce commercial nanocomposites [2]. In this work, melt blending via an asymmetric batch minimixer [3] was used for preparation of the PET nanocomposites. Effects of nanoreinforcements upon the polymer bulk degradation, particles dispersion, thermal and mechanical properties of the nanocomposites in comparison to the neat PET were evaluated.

## 8.2. Materials and preparation of PNCs

### 8.2.1. Materials

As a polymer matrix was used PET with intrinsic viscosity of  $0.74 \pm 0.02 \text{ dl.g}^{-1}$  – bottle grade; density of  $1.40 \text{ g.cm}^{-3}$  and average molar mass of  $M_n \approx 20000 \text{ g.mol}^{-1}$ .

As nanoreinforcements were used different nanoparticles:

(i) 1D nanoparticles - MMT with different powder agglomerates size, supplied by Süd-Chemie AG, Germany, namely: Nanofil32 (MMT32) and Nanofil2 (MMT2). Both MMTs are organo-modified with stearylbenzyltrimethyl-ammonium chloride, and have an interlayer distance by basal plane (001) of 1.8 nm. The MMT nanofiller have untamped bulk density, UTBD, respectively: MMT32 of  $350 \text{ g.l}^{-1}$  and with  $150 \text{ g.l}^{-1}$  for MMT2.

(ii) 3D nanofillers: nanotitanium dioxide, TiO<sub>2</sub>, particles (AEROXIDE TiO<sub>2</sub> P25) with surface area  $50 \pm 15 \text{ m}^2\text{g}^{-1}$ , and nanosilica, SiO<sub>2</sub>, (AEROSIL 200) with specific surface area  $200 \pm 25 \text{ m}^2\text{g}^{-1}$ , both from Degussa AG, Germany.

Nanoparticles specifications are listed in *Table 8.1*.

*Table 8.1. Nanoparticles specifications (supplier data).*

Nanofiller	Shape	D <sub>aggl.</sub>	Particle [nm]	Surfactant
MMT32	platelet	30 ÷ 80 μm	≈200x1	long chain hydrocarbon / benzyl group
MMT2	platelet	8 ÷ 12 μm	≈200x1	long chain hydrocarbon / benzyl group
TiO <sub>2</sub>	spherical	≈100 nm	≈21	-----
SiO <sub>2</sub>	spherical	≈100 nm	≈12	-----

(D<sub>aggl.</sub> – powder agglomerates average diameter)

### 8.2.2. Preparation of PET nanocomposites

The PET nanocomposites were prepared via melt blending in an Asymmetric Batch MiniMixer, ABM, similar to those presented in [3]. For that, PET dried pellets (drying conditions: 170°C for 4 ÷ 7 h) and nanoparticles were mechanically blended in a tumbler mixer for 15 min, whereupon 20 g from each blend was melted (for 10 min) and mixed at 280°C for 5 min into the ABM. Further, the neat and blended PET nanocomposites melts were casted on a preheated stainless steel plate (280°C) covered with a Teflon foil, and used to prepare plaques with dimension of 200x200x0.3 mm by compression moulding. The plaques were then rapidly quenched in cold water at around 5 ± 0.5°C.

### 8.2.3. Characterization

#### 8.2.3.1. Intrinsic viscosity; IV

The intrinsic viscosity,  $\eta$ , measurements were performed according to the ASTM D4603-03 standards. A glass capillary viscometer (Ubbelohde type) was used and the solutions were prepared using a solvent mixture composed of 60/40 phenol/1,1,2,2- tetrachloroethane. All PET nanocomposites solutions were prepared with 0.3 wt.% concentration correction. After complete dissolution they were centrifuged for 30 min at 3500 rpm and filtered in order to remove the nanoparticles sediment.

#### 8.2.3.2. Transmission electron microscope, TEM

Ultramicrotome cuts made through the thickness sections of the compression moulded samples, with approx. thickness of 60 nm, were used. TEM observation was carried out under an operation voltage of 100 kV on a JEOL JEM 1010.

#### 8.2.3.3. Dynamic mechanical analysis, DMA

The DMA analysis was carried out using a Triton Tritec 2000 from Triton Technology Ltd. All samples were measured in a tension mode over the temperature range of -140 to 240°C, at a heating rate of 4°C.min<sup>-1</sup> and frequency of 1 Hz. Samples were cut into rectangular shapes 3x20x0.3 mm from compression moulded plaques. An average of three samples was tested (T<sub>g</sub> was calculated by the peak position of tanδ curve).

### 8.2.3.4. Differential Scanning Calorimetry, DSC

Thermal properties of neat and PET nanocomposites were measured using a Perkin Elmer DIAMOND PYRIS DSC instrument. The samples were scanned in the temperature range from 30 to 270°C, at a heating rate of 20°C.min<sup>-1</sup>, in a dry nitrogen atmosphere. The reported transition temperatures ( $T_{cc}$  and  $T_m$ ) are referred to the respective peak maximum positions and the degree of crystallinity ( $\chi_c$ ) was calculated based on a two-phase (crystalline–amorphous) peak area method, considering the heat of fusion of 100% PET crystalline sample to be 120 J.g<sup>-1</sup>. The reported results are the average of three samples.

### 8.2.3.5. Mechanical characterization

Tensile mechanical behaviour of the studied materials was assessed using a universal testing machine - Zwick/Roell Z005. The testes were carried at room temperature, at the rate of 2 mm.min<sup>-1</sup>. Tensile specimens with a curved axisymmetric shape (30 length and cross-section 13.9x0.3 mm) were used.

## 8.3. Results and discussion

### 8.3.1. Intrinsic viscosity

The intrinsic viscosity,  $\eta$ , of the PET nanocomposites is listed in **Table 8.2.**, in terms of the percentage of reduction of  $\eta$  of the processed samples to the pristine PET pellets. A reduction of 28.5% for processed PET in respect to the PET granules is observed, meaning that some degradation of PET occurring during the composite preparation. This result may be explained by the high temperature, shear rate and residence time applied. The incorporation of the nano-reinforcements reduce even more the  $\eta$ , compared to the processed PET, being the TiO<sub>2</sub>, the type of reinforcement producing greater reduction in the viscosity (around 41.3%). Nevertheless, there is no relation between the shape of the filler and the reduction in viscosity. When comparing the size of the reinforcements used, one can observe that among the platelet-like and the spherical particles, the ones having biggest sizes are those presenting higher reduction in the viscosity.

**Table 8.2.** Percent of reduction of intrinsic viscosity.

Sample	PET	PET/MMT32	PET/MMT2	PET/TiO <sub>2</sub>	PET/SiO <sub>2</sub>	Var. %
$\eta_{red}^*$ [%]	28.5	34.3	32.2	41.3	31.7	45.2

\*( $\eta_{red}$  – percentage of reduction of intrinsic viscosity,  $\eta_{red} = ((\eta_{pristine} - \eta_x) / \eta_{pristine}) \times 100$ ; where  $\eta_x$  is the intrinsic viscosity of each of the processed specimens and  $\eta_{pristine}$  of pristine PET granules; Var. - percentage of variation [(max - min)/min])

### 8.3.2. Transmission electron microscopy, TEM

TEM micrographs of the different PET nanocomposites are depicted in **Figure 8.1.** TEM revealed the existence of small sized agglomerates for all types of nanofillers used. For the

platelet like fillers, shown in **Figure 8.1 a)** and **b)**, an inter-plate distance of 2.7 nm for the MMT32 and 1.9 nm for the MMT2, respectively, was measured. For the smaller particles (MMT2) the inter-plate distance is about the same of the original particles, while for bigger particles (MMT32) the distance is increased, showing some particle intercalation.

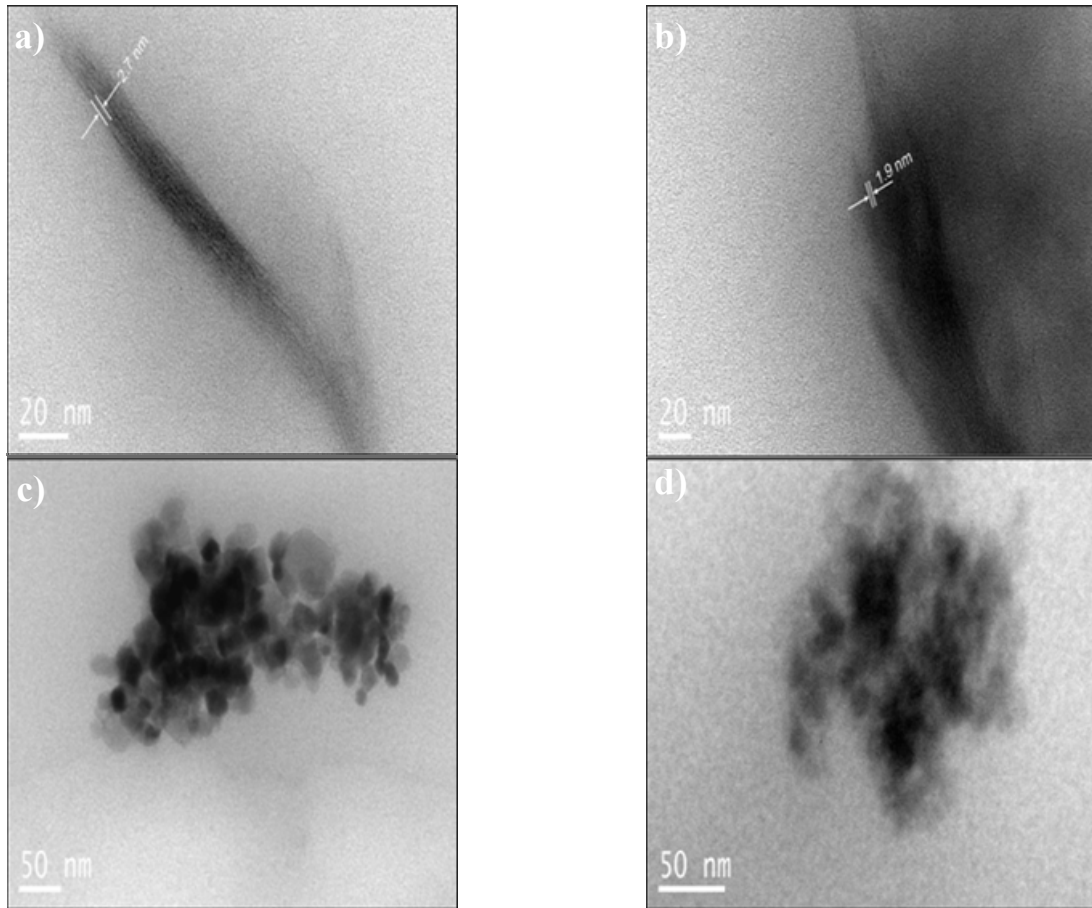


**Figure 8.1.** TEM micrographs of nanocomposites: a) PET/MMT32, b) PET/MMT2, c) PET/TiO<sub>2</sub> and d) PET/SiO<sub>2</sub>

### **8.3.3. Dynamic mechanical analysis, DMA**

In **Figure 8.2.**, it is shown the storage modulus,  $E'$ , and the loss factor ( $\tan\delta$ ) of the different PET nanocomposites. As observed, the storage modulus varies between 1.7 to 1.9 GPa (at 23°C) depending on the type of nanofiller used (**Table 8.3.**). Incorporation of platelet-like filler MMT32 caused slightly improvement on the  $E'$  in comparison to processed PET. Significant higher storage modulus exposed PET-SiO<sub>2</sub> composite in respect to neat PET. Identical decreased storage modulus values showed 1D MMT2 and 3D TiO<sub>2</sub> particles.

In terms of the  $\tan \delta$  peak, it is observed a movement towards higher temperature, together with its broadening, in the cases of PET/SiO<sub>2</sub> and PET/MMT2 composites, as compared to processed PET. This result shows an increase of  $T_g$  of these two materials. In the first case, the increase is about 1.6°C, while in the second case is about 1.4°C. No significant change is observed for the peak position of the  $\tan \delta$  of the other two types of fillers, although it



is observed a somewhat broader peak. The smaller sized particles among the platelet and spherical type are the ones showing higher influence on  $T_g$  and broadening of this transition. This behaviors was also observed by other authors [4].

**Table 8.3.** Thermo-mechanical parameters

Sample	$E'$ [GPa]	$T_g$ [°C]	$\Delta T_g$ [°C]
PET	1.80±0.15	82.2±0.4	11.0±0.8
PET/MMT32	1.84±0.11	82.8±0.7	11.6±0.2
PET/MMT2	1.72±0.05	83.8±0.9	12.5±0.7
PET/TiO <sub>2</sub>	1.72±0.02	81.8±0.5	11.4±0.2
PET/SiO <sub>2</sub>	1.92±0.08	83.5±0.1	12.7±0.3
Var. %	11.73	2.44	15.6

( $E'$  - storage modulus at 23°C;  $T_g$  - peak position of  $\tan\delta$  curve;  $\Delta T_g$  - breadth by means half width of full maximum of loss factor,  $\tan\delta$ , peak fitted by Gaussian function; Var. - percentage of variation [(max - min)/min])

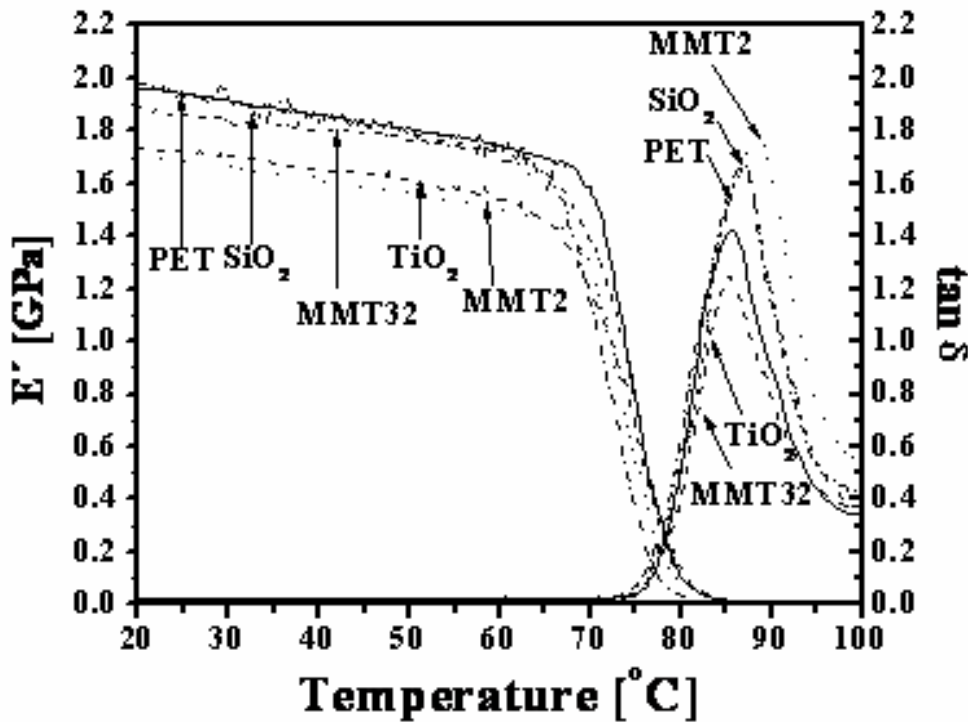


**Figure 8.2.** Effect of the nanofillers on the  $E'$  and  $\tan\delta$  peak from DMA.

#### 8.3.4. Thermal characterization

The thermal parameters assessed by DSC are listed in **Table 8.4**. The presence of nanofillers is mainly affecting the cold crystallization temperature,  $T_{cc}$ , and the final degree of crystallization of PET nanocomposites. All nanoparticles leads to decrement of  $T_{cc}$  in comparison to neat PET, which means that used nanofillers are acting as nucleating agents [4]. Among all, the PET-SiO<sub>2</sub> is the composite presenting the biggest variation. This differences might be attributed to the presence of smaller agglomerates size and its better dispersion in the polymer matrix, as suggested elsewhere [4].

All selected nanofillers increase the degree of crystallinity of PET, thus acting as nucleating agents. The PET/MMT32 nanocomposite shows the smallest increment upon  $\chi_c$  as compared with neat PET perhaps due to the higher level of intercalation observed for this system. According to other authors, the intercalation may reduce the ability of polymer to crystallize [4]. On the other hand, the 3D nanofiller, namely the SiO<sub>2</sub> promotes a higher crystallization of the PET matrix.

Table 8.4. Thermo parameters

Sample	T <sub>cc</sub> [°C]	T <sub>m</sub> [°C]	χ <sub>c</sub> [%]
PET	141.7±0.2	249.8±0.0	7.6±0.6
PET/MMT32	137.2±0.9	249.8±0.5	8.1±0.5
PET/MMT2	138.3±0.4	249.3±0.3	9.1±0.7
PET/TiO <sub>2</sub>	139.6±0.4	250.2±0.6	8.8±0.6
PET/SiO <sub>2</sub>	136.7±0.8	250.2±0.3	9.2±0.3
Var. %	3.62	0.36	24.33

(T<sub>cc</sub> - cold crystallization peak temperature, T<sub>m</sub> - melting peak temperature, χ<sub>c</sub> - degree of crystallinity, Var. - percentage of variation [(max - min)/min])

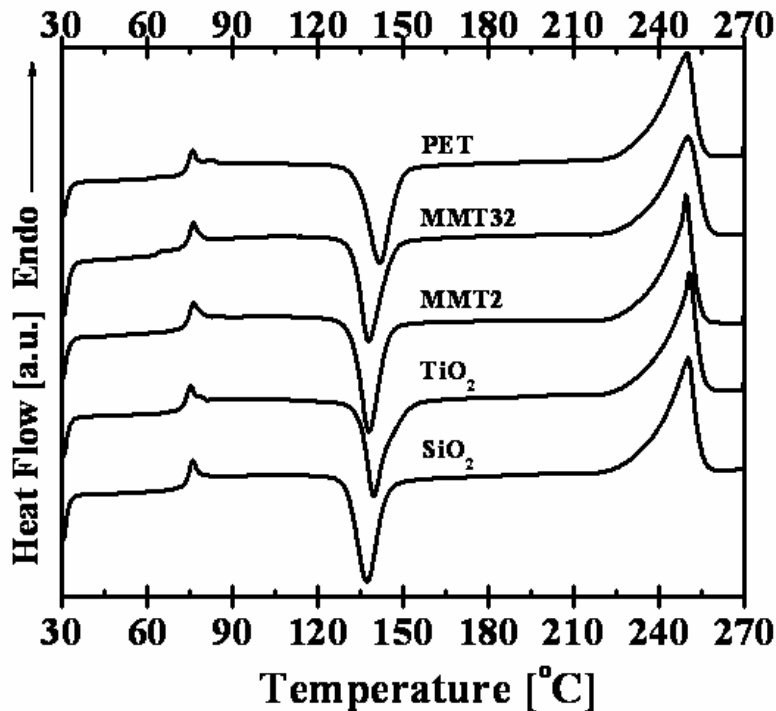


Figure 8.3. DSC thermograms at 20 °C.min<sup>-1</sup> heating rate for all samples.

### 8.3.5. Mechanical behaviour.

The stress-strain curves of PET nanocomposites are shown in *Figure 8.4*, and the summary of some mechanical properties are listed in *Table 8.5*. The different reinforcing nature

of the nanoparticles is evidenced mainly in terms of deformation capabilities (i.e., the strain at break,  $\epsilon_b$ ).  $\epsilon_b$  diminishes drastically with respect to that of PET in case of both MMT (MMT32 and MMT2) nanocomposites. The MMT32 filler contributes for nearly 50% of reduction comparing to the neat PET deformability. The smallest MMT2 nanofillers contribute by 17.6% reduction for  $\epsilon_b$ . For  $\text{TiO}_2$ , the deformation capability improved by 5.2% , which is in agreement with other works [4]. Adding  $\text{SiO}_2$  nanoparticles led to a significant enhancement of the strain at break with an increment of 37.8%. The strain at break of PET nanocomposites seems to be very sensitive to the shape/size of incorporated nanofillers.

**Table 8.5. Mechanical test values**

Sample	E [MPa]	$\sigma_y$ [MPa]	$\epsilon_b$ [%]
PET	675.7±155.0	41.2±7.4	120.1±36.9
PET/MMT32	590.5±132.4	37.7±5.2	56.7±22.2
PET/MMT2	714.6±117.6	42.5±6.5	98.9±32.4
PET/ $\text{TiO}_2$	672.5±121.3	43.7±6.3	126.3±37.9
PET/ $\text{SiO}_2$	608.4±86.5	39.2±4.2	165.4±41.3
Var. [%]	21.02	15.75	191.80

(E – initial modulus;  $\sigma_y$  - yield stress;  $\epsilon_b$  – strain at break; Var - percentage of variation [(max - min)/min])

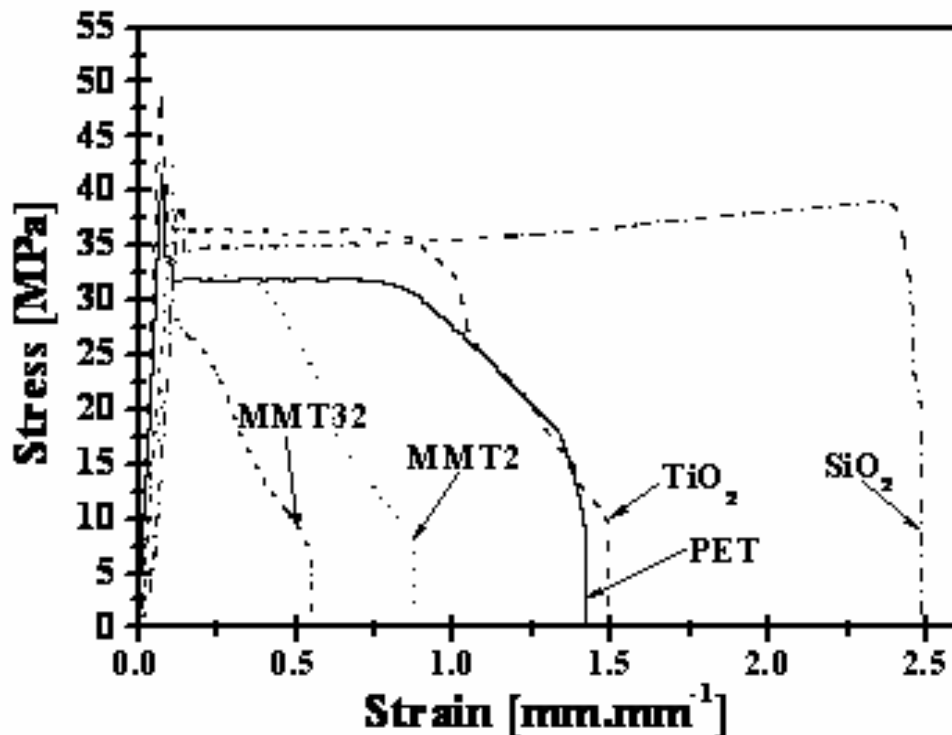


**Figure 8.4. Experimental stress-strain curves.**

## 8.4. Conclusions

Incorporation of nanoparticles into the polymer matrix contributes for polymer degradation during the processing. Interaction on the interface of nanofillers-polymer caused

increase of glass transition temperature and broadening of the transition. All characterized nanoparticles have nucleating effect regardless of nanoparticles shape/size. Deformability of PET nanocomposites improves with incorporation of smaller size nanofillers and application of the spherical shape nanoparticles.

## 8.5. References

1. Ray, S.S. and M. Okamoto, *Polymer/layered silicate nanocomposites: A review from preparation to processing*. Progress in Polymer Science (Oxford), 2003. **28**(11): p. 1539-1641.
2. Koo, J.H., *Polymer Nanocomposites Processing, Characterization, and Applications*. 2006, New York: McGraw-Hill.
3. Breuer, O., U. Sundararaj, and R.W. Toogood, *The design and performance of a new miniature mixer for specialty polymer blends and nanocomposites*. Polymer Engineering and Science, 2004. **44**(5): p. 868-879.
4. Jordan, J., et al., *Experimental trends in polymer nanocomposites - A review*. Materials Science and Engineering A, 2005. **393**(1-2): p. 1-11.

## CHAPTER IX

# *In situ* WAXS/SAXS structural evolution study during uniaxial stretching of PET nanocomposites in solid state: PET/MMT nanocomposites

This chapter reports an investigation on the solid state uniaxial stretching of neat PET and its MMT (0.3wt%) nanocomposites showing intercalated (PET/MMT32) and tactoid (PET/MMT2) morphologies, followed by *in situ* WAXS/SAXS (under X-ray synchrotron source radiation). PET and its nanocomposite multiscale structure evolution has three main common stages: i) stage I (before necking), a small amount of amorphous phase evolves into mesophase at constant molecular orientation level; ii) stage II (neck propagation), a rapidly increase of polymer molecular orientation originates a sharp increment of mesophase at the expense of the amorphous phase and the formation of a periodical mesophase from the mesophase. Also a crazes are form and widen in the polymer bulk and in case of nanocomposites appears the voids inside the MMTs particles; iii) stage III (necking), at leveling off of the average molecular orientation, the highest periodical mesophase content is achieved, as well as a slight increment of mesophase upon further deformation. Along this stage, within polymer matrix the crazes and voids from the MMTs breakage evolve into micro-voids. The incorporation of the nanofillers promoted a higher fraction of periodical mesophase as compared to pure PET. PET/MMT32 intercalated nanoparticles cause an earlier formation of periodical mesophase than tactoid PET/MMT2. Superior deformation capability, in respect to neat PET, was observed for the nanocomposites. Both morphologies retard a crazes widen in respect to the PET. Intercalated morphology results into smallest voids size in between all samples, while the tactoid exposed similar to pure sample.

*This chapter is adapted from the following publication:*

Todorov L.V., Martins C.I., Viana J.C. *In situ* WAXS/SAXS structural evolution study during uniaxial stretching of PET nanocomposites in solid state: PET/MMT nanocomposites. Composites Science and Technology, Submitted

## 9.1. Introduction

Within the last decade it has been clearly recognized that inorganic nanoscale reinforcement has become an attractive mean of improving the properties and stability of polymers. This leads to a new and improved class of composites, the polymer nanocomposites, PNCs [1]. PNC are thought to have improved performance, namely enhanced mechanical behaviour for very low incorporation of nanoparticles (typically less than 5wt%) [1]. In fact, due to the high surface-to-volume ratio of the nanofillers, innumerable interactions are developed with the polymer macromolecular chains. In polymer nanocomposites, this predominant interfacial and local effects can operate as structure and morphology directors that also may introduce new energy dissipation mechanisms [2].

In recent years special attention was paid to poly(ethylene terephthalate), PET, nanocomposites reinforced with layered silicates, particularly montmorillonite, MMT, as alternative for neat PET as packaging material with improved performance. Generally, these improvements are consistent with the enhancement of mechanical, barrier, thermal and optical properties and are related to the level of delamination of MMT nanoparticles into the polymer matrix. Incorporation of MMT in polymer may lead to different morphologies: i) tactoid – un-separated MMTs layers, ii) intercalated - regularly alternating MMT's and polymer layers with a repeat distance of a few nanometers and iii) exfoliated - irregularly delaminated and dispersed lamellas of MMT [3]. These distinct morphologies play a key role in the enhancement of the PNC properties. Normally, exfoliated PNCs have superior mechanical properties than intercalated nanocomposites [4-8]. In order to change the MMT's substrate from hydrophilic to hydrophobic for better insertion of hydrophobic PET molecular chains into the gallery between the layers of MMT is necessary to introduce organic modifiers (organo modified MMT, oMMT). This process may provide a favourable way to better delaminate and disperse MMT in the PET matrix. On the other hand, a critical role for mechanical performance improvement is also played by the nanocomposites preparation method (processing).

The incorporation of MMT nanofillers in the PET polymer matrix have been made via various methods, namely: i) *in situ* polymerization [9-19], ii) solvent assisted blending [20-22] and direct melt blending [23-34]. Melt blending techniques are recognized as the most attractive pathways to produce PNC in a commercial scale, as a consequence of: i) fast dispersion of nanofillers in the melt, ii) available melt compounding capacities and iii) environmentally friendly preparation [1]. A variety of blending apparatus were used for compounding of PET with MMT nanoparticles, specifically: i) co-rotating twin-screw extruder [23, 25, 26, 32, 33, 35, 36], ii) co-rotating twin-screw micro extruder [30, 31], iii) contra-rotating extruder [27], iv) extrusion and subsequent injection moulding [28, 29, 34], direct injection moulding [28, 34].

However, the main limitations of melt blending methods are delamination of MMT's layers into polymer matrix and the thermal decomposition of the organic surfactants [32]. Successful melt dispersion requires the presence of strong interactions between the inorganic nanofillers and the macromolecules, an appropriate stress field and an enough residence time. In the literature are many works reporting about PET/MMT nanocomposites with enhanced tensile mechanical properties, produced via melt blending, namely: i) modulus [23, 26-29, 36], ii) strength [23, 25, 29] and iii) deformability [25].

Until now, many research efforts have been devoted to the characterization of the deformation mechanism of PNCs with MMT during uniaxial stretching, as a function of the degree of delamination of MMT, based on the investigations with *in situ* high-voltage electron microscope. Kim et al. [37, 38] recognized as main deformation mechanism microvoid formation inside tactoids or intercalated MMT particles. Three possible modes of deformation were identified depending on MMT's particles position toward the stretching direction: i) perpendicular (splitting) - deformation initiates at the middle region of the stacked MMT's particles (tactoid) or splitting of the platelets takes place in the middle of intercalated MMT particle, ii) at a certain angle (opening) - opening of bundles of the stacked particles (tactoids) or bundles of the intercalated MMT layers occurs during the deformation process, and iii) parallel (slipping) - slipping bundles of the stacked MMT's particles in case of tactoid morphology and sliding of pallets of MMT particles for intercalated one. The originated void size is directly related to the MMTs morphology: intercalated state results in smaller voids than the tactoid one [37]. Recently, were also reported a few research works based on the *in situ* SAXS investigation of PET nanocomposites with: carbon nanotubes [39, 40] and carbon black [40]. Those studies evidenced main deformation mechanism being polymer matrix craze like formation with voiding during uniaxial stretching in the solid state. Incorporation of the inorganic nanoparticles retarded the growth and fracture of the crazes during deformation [39, 40].

To improve and control the ultimate mechanical properties for a wide range of applications and, in particular to optimize the stiffness/toughness balance, a better understanding of the interrelationship between the MMT morphologies and structure evolution during the mechanical deformation processes is clearly required. In this context, this work aims at understanding the effect of MMT nanofillers incorporation within PET matrix on the structure evolution and deformation mechanism taking place during uniaxial stretching in the solid state.

## **9.2. Experimental**

### **9.2.1. Materials**

In this work the following materials were used:



- Poly(ethylene terephthalate), PET, with intrinsic viscosity of  $0.74 \pm 0.02 \text{ dl.g}^{-1}$  (bottle grade),
- reinforcements: organo-modified (with stearylbenzyltrimethyl-ammonium chloride) MMT, with different powder agglomerates size, supplied by Süd-Chemie AG, Germany, namely: i) Nanofil<sup>®</sup>32, MMT32 and ii) Nanofil<sup>®</sup>2, MMT2, which specifications are given in Table 1.

**Table 9.1. Nanoparticles specifications (supplier data).**

Nanoparticles	$D_{\text{aggl.}}^*$ [ $\mu\text{m}$ ]	$d_{(001)}$ [nm]	UTBD [ $\text{g l}^{-1}$ ]	Surfactant
MMT32	30 - 80	1.8	350	long chain hydrocarbon / benzyl group
MMT2	8 - 12	1.8	150	long chain hydrocarbon / benzyl group

( $D_{\text{aggl.}}$  – powder agglomerates main average diameter,  $d_{(001)}$  - interlayer distance of basal plane (001); UTBD - untamped bulk density)

Samples used in this work were produced via direct melt blending with content of 0.3 wt% of MMT, according to the experimental protocol described in our previous work [41].

## 9.2.2. Nanocomposites characterization

### 9.2.2.1. Low-angle region Wide Angle X-ray Scattering, WAXS

As-moulded plaques were characterized at low-angle region of  $2\Theta < 10^\circ$  by WAXS, performed at AXS NanoStar Bruker equipment working with  $\text{CuK}\alpha$  radiation ( $\lambda=0.154 \text{ nm}$ ). Equipment was setup at sample-to-detector distance of 99 mm and 2D WAXS patterns were acquired with 2D HI-STAR Area Detector with accumulation time of 600 s. The WAXS patterns were investigated in range of  $2\Theta = 1.6 - 10^\circ$ , in order to study delamination of the MMTs.

### 9.2.2.2. Transmission Electron Microscope, TEM

Ultramicrotome cuts made through the thickness of the compression moulded samples, with approx. thickness of 60 nm, were used. TEM observation was carried out under an operation voltage of 100 kV on a JEOL JEM 1010. Three micrographs per nanocomposite were used for particles agglomerates measurements from randomly transversal cuts. MMT's particles incorporated into PET nanocomposites were assumed to be elliptical. The average agglomerate, cluster of intercalated particles or factoids, diameter,  $D_{\text{av}}$ , was calculate by following formula:

$$D_{\text{av}} = \frac{\sum_{i=1}^n [(d_1 + d_2)_i / 2]}{n} \quad (9.1)$$

where  $d_1$  and  $d_2$  are main diameters of each agglomerate and  $n$  is the number of considered agglomerates. At least five TEM measurements were considered to obtain an average agglomerate diameter.

### 9.2.3. *In situ* synchrotron characterization

Simultaneous uniaxial continuous stretching in the solid state (at 23°C) and *in situ* WAXS and SAXS characterization were performed under synchrotron radiation (Ge (111)  $\lambda=0.15$  nm) at HASYLAB, DESY, Hamburg (A2 beamline). The tensile specimens with a curved axisymmetric shape (30 mm length, minimal cross-section of 13.9x0.3 mm and radius of 10.4 mm) were deformed on a special stretching device with both grips move simultaneously in opposed directions. Stretching apparatus output (force and displacement) was converted into homogeneous stress-strain curves ( $\sigma_H$  versus  $\ln\lambda$ ). It was assumed that the curved axisymmetric tensile specimen deforms through rectangular neck. The stretching ratio,  $\lambda$ , was defined as:

$$\lambda = \frac{l}{l_0} \quad (9.2)$$

where  $l$  is actual tensile specimen length and  $l_0$  the grip distance in mm. Also the homogeneous stress was calculated as follows:

$$\sigma_N = \frac{F}{A_0} \lambda \quad (9.3)$$

where  $F$  is the force and  $A_0$  the initial minimum tensile specimen cross-section area.

The specimens were mounted perpendicular to the incident X-ray beam and stretched vertically. Background scattering was subtracted and all plots were homogeneous with respect to the incident X-ray intensity, accumulation time and specimen thickness (assuming a homogeneous deformation [42]). Equipment set was as follows:

i) WAXS: sample-to-detector distance of 145 mm and 2D WAXS patterns were acquired with accumulation time of 20 s. Samples stretched at a constant cross-head velocity of 2 mm.min<sup>-1</sup> (stretching rate 0.002 s<sup>-1</sup>). WAXS was calibrated by means of a crystalline PET sample.

ii) SAXS: sample-to-detector distance of 3025 mm and 2D SAXS patterns were acquired with accumulation time of 30 s. Samples stretched at a constant cross-head velocity of 5 mm.min<sup>-1</sup> (stretching rate 0.006 s<sup>-1</sup>).

#### WAXS data analysis

##### Phase's mass fractions

The two linear intensity profiles, taken along the equatorial and meridional directions from the 2D WAXD patterns, were used to estimate mass fractions of the phases. A peak-fitting programme was used to deconvolute the distinct phase's peaks that were fitted by a Gaussian function. Studied samples morphologies were assumed to consist of two phases: i) amorphous – isotropic and ii) mesophase - anisotropic phase with degree of packing and order between the crystalline and the amorphous phase. The amount of amorphous phase was assumed to be

proportional to the area of the meridional profile. The subtraction of the amorphous fraction from the total area in the equatorial profile was proportional to the amount of the mesophase. The mass fractions of the individual phases were taken as the ratio of the area for each phase to the total area of the equatorial profile.

At higher strains, the WAXS patterns can exhibit a pair of meridional mesomorphic reflections (10-3) at about  $2\Theta = 25.8^\circ$ , indicating conformational regularity, called here periodical mesophase. The area of fitted (10-3) peak profile was used to determine the mass fraction of the periodical mesophase. At this stage of deformation the sample morphologies were assumed to be composed of three phases: i) amorphous – isotropic, ii) mesophase - anisotropic phase with degree of packing and order between the crystalline and the amorphous and iii) periodical mesophase – mesophase with conformational periodicity perpendicular to the stretching direction. The three phase total area was assumed to be equal to the sum of area convoluted under the equatorial and the area under the meridional (10-3) peak. The subtraction of the amorphous fractions, convoluted under isotropic peak at the meridian, from the assumed total area profile was proportional to the amount of the mesophase. The mass fractions of the individual phase were taken as the ratio of the area for each phase to the total area.

#### Average polymer orientation

The WAXS patterns were integrated along an azimuthal angle of  $\mu = 0 - \pi/2$  ( $\mu = 0$  equator), over a section with width of  $2\Theta = 13 - 28^\circ$ , in order to calculate the average polymer orientation,  $f_{av}$ . That sector encloses all possible crystal reflections of crystallographic planes, isotropic amorphous phase and mesophases of PET [43]. The Hermans' orientation function was used to evaluate the average polymer orientation,  $f_{av}$ , calculated as [44]:

$$f = \frac{3\langle \cos^2 \phi \rangle - 1}{2} \quad (9.4)$$

where the  $\langle \cos^2 \phi \rangle$  is defined as:

$$\langle \cos^2 \phi \rangle = \frac{\int_0^{\pi/2} I(\phi) \cos^2 \phi \sin \phi d\phi}{\int_0^{\pi/2} I(\phi) \sin \phi d\phi} \quad (9.5)$$

where  $\phi$  is the azimuthal angle,  $I$  the diffracted intensity and  $\langle \cos \phi \rangle$  the average angle that the normal makes with principal deformation direction.

## 9.3. Results and discussion

### 9.3.1. Neat PET structure evolution by WAXS

*Figure 9.1.* presents the homogeneous stress-strain curves obtained during the uniaxial stretching and selected 2D WAXS patterns (arrows indicate the strain where patterns were

acquired) for neat PET sample. Upon the stretching till strain of  $\ln\lambda=0.3$ , in 2D WAXS patterns no notable changes occurs, remaining an amorphous halo as prior stretching. From  $\sigma$ - $\ln\lambda$  curve might be recognized the yielding at strain of  $\ln\lambda=0.06$ . Generally yielding point is related to thinning to smaller section at minimum cross-sections of the tensile specimen [45] (neck initiation) as revealed by *in situ* video investigation depicted in **Figure 9.2 b**). Thereafter, neck forms out of the sample centre where the WAXS investigation was carried out (see **Figure 9.2 c**). As a consequence, a lack of structural evolution in the 2D WAXS patterns was observed up to this strain level. Nevertheless, the material under the X-ray beam is subjected to a load and it can be assumed as being before necking (plastic deformation). During following interval of strain between  $0.3 < \ln\lambda < 0.5$ , in 2D WAXS patterns appears a two diffused spots at equator, suggestive for considerable polymer chains orientation into stretching direction [46-50] and a meridional reflection recognized as distinct for periodical mesophase (10-3) reflection [51, 52]. These changes can be associated to the neck propagation through the examined region of the sample (**Figure 9.2 d**). At strain greater than  $\ln\lambda=0.6$  till strain of break, the stress level decreases gradually and the 2D WAXS patterns feature an amorphous halo that is suggestive of local polymer chains relaxation, originated by a macroscopic cracks occurrence out of observed zone of the tensile bar (**Figure 9.2 f**). Their growing lead to the specimen breakage [53].

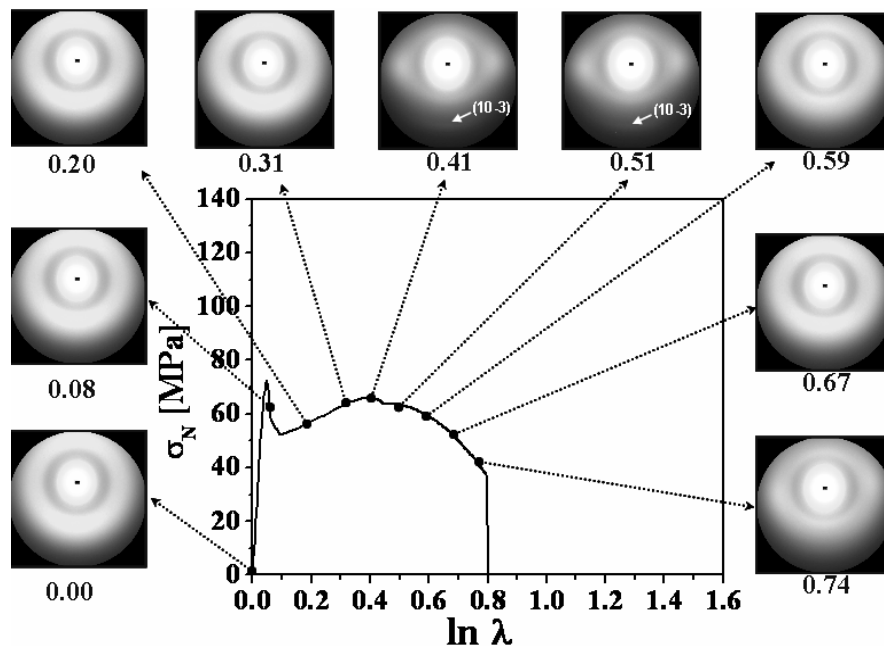


**Figure 9.1.** Neat PET homogeneous stress-strain curve and selected 2D WAXS patterns.

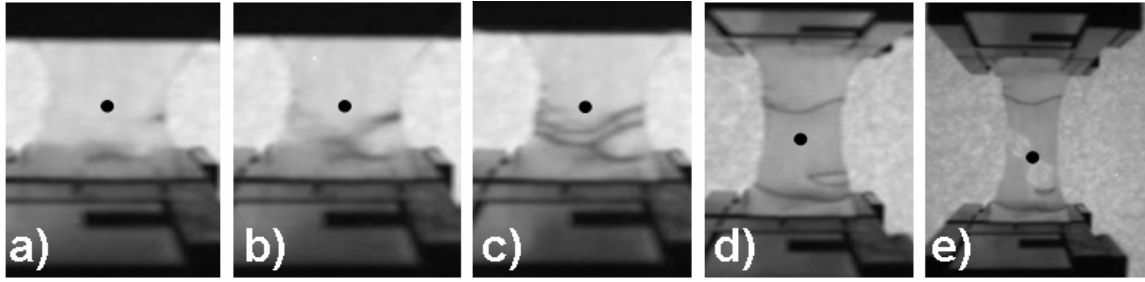


**Figure 9.2.** In situ video images of neat PET sample: a) prior deformation, b) neck initiation, c) neck formation, d) neck propagation and e) tensile bar rupture (the black spot represents approximate X-ray beam incident point).

Equatorial and meridional intensity profiles extracted from 2D WAXS patterns are shown in **Figure 9.3a)** and **Figure 9.3b)** respectively. Initial equatorial and meridional I-2 $\theta$  profiles show an amorphous peak at about  $2\theta = 20^\circ$ . These peaks intensify, up to strain of  $\ln\lambda=0.3$ ; in case of equatorial profile at same radial position, while initial meridional diffraction shifts to a minor angle of around  $2\theta = 19^\circ$ . In the meridional profile stretching progress leads to the appearance at about  $2\theta = 26^\circ$  of the periodical mesophase (10-3) peak and amorphous peak change to an angle around  $2\theta = 16.5^\circ$  [49, 54] Simultaneously the equatorial amorphous peak narrows without significant position change. At strain of  $\ln\lambda=0.6$ , the meridional (10-3) peak disappears and recovers similar to primary profiles shape in both intensity profiles.

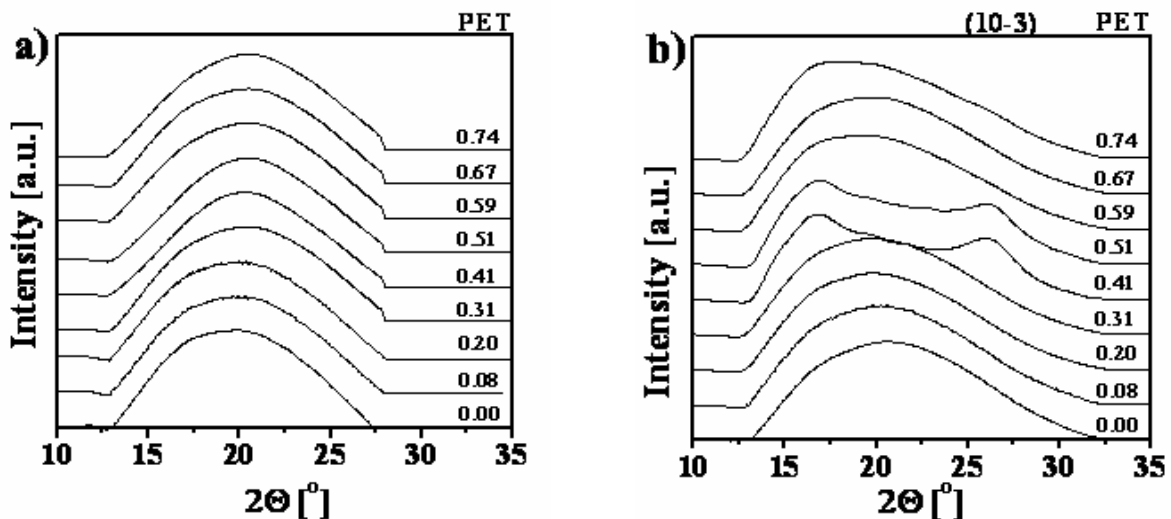


**Figure 9.3.** Linear intensity profiles extracted from 2D WAXS patterns of neat PET: a) equatorial and b) meridional

Phase's and average polymer orientation evolution as function of strain are plotted in the **Figure 9.4**. Judging by the average polymer orientation – strain curve can be divided into three main stages, as designated in **Figure 9.4**. Along the stage I, the average polymer orientation remain constant as the strain increases and originally insignificant mesophase fraction undergoes

a slight increment (with 8.5%). In stage II, a rapid rise of average polymer orientation (about 4 times) into stretching direction is observed, at relatively low change in strain, which caused the sharp increase of mesophase (with 68%) and formation of a small amount of periodical mesophase. Between strain  $0.4 < \ln \lambda < 0.6$  takes place the stage III, where it is observed a plateau reaching a maximum orientation level together with highest mesophase (about 80%) and periodical mesophase (1.5%) contents. Further stretching causes a sudden drop of orientation, to level equal to the stage I, concomitant with polymer chains relaxation, i.e. periodical mesophase is converted into mesophase and mesophase into amorphous one.

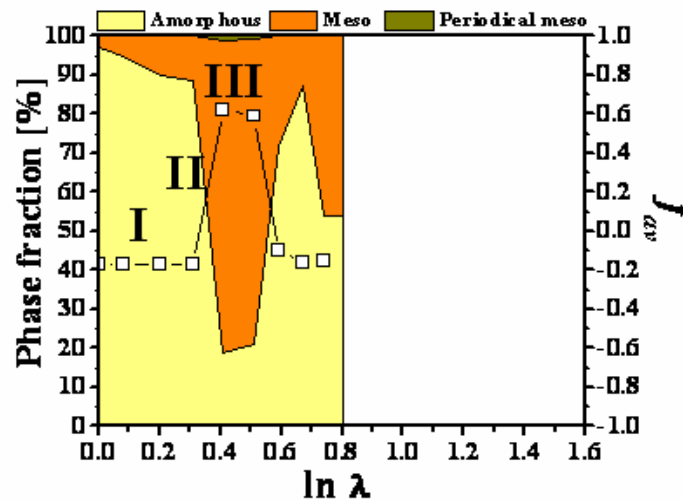


Figure 9.4. Neat PET phase fraction and average polymer orientation,  $f_{av}$ , evolution.

Hereafter, and grounded on the above discussion, the structure evolution of neat PET sample might be summarized as follows:

- Stage I, starts when the stretching initiates and is related to the neck initiation and formation somewhere out of the monitored central part of the tensile bar that caused no changes of average polymer orientation together with some mesophase formation. In this stage, the 2D WAXS patterns is characterized by an amorphous halo correspondent to an equatorial I-20 profiles with amorphous peak at  $2\theta = 20^\circ$  while the meridional one shifts to angle of  $2\theta = 19^\circ$ .

- Stretching advance leads to stage II beginning at  $\ln \lambda = 0.3$  and it last till  $\ln \lambda = 0.4$ . It is associated to the neck propagation through the observed region of the sample. A sharp arise of average polymer orientation. During stage II emerges the meridional reflection (10-3), at around  $2\theta = 26^\circ$ , and two spots at the equator in the 2D WAXS patterns, which translates into narrowing at same position of equatorial peak and shift from  $2\theta = 19^\circ$  to  $2\theta = 16.5^\circ$  of meridional amorphous peak. At the same time, a tremendous amount of amorphous phase transforms into mesophase and subsequently a small of highly oriented mesophase is converted into a periodical mesophase.

○ With end of stage II, becomes the Stage III representative of stable deformation through necking, up to strain of  $\ln\lambda=0.6$ . As a result of this, the polymer chains achieve the plateau of maximum molecular orientation level. This is related to intensification of the two spots on the equator and of the (-103) meridional reflection in the 2D WAXS patterns, as well as without peaks position alterations in the linear intensity profiles. Typical for this stage is a high periodical mesophase and mesophase content. At strain of  $\ln\lambda=0.6$ , rupture of the tensile bar initiates via a macroscopic cracks formation [53], that results loosing and relaxation molecular orientation level evidenced an amorphous halo, in the 2D WAXS pattern that identical to before deformation. But, a high amount of msophase is remained. Such structural changes results into phase's relaxation, i.e. disordering of periodical mesophase into mesophase and mesophase into amorphous one, till phase ratio similar to the as-moulded sample.

### 9.3.2. PET/MMT nanocomposites

#### 9.3.2.1. Nanocomposites morphology

Delamination of MMTs into the polymer matrix was observed by WAXS at low-angle range and TEM experiments. WAXS measurements had not detected any MMT basal peak (001) reflection, which could be attributed to the very low concentration of inorganic nanofillers. The dimensions of MMTs particles measured by TEM are listed in **Table 9.2**. TEM results revealed comparatively homogenous dispersion of both types of MMT's. Intercalated morphology was observed in PET/MMT32 and MMT tactoids morphology for PET/MMT2, as discussed elsewhere [41].

**Table 9.2.** PET/MMT nanocomposites.

Nanocomposite	$D_{av}$ [nm]	$d$ [nm]	Morphology
PET/MMT32	$80 \pm 55$	2.7	Intercalated
PET/MMT2	$365 \pm 300$	1.9	Tactoid

( $D_{av}$  – average agglomerate diameter as calculated by eq.9.1,  $d$  – interplate distance)

#### 9.3.2.2. Structure evolution by WAXS

Homogeneous stress-strain curves and selected 2D WAXS patterns of PET/MMT nanocomposites with different morphologies, PET/MMT32 - intercalated and PET/MMT2 – tactoid, are depicted in **Figure 9.5**. The different reinforcing nature of the intercalated and tactoid MMT's morphologies are evidenced, mainly in terms of attainment stress levels,  $\sigma$ - $\ln\lambda$  curve shape, and deformation capabilities. Intercalated PET/MMT32 morphology improved the deformability and promotes higher stress levels as compare to the PET/MMT2 sample, suggestive for unlike energy dissipation and deformation mechanism [37, 38]. When compared to the pure polymer sample (**Figure 9.1**), PET/MMT32 shows considerable enhancement of the deformation capability and the tactoid structure of PET/MMT2 causes a slight improvement and

a similar curve shape. Nanocomposites specimens, regardless to their morphology, exposed identical neck evolution as the neat PET sample (**Figure 9.2**), due to small concentration of the nanofiller (e.g. 0.3wt%). Hence both nanocomposites feature amorphous 2D WAXS patterns, during the first part of  $\sigma$ - $\ln\lambda$  curve, similar to those of pure PET. This is correspond to a lack of structural evolution as detected by WAXS, originated by delay of the neck propagation thought incident X-ray point on the tensile bar. In 2D WAXS patterns of nanocomposites, when neck propagates through observed region, the periodical mesophase reflection (10-3) at meridian and two spots on the equator envisage at dissimilar strain level, i.e.  $\ln\lambda=0.3$  in case of PET/MMT32 and at  $\ln\lambda=0.4$  for PET/MMT2.

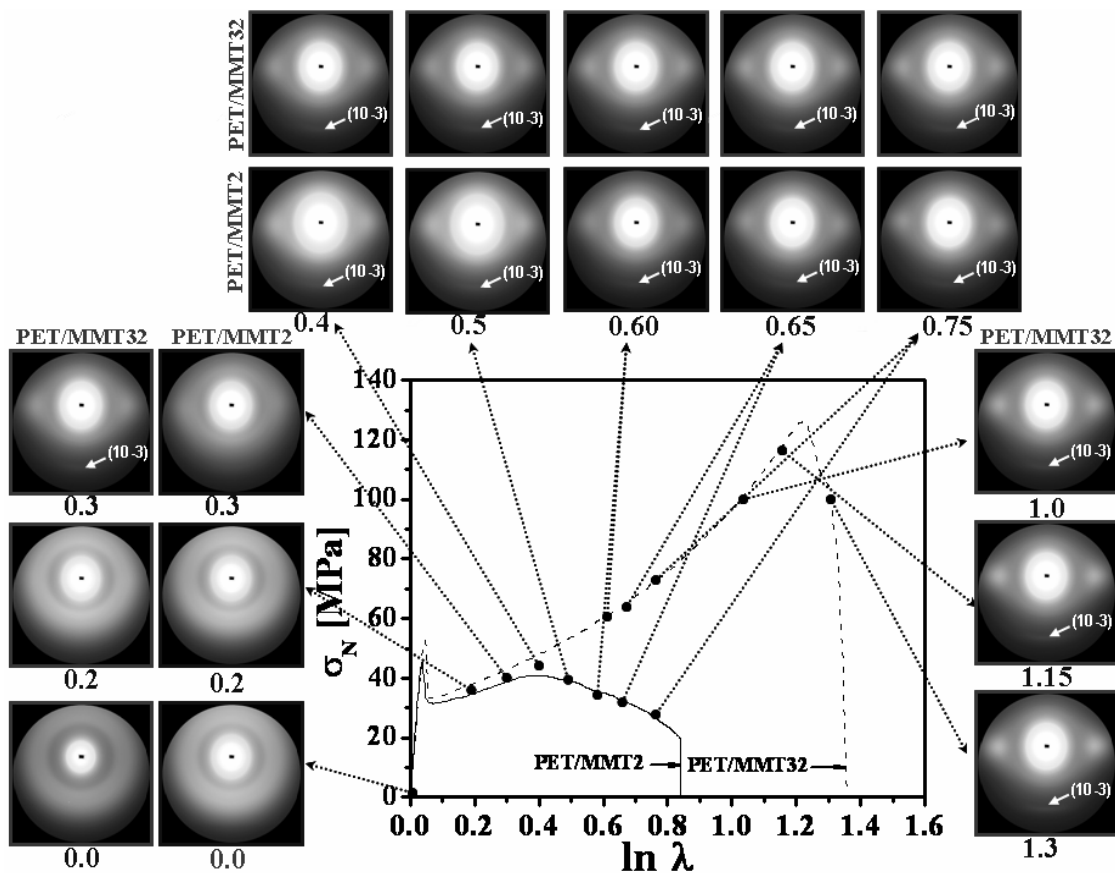


**Figure 9.5.** PET/MMT32 and PET/MMT2 nanocomposites homogeneous stress-strain curve and selected 2D WAXS patterns.

**Figure 9.6.** shows the equatorial and meridional intensity profiles extracted from the 2D WAXS patterns of both PET/MMT nanocomposites. In equatorial the intensity profiles of nanocomposites are observed, before stretching, the amorphous peaks at about  $2\Theta = 20^\circ$ , which intensify with stretching advancement till different strain levels, namely for PET/MMT32 up to  $\ln\lambda=0.3$  and PET/MMT2 respectively to  $\ln\lambda=0.4$ . From these strain further, they intensify with stretching and shift to angle approximately  $2\Theta=21^\circ$ , (**Figure 9.6.a**) and **c**). On the other hand,



the amorphous peaks in the meridional I- $2\Theta$  profiles, during low strain interval, i.e.  $0 < \ln\lambda < 0.3$  for PET/MMT32 and  $0 < \ln\lambda < 0.4$  for PET/MMT2, intensify and shifts from  $2\Theta = 20^\circ$  to  $2\Theta = 19^\circ$ . Thereafter, at about  $2\Theta = 26^\circ$  appears the periodical mesophase peak reflections (10-3), whilst amorphous one change position to around  $2\Theta = 16.5^\circ$ , these peaks intensity increase with stretching (*Figure 9.6.b* and *d*).

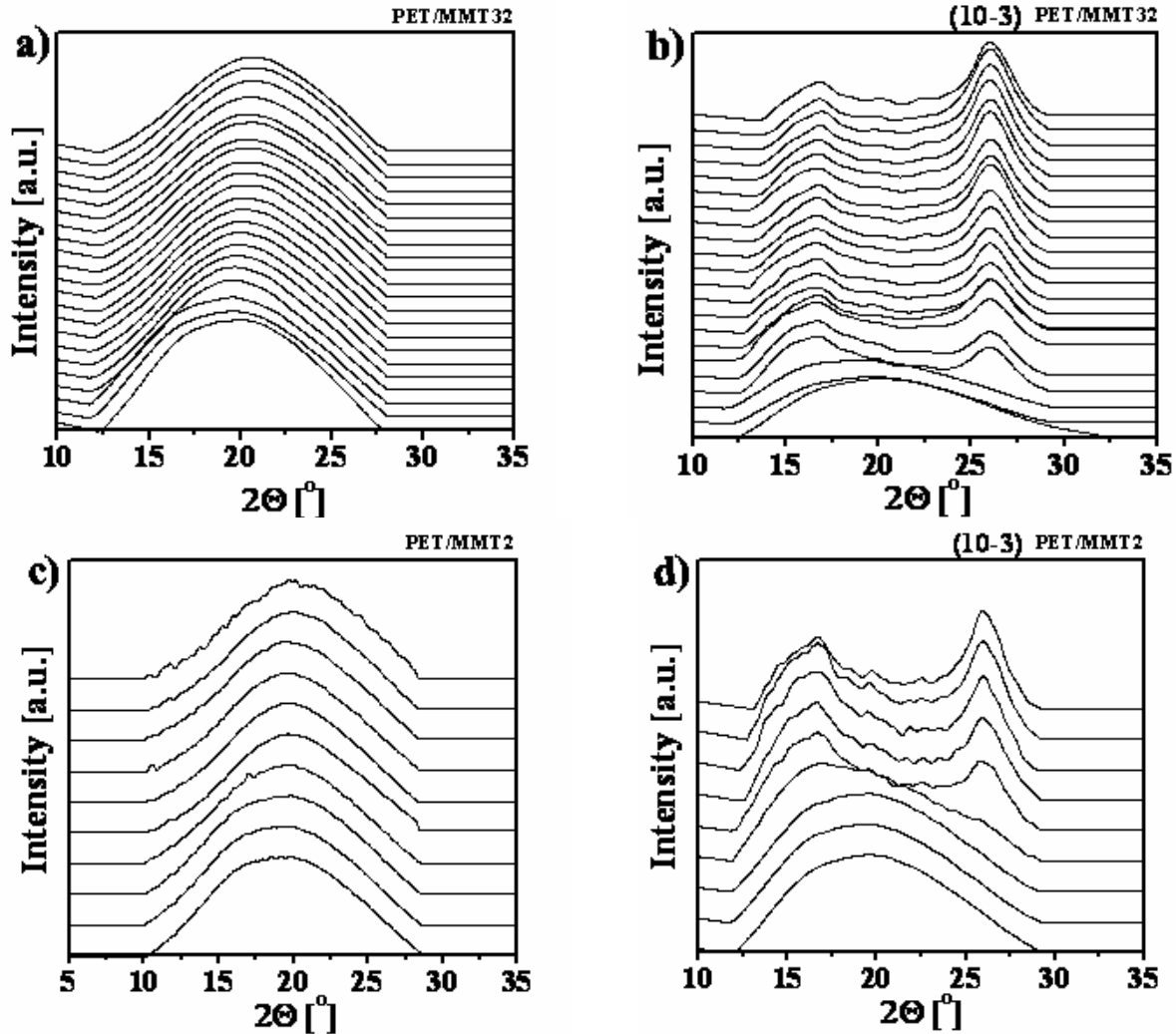


*Figure 9.6.* Linear intensity profiles extracted from 2D WAXS patterns of: PET/MMT32 nanocomposite a) equatorial and b) meridional and PET/MMT2 nanocomposite: c) equatorial and d) meridional,.

Nanocomposites phases and average polymer orientation evolutions with deformation are depicted in *Figure 9.7.a*) for PET/MMT32 and in *Figure 9.7.b*) for PET/MMT2 samples. Based on the similar shapes of the average polymer orientation vs.  $\ln\lambda$  curve, of both nanocomposites, might be defined three main stages as designated in *Figure 9.7*.: i) during stage I, is no variation of polymer orientation while moderate amount of amorphous phase organizes into mesophase. ii) In stage II, there is a sharp increment of average orientation assisted by a rapid mesophase increase due to amorphous phase consumption and a little portion of mesophase orders into periodical mesophase. iii) Finally, in stage III, the samples reach a plateau of maximum

orientation level and also a maximum periodical mesophase content that remain almost without alterations along this stage. The mesophase fraction slightly increases during stretching.

The structure evolution trends for both nanocomposites. Initially, as-moulded PET/MMT2 nanocomposite sample has almost the double amount of mesophase than the PET/MMT32 one (with 18%), due to the nucleation effect of the intercalated MMT morphology [41]. Intercalated PET/MMT32 sample shown anticipate formation of periodical mesophase, at strain of  $\ln\lambda=0.3$ , than the tactoid PET/MMT2 one ( $\ln\lambda=0.4$ ). Along stage III, the nanocomposites are characterized by similar maximum average orientation level (of around  $f_{av}=0.6$ ) and slightly different of periodical mesophase fraction, i.e. about 4% for PET/MMT32 and about 3% for PET/MMT2.

In respect to the PET sample, the nanocomposites apart from their morphology, attained during the stage III: i) similar maximum orientation level and ii) improved amount of mesophase and consequently periodical mesophase. On the other hand, intercalated morphology of PET/MMT32 nanocomposite caused an earlier formation of periodical mesophase than neat PET.

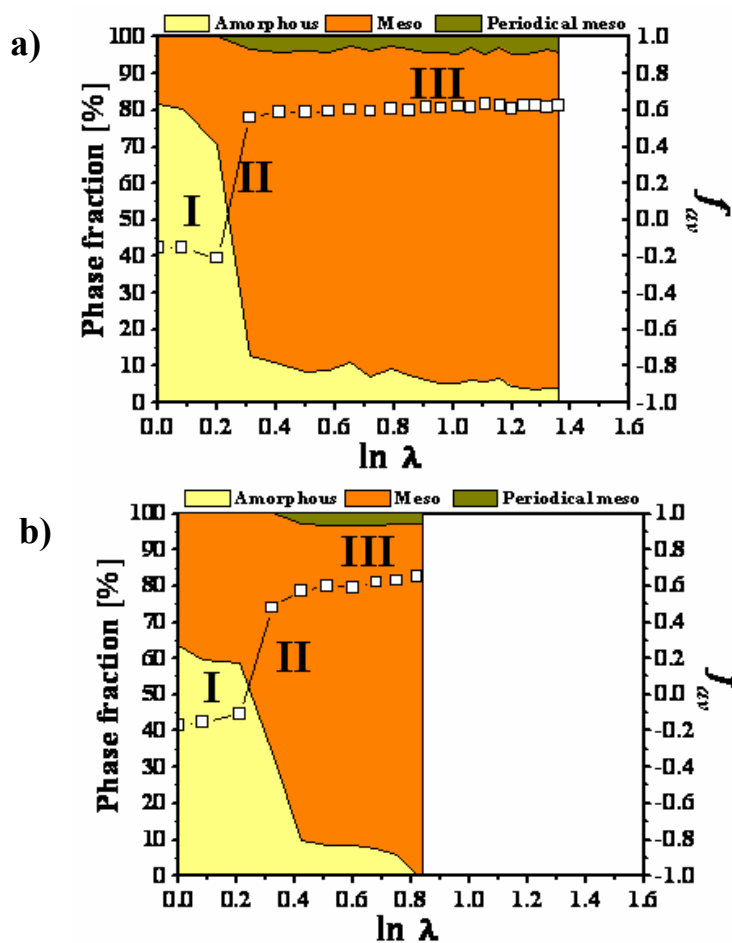


Figure 9.7. Phase fraction and average polymer orientation,  $f_{av}$ , evolution of: a) PET/MMT32 and b) PET/MMT2 nanocomposites.

In summary the general structure evolution of the PET/MMT nanocomposites, assessed by the WAXS investigation, follow three stages:

- Stages I, embraces the low strain levels of mechanical response, before neck forms (out of the sample centre) causing no alterations neither of polymer orientation and nor of amorphous halo in the 2D WAXS pattern, but a slight intensification in both I-2 $\Theta$  profiles and shift to  $2\Theta = 19^\circ$ , associated to transformation of some amorphous phase into mesophase.
- Start of stage II is marked by sharp average polymer orientation increment, caused by necking (over the observed WAXS region), being translated into emergence of two equatorial spots and a meridional (10-3) reflection in the 2D WAXS patterns. Such rapid increase of polymer chains orientation leads to fast formation of a high fraction of mesophase at expansion of the amorphous phase and the nucleation of a periodical mesophase as a result of the mesophase orientation.
- The stable deformation through necking corresponds to the stage III, correspondent to the polymer orientation levelling off at maximum level, where with strain the equatorial spots and the (10-3) reflection in 2D WAXS patterns intensify. Other features of stage III are: intensification and shift of equatorial peak to  $2\Theta = 21^\circ$  and amplification of meridional periodical mesophase peak (10-3), at about  $2\Theta = 26^\circ$ , with amorphous one, at around  $2\theta = 16.5^\circ$ . Whereas periodical mesophase content remains almost intact and the mesophase fraction slightly increase till sample rupture.

### 9.3.3. Structure evolution by SAXS

*Figure 9.8.* shows selected 2D SAXS patterns of neat PET and its MMT nanocomposites obtained along the plastic deformation region of the  $\sigma$ - $\ln\lambda$  curve. Based on the characteristic features occurring in 2D SAXS patterns during stretching it can be denoted distinct differences in structure evolution of nanocomposites, due to dissimilar deformation mechanisms taking place. These are dependent on the specimen morphology.

All samples shown in first patterns a streak parallel to the stretching direction, at  $\ln\lambda=0.2$ , which is originated by crazes within polymer matrix. This is descriptive of reflection at craze/polymer interfaces [55]. Crazes are typical for amorphous polymer during deformation, as reported for neat PET [56-58] and for its nanocomposites [39, 40]. With further stretching, at strain of  $\ln\lambda=0.46$ , the 2D SAXS patterns show different shapes: the streak perpendicular to the loading direction, in case of neat PET, caused by the fibril/void structure elongated in the stretching direction [55, 59] and ii) a cross-shaped pattern was observed for both MMT nanocomposites, where the meridional streak is representative of reflection at the craze/polymer

interfaces [55, 59] and the equatorial one originated mainly by fibril/void structure of crazes and some of the voids formed inside the MMT particles and tactoid respectively [37, 38].

These dissimilar patterns shape, at identical strain, can be related to retarded growth of the crazes in the polymer bulk, as compared to the neat PET, due to MMT's incorporation, [39, 40]. Further stretching, greater than  $\ln\lambda=0.7$ , leads to the transformation of 2D SAXS patterns of all investigated samples into equatorial streaks associated to voids elongated parallel to the stretching direction [59]. Those might caused by elongated voids inside the crazes within polymer matrix and by voids between the MMTs particles [60].

On the other hand, by the equatorial streaks height it may be estimated the void's height and from its length their diameter [55, 59]. Qualitatively analyses at the dimensions of the equatorial streaks, at strains greater than  $\ln\lambda=0.7$  till samples breakage, suggested that voids in the neat PET sample have a slightly bigger or similar height and diameter to those in the PET/MMT2 nanocomposites. The PET/MMT32 nanocomposite seems to have the voids with smallest height and diameter in between the studied samples. Whereas among the PET/MMT nanocomposites its appears that tactoid morphology of PET/MMT2 nanocomposite induce a bigger size voids than the intercalated PET/MMT32 one [37, 38].

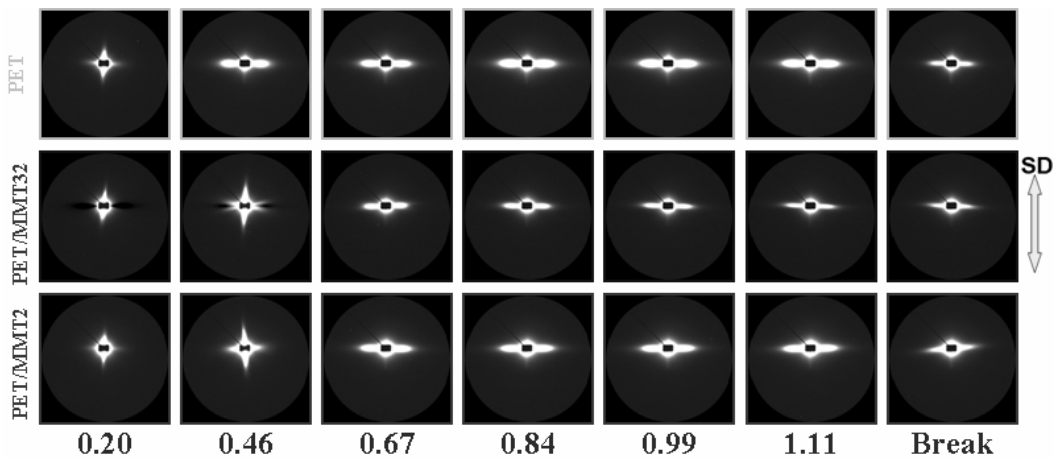


**Figure 9.8.** Selected 2D SAXS patterns and corresponding homogeneous strain,  $\ln\lambda$ , obtained during the in situ SAXS characterization.

## 9.4. Multi scale structure evolution model

Strain-induced structure transitions and deformation mechanism upon uniaxial stretching in solid state of PET and its MMT nanocomposites can be interpreted by the multiscale models depicted in *Figure 9.9.* to *Figure 9.11.*

### 9.4.1. Multiscale structure evolution of neat PET

Multiscale structure evolution of neat PET sample can be resumed:

- Stage I: where neck forms along the tensile bar out of observed region, descriptive for the structure evolution at initial strain levels before necking. A small amount of initial isotropic amorphous phase transform into mesophase, at levelled off polymer orientation.
- Stage II: is the shortest stage correspondent to the neck formation under X-ray beam: crazes are formed and widen perpendicular to the stretching direction. The polymer chains achieve the maximum orientation level causing a rapid transformation of oriented amorphous phase into mesophase and promote appearance of periodical mesophase originated by the orientation of the mesophase.
- Stage III: is related to the tensile bar lengthening through necking, where voids within crazes extent into the stretching direction, causing maximum polymer chains orientation. This orientation level corresponds to the polymer chains extensibility limits resulting into maximum content of highly oriented mesophase and periodical mesophase. At ultimate strain levels, sample ruptures, via fail of fibrils within crazes so originating the micro-voids enlargement till sample collapse. In this case, micro-voids evolve into macro-cracks [55] causing a local relaxation of polymer orientation, and periodical mesophase into mesophase and mesophase into amorphous phase.

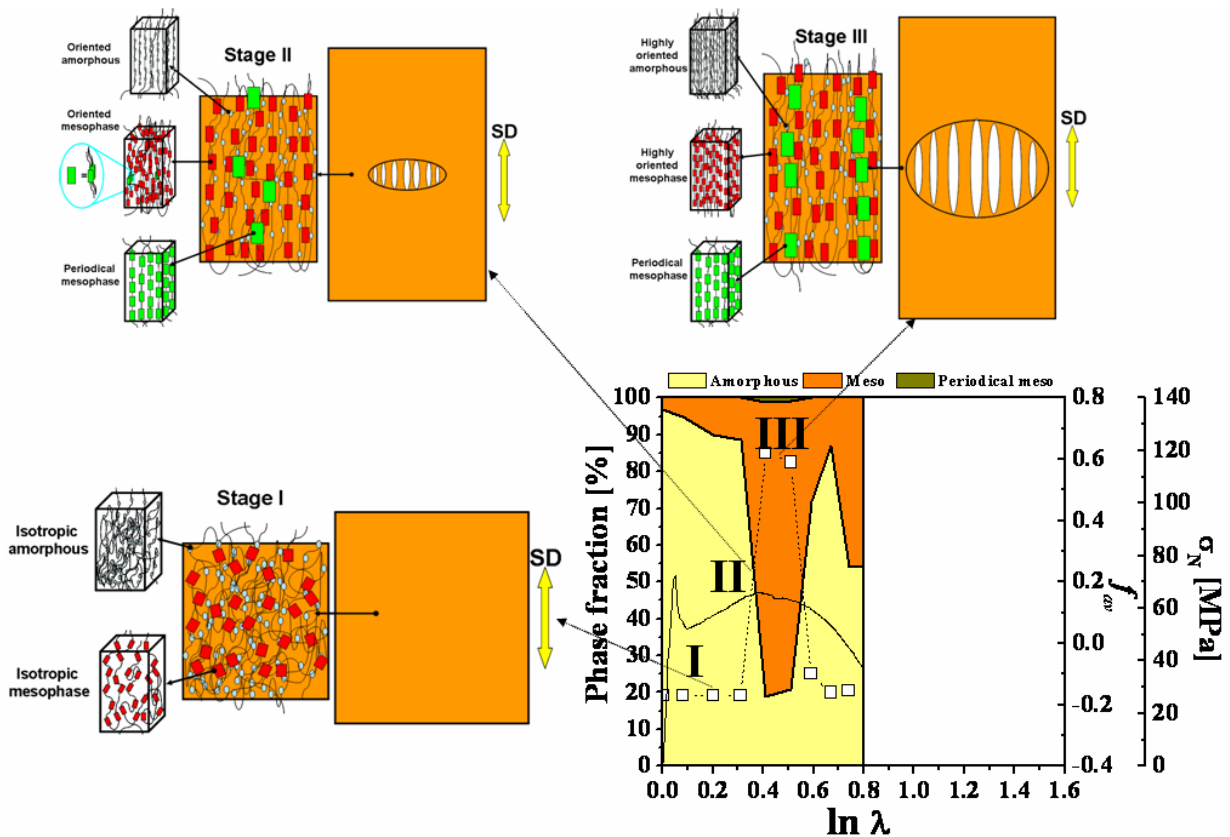
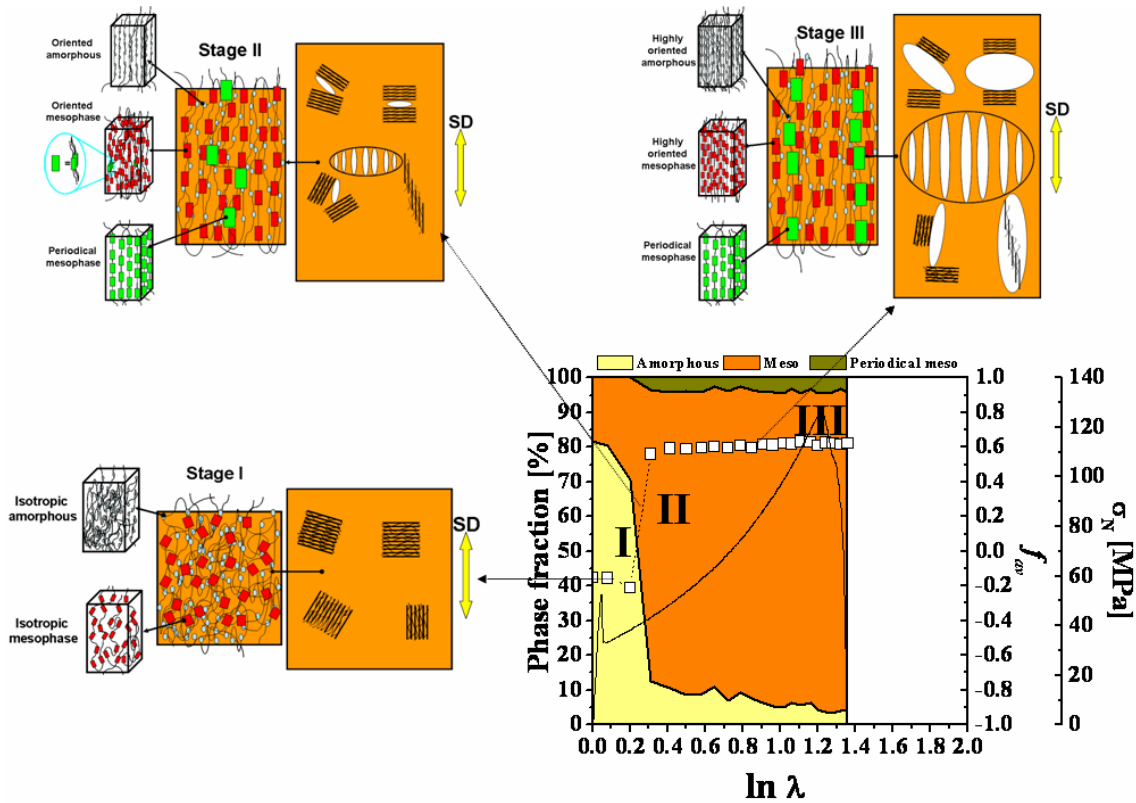


Figure 9.9. Schematic diagram illustrates the multiscale structure evolution during in solid state uniaxial stretching of neat PET.

### 9.4.2. Multiscale structure evolution of PET/MMT nanocomposites

The description of multiscale model of strain-induced structure evolution of intercalated PET/MMT nanocomposite during the stretching in solid state, considering the MMT's agglomerates three possible modes of deformation [37, 38], is shown in **Figure 9.10**.



**Figure 9.10.** Schematic diagram illustrates the multiscale structure evolution during in solid state uniaxial stretching of intercalated PET/MMT nanocomposite

Main three stages are:

- Stage I: its duration is from start of stretching till necking under the X-ray beam, along which is absent an increment of average polymer orientation values, although a minor amount of amorphous phase fraction organises into mesophase.
- Stage II: is representative of the fast neck spread over the tensile bar centre, leading to crazes formation/widening within polymer bulk, and concomitant by voids inside the intercalated MMT's particles. A rapid polymer chains orientation into stretching direction is promoted, causing the phase's orientation and evolution of an orientated amorphous phase into mesophase and of a little part of oriented mesophase into periodical mesophase.
- During Stage III, sample deforms and in polymer matrix the crazes enlarge perpendicular to the stretching direction, which is partially impeded by inorganic particles [39], while voids within the crazes and those from the MMTs particle elongate into micro-voids

parallel to the stretching direction. Here, the polymer chains are approaching their extensibility limit causing a plateau of orientation level. It is formed a maximum periodical mesophase fraction, which is maintained alike up to sample rupture. Despite that, with strain progress a slow transformation of remaining amorphous phase fraction into mesophase is observed. At ultimate strain, sample ruptures via macro-cracks formed.

Generally, the evolution of both nanocomposite morphologies, i.e. intercalate and tactoid, have a quite similar pathway, main difference is the bigger size of voids caused by the deformation of the MMTs tactoids [37]. Multiscale model of tactoid PET/MMT nanocomposite is illustrated in *Figure 9.11*.

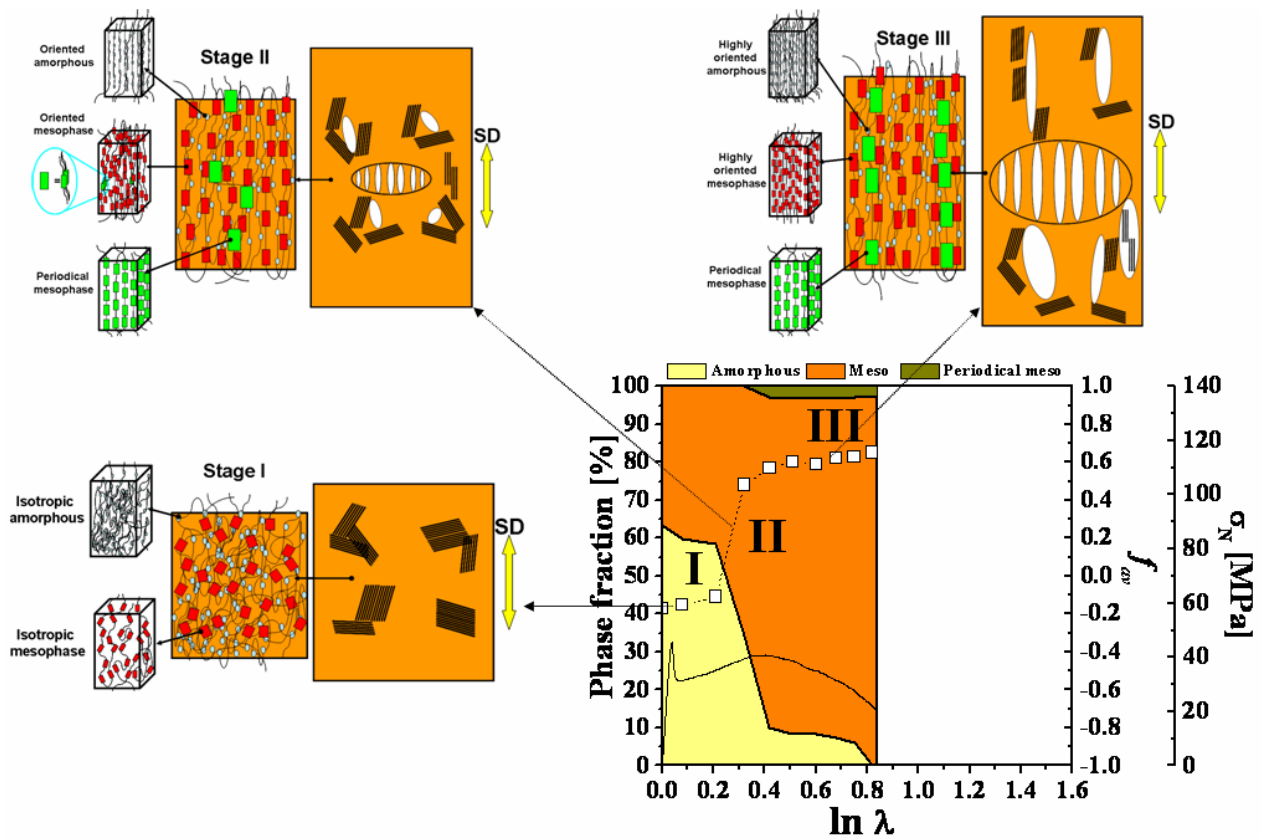


*Figure 9.11. Schematic diagram illustrates the multiscale structure evolution during in solid state uniaxial stretching of tactoid PET/MMT nanocomposite.*

Main stages are:

- Stage I: has a duration from start of stretching till neck reaches the observed part of the sample, where no evolution of polymer orientation is detected, but a slight development of mesophase from isotropic amorphous is present.
- As the neck disseminates over the region, polymer crazes and the MMT's tactoids break, creating voids inside the tactoids [37, 38], this taking part during the Stage II. However, process of crazes widening is hampered by MMTs tactoids [39]. The polymer chains orient fast

into stretching direction that leads to development of a mesophase from the amorphous phase and to formation of a periodical mesophase.

- Stage III: is characterized by stable necking, together with voids within crazes and those originate by the MMTs tactoids advancing into micro-voids. All that results into a plateau of polymer orientation and greatest amount of periodical mesophase, till sample breakage. With deformation progress, a slow transformation of oriented amorphous into mesophase occurs.

## **9.5. Conclusions**

The evolution of strain-induced phase transition and average polymer orientation with strain increment was investigated for all samples. Both MMT morphologies show distinct structure evolution during stretching. Distinct structural models were proposed for each type of initial MMT nanocomposite morphology and neat PET, interpreting the obtained experimental results.

Intercalate PET/MMT32 exposed considerable enhancement of attained stress level and deformation capability of polymer matrix in comparison to the neat PET, while the tactoid structure of PET/MMT2 cause only a slight improvements. All investigate samples, regardless there morphology, reached similar maximum orientation level. Incorporating MMT nanofillers in PET matrix promoted a higher fraction of mesophase and at elevated strains of periodical mesophase as compared to neat PET. MMT intercalation in case of PET/MMT32 causes an earlier formation and enhanced amount of periodical mesophase than the tactoid PET/MMT2 and neat PET samples, while in case of pure matrix, the improvement was significantly bigger than the PET/MMT2. Crazes appear within the PET matrix in all samples, at earlier stages of plastic deformation. Both nanocomposites morphologies retarded crazes widen within the polymer bulk. Intercalated morphology PET/MMT32 leads to formation of voids with smallest height and diameter in between the considered specimens. Tactoid PET/MMT2 sample results into voids with dimensions alike to the pure PET. WAXS/SAXS results indicated a three stages multiscale mechanism of structure evolution for neat PET and its nanocomposites.



## 9.6. References

1. Koo, J.H., *Polymer Nanocomposites Processing, Characterization, and Applications*. 2006, New York: McGraw-Hill.
2. Shah, D., et al., *Dramatic Enhancements in Toughness of Polyvinylidene Fluoride Nanocomposites via Nanoclay-Directed Crystal Structure and Morphology*. *Advanced Materials*, 2004. **16**(14): p. 1173-1177.
3. Dennis, H.R., et al., *Effect of melt processing conditions on the extent of exfoliation in organoclay-based nanocomposites*. *Polymer*, 2001. **42**(23): p. 9513-9522.
4. Jordan, J., et al., *Experimental trends in polymer nanocomposites - A review*. *Materials Science and Engineering A*, 2005. **393**(1-2): p. 1-11.
5. Paul, D.R. and L.M. Robeson, *Polymer nanotechnology: Nanocomposites*. *Polymer*, 2008. **49**(15): p. 3187-3204.
6. Tjong, S.C., *Structural and mechanical properties of polymer nanocomposites*. *Materials Science and Engineering: R: Reports*, 2006. **53**(3-4): p. 73-197.
7. Liu, J., et al., *Intercalation and Exfoliation: A Review on Morphology of Polymer Nanocomposites Reinforced by Inorganic Layer Structures*. *Materials and Manufacturing Processes*, 2006. **21**(2): p. 143 - 151.
8. Ray, S.S. and M. Okamoto, *Polymer/layered silicate nanocomposites: A review from preparation to processing*. *Progress in Polymer Science (Oxford)*, 2003. **28**(11): p. 1539-1641.
9. Ke, Y.C., Z.B. Yang, and C.F. Zhu, *Investigation of properties, nanostructure, and distribution in controlled polyester polymerization with layered silicate*. *Journal of Applied Polymer Science*, 2002. **85**(13): p. 2677-2691.
10. Ke, Y., C. Long, and Z. Qi, *Crystallization, properties, and crystal and nanoscale morphology of PET-clay nanocomposites*. *Journal of Applied Polymer Science*, 1999. **71**(7): p. 1139-1146.
11. Wan, T., et al., *Crystalline morphology and isothermal crystallization kinetics of poly(ethylene terephthalate)/clay nanocomposites*. 2004. **94**(4): p. 1381-1388.
12. Chang, J.H., et al., *Poly(ethylene terephthalate) nanocomposites by in situ interlayer polymerization: The thermo-mechanical properties and morphology of the hybrid fibers*. *Polymer*, 2004. **45**(3): p. 919-926.
13. Kim, S.H. and S.C. Kim, *Synthesis and properties of poly(ethylene terephthalate)/clay nanocomposites by in situ polymerization*. 2007. p. 1262-1271.
14. Choi, W.J., et al., *Preparation and barrier property of poly(ethylene terephthalate)/clay nanocomposite using clay-supported catalyst*. *Journal of Applied Polymer Science*, 2006. **100**(6): p. 4875-4879.
15. Chang, J.H. and S.J. Kim, *Polyester nanocomposite fibers: comparison of their properties with poly(ethylene terephthalate) and poly(trimethylene terephthalate) (II)* *Polymer Bulletin*, 2004. **52**: p. 289-296.
16. Zhang, G., T. Shichi, and K. Takagi, *PET-clay hybrids with improved tensile strength*. *Materials Letters*, 2003. **57**(12): p. 1858-1862.
17. Hao, J., et al., *Synthesis of poly(ethylene terephthalate)/clay nanocomposites using aminododecanoic acid-modified clay and a bifunctional compatibilizer*. *Journal of Applied Polymer Science*, 2006. **101**(2): p. 1057-1064.
18. Tsai, T.Y., et al., *Preparation of Exfoliated Polyester/Clay Nanocomposites*. *Advanced Materials*, 2005. **17**(14): p. 1769-1773.
19. Ke, Y., C. Long, and Z. Qi, *Crystallization, Properties, and Crystal and Nanoscale Morphology of PET-Clay Nanocomposites*. *Journal of Applied Polymer Science*, 1999. **71**: p. 1139-1146.

20. Ou, C.F., M.T. Ho, and J.R. Lin, *Synthesis and characterization of poly(ethylene terephthalate) nanocomposites with organoclay*. Journal of Applied Polymer Science, 2004. **91**(1): p. 140-145.
21. Barber, G.D. and R.B. Moore. *Application of an Ionomeric Compatibilizer for Organically-modified Montmorillonite/PET Nanocomposites*. in ACS PMSE Proceedings. 2000.
22. Ou, C.F., M.T. Ho, and J.R. Lin, *The Nucleating Effect of Montmorillonite on Crystallization of PET/Montmorillonite Nanocomposite*. Journal of Polymer Research, 2003. **10**(2): p. 127-132.
23. Sanchez-Solis, A., A. Garcia-Rejon, and O. Manero, *Production of nanocomposites of PET-montmorillonite clay by an extrusion process* Macromol. Symp., 2003. **192**: p. 281-292
24. Davis, H.R., et al., *Effects of melt-processing conditions on the quality of poly(ethylene terephthalate) montmorillonite clay nanocomposites*. Journal of Polymer Science: Part B: Polymer Physics, 2002. **40**(23): p. 2661-2666.
25. Wang, Y., et al., *Study on mechanical properties, thermal stability and crystallization behavior of PET/MMT nanocomposites*. Composites Part B: Engineering, 2006. **37**(6): p. 399-407.
26. Barber, G.D., B.H. Calhoun, and R.B. Moore, *Poly(ethylene terephthalate) ionomer based clay nanocomposites produced via melt extrusion*. Polymer, 2005. **46**(17): p. 6706-6714.
27. Sanchez-Solis, A., et al., *Mechanical and rheological studies on polyethylene terephthalate-montmorillonite nanocomposites*. Polymer Engineering and Science, 2004. **44**(6): p. 1094-1102.
28. Pegoretti, A., et al., *Recycled poly(ethylene terephthalate)/layered silicate nanocomposites: morphology and tensile mechanical properties*. Polymer, 2004. **45**(8): p. 2751-2759.
29. Bizarria, M.T.M., et al., *Morphology and thermomechanical properties of recycled PET-organoclay nanocomposites*. Journal of Applied Polymer Science, 2007. **104**(3): p. 1839-1844.
30. Kracalik, M., et al., *Recycled PET-organoclay nanocomposites with enhanced processing properties and thermal stability*. Journal of Applied Polymer Science, 2007. **106**(3): p. 2092-2100.
31. Kracalik, M., et al., *Effect of 3D structures on recycled PET/organoclay nanocomposites*. Polymer Bulletin, 2007. **58**(1): p. 313-319.
32. Chung, J.W., et al., *Thermally stable exfoliated poly(ethylene terephthalate) (PET) nanocomposites as prepared by selective removal of organic modifiers of layered silicate*. Polymer Degradation and Stability, 2008. **93**(1): p. 252-259.
33. Sanchez-Solis, A., et al., *Properties of poly(ethylene terephthalate)-poly(ethylene naphthalene 2,6-dicarboxylate) blends with montmorillonite clay*. Polymer International, 2005. **54**(12): p. 1669-1672.
34. Todorov, L.V. and J.C. Viana, *Characterization of PET nanocomposites produced by different melt-based production methods*. Journal of Applied Polymer Science, 2007. **106**(3): p. 1659-1669.
35. Bizarria, M.T.M., et al., *Morphology and thermomechanical properties of recycled PET-organoclay nanocomposites*. 2007. p. 1839-1844.
36. Alyamac, E. and U. Yilmazer, *Reactive extrusion of poly(ethylene terephthalate)-(ethylene/methyl acrylate/glycidyl methacrylate)-organoclay nanocomposites*. Polymer composites, 2007. **28**(2): p. 251-258.
37. Kim, G.M., et al., *Influence of nanofillers on the deformation process in layered silicate/polyamide-12 nanocomposites*. Polymer, 2001. **42**(3): p. 1095-1100.
38. Kim, G.M., S. Goerlitz, and G.H. Michler, *Deformation mechanism of nylon 6/layered silicate nanocomposites: Role of the layered silicate*. Journal of Applied Polymer Science, 2007. **105**(1): p. 38-48.

39. Kobayashi, H., et al., *Synchrotron radiation small-angle X-ray scattering study on fracture process of carbon nanotube/poly(ethylene terephthalate) composite films*. Composites Science and Technology, 2007. **67**(15-16): p. 3209-3218.
40. Kobayashi, H., et al., *A comparative study of fracture behavior between carbon black/poly(ethylene terephthalate) and multiwalled carbon nanotube/poly(ethylene terephthalate) composite films*. Journal of Applied Polymer Science, 2007. **106**(1): p. 152-160.
41. Todorov, L.V., C.I. Martins, and J.C. Viana, *Characterization of PET nanocomposites with different nanofillers*. Solid State Phenomena, 2009. **151**: p. 113-117.
42. Oultache, A.K., et al., *Orientation and relaxation of orientation of amorphous poly(ethylene terephthalate)*. Polymer, 2001. **42**(21): p. 9051-9058.
43. Goschel, U., K. Deutschert, and V. Abetz, *Wide-angle X-ray scattering studies using an area detector: crystalline orientation in semisrystalline PET structures*. Polymer, 1996. **37**(1): p. 1-6.
44. Stribeck, N., *X-Ray Scattering of Soft Matter*. 2007: Springer Berlin Heidelberg New York.
45. Michler, G.H. and F.J. Baltá-Calleja, *Mechanical Properties of Polymers Based on Nanostructure and Morphology*. 2005, Boca Raton, London, New York, Singapore: Taylor & Francis Group.
46. Ran, S., et al., *Mesophase as the Precursor for Strain-Induced Crystallization in Amorphous Poly(ethylene terephthalate) Film*. Macromolecules 2002(35): p. 10102-10107
47. Blundell, D.J., et al., *Characterization of strain-induced crystallization of poly(ethylene terephthalate) at fast draw rates using synchrotron radiation*. Polymer, 1996. **37**(15): p. 3303-3311.
48. Kawakami, D., et al., *Mechanism of Structural Formation by Uniaxial Deformation in Amorphous Poly(ethylene terephthalate) above the Glass Temperature*. Macromolecules, 2003(36): p. 9275-9280.
49. Kawakami, D., et al., *Structural formation of amorphous poly(ethylene terephthalate) during uniaxial deformation above glass temperature*. Polymer, 2004. **45**(3): p. 905-918.
50. Kawakami, D., et al., *Superstructure Evolution in Poly(ethylene terephthalate) during Uniaxial Deformation above Glass Transition Temperature*. Macromolecules, 2006. **39**: p. 2909-2920.
51. Parravicini, L., et al., *Crystallization of poly(ethylene terephthalate) (PET) from the oriented mesomorphic form*. Journal of Applied Polymer Science, 1994. **52**(7): p. 875-885.
52. Goschel, U., *Thermally stimulated structural changes in highly oriented glassy poly(ethylene terephthalate)*. Polymer, 1996. **37**(18): p. 4049-4059.
53. Takemori, M.T., *Competition between crazing and shear flow during fatigue*. Advances in Polymer Science 1990. **91/92**: p. 263-300.
54. Kawakami, D., et al., *Mechanism of Structural Formation by Uniaxial Deformation in Amorphous Poly(ethylene terephthalate) above the Glass Temperature*. Macromolecules, 2003. **36**: p. 9275-9280.
55. Shioya, M., et al., *Small-Angle X-ray Scattering Study on the Tensile Fracture Process of Poly(ethylene terephthalate) Fiber*. Macromolecules, 2008. **41**(13): p. 4758-4765.
56. Liu, Y., et al., *Characterization of stress-whitening of tensile yielded isotactic polypropylene*. Polymer, 1997. **38**(11): p. 2797-2805.
57. Viana, J.C., et al., *Nanostructure Evolution during Uni-axial Deformation of PET – a WAXS and SAXS Study using Synchrotron Radiation*. Materials Science Forum, 2006(514-516 ): p. 1583-1587.
58. Efimov, A.V., V.Y. Shcherba, and N.F. Bakeyev, *Effect of drawing conditions on structural parameters of crazes in crystalline poly(ethylene terephthalate)*. Polymer Science U.S.S.R., 1991. **33**(3): p. 568-574.

59. Stribeck, N., et al., *SAXS-Fiber Computer Tomography. Method Enhancement and Analysis of Microfibrillar-Reinforced Composite Precursors from PEBA and PET*. *Macromolecules* 2008. **41**: p. 7637-7647.
60. Ren, C., et al., *Microstructure and Deformation Behavior of Polyethylene/Montmorillonite Nanocomposites with Strong Interfacial Interaction*. *The Journal of Physical Chemistry B*, 2009. **113**(43): p. 14118-14127.



# CHAPTER X

## *In situ* WAXS/SAXS structural evolution study during uniaxial stretching of PET nanocomposites in solid state: PET/SiO<sub>2</sub> and PET/TiO<sub>2</sub> nanocomposites

This work reports an *in situ* WAXS and SAXS investigation on the structure evolution during solid state uniaxial deformation, under X-ray synchrotron source radiation, of PET nanocomposites with 0.3wt% of nanotitanium dioxide, TiO<sub>2</sub> and nanosilica, SiO<sub>2</sub>. Good dispersion and alike average agglomerate sizes of about 80 nm for both nanocomposites were revealed by TEM characterization. The influence of the nanofillers on the deformation-induced phase's formation and their evolution along stretching process were compared with respect to the neat PET. WAXS results indicated that all samples evolution pass through three stages: i) stage I (before necking), a small amount of amorphous phase evolves into mesophase at constant molecular orientation level; ii) stage II (neck propagation), originate crazes and voids appearance and a rapid increase of polymer molecular orientation causes a sharp increment of mesophase at the expense of the amorphous phase and the formation of a periodical mesophase from the oriented mesophase; iii) stage III (necking), corresponds to voids lengthening and at leveling off of average polymer molecular orientation; the highest periodical mesophase content is achieved, as well as a slight increment of mesophase. Incorporation of the nanofillers promoted a higher fraction and an earlier formation of periodical mesophase during stretching, as compared to pure PET. Superior deformation capability, in respect to neat PET, was observed by the nanocomposites. By SAXS experiments, it is observed a craze/void formation, where the TiO<sub>2</sub> caused some bigger voids than the SiO<sub>2</sub>. A multiscale structure evolution mechanism was proposed.

*This chapter is adapted from the following publication:*

**Todorov L.V., Martins C.I., Viana J.C.** *In situ* WAXS/SAXS structural evolution study during uniaxial stretching of PET nanocomposites in solid state: PET/SiO<sub>2</sub> and PET/TiO<sub>2</sub> nanocomposites. Composites Science and Technology, Submitted

## 10.1. Introduction

Nowadays one of the most widely used material for plastic packaging is poly(ethylene terephthalate), PET, due to its enhanced mechanical, thermal and barrier properties. An alternative for performance improvement of PET, generally consisting in the enhancement of mechanical, thermal and barrier properties, is the reinforcement of neat polymer matrix with different inorganic nanoparticles, i.e. PET nanocomposites. PET can be reinforced with three main types of nanofillers, depending on the number of dimensions on the nanometer scale, namely: (i) 1D, with one dimension (e.g. nanoclays), (ii) 2D, with two dimensions, (e.g. carbon nanotubes), (iii) 3D, with three dimensions, usually with spherical like shape, (e.g. nanosilica, SiO<sub>2</sub>, and nanotitanium dioxide, TiO<sub>2</sub>) [1].

Recently, specific interest was devoted to PET/3D nanocomposites, in particular PET/TiO<sub>2</sub> [2-5] and PET/SiO<sub>2</sub> [5-15], obtained via various preparation methods. Incorporation of isodimensional nano TiO<sub>2</sub> into PET matrix was carried out via: i) *in situ* polymerization [3], ii) solvent-assisted [2] and iii) melt blending [4] techniques. Much more interest received SiO<sub>2</sub> as nanoreinforcement for PET, as compared to TiO<sub>2</sub>. For PET/SiO<sub>2</sub> nanocomposites, preparation methods being used are: i) *in situ* polymerization [6, 7, 10-12], ii) solvent-assisted [2], iii) melt blending [4, 13] and iv) cryomilling blending [14, 15]. Between all compounding methods, the melt blending was recognized as most suitable for commercial scale production [16]. Enhanced mechanical performance, in comparison to neat PET, was reported for PET/TiO<sub>2</sub> and PET/SiO<sub>2</sub> nanocomposites, prepared via melt blending techniques, i.e. increment of: i) elastic modulus [4, 5, 12, 13], ii) yield stress [5], iii) maximum stress [4] and iv) deformation capability [12, 13].

The understanding of the mechanisms underlying these enhancements, as well as the effect of inorganic nanofillers on the structure evolution, is crucial for successful application of polymer nanocomposites. In this regards, a very few attempts have been made to study those in details. Kim and Michler [17, 18] studied the toughening mechanisms occurring in semicrystalline polymer nanocomposites by several electron microscopic techniques. Based on these investigations they proposed three stages deformation mechanisms for nanocomposites with spherical nanofillers, namely: i) stage I, where the nanoparticles agglomerates act as a stress concentrators, due to their different elastic properties that leads to agglomerates dilatation; ii) stage II, due to stress concentration, voids formation through debonding occurs within the agglomerates; iii) stage III - once the voids have occurred, corresponding to an increase in the shear stress component, and as a consequence further shear yielding is greatly induced in the matrix. Reynaud et al. [19] investigated the effect of SiO<sub>2</sub> nanoparticle size and suggested that: i) smaller nanoparticles gather into smaller aggregates that leads to a multiple debonding process, correspondent to multiple voids with dimensions similar to the particle size and ii) bigger

nanoparticles forming bigger aggregates, respectively undergoes a single debonding process, causing bigger size voids [17, 18]. It is also well known [20-22], grounded on the time resolved SAXS investigations, that during uniaxial stretching in solid state of amorphous polymers is accompanied by a substantial structural damage that occurs by voids nucleation and propagation. Macroscopically this is revealed by the whitening of the specimen upon deformation.

To improve and control the ultimate mechanical properties for a wide range of applications and, in particular, to optimize the stiffness/toughness balance, a better understanding of the interrelationships between nanoparticles nature and structure evolution during the deformation processes is clearly required. In this regards, this work aims on revealing the effect of incorporated different 3D nanoparticles, i.e. TiO<sub>2</sub> and SiO<sub>2</sub>, into PET polymer matrix on the structural evolution and deformation mechanism during the uniaxial stretching in the solid state.

## 10.2. Experimental

### 10.2.1. Materials

In this work the following materials were used:

- Poly(ethylene terephthalate), PET, with intrinsic viscosity of  $0.74 \pm 0.02 \text{ dl.g}^{-1}$  (bottle grade) as polymer matrix,
- 3D nanoreinforcements with spherical-like shape: i) nanotitanium dioxide, TiO<sub>2</sub>, (AEROXIDE TiO<sub>2</sub> P25) consists of 80% anatase and 20% rutile and ii) nanosilica, SiO<sub>2</sub>, (AEROSIL 200), which specifications are given in Table 1 according to the supplier Degussa AG, Germany.

*Table 10.1. Nanoparticles specifications (supplier data).*

Nanofiller	$D_{av}$ [nm]		Surface area* [m <sup>2</sup> g <sup>-1</sup> ]
	Aggl.	Particles	
TiO <sub>2</sub>	100	≈ 21	50 ± 15
SiO <sub>2</sub>	100	≈ 12	200 ± 25

*(D<sub>av</sub> – main average diameter, Aggl. – powder agglomerate, \* - Specific surface according to BET).*

Samples used in this work were produced via direct melt blending with content of 0.3 wt% of each nanofiller, according to the experimental protocol described in our previous work (*Chapter IX*) [23]. Specimens were cut from compression moulded plaques.

### 10.2.2. Transmission Electron Microscope, TEM

Ultramicrotome cuts made through the thickness sections of the compression moulded samples, with an approximate thickness of 60 nm, were used. TEM observation was carried out under an operation voltage of 100 kV on a JEOL JEM 1010. Three micrographs per nanocomposite were used for particles agglomerates measurements from randomly transversal



cuts. 3D particles agglomerates incorporated into PET nanocomposites were assumed to be elliptical. The average agglomerates diameter,  $D_{av}$ , was calculate by:

$$D_{av} = \frac{\sum_{i=1}^n [(d_1 + d_2)_i / 2]}{n} \quad (10.1)$$

where  $d_1$  and  $d_2$  are main diameters of each particle and  $n$  is the number of considered agglomerates. At least five TEM measurements were considered to obtain an average agglomerate diameter.

### 10.2.3. *In situ* synchrotron characterization

Simultaneous uniaxial continuous stretching in the solid state (at 23°C) and *in situ* WAXS and SAXS characterization were performed under synchrotron radiation (Ge (111)  $\lambda=0.15$  nm) at HASYLAB, DESY, Hamburg (A2 beamline). The tensile specimens with a curved axisymmetric shape (30 mm length, minimal cross-section of 13.9x0.3 mm and radius of 10.4 mm) were deformed on a special stretching device with both grips moving simultaneously in opposed directions. Stretching apparatus output (force and displacement) was converted into homogeneous stress-strain curves,  $\sigma_N$ - $\ln\lambda$ , (assuming that the curved axisymmetric tensile specimens deforms through rectangular neck). The stretching ratio,  $\lambda$ , was defined as:

$$\lambda = \frac{l}{l_0} \quad (10.2)$$

where  $l$  is actual tensile specimen length and  $l_0$  the grip distance. Also the homogeneous stress was calculated as follow:

$$\sigma_N = \frac{F}{A_0} \lambda \quad (10.3)$$

where  $F$  is the force,  $A_0$  is initial tensile specimen cross-section area.

The specimens were mounted perpendicular to the incident X-ray beam and stretched vertically. Background scattering was subtracted and all plots were normalized with respect to the incident X-ray intensity, accumulation time and specimen thickness (assuming a homogeneous deformation [24]). Equipment set up was as follows:

i) WAXS: sample-to-detector distance of 145 mm and 2D WAXS patterns were acquired with accumulation time of 20 s. Samples stretched at a constant cross-head velocity of 2 mm.min<sup>-1</sup> (stretching rate of 0.002 s<sup>-1</sup>). WAXS was calibrated by means of a crystalline PET sample.

ii) SAXS: sample-to-detector distance of 3025 mm and 2D SAXS patterns were acquired with accumulation time of 30 s. Samples stretched at a constant cross-head velocity of 5 mm.min<sup>-1</sup> (stretching rate of 0.006 s<sup>-1</sup>).

**WAXS data analysis*****Phase's mass fraction***

From the 2D WAXD patterns the two linear intensity profiles taken along the equatorial and meridional directions were used to estimate mass fractions of the phases. A peak-fitting program was used to deconvolute the distinct phase's peaks, which were fitted by a Gaussian function. Studied samples morphologies were assumed to consist of two main phases: i) amorphous – isotropic and ii) mesophase - anisotropic phase with degree of packing and order between the crystalline and the amorphous phases. The amount of amorphous phase was assumed to be proportional to the area of the linear meridional profile. The subtraction of the amorphous fractions from the total area in the equatorial profile was proportional to the amount of the mesophase. The mass fractions of the individual phase were taken as the ratio of the area for each phase to the total area of the equatorial profile. At higher strains, the WAXS patterns can exhibit a pair of meridional mesomorphic reflections (10-3) at about  $2\Theta = 25.8^\circ$ , indicating conformational regularity perpendicular to the stretching direction [25-27], called here periodical mesophase. Periodical mesophase has a similar packing symmetry to the crystalline phase [28], described by meridional crystalline unit cell reflection (-103) at  $2\Theta = 26.6^\circ$  [25] representative for the 3D crystalline ordered, as reported elsewhere [29, 30]. The area of fitted (10-3) peak profile was used to determine the mass fraction of the PM. At this stage of deformation the sample morphologies were assumed to be composed of three phases: i) amorphous – isotropic, ii) mesophase - anisotropic phase with degree of packing and order between the crystalline and the amorphous phases and iii) periodical mesophase – mesophase with conformational periodicity perpendicular to the stretching direction. The three phase total area was assumed to be equal to the sum of area convoluted under the equatorial and the area under the (10-3) peak. The mass fractions of the individual phase were taken as the ratio of the area for each phase to the total area.

***Average polymer orientation***

The WAXS patterns were integrated along an azimuthal angle of  $\mu = 0 - \pi/2$  ( $\mu = 0$  equator), over a section with a  $2\Theta = 13 - 28^\circ$ , in order to calculate the average polymer orientation,  $f_{av}$ . That sector encloses all possible crystal reflections of crystallographic planes, isotropic amorphous phase and mesophases of PET [27]. The Hermans' orientation function was used to evaluate the average polymer orientation,  $f_{av}$ , calculated by [31]:

$$f = \frac{3\langle \cos^2 \phi \rangle - 1}{2} \quad (10.4)$$

where the  $\langle \cos^2 \phi \rangle$  is defined as:

$$\langle \cos^2 \phi \rangle = \frac{\int_0^{\pi/2} I(\phi) \cos^2 \phi \sin \phi d\phi}{\int_0^{\pi/2} I(\phi) \sin \phi d\phi} \quad (10.5)$$

where  $\phi$  is azimuthal angle,  $I$  the diffracted intensity and  $\langle \cos \phi \rangle$  the average angle that the normal makes with principal deformation direction

## 10.3. Results and discussion

### 10.3.1. Nanocomposites morphology

TEM investigation shows relatively good dispersion of nanofillers into polymer matrix for both nanocomposites. Average agglomerates diameter measured by TEM results, listed in **Table 10.2**, revealed that the agglomerates of each nanofiller were slightly reduced, by melt blending processing, as compared to the initial powder size.

**Table 10.2.** PET nanocomposites.

Sample	$D_{av.}$ [nm]	
	Powder*	Composite
PET/TiO <sub>2</sub>	100	88±58
PET/SiO <sub>2</sub>	100	87±60

(\* - supplier data,  $D_{av}$  – average agglomerates diameter as calculated by eq. 10.1)

### 10.3.2. Structure evolution by WAXS

**Figure 10.1.** presents the homogeneous stress-strain curves obtained during the uniaxial stretching and selected 2D WAXS patterns of PET/TiO<sub>2</sub> and PET/SiO<sub>2</sub> nanocomposites (arrows indicate the strains where patterns were acquired). The different reinforcing nature of the 3D nanoparticles is evident, mainly in terms of attained stress levels and deformation capabilities. Namely, incorporation of TiO<sub>2</sub> nanofillers improved the deformability by 75% as compare to the PET/SiO<sub>2</sub> sample. Conversely, both specimens shown similar evolution of the 2D WAXS patterns, as can be seen in **Figure 10.1**. On the other hand, nanocomposites shown a yielding point at equal strain of  $\ln \lambda = 0.05$ . Both nanocomposites despite the different nanofillers size and nature have similar neck evolution during the stretching, as depicted in **Figure 10.2**. From load applying till strain of about  $\ln \lambda = 0.2$ , the 2D WAXS patters are characterized by an amorphous halo, which slightly intensifies in this interval of stretching. This part of stretching, corresponds to region of strain-stress curve including the elastic deformation and yielding, where necking initiates near the middle of tensile bar as shown in **Figure 10.2.b**), followed by strain softening and strain increase. Neck forms out of the sample centre where the WAXS investigation was carried out (see **Figure 9.2 c**). Since strain of  $\ln \lambda = 0.2$  till sample brakeage, both PET/3D nanocomposites 2D WAXS patterns are characterized by two diffused spots in equator, indicative for considerable polymer chains orientation into stretching direction [28-30, 32, 33]

and a distinct periodical mesophase meridional (10-3) reflection [25, 26]. This is connected to the neck propagation through the examined region of the sample and stress increase (*Figure 10.2 d*).

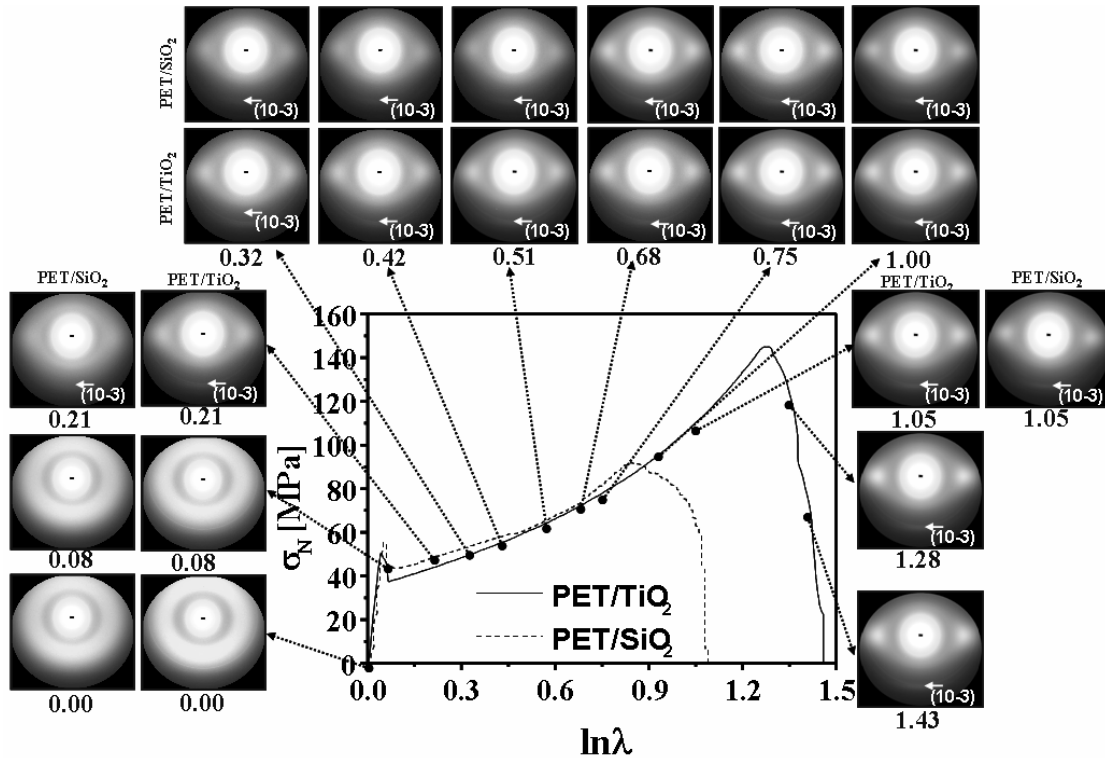


*Figure 10.1. PET/TiO<sub>2</sub> and PET/SiO<sub>2</sub> nanocomposites homogeneous stress-strain curve and selected 2D WAXS patterns.*

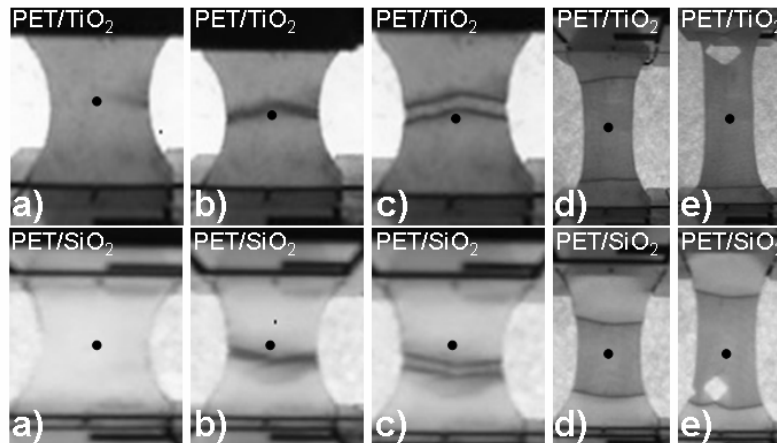


*Figure 10.2. In situ video images of PET/TiO<sub>2</sub> and PET/SiO<sub>2</sub> nanocomposites: a) prior deformation, b) neck initiation, c) neck formation, d) neck propagation and e) tensile bar rupture (the black spot represents approximate X-ray beam incident point).*

Equatorial and the meridional intensity vs.  $2\theta$  profiles extracted from the 2D WAXS patterns for both samples are depicted in *Figure 10.3*. Distinct amorphous PET equatorial reflection peak, at about  $2\theta \approx 19^\circ$ , might be identified for both nanocomposites at lower strain level (up to  $\ln\lambda=0.2$ ) (*Figure 10.3a*) and *c*). This peak intensifies with stretching advance and shifts to the angle of  $2\theta \approx 21^\circ$ , at ultimate strain. While meridional profiles, *Figure 10.3b*) and

d), initially features isotropic (amorphous) meridional peaks at  $2\Theta \approx 19^\circ$ , which shift to lower diffraction angle at lower stretching levels. At strain of  $\ln\lambda=0.2$ , emerges the mesomorphic peak (10-3) at about  $2\Theta \approx 26^\circ$ , which increase in intensity with strain till sample breakage. Whereas the meridional amorphous peak moves to smaller angle at about  $2\Theta \approx 17^\circ$  [29, 33] and significantly narrows. However, at strain of  $\ln\lambda=0.2$ , PET/SiO<sub>2</sub> sample shown a weakly (10-3) peak, evidencing a small amount of periodical mesophase, in contrast to the PET/TiO<sub>2</sub> sample that is more intense, which corresponding to a greater content of periodical mesophase.

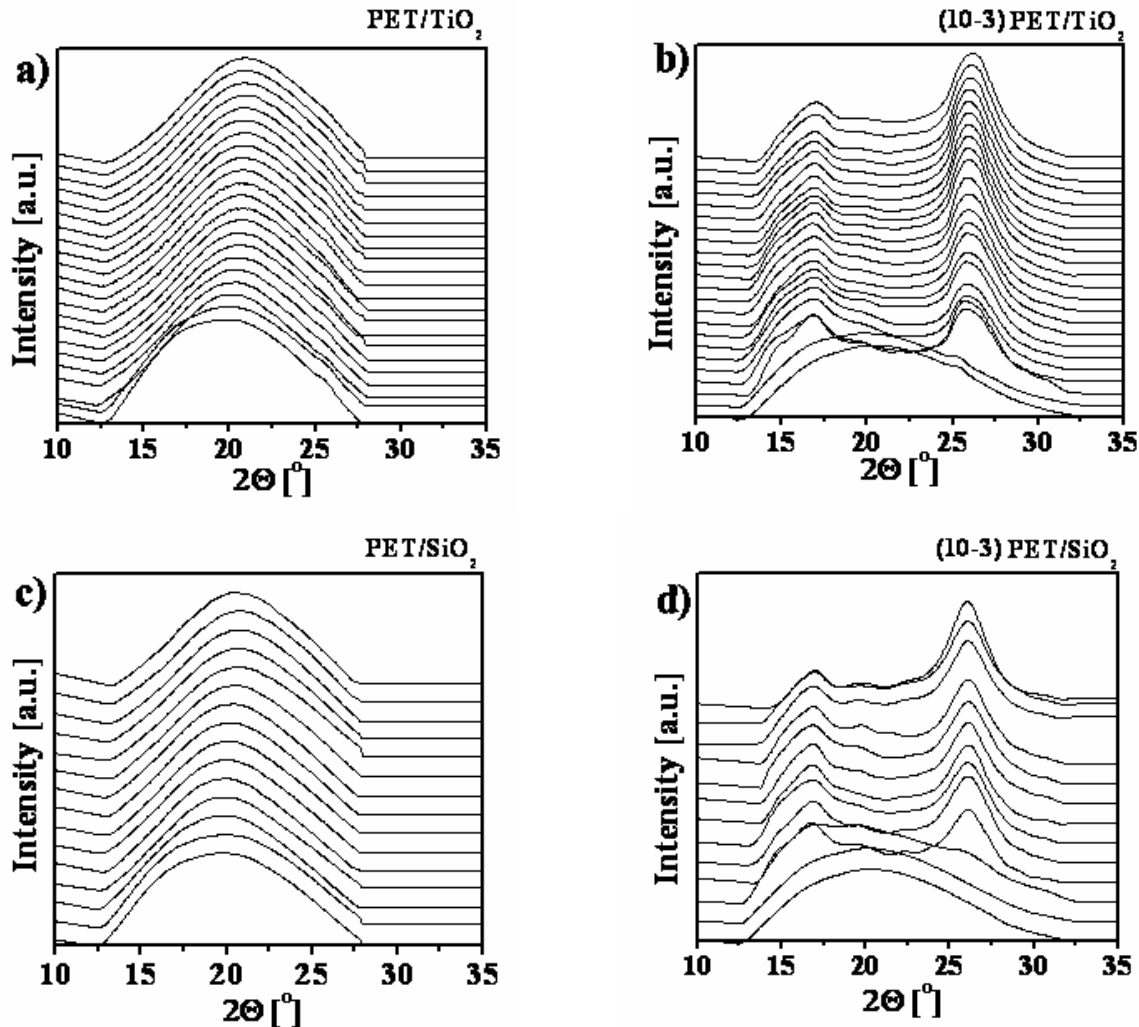


**Figure 10.3.** Linear intensity profiles extracted from 2D WAXS patterns of: PET/TiO<sub>2</sub> nanocomposite a) equatorial and b) meridional and PET/SiO<sub>2</sub> nanocomposite c) equatorial and d) meridional

Phases and average polymer orientation evolutions with strain for both nanocomposites pass through similar pathway, judging by **Figure 10.4**. Based on the average polymer orientation curve shape it can be identified three stages, as designated in the **Figure 10.4**. In the first stage, stage I, the average polymer orientation remains almost constant as the strain increases up to  $\ln\lambda = 0.2$ . Suddenly there is a fast increase of the average polymer orientation, from around  $f_{av} = -0.2$  up to  $f_{av} = 0.6$ , in short interval of strain, between  $0.08 < \ln\lambda < 0.3$ , which corresponds to stage II.

Hereafter at strain of  $\ln\lambda = 0.3$  starts stage III, where a plateau on the maximum orientation is reached that is maintained till the end of the deformation process. Phase's evolution by stages can be described as: stage I, is characterizes by slight decrease of amorphous phase due to its transformation into more organized mesophase; stage II, along which it can be observed a sharp increment of mesophase due to consumption of amorphous, together with indication of periodical mesophase formation; stage III features modest transformation of amorphous phase into mesophase with strain, at almost constant maximum periodical mesophase content.

Nevertheless, some dissimilarity between the PET/3D nanocomposites evolution can be noted. As-moulded nanocomposites are characterized by equal fraction of mesophase, c.a. 12%. Presence of TiO<sub>2</sub> nanoparticles into PET matrix promoted increment of mesophase with 10%, during the stage I, while the SiO<sub>2</sub> do not alternate this fraction. Also PET/TiO<sub>2</sub> samples achieved maximum periodical mesophase content at the middle ( $\ln\lambda=0.2$ ) of stage II, while nanocomposite reinforced with SiO<sub>2</sub> only at the end ( $\ln\lambda=0.3$ ) of stage II. In contrast, both samples fail at dissimilar strain, but with similar phase fractions content of mesophase and amorphous phase, respectively of 90% and 4%, while periodical mesophase content in PET/TiO<sub>2</sub> specimen was 7% and 4% in case of PET/SiO<sub>2</sub>. Such difference might be related to the different nature of nanofillers and its effect on the material morphology, leading to unlike deformation capability of PET nanocomposites.

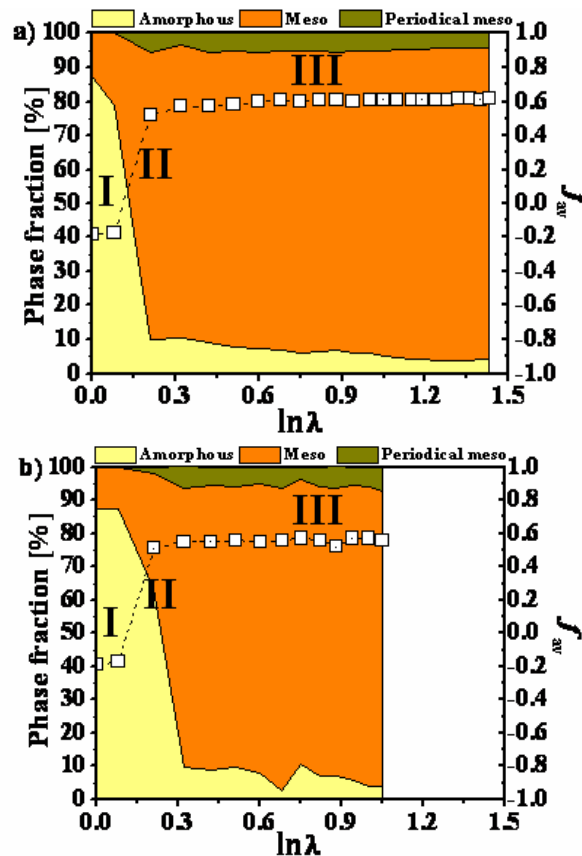


Figure 10.4. Phase fraction and average polymer orientation,  $f_{am}$ , evolution of: a) PET/TiO<sub>2</sub> and b) PET/SiO<sub>2</sub> nanocomposites.

The structure evolution of PET/3D nanocomposites, as detected by WAXS investigation, can be summarized as:

- Stage I is related to the neck formation out specimen central area that leads to an amorphous halo in the 2D WAXS patterns, centred at about  $2\theta \approx 19^\circ$  presented in equatorial and meridional intensity profiles and no change of average polymer orientation. That results into slightly increment of the mesophase fraction due to amorphous consumption.
- Further stretching lead to stage II beginning, which lasts in strain between  $0.08 < \ln\lambda < 0.3$ , and is associated to neck propagation on the tensile bar over X-ray incident point that promoted the average polymer orientation rapidly rise into the stretching direction, which translates into two spots at the equator and a reflection (10-3) at meridional of the 2D WAXS patterns. Whereas the I-2 $\theta$  linear profiles featured intensified and concentrated at about  $2\theta \approx 20^\circ$  peak in equatorial and an amorphous peak at  $2\theta \approx 16^\circ$  together with mesophase peak at about  $2\theta \approx 26^\circ$  in meridional. During the stage II, increment of polymer chains orientation leads to fast transformation of amorphous phase into mesophase together with nucleation of a small amount periodical mesophase from an oriented mesophase portion.
- At end of stage II, strain of  $\ln\lambda=0.3$ , starts stage III, and it ends with sample rupture, for duration of which is typical stable necking, related to achievement of plateau of polymer orientation level that is descriptive for network extensibility limits attainment. This is concomitant by equatorial spots and meridional reflection (10-3) intensification with strain in the 2D WAXS patterns, which is translated into slight shifts to higher angle of equatorial and isotropic meridional peaks while the (10-3) meridional peak intensifies without change of position. On the other hand, periodical mesophase content remains alike throughout the stage, and mesophase content somewhat increase due to amorphous phase decrement. Tensile bar rupture occurs as a result of a macroscopic cracks occurrence along the necked zone [34] (as shown in *Figure 10.2e*).

Effect of incorporation of TiO<sub>2</sub> and SiO<sub>2</sub> nanoparticles into the PET matrix upon structural evolution, as compared to the neat PET (see Chapter IX) is shortened hereafter. Considerable enhancement of the deformability of nanocomposites with respect to the neat PET samples was observed, correspondingly of 168% for PET/TiO<sub>2</sub> and 60% for PET/SiO<sub>2</sub>. The nanofillers presence promoted the higher strain levels during the plastic deformation of the matrix and enhanced its toughness. Both nanocomposites exposed yield point at  $\ln\lambda=0.05$  while the neat PET at  $\ln\lambda=0.04$ . Initially nanocomposites, regardless of the nanofillers nature, have identical amount of mesophase of about 12% that is about 4 times higher than the neat PET (i.e. 3%), due to their nucleation effect [23]. Nanocomposites apart from their nanofiller type, in respect to the PET samples, promoted: i) shorter strain stage I, ii) earlier periodical phase

formation in stage II, and iii) improved amount of mesophase and consequently about 4 time greater maximum periodical mesophase content, during stage III.

### 10.3.3. Structure evolution by SAXS

**Figure 10.5.** shows selected 2D SAXS patterns of neat PET and its nanocomposites obtained during the plastic deformation region, after yielding point. Based on the characteristic features occurring in 2D SAXS patterns along stretching it can be denoted distinct differences in structure evolution, due to dissimilar deformation mechanisms taking place.

Neat PET sample first 2D SAXS image, at  $\ln\lambda = 0.2$ , shows a cross-shaped pattern. This pattern is representative of craze/void morphology, where the streak parallel to the loading direction is related to the total reflection at the craze/intact polymer interfaces, and the streak perpendicular to the loading direction is associated to the fibril/void scattering [35]. Crazes are typical of amorphous polymer during deformation and have been observed, for neat PET [20-22] and for its nanocomposites [36, 37]. 2D SAXS patterns of neat PET at strain of  $\ln\lambda=0.46$  evolve into the streak perpendicular to the loading direction, present till samples breakage, caused by the fibril/void structure elongated into the stretching direction [35, 38].

At lower strain, certain dissimilarity in 2D SAXS patterns shape of both nanocomposites could be denoted. At strain about  $\ln\lambda=0.2$ , PET/TiO<sub>2</sub> sample SAXS image feature a ring shape, indicative of an isotropic orientation of voids in the sample, originated by cavitation of polymer matrix and/or of nanoparticles agglomerates debonding. Evident is also the craze formation, which cross-shaped reflection is overlapped by the ring scattering of the voids. Up to strain of  $\ln\lambda=0.8$ , in the PET/TiO<sub>2</sub> 2D SAXS might be traced the cross-shape scattering that is suggestive for retardation of crazes widening and growth suppressing, within the polymer bulk, due to the nanoparticles bridging effect [37]. Since strain of  $\ln\lambda=0.95$  till strain at break, SAXS image evolve into a single streak perpendicular to the stretching direction representative for fibril/void structure of highly elongated crazes and voids caused by the agglomerates debonding [36, 37]. Intensively, the streak sizes reduce till sample breakage.

On the other hand, first 2D SAXS patterns of PET/SiO<sub>2</sub> specimen feature a cross-shaped scattering (**Figure 10.5**), which is associated to the craze/void morphology [37]. Here further, at strains greater than  $\ln\lambda=0.5$ , in 2D SAXS patterns can be traced the individual streak perpendicular to the stretching direction, originated by scattering of the elongated crazes and voids [36, 37].

Equatorial streaks profile can be used for qualitatively estimation of void sizes, i.e. streak height correspond to void's height and its length to the voids diameter [35, 38]. Based on qualitatively analysis of 2D SAXS patterns evolution in **Figure 10.5**, it might be suggested that:



- i) adding of  $\text{TiO}_2$  nanoparticles promote retardation of the crazes widening and growth, as compared to neat PET samples and PET/ $\text{SiO}_2$  nanocomposite,
- ii) both nanocomposites evolves by voids with somewhat shorter height and smaller diameter than the pure PET sample, whereas the  $\text{TiO}_2$  particles cause formation of voids with slightly bigger diameter and similar length as compared to the  $\text{SiO}_2$  ones [19].

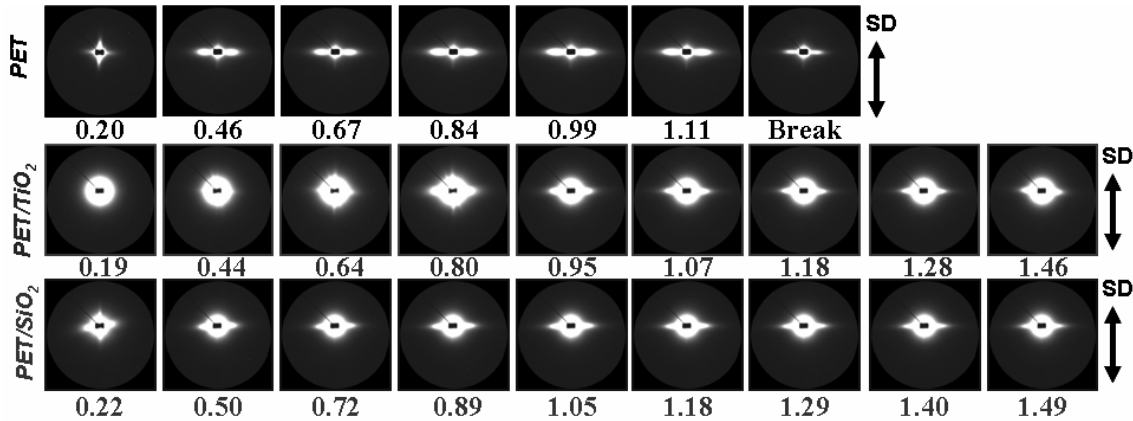


*Figure 10.5. Selected 2D SAXS patterns and corresponding homogeneous strain,  $\ln\lambda$ , obtained during the in situ SAXS characterization*

#### 10.4. Multi scale structure evolution model

The focus of this study was to investigate the influence of nanofiller with spherical shape on the structure evolution during the uniaxial stretching, in particular strain-induced structure development and its dependence on deformation mechanism taking part. In addition, the effect of different nature and size of nanofillers on all above mentioned physical phenomenon. In this regards, it is proposed the multiscale model illustrated in *Figure 10.6.*, to interpret the structural evolution during tensile deformation of PET/ $\text{TiO}_2$  and PET/ $\text{SiO}_2$  nanocomposites. In the model, the mechanical behaviour and average polymer orientation are related to the structure changes in three stages:

- Stage I: its duration is from start of stretching till neck propagation, during which is absent any change of average orientation and a slight portion of amorphous phase evolves into mesophase. On the other hand, the inorganic agglomerates within the matrix of an as-moulded morphologies become stress concentration centres [17, 18].
- With Stage II beginning, associated to the neck dissemination through observed region, in a short interval of strain occur crazes within the polymer matrix and the voids forms inside of agglomerates via multiple debonding process [17, 18]. The deformation volume is reduced, and polymer chains orient fast along the stretching direction. There is also a mesophase development from the oriented amorphous phase, and a small part of the oriented mesophase orders into periodical mesophase.

○ Stage III, which last till tensile bar fails, corresponds to sample lengthening through necking. During this stage, crazes within polymer bulk widen and lengthen with strain, causing individual fibrils rupture till those becoming micro-voids, while the void originated by deboning of agglomerates lengthens along the stretching direction. The polymer average orientation levels off at maximum value, associated to the achievement of bulk chains extensibility limit, a maximum periodical mesophase fraction is formed, which maintains alike up to samples breakage. With strain advancement a little of highly oriented amorphous phase transforms into mesophase, till tensile bar breaks.

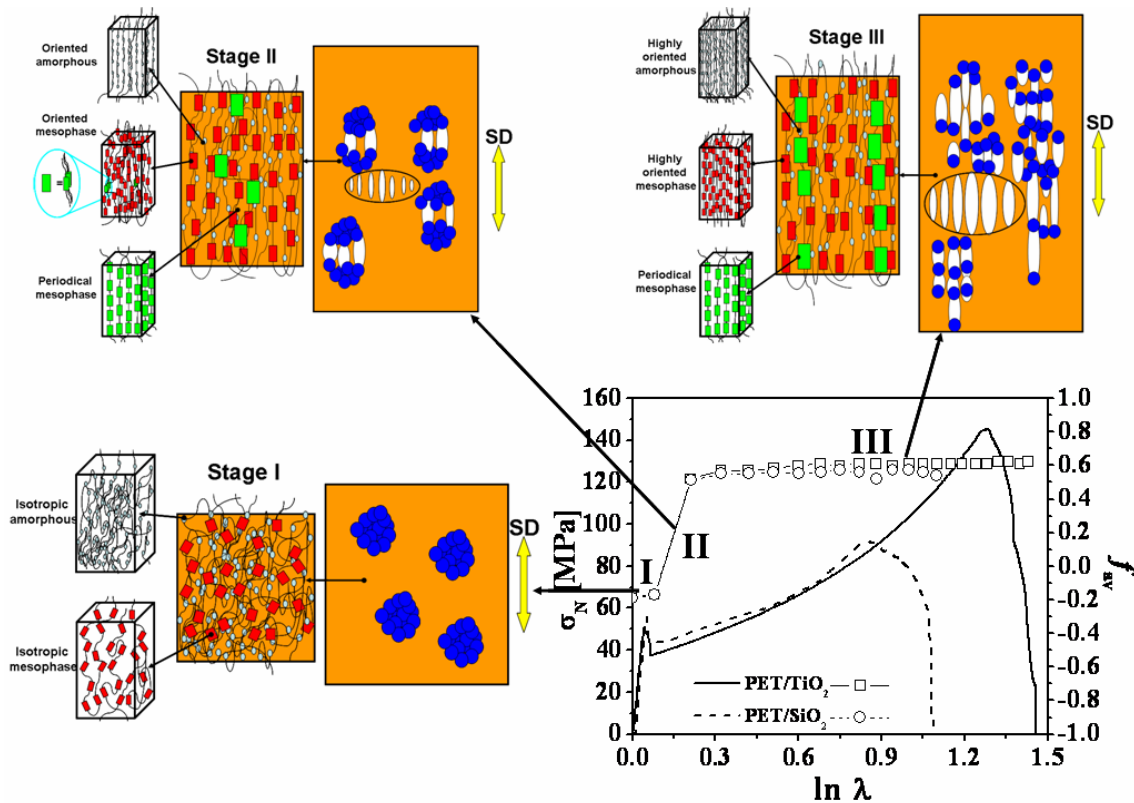


**Figure 10.6.** Schematic diagram to illustrate the multiscale structure evolution during in solid state uniaxial stretching of PET/3D (spherical) nanocomposites.

## 10.5. Conclusions

Enhanced deformability and stress levels of nanocomposites with respect to neat PET were observed. Comparing PET/TiO<sub>2</sub> and PET/SiO<sub>2</sub> nanocomposites, the incorporation of TiO<sub>2</sub> promoted increment of the stress level and strain at break. Nanocomposites, regardless of the nanofiller type, and with respect to neat polymer specimen, lead to improved amount of mesophase and four time greater content of maximum periodical mesophase. TiO<sub>2</sub> nanofillers caused a slightly higher fraction of periodical mesophase and its earlier formation than SiO<sub>2</sub> during deformation. Crazes growth retardation is caused by incorporation of TiO<sub>2</sub> nanoparticles, as compared to PET and PET/SiO<sub>2</sub> samples. Nanocomposites form voids with somewhat shorter

height and smaller diameter than the neat PET, whereas the TiO<sub>2</sub> particles originated formation of wider voids with similar length than the SiO<sub>2</sub> ones. The structure evolution of PET nanocomposites passes through a three stages: i) stage I before necking, agglomerates becomes stress concentrators and a small amount of amorphous phase evolves into mesophase at constant molecular orientation level; ii) stage II, neck propagation, craze within matrix and voids from debonding of nanoparticles agglomerates appear, together with a rapid increase of polymer molecular orientation, a sharp increment of mesophase at the reduction of the amorphous phase and the initiation of the formation of a periodical mesophase from the mesophase; iii) stage III necking, where voids lengthen at plateau of average molecular orientation, the highest periodical mesophase content is achieved, as well as, a slight increment of mesophase. Incorporation of inorganic nanoparticles with spherical shape is highly promising for use as reinforcement in polymer nanocomposites with great potential in several applications.

## 10.6. References

1. Ray, S.S. and M. Okamoto, *Polymer/layered silicate nanocomposites: A review from preparation to processing*. Progress in Polymer Science (Oxford), 2003. **28**(11): p. 1539-1641.
2. Fray, E., M. Boccaccini, and R. Aldo, *Novel hybrid PET/DFA-TiO<sub>2</sub> nanocomposites by in situ polycondensation*. Materials Letters, 2005. **59**(18): p. 2300-2304.
3. Han, K. and M. Yu, *Study of the preparation and properties of UV-blocking fabrics of a PET/TiO<sub>2</sub> nanocomposite prepared by in situ polycondensation*. Journal of Applied Polymer Science, 2006. **100**(2): p. 1588-1593.
4. Taniguchi, A. and M. Cakmak, *The suppression of strain induced crystallization in PET through sub micron TiO<sub>2</sub> particle incorporation*. Polymer, 2004. **45**(19): p. 6647-6654.
5. Todorov, L.V. and J.C. Viana, *Characterization of PET nanocomposites produced by different melt-based production methods*. Journal of Applied Polymer Science, 2007. **106**(3): p. 1659-1669.
6. Zheng, H. and J. Wu, *Preparation, crystallization, and spinnability of poly(ethylene terephthalate)/silica nanocomposites*. Journal of Applied Polymer Science, 2007. **103**(4): p. 2564-2568.
7. Liu, W., et al., *Preparation and Characterization of PET/Silica Nanocomposites*. Journal of Applied Polymer Science, 2004. **91**(2): p. 1229-1232.
8. Tian, X., et al., *Isothermal Crystallization and Subsequent Melting Behavior of Poly(ethylene terephthalate)/Silica Nanocomposites*. Journal of macromolecular science, 2006. **45**(5): p. 835 - 848.
9. Bikiaris, D., V. Karavelidis, and G. Karayannidis, *A New Approach to Prepare Poly(ethylene terephthalate)/Silica Nanocomposites with Increased Molecular Weight and Fully Adjustable Branching or Crosslinking by SSP*. Macromolecular Rapid Communications, 2006. **27**(15): p. 1199-1205.
10. Yang, Y. and H. Gu, *Superfine structure, physical properties, and dyeability of alkaline hydrolyzed poly(ethylene terephthalate)/silica nanocomposite fibers prepared by in situ polymerization*. Journal of Applied Polymer Science, 2006. **102**(4): p. 3691-3697.
11. Zheng, J., et al., *Pyrolysis studies of polyethylene terephthalate/silica nanocomposites*. Journal of Applied Polymer Science, 2007. **104**(1): p. 9-14.
12. Yang, Y. and H. Gu, *Preparation and properties of deep dye fibers from polyethylene terephthalate/SiO<sub>2</sub> nanocomposites by in situ polymerization*. Journal of Applied Polymer Science, 2007. **105**(4): p. 2363-2369.
13. Chung, S.C., et al., *Poly(ethylene terephthalate)(PET) nanocomposites filled with fumed silicas by melt compounding* Macromolecular research, 2002. **10**(4): p. 221-229.
14. Wu, T. and Y. Ke, *The absorption and thermal behaviors of PET-SiO<sub>2</sub> nanocomposite films*. Polymer Degradation and Stability, 2006. **91**(9): p. 2205-2212.
15. Wu, T. and Y. Ke, *Melting, crystallization and optical behaviors of poly (ethylene terephthalate)-silica/polystyrene nanocomposite films*. Thin Solid Films, 2007. **515**(13): p. 5220-5226.
16. Koo, J.H., *Polymer Nanocomposites Processing, Characterization, and Applications*. 2006, New York: McGraw-Hill.
17. Kim, G.M. and G.H. Michler, *Micromechanical deformation processes in toughened and particle-filled semicrystalline polymers: Part 1. Characterization of deformation processes in dependence on phase morphology*. Polymer, 1998. **39**(23): p. 5689-5697.
18. Kim, G.M. and G.H. Michler, *Micromechanical deformation processes in toughened and particle filled semicrystalline polymers: Part 2. model representation for micromechanical deformation processes*. Polymer, 1998. **39**(23): p. 5699-5703.
19. Reynaud, E., et al., *Nanofillers in polymeric matrix: a study on silica reinforced PA6*. Polymer, 2001. **42**(21): p. 8759-8768.

20. Liu, Y., et al., *Characterization of stress-whitening of tensile yielded isotactic polypropylene*. Polymer, 1997. **38**(11): p. 2797-2805.
21. Viana, J.C., et al., *Nanostructure Evolution during Uni-axial Deformation of PET – a WAXS and SAXS Study using Synchrotron Radiation*. Materials Science Forum, 2006(514-516 ): p. 1583-1587.
22. Efimov, A.V., V.Y. Shcherba, and N.F. Bakeyev, *Effect of drawing conditions on structural parameters of crazes in crystalline poly(ethylene terephthalate)*. Polymer Science U.S.S.R., 1991. **33**(3): p. 568-574.
23. Todorov, L.V., C.I. Martins, and J.C. Viana, *Characterization of PET nanocomposites with different nanofillers*. Solid State Phenomena, 2009. **151**: p. 113-117.
24. Oultache, A.K., et al., *Orientation and relaxation of orientation of amorphous poly(ethylene terephthalate)*. Polymer, 2001. **42**(21): p. 9051-9058.
25. Parravicini, L., et al., *Crystallization of poly(ethylene terephthalate) (PET) from the oriented mesomorphic form*. Journal of Applied Polymer Science, 1994. **52**(7): p. 875-885.
26. Goschel, U., *Thermally stimulated structural changes in highly oriented glassy poly(ethylene terephthalate)*. Polymer, 1996. **37**(18): p. 4049-4059.
27. Goschel, U., K. Deuschert, and V. Abetz, *Wide-angle X-ray scattering studies using an area detector: crystalline orientation in semicrystalline PET structures*. Polymer, 1996. **37**(1): p. 1-6.
28. Ran, S., et al., *Mesophase as the Precursor for Strain-Induced Crystallization in Amorphous Poly(ethylene terephthalate) Film*. Macromolecules 2002(35): p. 10102-10107
29. Kawakami, D., et al., *Mechanism of Structural Formation by Uniaxial Deformation in Amorphous Poly(ethylene terephthalate) above the Glass Temperature*. Macromolecules, 2003(36): p. 9275-9280.
30. Kawakami, D., et al., *Superstructure Evolution in Poly(ethylene terephthalate) during Uniaxial Deformation above Glass Transition Temperature*. Macromolecules, 2006. **39**: p. 2909-2920.
31. Stribeck, N., *X-Ray Scattering of Soft Matter*. 2007: Springer Berlin Heidelberg New York.
32. Blundell, D.J., et al., *Characterization of strain-induced crystallization of poly(ethylene terephthalate) at fast draw rates using synchrotron radiation*. Polymer, 1996. **37**(15): p. 3303-3311.
33. Kawakami, D., et al., *Structural formation of amorphous poly(ethylene terephthalate) during uniaxial deformation above glass temperature*. Polymer, 2004. **45**(3): p. 905-918.
34. Takemori, M.T., *Competition between crazing and shear flow during fatigue*. Advances in Polymer Science 1990. **91/92**: p. 263-300.
35. Shioya, M., et al., *Small-Angle X-ray Scattering Study on the Tensile Fracture Process of Poly(ethylene terephthalate) Fiber*. Macromolecules, 2008. **41**(13): p. 4758-4765.
36. Kobayashi, H., et al., *Synchrotron radiation small-angle X-ray scattering study on fracture process of carbon nanotube/poly(ethylene terephthalate) composite films*. Composites Science and Technology, 2007. **67**(15-16): p. 3209-3218.
37. Kobayashi, H., et al., *A comparative study of fracture behavior between carbon black/poly(ethylene terephthalate) and multiwalled carbon nanotube/poly(ethylene terephthalate) composite films*. Journal of Applied Polymer Science, 2007. **106**(1): p. 152-160.
38. Stribeck, N., et al., *SAXS-Fiber Computer Tomography. Method Enhancement and Analysis of Microfibrillar-Reinforced Composite Precursors from PEBA and PET*. Macromolecules 2008. **41**: p. 7637-7647.

# CHAPTER XI

## Conclusions

The main key findings and conclusions of the present dissertation are summarized below in respect to each of the Chapters.

- **Statistical influence of stretching variables in rubbery state**

Upon variations of the stretching variables, different PET morphologies were developed, ranging from quasi-amorphous to semi-crystalline states. Stretching temperature and stretching ratio have both an important role on the structure development. High temperatures may hinder strain induced crystallization mechanism of PET. This is the result of two possible competing mechanisms: chain elongation due to mechanical deformation and chain relaxation due to the elevated temperature. Stretching ratio has a pronounced influence on the strain-induced crystalline phase, mainly when low temperatures are applied. In this way, deformation at low stretching ratio and high temperatures give rises to the highest amount of amorphous phase fraction. Or, on the opposite way, decreasing stretching temperature facilitates the strain-induced structure development. Structural characterization had shown that semi-crystalline morphology was developed only in condition which combined the high stretching ratio and low temperature. The combination of low stretching temperature, higher strain rate and higher stretching ratio, leads to a high degree of crystallinity.

In general, low stretching ratio results in low average polymer chain orientation, and hence low birefringence. The combination of high stretching ratio and high temperature results in samples with similar low orientation levels. Using high stretching ratio seems to have a positive influence on the transformation of the amorphous phase fraction into mesophase.

The highest crystalline PET shows the highest  $T_g$  suggesting that the crystalline phase geometrically constrains the amorphous phase, inhibiting the amorphous phase motions. There is an important effect of the stretching temperature on the  $T_{cc}$ , and consequently on orientation of amorphous phase.

Statistical analysis indicated the following main influences of the stretching variables on the structural and thermal parameters:

i) transformation of amorphous phase into mesophase is mainly controlled by stretching ratio and interaction between the stretching ratio and rate;

ii) strain-induced crystallization, measured by WAXS and DSC, governed by stretching temperature and ratio and interaction among them;

iii) level of molecular orientation, average and birefringence, is influenced mainly by stretching temperature, assisted by stretching ratio and the interaction between them with similar portions;

iv) glass transition temperature depends on the orientation level of amorphous phase, which is governed by the stretching ratio and its interaction with temperature, while the solely temperature influence is statistically small;

v) dominating influence over cold crystallization temperature is associated to the stretching temperature, followed by the stretching ratio and interaction among them.

### • **Structure evolution in solid state: different initial morphologies**

The evolution of strain-induced phase transition and average polymer molecular orientation with strain increment was investigated for different initial morphological states of PET. Quasi-amorphous, QA, and semicrystalline, SC, morphologies show distinct structure evolutions during stretching. Distinct structural models were proposed for each type of initial morphology, interpreting the obtained experimental results.

Solid state structural evolution upon deformation is strongly dependent on the initial state of the material. Initially amorphous samples evolve into highly oriented ones that are not able to crystallize, although a high level of average polymer molecular orientation is achieved. They are formed of highly oriented chains in different phases (amorphous, mesophase and periodical mesophase) whose mass fractions evolve during stretching, as a result of subsequent chain stretching/slippage and relaxation phenomena. A semicrystalline precursor gives rise to a final structure where a 3D crystalline order is attained, even when starting with 2D crystalline order. In all cases, the final average molecular orientation level attained is independent of the initial morphological state. Its evolution follows three stages, for any kind of samples that has not achieved a 3D crystalline order: firstly there is a small plateau of constant molecular orientation (stage I) until neck formation; followed by quick rise (stage II), that then stabilizes in a new plateau of maximum molecular orientation during necking propagation through the specimen (stage III). For 2D crystalline precursor, crystallite size enlarges during initial deformation stages, and then evolves due to rearrangements of benzene ring stacking during stretching. A 3D

crystalline precursor (SC2) leads to a continuous evolution of the average molecular orientation with strain until break, without almost no crystalline phase evolution.

Initially morphological distinct PET samples show different structural evolutions during stretching and also markedly distinct mechanical behaviours.

- **Characterization of PET nanocomposites: different production methods**

The structure of the polymer was varied by two production procedures (direct injection moulding, DIM, and extrusion blending followed by injection moulding, EIM) and different types of nanofillers. The PET nanocomposites are more sensitive to degradation than virgin PET, caused by presence of the nanofillers, which are inducing chain scission process leading to a reduction on the average molecular weight and respectively on the intrinsic viscosity. All the EIM samples show a higher variation of intrinsic viscosity, and then higher polymer degradation during processing.

Both production procedures are suitable for production intercalated MMT5, but slightly higher amount of intercalated phase for EIM is detected. Better dispersion in the polymer matrix of TiO<sub>2</sub> and SiO<sub>2</sub> nanoparticles was also obtained for EIM as compared with DIM, as would be expected. The different processing procedures represented slight influence on T<sub>g</sub> and negligible upon T<sub>m</sub>. In case of DIM, MMT and TiO<sub>2</sub> are acting as nucleating agents, but SiO<sub>2</sub> particles behave as crystallization inhibitors. This nucleating effect was shown by all used inorganic fillers for EIM procedure that is originated by the better nanofillers dispersion. Yield stress increases with T<sub>g</sub> and respectively decrease with the raise of the cold crystallization temperature. The strain at break is influenced mainly by better dispersion: better dispersion result in improved strain at break. Gloss is affected mainly by filler presence, and a small processing influence is reported. All nanofillers strongly increasing sample haziness.

- **Characterization of PET nanocomposites: asymmetric batch minimixer**

Incorporation of nanoparticles into the polymer matrix contributes for polymer degradation during the processing. Interaction on the interface of nanofillers-polymer caused increase of glass transition temperature and broadening of the transition. All characterized nanoparticles have nucleating effect regardless of nanoparticles shape/size. Deformability of PET nanocomposites improves with incorporation of smaller size nanofillers and application of the spherical shape nanoparticles.



- **Structure evolution in solid state: PET/MMT nanocomposites**

Intercalate PET/MMT32 exposed considerable enhancement of attained stress level and deformation capability of polymer matrix in comparison to the neat PET, while the tactoid structure of PET/MMT2 cause only a slight improvements. All investigate samples, regardless there morphology, reached similar maximum orientation level. Incorporating MMT nanofillers in PET matrix promoted a higher fraction of mesophase and at elevated strains of periodical mesophase as compared to neat PET. MMT intercalation in case of PET/MMT32 causes an earlier formation and enhanced amount of periodical mesophase than the tactoid PET/MMT2 and neat PET samples, while in case of pure matrix, the improvement was significantly bigger than the PET/MMT2. Crazes appear within the PET matrix in all samples, at earlier stages of plastic deformation. Both nanocomposites morphologies retarded crazes widen within the polymer bulk. Intercalated morphology PET/MMT32 leads to formation of voids with smallest height and diameter in between the considered specimens. Tactoid PET/MMT2 sample results into voids with dimensions alike to the pure PET. WAXS/SAXS results indicated a three stages multiscale mechanism of structure evolution for neat PET and its nanocomposites.

Structural model, consisting of three stages, was proposed for each type of initial MMT nanocomposite morphology, namely:

- *Stage I:* its duration is from beginning of stretching till necking under the X-ray beam, along which is absent an increment of average polymer orientation values, although a minor amount of amorphous phase fraction organises into mesophase.

- *Stage II:* is representative of the fast neck spread over the tensile bar centre, leading to crazes formation/widening within polymer bulk, and concomitant by voids inside the intercalated MMT's particles, while MMT's tactoids break creating voids inside the tactoids. A rapid polymer chains orientation into stretching direction is promoted, causing the phase's orientation and evolution of an orientated amorphous phase into mesophase and of a little part of oriented mesophase into periodical mesophase.

- *Stage III:* during it, sample deforms and in polymer matrix the crazes enlarge perpendicular to the stretching direction, which is partially impeded by inorganic particles, while voids within the crazes and those from the intercalated/tactoid MMTs particle elongate into micro-voids parallel to the stretching direction. Here, the polymer chains are approaching their extensibility limit causing a plateau of orientation level. It is formed a maximum periodical mesophase fraction, which is maintained alike up to sample rupture. Despite that, with strain progress a slow transformation of remaining amorphous phase fraction into mesophase is observed. At ultimate strain, sample ruptures via macro-cracks formed.

- **Structure evolution in solid state: PET/SiO<sub>2</sub> and PET/TiO<sub>2</sub> nanocomposites**


Enhanced deformability and stress levels of nanocomposites with respect to neat PET were observed. Comparing PET/TiO<sub>2</sub> and PET/SiO<sub>2</sub> nanocomposites, the incorporation of TiO<sub>2</sub> promoted increment of the stress level and strain at break. Nanocomposites, regardless of the nanofiller type and with respect to neat polymer specimen, lead to improved amount of mesophase and four time greater content of maximum periodical mesophase. TiO<sub>2</sub> nanofillers caused a slightly higher fraction of periodical mesophase and its earlier formation than SiO<sub>2</sub>. Crazes growth retardation is caused by incorporation of TiO<sub>2</sub> nanoparticles, as compared to PET and PET/SiO<sub>2</sub> samples. Nanocomposites form voids with somewhat shorter height and smaller diameter than the PET, whereas the TiO<sub>2</sub> particles originated formation of wider voids but with similar length than the SiO<sub>2</sub> ones. The structure evolution of nanocomposites passes through a three stages:

- *stage I*, before necking, agglomerates become stress concentrators and a small amount of amorphous phase evolves into mesophase at constant molecular orientation level;
- *stage II*, neck propagation, craze within matrix and voids from debonding of nanoparticles agglomerates appears together with a rapid increase of polymer molecular orientation, a sharp increment of mesophase at the reduction of the amorphous phase and the initiation of the formation of a periodical mesophase from the mesophase;
- *stage III*, necking, where voids lengthen at plateau of the average molecular orientation, the highest periodical mesophase content is achieved, as well as a slight increment of mesophase.



# APPENDIX

# A.1. Datasheet of Poly (ethylene terephthalate), PET S41T

	<b>MANUAL DE ESPECIFICAÇÕES</b>	Doc. nº S41T	
	<b>ESPECIFICAÇÕES TÉCNICAS</b>	Edição : A	Revisão : 1
		Data : 04-01-30	

## S41T

TIPO DE ANÁLISE	Unid	LIM. DE CONTROLE	
		Min.	Máx.
VISCOSIDADE ESPECÍFICA	SV	675	735
L*	CIE	71	
a*	CIE		0
b*	CIE		0
FLUORESCÊNCIAS	grão/ 100g	0	1
SPECKS	grão/ 100g		0
GROSSOS	g/900g	0	0,4
ACETALDEÍDO	ppm		
CRISTALINIDADE	%	40	
POEIRAS	ppm	0	500
HUMIDADE	%	0	0,2
TAMANHO DO GRÃO	grão/g	50	80

DSC |  $T_m: 235,6 \text{ }^\circ\text{C}$   
 $T_g: 78,3 \text{ }^\circ\text{C}$

E (MPa):  $2199 \pm 19$

MFI:  $63,6 \pm 5,2 \text{ g/10 min}$

InPacto |  $F(N): 127,5 \pm 30$   
 $E(J): 0,24 \pm 0,05$   
*Energia*

$\sigma_c$  (MPa):  $62,7 \pm 0,8$



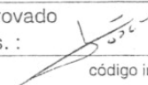
Flexão

$\epsilon_c$  (%):  $10,0 \pm 0,2$

$E_f$  (MPa):  $2568 \pm 25$

$\sigma_R$  (MPa):  $30,2 \pm 15,1$

$\epsilon_R$  (%):  $33,0 \pm 12,6$

Elaborado Ass.: 	Verificado Ass.: 	Aprovado Ass.: 
--	---	--

código informático: ET.doc código impresso: CQA0001

## A.2. Datasheet of Poly (ethylene terephthalate), PET T74 F9



JANVIER 2000

Ref AQ: COM 015. Ind. 02

### POLYESTER POLYMER

T74F9

CAS: N° 25038-59-9

#### CHARACTERISTICS:

⇒ Product description .....	White granulates
⇒ Melt point.....	Approx 252 °C
⇒ Bulk density.....	Approx 0,83 g/cm3
⇒ Density.....	Approx 1,40 g/cm3

#### SPECIFICATIONS

		METHODS
⇒ INTRINSIC VISCOSITY (dl/g).....	0.74 ± 0.02	05 - Poly. 3K - 310
⇒ COLOR	L*..... ≥ 81	05 - Poly. 3K - 250
⇒	a*..... -2<a<0	05 - Poly. 3K - 250
⇒	b*..... -2<b<+1	05 - Poly. 3K - 250
⇒ ACETALDEHYDE (ppm).....	<1	05 - Poly. 3K - 230
⇒ Carboxylic End Groups (m.....)	≤ 60	05 - Poly. 3K - 140
⇒ Diethylene Glycol (%) .....	≤ 2	05 - Poly. 3K - 280
⇒ Weight of 100 chips.....	1,4 g ± 0,1 05 - Poly- 3K - 300	

#### CONDITIONING AND TRANSPORT

⇒ Big Bags of 1000kg or road-tanker

#### STOCKHOLDING

⇒ Keep stock protected from humidity

#### USES

⇒ Bottles, films, yarns, fibres

HYGIENE AND SAFETY ⇒ This product presents no particular toxic features

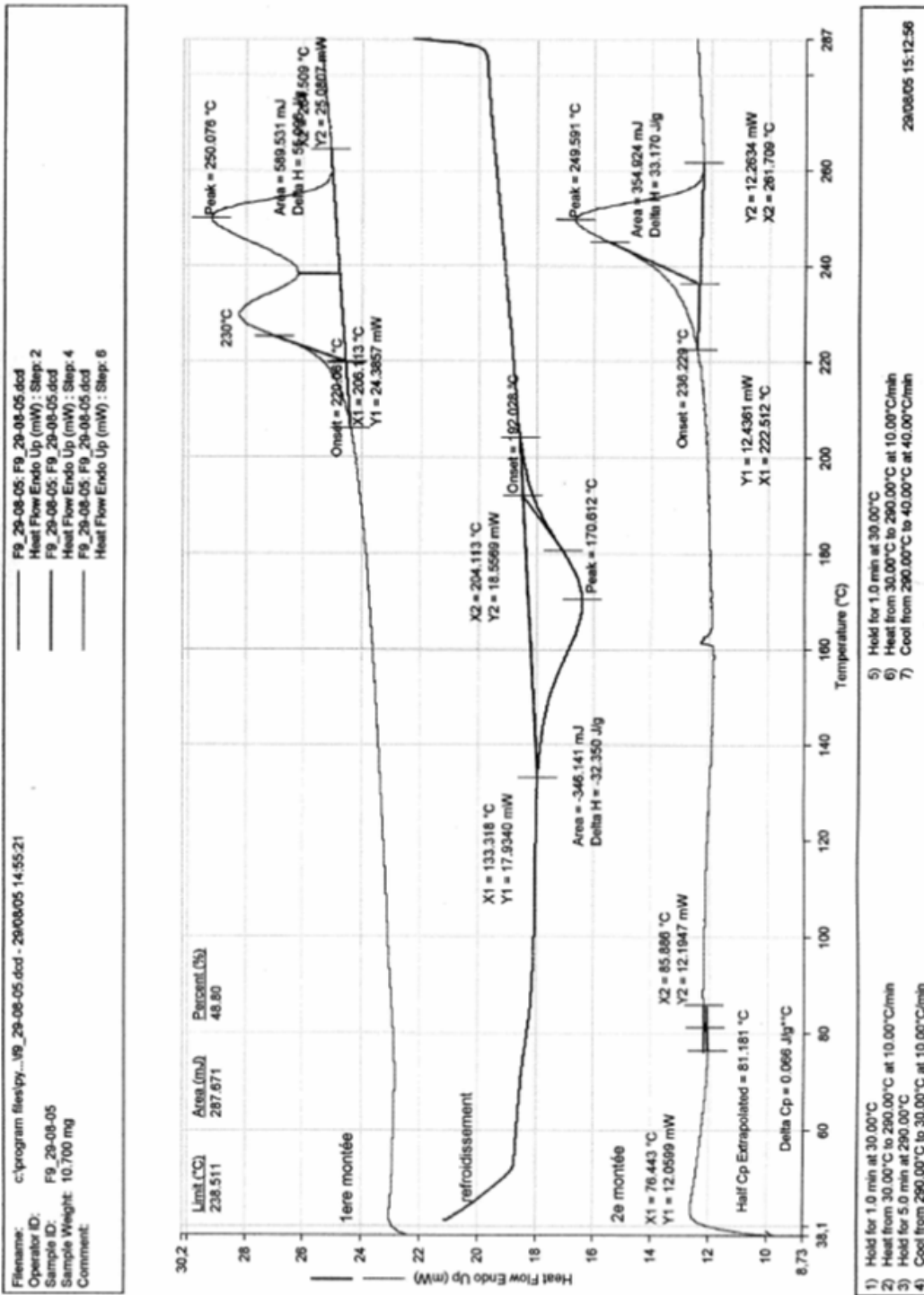
#### TRANSPORT REGULATIONS

⇒ Not applicable

PRODUCTION SITE ⇒ 02 430 GAUCHY / FRANCE

The information contained in this notice is based on the state of our knowledge of the product concerned at the issue date of the notice. The information is given in good faith and does not constitute a guarantee on our part. It is only offered as an indication, except for the actual specifications. It ought not, in any case, to be a substitute for evaluation trials which the user should out to verify, on each situation, its acceptability for the intended end use. Our services are at your disposal to give you all additional information and offer you our documentation. We reserve the right to carry out technical modifications to the product.

### A.3. DSC thermographs of PET T74 F9



1) Hold for 1.0 min at 30.00°C

2) Heat from 30.00°C to 290.00°C at 10.00°C/min

3) Hold for 5.0 min at 290.00°C

4) Cool from 290.00°C to 30.00°C at 10.00°C/min

5) Hold for 1.0 min at 30.00°C

6) Heat from 30.00°C to 290.00°C at 10.00°C/min

7) Cool from 290.00°C to 40.00°C at 40.00°C/min

29/08/05 15:12:56

## A.4. Datasheet of Nanofil 5, MMT5

### Datasheet



### Nanofil<sup>®</sup> 5

Active nanofillers for polymer applications

**Composition:** organic modified nanodispers layered silicate

**Chemical functionality:** long chain hydrocarbon

**Typical technical data:**

Product form:	powder
Colour:	creme
Specific weight:	approx. 1,8 g/cm <sup>3</sup>
Bulk density:	150 g/l
Medium particle size:	8 µm
Primary particle size after complete dispersion:	100 - 500 nm x 1nm
Moisture content:	< 3 %
Loss on ignition:	approx. 35 %

All information given in this technical information cannot be guaranteed. Variations from the indications mentioned above are possible because of the particular production facilities.



## A.5. Datasheet of Nanofil 32, MMT32

### Datasheet



### Nanofil<sup>®</sup> 32

Active nanofillers for polymer applications

**Composition:** organic modified nanodispers layered silicate

**Chemical functionality:** Long chain hydrocarbon / benzyl group

**Typical technical data:**

Product form:	powder
Colour:	creme
Specific weight:	approx. 1,8 g/cm <sup>3</sup>
Bulk density:	300 g/l
Medium particle size:	30 µm
Primary particle size after complete dispersion:	100 - 500 nm x 1 nm
Moisture content:	< 3 %
Loss on ignition:	approx. 30%

All information given in this technical information cannot be guaranteed. Variations from the indications mentioned above are possible because of the particular production facilities.

## A.6. Datasheet of Nanofil 2, MMT2

### Datasheet



### Nanofil<sup>®</sup> 2

Active nanofillers for polymer applications

**Composition:** organic modified nanodispers layered silicate

**Chemical functionality:** long chain hydrocarbon / benzyl group

**Typical technical data:**

Product form:	powder
Colour:	creme
Specific weight:	approx. 1,8 g/cm <sup>3</sup>
Bulk density:	130 g/l
Medium particle size:	8 µm
Primary particle size after complete dispersion:	100 - 500 nm x 1nm
Moisture content:	< 3 %
Loss on ignition:	approx. 30 %

All information given in this technical information cannot be guaranteed. Variations from the indications mentioned above are possible because of the particular production facilities.

A.7. Datasheet of AEROXIDE® TiO<sub>2</sub> P 25, TiO<sub>2</sub>

## Product Information

## ▶ AEROXIDE® TiO<sub>2</sub> P 25

### Hydrophilic Fumed Titanium Dioxide

AEROXIDE® TiO<sub>2</sub> P 25 is a highly dispersed titanium dioxide manufactured according to the AEROSIL®-process.

## Applications and Properties

## Applications

- Catalyst carrier
- Active component for photocatalytic reactions
- Heat stabilizer for silicone rubber

## Properties

- Process related high purity
- Heat stabilizing properties for silicone – elastomers through its effect on redox reactions

Thereby:

- Improvement of ageing properties at high temperature (= 200°C)
- Positive impact on flammability protection

## Physico-chemical Data

Properties	Unit	Typical Value
Specific surface area (BET)	m <sup>2</sup> /g	50 ± 15
Average primary particle size	nm	21
Tapped density* (approx. value) acc. to DIN EN ISO 7887/1, August 1983	g/l	approx. 130
Moisture* 2 hours at 105 °C	wt. %	≤ 1.5
Ignition loss, 2 hours at 1000 °C based on material dried for 2 hours at 105 °C	wt. %	≤ 2.0
pH in 4% dispersion		3.5 - 4.5
Titanium dioxide based on ignited material	wt. %	≥ 99.50
Al <sub>2</sub> O <sub>3</sub> -content based on ignited material	wt. %	≤ 0.300
SiO <sub>2</sub> -content based on ignited material	wt. %	≤ 0.200
Fe <sub>2</sub> O <sub>3</sub> -content based on ignited material	wt. %	≤ 0.010
HCl-content based on ignited material	wt. %	≤ 0.300
Sieve residue (by Mocker, 45 µm), acc. to DN EN ISO 787/18, April 1984	wt. %	≤ 0.050

\* or pl. ont

The data represents typical values and not production parameters.

## A.8. Datasheet of AEROSIL® 200, SiO<sub>2</sub>



### Product Information

#### ▶ AEROSIL® 200 Hydrophilic Fumed Silica

AEROSIL® 200 is a hydrophilic fumed silica with a specific surface area of 200 m<sup>2</sup>/g.

#### Applications and Properties

##### Applications

- Paints and coatings
- Unsaturated polyester resins, laminating resins and gel coats
- HTV- and RTV-2K-silicone rubber
- Adhesives and sealants
- Printing inks
- Cable compounds and cable gels
- Plant protection
- Food and cosmetics

##### Properties

- Rheology and thixotropy control of liquid systems, binders, polymers, etc.
- Used as anti-settling, thickening and anti-sagging agent
- Reinforcement of HTV- and RTV-2K-silicone rubber
- Improvement of free flow and anticaking characteristics of powders

#### Physico-chemical Data

Properties	Unit	Typical Value
Specific surface area (BET)	m <sup>2</sup> /g	200 ± 25
Average primary particle size	nm	12
Tapped density* (approx. value) acc. to DIN EN ISO 787/11, Aug. 1983	g/l	approx. 50
Moisture* 2 hours at 105 °C	wt. %	≤ 1.5
Ignition loss, 2 hours at 1000 °C, based on material dried for 2 hours at 105 °C	wt. %	≤ 1.0
pH in 4% dispersion		3.7 - 4.7
SiO <sub>2</sub> -content based on ignited material	wt. %	≥ 99.8

\* or plant

The data represents typical values and not production parameters.

## **A.9. List of publications**

Here below are listed works, published and presented, based on the thesis results.

### ***Papers in peer-reviewed journals:***

- L.V. Todorov, C.I. Martins, J.C. Viana - *Structure development of poly(ethylene terephthalate) during uniaxial stretching above the glass transition temperature: study of the statistical influence of the stretching variables*; Journal of Applied Polymer Science, Vol. 120, 1253–1265, 2011;
- L.V. Todorov, C.I. Martins, J.C. Viana - *Solid state structural evolution of poly (ethylene terephthalate) during step uniaxial stretching from different initial morphologies: an in situ WAXD*; Journal of Applied Polymer Science, Online
- L.V. Todorov, C.I. Martins, J.C. Viana - *In situ WAXS/SAXS structural evolution study during uniaxial stretching of PET nanocomposites in solid state: PET/MMT nanocomposites*; Composites Science and Technology, Submitted;
- L.V. Todorov, C.I. Martins, J.C. Viana - *In situ WAXS/SAXS structural evolution study during uniaxial stretching of PET nanocomposites in solid state: PET/SiO<sub>2</sub> and PET/TiO<sub>2</sub> nanocomposites*; Composites Science and Technology, Submitted;
- L.V. Todorov, C.I. Martins, J.C. Viana - *Characterization of PET nanocomposites with different nanofillers*; Solid State Phenomena, 151, 113-117, 2009;
- L.V. Todorov, J.C. Viana - *Structure evolution of PET under step-wise and continuous deformation modes: the effect of stress relaxation on the strain-induced morphology*; International Journal of Material Forming, 661–665, 2008;
- L.V. Todorov, J.C. Viana - *Characterization of PET nanocomposites produced by different melt-based production methods*; Journal of Applied Polymer Science, 106, 1659–1669, 2007;
- L.V. Todorov, J.C. Viana - *Morphology and mechanical properties of poly(ethylene terephthalate) stretched above the glass transition temperature*; AIP Conference Proceedings; 907, 795-800, 2007;

---

**Other papers:**

○ L.V. Todorov, C.I. Martins, J.C. Viana - *In situ structural evolution during uniaxial stretching of PET and its nanocomposites*, 14th International Conference on Deformation, Yield and Fracture of Polymers, Rolduc, Kerkrade, Netherlands April 2009, DYFP 2009 Book of Abstract, 443 – 446, 2009;

**Oral communications:**

○ L.V. Todorov, C.I. Martins, J.C. Viana - Multi scale structure evolution of PET/MMT and PET/SiO<sub>2</sub> nanocomposites upon solid state uniaxial deformation: an in situ WAXS/SAXS study; POLYCHAR 19 – World Forum on Advanced Materials March 20-24, 2011, Kathmandu, Nepal;

○ L.V. Todorov, J.C. Viana - *Phases and texture evolution during uniaxial deformation of polymers*; International Symposium on Plasticity and its Current Applications, 3-8 January 2010, St.Kitts;

○ L.V. Todorov, C.I. Martins, J.C. Viana - *In situ WAXS structural evolution during uniaxial stretching of PET and PET/MMT nanocomposites*; Fifth International Materials Symposium (Materiais 2009), April 2009, Lisbon, Portugal;

○ L.V. Todorov, J.C. Viana - *Deformation processes in polymer nanocomposites*; International Symposium on Plasticity 2009, St. Thomas, US Virgin Islands, 3-8 January 2009;

○ L.V. Todorov, C.I. Martins, J.C. Viana - *Characterization of PET nanocomposites with different nanofillers*; EMRS Fall Meeting, Warsaw, Poland, 15-19 September 2008;

○ L.V. Todorov, J.C. Viana - *Structure evolution of PET under step-wise and continuous deformation modes: the effect of stress relaxation on the strain-induced morphology*; ESAFORM 11; Lyon, France, April 2008;

○ L.V. Todorov, A.D. Kouyumdzhiev, J.C. Viana - *Structure evolution of amorphous and semicrystalline polymers during uniaxial stretching as observed by WAXS*; PPS 24 Polymer Processing Society Annual Meeting, Italy, Salerno 15-19 June 2008;

○ H. Smilkov, L.V. Todorov, R.S. Simoes, J.C. Viana, G.R. Dias - *Development of molecular orientation during stretching of amorphous polymers: complementary molecular dynamic*

## ***Appendix***

---

*simulations and WAXS studies*; Workshop on Multi-Scale Modelling of Nanostructured and Functional Polymeric Materials, Brno, Czech Republic, 7 - 10 October 2007;

### ***Poster communication:***

○ L.V. Todorov, C.I. Martins, J.C. Viana - *Multi scale structure evolution of PET nanocomposites upon solid state uniaxial deformation: an in situ WAXS/SAXS study*; 14th Nanostructured Polymers/Nanocomposites, Halle (Saale), Germany, 18-19 May 2010; (Awarded for best poster);

○ L.V. Todorov, C.I. Martins, J.C. Viana - *Structural evolution during uniaxial stretching of PET nanocomposites with 3D nanofillers: an in situ WAXS and SAXS study*; Institute of Nanostructures, Nanomodelling and Nanofabrication - I3N Annual meeting, Fatima, Portugal, February 2010;

○ L.V. Todorov, C.I. Martins, J.C. Viana - *In situ structural evolution during uniaxial stretching of PET and its nanocomposites*, DYFP 2009, 14th International Conference on Deformation, Yield and Fracture of Polymers, Rolduc, Kerkrade, Netherlands April 2009.





